

Spin Dynamics in 122-Type Iron-Based Superconductors

Von der Fakultät Mathematik und Physik der Universität Stuttgart
zur Erlangung der Würde eines Doktors der Naturwissenschaften
(Dr. rer. nat.) genehmigte Abhandlung

vorgelegt von

Jitae Park

aus Seoul (Südkorea)

Hauptberichter: Prof. Dr. Bernhard Keimer

Mitberichter: Prof. Dr. Harald Giessen

Tag der mündlichen Prüfung: 16. Juli 2012

Max-Planck-Institut für Festkörperforschung

Stuttgart 2012

Contents

Zusammenfassung in deutscher Sprache	3
1 Introduction	7
1.1 General overview	7
1.2 Scope of thesis	9
2 Iron-based superconductors	13
2.1 Basic characteristics	13
2.1.1 Zoo of iron-based superconductors	13
2.1.2 Crystal structure and reciprocal-space structure	14
2.1.3 Electronic band structure	18
2.2 Phase diagram	21
2.2.1 External parameters for modification of the system	22
2.2.2 Long-range magnetic order and its spin dynamics	27
2.2.3 Coexistence of magnetic and superconducting phases	31
2.2.4 Spin dynamics in the parent compound	34
2.3 Superconducting properties	42
2.3.1 Pairing symmetry	43
2.3.2 Coupling constant $2\Delta/k_B T_c$	45
2.4 Magnetic resonant mode in the spin-excitation spectra	47
2.4.1 Theoretical approach	48
2.4.2 Experimental observations	49
3 Experimental methods	51
3.1 Preparation of single crystalline samples	51
3.1.1 Flux method for single crystal growth	51
3.1.2 Sample characterization	54
3.2 Neutron scattering technique	59
3.2.1 Scattering formulae	60
3.2.2 Triple-axis neutron spectrometer	70
3.2.3 Spurious	76

4	Results and discussion	79
4.1	Hole-doped $\text{Ba}_{1-x}\text{K}_x\text{Fe}_2\text{As}_2$	79
4.1.1	Characterization of physical properties	79
4.1.2	Neutron and X-ray diffraction	81
4.1.3	μSR and magnetic force microscopy measurements	84
4.1.4	Magnetic field effect	88
4.2	Electron-doped $\text{BaFe}_{1.85}\text{Co}_{0.15}\text{As}_2$ and $\text{BaFe}_{1.91}\text{Ni}_{0.09}\text{As}_2$	89
4.2.1	Sample characterization and experimental details	89
4.2.2	The spin-excitation spectrum in the SC state	91
4.2.3	The spin-excitation spectrum in the normal state	102
4.2.4	Asymmetric spin-excitation spectrum	103
4.3	Superconducting $\text{Rb}_{0.8}\text{Fe}_{1.6}\text{Se}_2$ compound	118
4.3.1	Sample characterization	119
4.3.2	$\sqrt{5} \times \sqrt{5}$ magnetic order	120
4.3.3	Magnetic resonance mode	122
5	Summary	127
5.1	Spin-dynamics in Fe-based superconductors within the itinerant framework	127
5.2	The magnetic resonant mode: Scaling relationships	129
A	TABLES	133
	Acknowledgements	155

Zusammenfassung

in deutscher Sprache

Die Entdeckung einer neuen Familie von Hochtemperatursupraleitern, die eisenbasierten Supraleiter (SL), erregte Aufsehen in der wissenschaftlichen Gemeinschaft. Die Sprungtemperatur für diese Materialien (T_c) ist bis zu 55 K hoch, was die bekannte Theorie der konventionellen Supraleitung nicht erklären kann. Das starke Interesse war nicht allein auf die hohe Sprungtemperatur zurückzuführen, sondern auch auf die vielen Gemeinsamkeiten mit Kupferoxid-basierten Hochtemperatursupraleitern, wie zum Beispiel die stark magnetische Ausgangsverbindung und die geschichtete chemische Struktur. Im Gegensatz zu den Kupraten besitzen diese neuen Supraleiter vermutlich weniger Komplikationen in der zugrundeliegenden Physik. Aus diesem Grund gab es die breite Meinung, dass diese Materialien eine wichtige Rolle in der Suche nach der Auflösung zu eines der größten Rätsel in der Festkörperphysik spielen: Was ist der Mechanismus der Hochtemperatursupraleitung?

Diese Dissertation enthält größtenteils experimentelle Ergebnisse. Die erste Zielstellung dieser Arbeit ist das Ausarbeiten des relevanten experimentellen Befunds, welcher Klarheit über die langwierige Frage nach dem Mechanismus der Cooper-Paarung in den Hochtemperatursupraleitern bringen soll. Ein aussichtsreicher Kandidat für den Paarungsklebstoff in den eisenbasierten Supraleitern sind magnetische Spinfluktuationen, analog zu den Gitterschwingungen in der BCS Theorie. Diese liegen nahe, aufgrund der Nähe zwischen antiferromagnetischen und supraleitenden Grundzustand und der relative schwachen Elektron-Phonon-Kopplung. Aus diesem Grund haben wir Neutronstreuung als primäre experimentelle Methode in dieser Studie angewendet, da man mit Neutronen hervorragend die magnetische Struktur und die dynamischen Eigenschaften von kondensierter Materie untersuchen kann. Vier verschiedene supraleitende Verbindungen waren Gegenstand der Forschung: leicht unterdotiertes $\text{Ba}_{1-x}\text{K}_x\text{Fe}_2\text{As}_2$, optimal elektrondotiertes $\text{BaFe}_{1.85}\text{Co}_{0.15}\text{As}_2$ und $\text{BaFe}_{1.91}\text{Ni}_{0.09}\text{As}_2$, und das kürzlich entdeckte $\text{Rb}_{0.8}\text{Fe}_{1.6}\text{Se}_2$.

Am Anfang dieser Dissertation werden wir anhand der verfügbaren Literatur den Wissenstand über eisenbasierten Supraleiter diskutieren, wobei der Schwerpunkt auf den magnetischen Eigenschaften liegt, z.B. Spinwellenanregungen in der Aus-

gangsverbindung und in den dotieren Materialien.

Darauffolgend werden wir einige experimentelle Aspekte meiner Dissertation ansprechen, zum Beispiel Einkristallpräparation und die Grundlagen der Neutronenstreuung am Dreiachsenspektrometer.

Für eine leicht unterdotierte $\text{Ba}_{1-x}\text{K}_x\text{Fe}_2\text{As}_2$ Probe werden wir die Phasenseparation in eine magnetisch geordnete und supraleitende Phase bei tiefen Temperaturen aufzeigen, was mittels komplementärer Methoden, wie Neutronen- und Röntgenstreuung, Myon-spin-relaxation und Magnetkraftmikroskopie beobachtet wurde. Anhand der experimentellen Daten können wir ausschließen, dass die Phasenseparation allein auf die inhomogene Verteilung von Kalium zurückzuführen ist.

Der bekannteste Effekt im Spinanregungsspektrum des SL Zustandes ist die magnetische Resonanzmode, welche die Charakteristik einer exzitonischen, kollektiven Spin-1-Mode unterhalb des Teilchen-Loch-Kontinuums hat. Unsere experimentelle Beobachtung der magnetischen Resonanzmode in $\text{BaFe}_{1.85}\text{Co}_{0.15}\text{As}_2$, $\text{BaFe}_{1.91}\text{Ni}_{0.09}\text{As}_2$, und $\text{Rb}_{0.8}\text{Fe}_{1.6}\text{Se}_2$ Verbindungen und ihre physikalische Bedeutung wird ausführlich in Kapitel 4 präsentiert. Weiterhin zeigt die temperaturabhängige Resonanzenergie ein Ordnungsparameter ähnliches Verhalten, in gleicher Art und Weise wie die SL-Energielücke, was innerhalb der itineranten Beschreibung der magnetischen Resonanzmode verstanden werden kann.

Da die meisten Theorien der Supraleitung auf dem Paarungsboson mit hinreichend spektralem Gewicht im Normalzustand basieren, hat die genaue Kenntnis des Spinanregungsspektrums oberhalb der SL Sprungtemperatur essentielle Bedeutung, um die Möglichkeit der magnetisch vermittelten Cooper-paarung zu untersuchen. Deshalb präsentieren wir Ergebnisse des Spinfluktuationsspektrums in absoluten Einheiten, wobei wir feststellen, dass das Normalzustandsspektrum ein spektrales Gewicht enthält, welches vergleichbar mit dem von unterdotierten Kupraten ist. Jedoch stimmt es mit den Vorhersagen der Theorie über nah antiferromagnetischen Metallen überein. Anschließend zeigen wir, dass die Temperaturentwicklung der Resonanzenergie monoton dem Schließen der SL Energielücke Δ folgt, was auch in der konventionelle Fermiflüssigkeitsnäherung zu erwarten ist. Die auf ersten Prinzipien basierte Berechnungen können unsere inelastische Neutronenstreudaten erstaunlich gut reproduzieren, insbesondere für die anisotropische Form der intraplanaren Spinanregungen. Dies impliziert, dass die Spindynamik in diesen Systemen mit Näherungen itineranter Modelle verstanden werden kann.

Schließlich sammeln wir alle veröffentlichten Daten der Resonanzenergien in verschiedenen Materialien und Dotierungen von eisenbasierten Supraleiter und vergleichen sie in einem Graph. Ein linearer Zusammenhang zwischen Resonanzenergie und T_c besteht mit $\omega_{\text{res}} \approx 4.8k_B T_c$, was ein wenig kleiner ist als der Wert für die Kuprate. Eine bestimmte Korrelation zwischen der Resonanzenergie und der SL Energielücke

wurde ebenfalls abgeleitet und ihre physikalische Bedeutung wird im Folgenden diskutiert.

Das Fazit dieser Dissertation wird lauten, dass die magnetische Dynamik in den eisenbasierten Materialien eine starke Korrelation mit Supraleitung zeigt, was durch die magnetische Resonanzmode, welche ein Kennzeichen unkonventioneller Paarungssymmetrie im supraleitenden Zustand ist, offenbart wird. Basierend auf der guten Übereinstimmung zwischen unseren INS Daten und den First-Principle-Berechnungen lässt sich sagen, dass die magnetische Dynamik in den eisenbasierten Supraleitern auf die Bewegung von itineranten Elektronen zurückzuführen ist.

Chapter 1

Introduction

1.1 General overview

Superconductivity is among the most exciting phenomena in condensed matter. Its extraordinary properties are a resistanceless flow of electrical current and an expulsion of magnetic field below a critical temperature, T_c . Although these phenomena appear on a macroscopic scale, they originate from the quantum mechanics of electrons: Formation of electron pairs that are bound together via a small attractive interaction between them, also called *Cooper pairs*. In conventional superconductors, this electron pairing is mediated by an electron-phonon interaction, and can be well understood within the microscopic-model Bardeen-Copper-Schrieffer (BCS) theory, developed in 1956 [1, 2]. For the superconductivity driven by phonon-mediated Cooper pairs, it has been theoretically shown that the highest T_c cannot exceed 40 K [3].

However, the advent of copper-oxide materials in 1986 broke that theoretical limitation by showing a superconducting (SC) transition temperature, for example, up to 133 K in a mercury-based copper-oxide superconductor [4, 5]. Since then, a number of different materials, named *unconventional* superconductors, have been subsequently discovered, whose SC behavior can not be understood within the phononic electron-pairing mechanism. Although other possible mechanisms for electron pairing in high- T_c superconductivity, such as spin fluctuations or polaron/bipolaron mediated pairing, have been proposed during the last two decades, no consensus has been reached yet in the academic community. The biggest obstacle mostly arises from the complexity of phase diagrams of unconventional superconductors. In cuprates, for example, there are several dominant physical phases – presumably originated from the strong-correlation effects in the form of on-site Coulomb repulsion between electrons – such as the Mott-insulating phase in a mother compound, complicated normal-state pseudogap phenomena, or spin- and charge-modulated phases in the underdoped regime [6, 7, 8]. Therefore, it is always desirable to discover a material-family that retains high- T_c

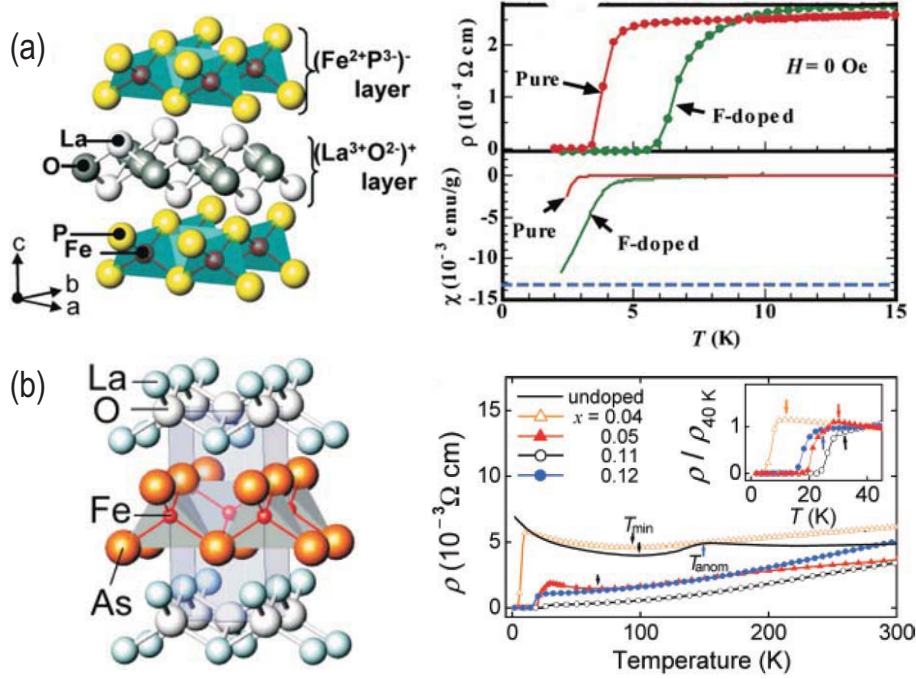


Figure 1.1: (a) The ZnCuSiAs-type crystal structure of LaFePO_{1-x}F_x, where the FeP-plane is stacking along *c*-axis alternating with blocking LaO-layers. The SC transition below 10 K is observed in resistivity and magnetization measurements [9]. (b) Left panel shows the same crystal structure of LaFeAsO_{1-x}F_x. Right panel displays the SC transition in resistivity measurement [10].

superconductivity with less complications in the underlying physics.

In 2006, a Japanese group led by H. Hosono synthesized a new class of superconductors, LaFePO_{1-x}F_x, which consists of FeP layers stacking alternatively with LaO-block layers along the *c*-axis, and observed the SC behavior below 4 K from resistivity and magnetization measurements [Fig. 1.1 (a)] [9]. A surprise came up later, when the same group discovered LaFeAsO_{1-x}F_x material by replacing P with As [Fig. 1.1 (b)] [10]. The SC transition temperature went up to 26 K [10] and reached even higher *T_c* of 45 K under pressure [11]. Such an enhancement of *T_c* in FeAs superconductors immediately attracted attention since LaFeAsO_{1-x}F_x could be the next candidate to beat the world highest *T_c* record in Hg-based cuprates with *T_c* of 133 K [5]. More importantly, Fe-based superconductors (FeSC) could represent a better testing ground for microscopic theories of the Cooper-pairing mechanism in unconventional superconductors because FeSC shares many similar physical phenomena with cuprates, but with presumably less complications in the underlying physics.

Common physical properties of FeSC with high-*T_c* copper-oxide perovskites are known to be following [12, 13, 14, 15, 16, 17, 18, 19, 20, 21, 22, 23, 24, 25, 26]:

1. Layered crystal structure: Transition-metal pnictide (FeAs) layers play an impor-

tant role for most of physical properties in this family of compounds.

2. Static magnetism: The parent compounds of FeSC possess an antiferromagnetic (AFM) order (spin-density wave) at low temperature accompanied by an orthorhombic structural distortion. The spin-density-wave (SDW) state can be suppressed either by substituting different chemical elements or applying uniaxial pressure.
3. Emergence of superconductivity under charge doping: Upon chemical doping, superconductivity appears above a certain doping level, and the static magnetic order gets suppressed gradually.
4. Dome shaped SC transition temperature: T_c gradually increases as doping level increases, then reaches the maximal T_c at the optimal doping level. The SC transition temperature then slowly goes down in the overdoped regime.

On the other hand, in following respects FeSC are different from cuprates.

1. Poor metallic parent compound: While the parent compounds of cuprates exhibit Mott-insulating behavior (strongly localized electrons), parent compounds of FeSC behave as poor metals (itinerant electrons).
2. Emergence of superconductivity in the undoped compound under pressure: The superconductivity can be induced purely by applying pressure to a parent FeSC without introducing chemical substitution, whereas in cuprates application of pressure only enhances already existing T_c .

Details of each property will be described throughout Sec. 2.1-2.3. In addition to similar and distinct aspects with cuprates in FeSC, early electron-phonon coupling calculations using Migdal-Eliashberg theory on this family compound predicted that the electron-phonon coupling strength is not strong enough to explain the reported highest T_c ($\text{Gd}_{1-x}\text{Th}_x\text{FeAsO}$, $T_c=56.3\text{ K}$ [28]) in FeSC [27], thus suggesting that the SC Cooper-pairing in this material is not driven purely by phonons, but requires an alternative pairing “glue”. Similar to the cuprates, the most feasible candidate for electron-pairing mediator in FeSC is the spin excitations since superconductivity is found to be in close proximity to the magnetism in this system.

1.2 Scope of thesis

In this thesis, we present the experimental data on four different iron-based SC materials. It is mainly about the magnetic-dynamics study in the FeSC that is assumed to be among the most crucial ingredients for superconductivity in this system. Thus, the

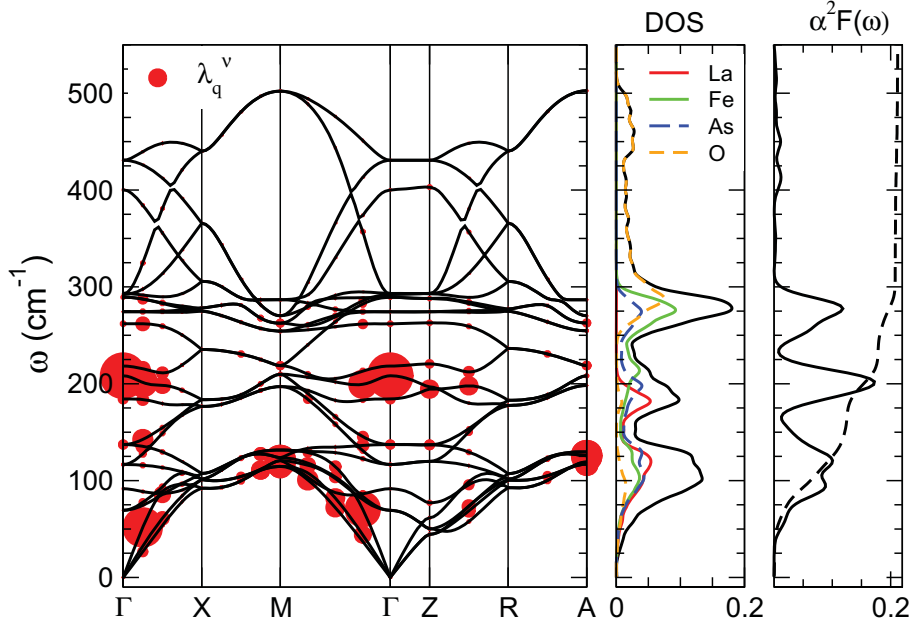


Figure 1.2: Electron-phonon coupling strength in $\text{LaFeAsO}_{1-x}\text{F}_x$ depicted in the phonon-dispersion relation of $\text{LaFeAsO}_{1-x}\text{F}_x$ from Ref. [27]. The radius of red circles is proportional to the strength of electron-phonon coupling in corresponding phonon modes. From this calculation, authors claimed that the electron-phonon coupling in FeSC is not strong enough to establish the reported high SC transition temperature in FeSC.

main goal of this thesis is to figure out the exact relationship between spin dynamics and superconductivity, and then further to realize what is the contribution of magnetic fluctuations for superconductivity by providing experimental data for modeling a microscopic mechanism of electron pairing in the FeSC system.

In Chap. 2, we first discuss basic characteristics of FeSC, such as crystal structure and electron band-structure by briefly reviewing the relevant literature. Then, an introduction about magnetic and SC phases will follow based on the generic phase diagram. Details about current understanding of magnetic ground state in the parent compounds will be discussed in terms of spin-wave excitations which would be important when we are considering the spin dynamics in doped materials.

To study magnetic dynamics in FeSC, we employed the inelastic-neutron-scattering (INS) method which can uniquely probe the underlying spin dynamics in the four-dimensional energy and momentum space in a wide range. By taking advantage of the well developed theory for the magnetic neutron-scattering process, one can quantify the imaginary part of spin susceptibility that is an essential physical quantity the description of elementary magnetic excitations and can be compared with theoretical calculations directly. Moreover, the technique's energy-resolving scale spans over the most relevant energy range of magnetic fluctuations (from 0 to 100 meV). For these reasons, neutron scattering is a very powerful technique for magnetism study, and we

introduce how neutron-scattering experiment works theoretically and practically in Chap. 3.

Usually the sample size is a bottleneck for INS measurements since reasonable scattering intensity can only be acquired with a massive sample. Owing to availability of sizable $\text{BaFe}_{1.85}\text{Co}_{0.15}\text{As}_2$ ($T_c = 25$ K), $\text{BaFe}_{1.91}\text{Ni}_{0.09}\text{As}_2$ ($T_c = 19$ K), and $\text{Rb}_{0.8}\text{Fe}_{1.6}\text{Se}_2$ ($T_c = 32$ K) single crystals grown either by flux- or Bridgman-method, we have successfully carried out a number of INS experiments to measure spin-excitations spectra both in the SC and in the normal states. A brief description about the single-crystal growth and basic characterization of studied samples is also presented in Chap. 3.

For a slightly underdoped $\text{Ba}_{1-x}\text{K}_x\text{Fe}_2\text{As}_2$ compound, we report the phase separation between magnetically ordered and SC phases at low temperatures, which was confirmed by complementary experimental techniques such as neutron and X-ray scattering, muon-spin relaxation, and magnetic-force microscopy measurements. Based on our experimental data, we discuss the possibility of this phase separation being an intrinsic property of the $\text{Ba}_{1-x}\text{K}_x\text{Fe}_2\text{As}_2$ system. However, this view has been recently challenged by several new measurements performed on the next generation of single crystals [29, 30], which apparently exhibit a much more homogeneous behavior. These results are presented and discussed in Chap. 4.

The most prominent feature in the spin-excitation spectrum of the SC state is the magnetic resonant mode that is characterized as spin-1 excitonic collective mode below the edge of the particle-hole continuum. Our experimental observations of magnetic resonant modes in $\text{BaFe}_{1.85}\text{Co}_{0.15}\text{As}_2$, $\text{BaFe}_{1.91}\text{Ni}_{0.09}\text{As}_2$, and $\text{Rb}_{0.8}\text{Fe}_{1.6}\text{Se}_2$ compounds will be presented and a discussion about their physical implications will follow in Chap. 4. In addition, we will show that the temperature-dependent resonance energy displays an order-parameter-like behavior in the same manner as the SC energy gap that is expected within the conventional Fermi-liquid approaches for the magnetic resonant mode.

As most theories of superconductivity are based on a pairing boson of sufficient spectral weight in the normal state, detailed knowledge of the spin-excitation spectrum above the SC transition temperature is fundamentally required to assess the viability of magnetically mediated Cooper pairing. Thus, in Chap. 4, we present the results of normal-state spin-fluctuation spectra in absolute units and find that the normal-state spectrum carries a weight comparable to that in the underdoped cuprates, while the spectrum agrees well with predictions of the theory of nearly antiferromagnetic metals [31]. In the following, we show that the first-principles calculations can remarkably well reproduce our INS data, especially for anisotropic shape of in-plane spin fluctuations, implying that the spin dynamics for paramagnetic state in this system can be well described within the itinerant approach.

Finally, in Chap. 5, we collect all the reported resonant mode data in various materials and doping levels of FeSC, and compare them after putting in the same plot. A linear relation between resonance energy and T_c is realized with a ratio of $\omega_{\text{res}}/k_B T_c \approx 4.8$, which is slightly lower than the respective value for cuprates. A certain correlation between the resonance energy and SC energy gap is also found, and its physical implications will be further discussed.

Chapter 2

Iron-based superconductors

2.1 Basic characteristics

2.1.1 Zoo of iron-based superconductors

After the discovery of $\text{LaFeAsO}_{1-x}\text{F}_x$, so-called ‘1111’ or oxypnictide superconductors, a series of different structure types of FeSC have been subsequently found as shown in Fig. 2.1 from Ref. [32]. For the sake of convenience, such different types of compounds are usually denoted by their stoichiometric ratios of chemical constituents, e. g., ‘122’ represents the materials based on $A\text{Fe}_2\text{As}_2$ (A = alkaline metals). Despite the variety of different structure types in these compounds, they all share a common building block consisting of a square planar sheet of Fe, which is tetrahedrally coordinated by neighboring pnictogen or chalcogen atoms. Such FeAs planes are separated by spacer layers in 1111-, 122-, and 111-ferropnictides along the c -axis. On the other hand, in 11-type superconductors FeSe layers are stacking along the c -axis without any blocking layers in between (Fig. 2.1). In spite of minor differences among different families, the Fe-pnictide or -chalcogenide layers are believed to determine for the most important physical properties in FeSC systems [12, 13, 14, 15, 16, 17, 18, 19, 20, 21, 22, 23, 24, 25, 26]. Therefore, numerous attempts have been made in order to optimize the structural parameters of this layer for the highest T_c .

Early on, it was suggested that the interlayer distance between neighboring Fe-pnictogen or -chalcogen layers could be well correlated with the SC transition temperature. Such prediction led to an attempt to synthesize materials with significantly longer unit cells along the c -axis, such as $(\text{Sr}_3\text{Sc}_2\text{O}_5)\text{Fe}_2\text{As}_2$, shown in Fig. 2.1, denoted as the 32522 family [33]. Soon thereafter, however, it was found that the angle between As-Fe-As bonds, where two arsenic atoms are located within the same plane, shows a better correlation with T_c : T_c becomes maximized in the vicinity of bonding angle of 109.47° [Fig. 2.2 (left)] [24]. This criterion applies to most of the FeSC families, indicating that such correlation can be regarded as a universal characteristic. In addition,

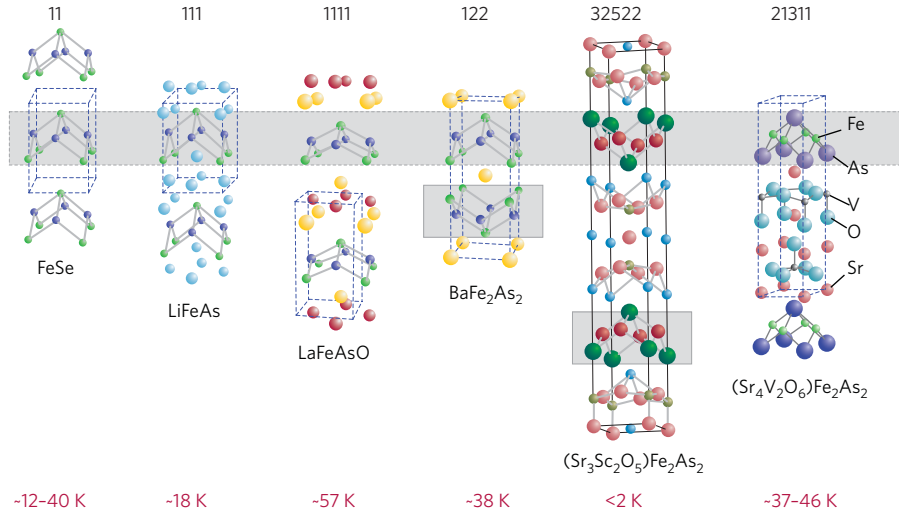


Figure 2.1: The variety of different FeSC types, which have been discovered up to date [15]. Commonly Fe-pnictide or -chalcogenide layers separated by different blocking layers depending on chemical composition of materials are accommodated in all compounds.

alternative relation has been also found between T_c and pnictogen height from the Fe plane, revealing that the highest T_c can be always found when the pnictogen height is close to $h \sim 1.4 \text{ \AA}$ [Fig. 2.2 (right)] [24]. So far, there is no clear understanding of which structural parameter between the bonding angle and pnictogen height is more sensitive to the SC transition temperature. Nevertheless those experimental data clearly reveal a convincing universal relation between T_c and structural parameters in the FeSC systems.

The constantly ongoing search for the new high- T_c materials recently yielded a new type of FeSC, $A_x\text{Fe}_{2-y}\text{Se}_2$ ($A = \text{K, Rb, Cs}$), with exotic structural and magnetic properties [34, 35, 36]. Yet, a detailed study is required to check the validity of the universal relation in these compounds.

Among the variety of such stoichiometric materials serving as “parent” phases for numerous FeSC, only a few have so far gained proper experimental attention, especially by inelastic neutron scattering (INS), due to miscellaneous reasons related to the availability of sizeable single crystals or their chemical stability. For instance, to the best of our knowledge, spin-excitation studies of iron pnictides have so far remained limited to the ‘122’ family, whose single crystals are typically stable in air and are readily available in large sizes necessary for INS experiments. Hence, most of the work in this thesis focuses on the 122-type FeSC.

2.1.2 Crystal structure and reciprocal-space structure

A landmark of the crystallographic structure in FeSC is the square Fe-pnictide or -chalcogenide basal plane [12, 13, 14, 15, 16, 17, 18, 19, 20, 21, 22, 23, 24, 25].

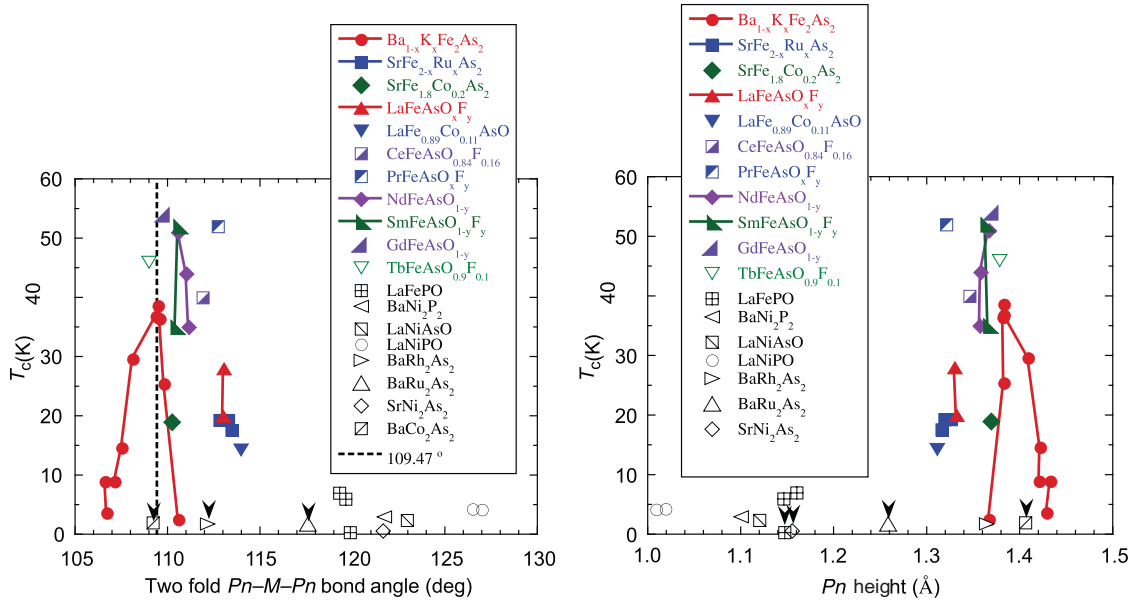


Figure 2.2: From Ref. [24]. **Left.** SC transition onset temperatures versus As-Fe-As bonding angle at the room temperature among different species of FeSC. T_c becomes maximized at an angle close to 109.47° . **Right.** Variation of onset T_c depending on the pnictogen height from Fe plane. Maximum T_c of each family materials are found around $h \sim 1.4 \text{\AA}$.

Fig. 2.3 (e) displays a representative conventional unit cell of a 122-ferropnictide, $BaFe_2As_2$, where the room-temperature lattice parameters are $a = b = 3.96 \text{\AA}$ and $c = 13.02 \text{\AA}$ [37]. Although this is not the primitive unit cell for the body-centered-tetragonal $ThCr_2Si_2$ -type structure with the $I4/mmm$ space group, it has been widely used in most of the experimental studies due to its simplicity and convenience. The primitive unit cell of 122 is drawn in Fig. 2.3 (b), and as one can see in the figure, not like most of the FeSC families where it contains one Fe atom in their formula units, the 122-compound possesses two iron atoms in its formula unit. The number of Fe atoms per formula unit is reflected in the c -axis lattice-constant of the conventional unit cell, which for the 122-family is about $\sim 13 \text{\AA}$ [38], whereas for 1111- and 111-families c lattice constants are about a half of 122's ($\sim 7 \text{\AA}$) [9, 39, 40]. On the other hand, the in-plane lattice constant ($\sim 4 \text{\AA}$) hardly varies among all families of compounds [24]. This fact governs the nontrivial complication in comparison of the reciprocal-space structure among FeSC families.

The body-centered-tetragonal structure of parent 122-compound (space group: $I4/mmm$) undergoes a structural phase-transition to the orthorhombic phase (space group: $Fmmm$) at low temperatures. In the orthorhombic phase, the tetrahedron $FeAs_4$ becomes distorted by rearranging iron atoms in a slightly different way. As a result, in-plane lattice constants a and b are no longer equivalent, and in-plane crystallographic axes are rotated by 45° .

We now turn to the reciprocal space structure of the body-centered-tetragonal

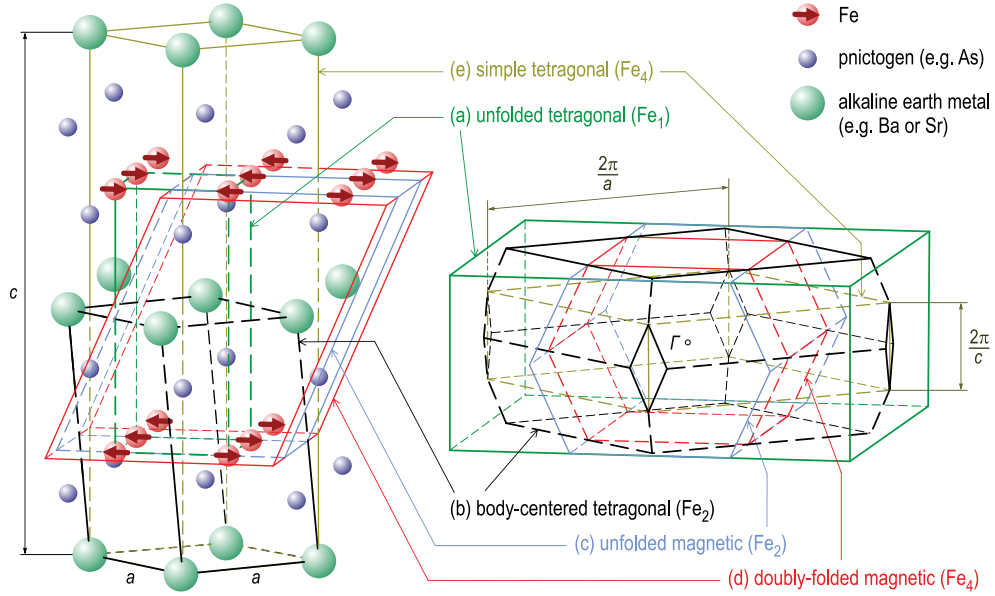


Figure 2.3: Different primitive unit cells in direct space (left) that can be introduced in 122-ferropnictides and their respective Brillouin zones (right): (a) unfolded tetragonal BZ of the Fe sublattice with one Fe atom per unit cell (Fe_1); (b) structural body-centered-tetragonal BZ that corresponds to two iron atoms per primitive unit cell (Fe_2); (c) unfolded magnetic BZ that corresponds to the magnetically ordered Fe sublattice in the SDW state (Fe_2); (d) doubly folded magnetic BZ that results if both the lattice and magnetic structures are taken into account (Fe_4); (e) one of the most commonly used and experimentally convenient reciprocal-space coordinate systems that corresponds to the BZ of a simple-tetragonal direct lattice with the parameters of the real body-centered-tetragonal crystal.

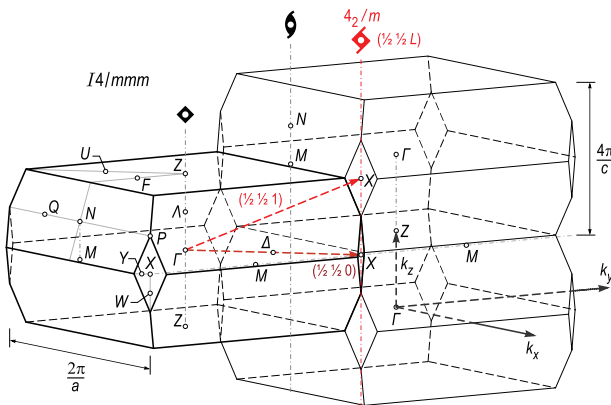


Figure 2.4: The reciprocal-space structure of the body-centered-tetragonal $I4/mmm$ system. The BZ polyhedron of $BaFe_2As_2$ is drawn at the left in solid black lines, and two more such polyhedra are drawn to illustrate the 3D stacking of the BZ. Two $\Gamma\bar{X}$ vectors are shown by dashed arrows: The SDW ordering wave-vector of the parent compound $\mathbf{Q}_{AFM,Fe_4} = \left(\frac{1}{2} \frac{1}{2} 1\right)_{Fe_4}$ and its in-plane projection $\mathbf{Q}_{\parallel,Fe_4} = \left(\frac{1}{2} \frac{1}{2} 0\right)_{Fe_4}$. Symmetry axes are denoted by dash-dotted lines.

primitive unit cell of BaFe_2As_2 . The 3D stacking of the $I4/mmm$ tetragonal Brillouin zones (BZ) with the dimensions of $\frac{2\pi}{a} \times \frac{2\pi}{b} \times \frac{4\pi}{c}$ (here a, b, c are the lattice constants of conventional unit-cell) is illustrated in Fig. 2.4 and is valid both for the momentum (\mathbf{k}) and momentum transfer (\mathbf{Q}) spaces. In this notation, the quasi-two-dimensional (2D) warped hole- and electron-like FS cylinders [41, 42, 43, 44] are centered around $\Gamma\Lambda Z$ and XPX symmetry axes along the zone boundaries, respectively. The crystal symmetry axes are shown in Fig. 2.4 by dash-dotted lines. In particular, the $4_2/m$ screw symmetry along the XPX axis appears only in the body-centered-tetragonal BZ with 2 Fe atoms per primitive cell as a result of folding, but is found neither in the unfolded BZ corresponding to the Fe-sublattice because of the missing (1 0 1) translation, nor in the magnetic BZ because of the spontaneously broken 4-fold rotational symmetry in the SDW or orthorhombic phases (see Fig. 2.3). This $4_2/m$ screw symmetry, which is imposed by alternatively located arsenic atoms with respect to Fe layer, is especially important because it appears only in 122-ferropnictides, affecting some of its physical characteristics. It is also essential that the $4_2/m$ symmetry axis coincides with the \mathbf{Q} -space location of the spin excitations found in inelastic neutron scattering (INS) experiments, which allows one to compare the magnetic intensities along this direction. These excitations originate from the nested hole- and electron-like Fermi surfaces [45, 46, 41, 47, 48, 49, 42] and will be intensively discussed in Sec. 4.2.3.

In Fig. 2.3, we summarize some of the possible coordinate systems and reciprocal-space notations that can be introduced in the 122 compounds. The figure shows five different BZs in the reciprocal space (right) and their respective primitive unit cells in direct space (left). It is natural to consider two BZ types: *unfolded*, i. e., corresponding to the Fe sublattice only, and *folded*, which takes full account of the remaining nonmagnetic atoms in the unit cell. Because of the higher symmetry of the Fe sublattice with respect to the crystal itself, the unfolded zones have twice larger volume than their folded counterparts. Next, one can also distinguish between the *nonmagnetic* and *magnetically folded* BZ, which correspond to the normal and SDW states, respectively. As a result, we end up with four different direct-space lattices, reciprocal-space coordinate systems, and BZ geometries that can be naturally introduced in the 122-compounds: (a) unfolded tetragonal (Fe_1); (b) body-centered-tetragonal (Fe_2), where the $4_2/m$ screw symmetry is present along c -axis; (c) unfolded magnetic (Fe_3); and (d) doubly folded magnetic (Fe_4). The formulas in brackets give the number of iron atoms in the primitive unit cell. In addition, Fig. 2.3 (e) shows the simple tetragonal unit cell (Fe_4), which defines the reciprocal-space notation commonly used in the literature, but does not represent a primitive unit cell of the crystal. Throughout this thesis, we are going to mainly use the unfolded tetragonal iron-sublattice notation since we have proven that the spin-excitation spectrum is insensitive to the structural folding, thus the unfolded description of the spectrum

becomes physically justified [50]. If it's necessary to use different notation anywhere, we will introduce a notation with subscript, \mathbf{Q}_{Fe_n} , where n represent the number of Fe atoms contained in the corresponding unit cells.

2.1.3 Electronic band structure

Electronic band structure, which is described by a electron wave function in the periodic potential of a lattice, is one of the most important characteristics of a material since many physical phenomena, such as transport and optical properties, photoelectron spectra, and dynamic magnetic susceptibility, can be determined from the electronic band structure [51, 52].

Fig. 2.5 shows the electronic band structure calculated within the local-density approximation (LDA) in density functional theory (DFT) for LaFeAsO in panel (a) [53] and for BaFe₂As₂ compound in panel (b) [41]. According to these calculations for both compounds, only Fe 3d orbital bands are present near the Fermi energy, while pure As 4p bands only appear around ~ 3 eV. In Fig. 2.5, one can see that five 3d bands are located close to each other, crossing the Fermi level, which reveals the multi-band character of FeSC. In both materials, three out of five iron bands show an upward dispersion at Γ and Z points where these can be assigned to hole-like Fermi pockets, and rest of bands posses a downward dispersion, forming an electron-like Fermi pocket at the M point for 1111 and at the X point for the 122 system. The different location of electron Fermi pockets in the reciprocal space between 1111 and 122 is not a true effect, but it is a consequence of different notation resulting from crystal symmetry [24]. As discussed in Sec. 2.1.2, 122 ferropnictides have a body-centered tetragonal crystal structure ($I4/mmm$), and its reciprocal lattice is therefore faced-centered tetragonal. However, the faced-centered tetragonal cell does not belong to a conventional Bravais lattice [24]. Hence, one can alternatively choose the reduced body-centered tetragonal reciprocal unit cell, which would result in a reduction of reciprocal lattice length and rotation of in-plane reciprocal lattice vectors by 45° with respect to the crystallographic directions [24]. Therefore, essentially the positions of the electron-like Fermi pocket in 1111 and 122 system are not different. By using Fe-sublattice (Fe_1) notation, corresponding to unfolded BZ, we avoid such complications throughout this thesis. This unfolded zone is often introduced to simplify the band-structure description of the iron pnictides [54, 46], but is usually considered only as a theoretical abstraction because every realistic band structure is certainly affected by the pnictogen atoms that lowers the symmetry of the direct lattice, and as a result an additional translational symmetry is introduced in the reciprocal space due to the BZ folding. These effects have been recently quantified in Ref. [55]. Nevertheless, as we will demonstrate in the following, the absence of any appreciable magnetic moment on the pnictogen atoms

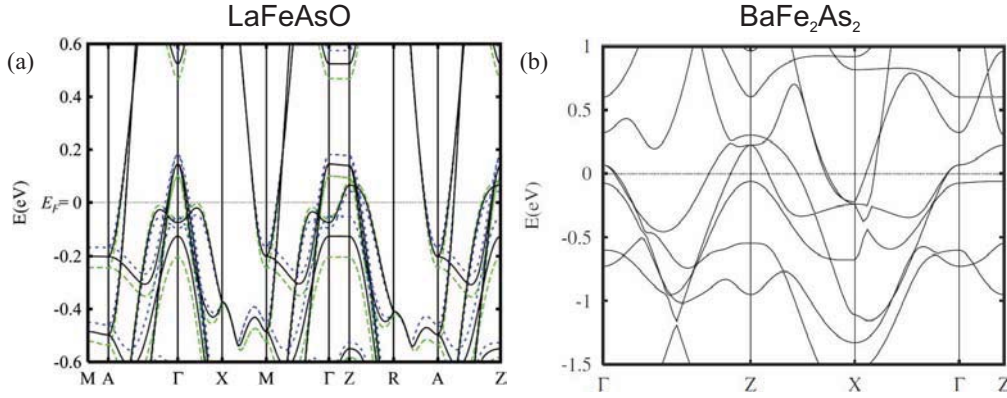


Figure 2.5: Calculated electronic band structure by LDA for (a) LaFeAsO [53] and (b) BaFe₂As₂ compound [41]. Both panels only show Fe 3d-orbital bands close to the Fermi energy since the pure arsenic 4p-bands are present far below from the Fermi level (~ 3 eV). Five of Fe 3d bands are located near the Fermi level, indicating a multiband character of Fe-based superconductors. Blue and green dashed lines in panel (a) display shifted bands introduced by a little displacement of As atoms away and toward from Fe plane along c -axis. For both compounds, hole bands are placed at Γ position whereas electron bands appear at M position for 1111-compound and at X position for 122-compound.

allows for a much simpler description of the magnetic dynamics, which experiences no structural folding and hence does not acquire the additional reciprocal-space symmetry expected in the back-folded tetragonal (structural, nonmagnetic) BZ.

In panel (a) of Fig. 2.5, blue and green dashed lines represent shifted bands caused by a weak displacement of arsenic atoms (0.035 \AA) away and toward from Fe plane along c -axis [53]. Such high sensitivity of electronic band shift to dislocation of As atoms is quite interesting, and it is also known that depending on the pnictogen height in the calculated magnetic moment by LDA can vary dramatically, which creates a considerable discrepancy between the calculated [45, 56] and experimentally measured magnetic moment [57, 58] in FeSC. We will discuss the magnetic moment in more detail in the SDW state in Sec. 2.2.2.

As seen in Fig. 2.5, simultaneously existing hole- and electron-like Fermi pockets lead to a significant interband scattering at the nesting vector $\mathbf{Q}_{\parallel, \text{Fe}_1} = (\pi, 0)$, which is believed to be one of the main driving forces for the magnetic instability and superconductivity in FeSC [54]. The in-plane projection of nesting vectors is depicted in Fig. 2.6 by the red arrow.

Three-dimensional (3D) LDA Fermi surfaces for LaFeAsO and BaFe₂As₂ materials are shown in Fig. 2.6 (a) and (b) respectively [53, 41]. In general, both hole (corner of the depicted BZ) and electron (centre of the depicted BZ) Fermi pockets exhibit cylindrical-shape Fermi barrels along c -axis. For 1111 system [Fig. 2.6 (a)], there are three hole Fermi barrels along $\Gamma Z \Gamma$ and two electron Fermi barrels at M with the

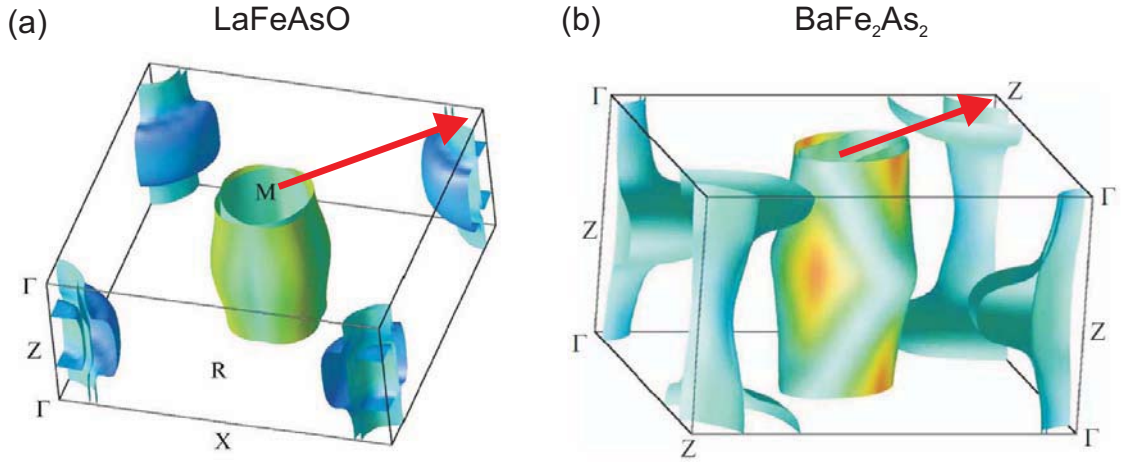


Figure 2.6: Three-dimensional LDA Fermi surface for (a) LaFeAsO [53] and (b) BaFe₂As₂ compound [41]. Three cylindrical hole Fermi pockets are at Γ point (corner of a rectangular parallelepiped), and two electron Fermi pockets are at M for 1111 and X for 122 ferropnictides. While the Fermi surface of 1111 systems shows moderate k_z -dispersion, 122 system exhibits the strong k_z dependence especially for electron Fermi pocket: The elliptical in-plane shape changes direction of elongated axis by 90° at every half of BZ size along c -axis that is imposed by $4_2/m$ screw symmetry. Schematic in-plane projection of nesting vectors is drawn by the red arrows.

moderate k_z dependent dispersion. On the other hand, for BaFe₂As₂ Fermi surface shows stronger k_z -dispersion than for 1111, especially for the electron Fermi pocket at X position [Fig. 2.6 (a)]. The in-plane shape of the electron Fermi pocket at X point (again M for 1111 and X for 122 in the reciprocal notation are the physically equivalent position) in 122 system is elliptical consisting of two iron bands, and such elliptical in-plane configuration alters its elongated axis by 90° at every half of BZ size along c -axis. This peculiar symmetry is the unique property of the 122 ferropnictide system invoked by the $4_2/m$ screw symmetry along the XPX axis, as discussed in Sec. 2.1.2.

These theoretically predicted 3D electronic band structures have been confirmed by a number of angle-resolved photoemission spectroscopy (ARPES) experiments on parent [59, 60, 61, 44, 62] or underdoped-ferropnictide materials [63, 64, 65, 43, 66, 67], and by the de Haas-van Alphen effect measurements on the undoped compounds [68, 69, 70, 71]. Fig. 2.7 (a) and (b) show representative ARPES data on BaFe₂As₂ compound measured by different groups [59, 44]. In the panel (a) of Fig. 2.7, the in-plane Fermi surface map integrated over 10 meV about the chemical potential is shown. The hole Fermi pocket at Γ and four blade-like pockets at the X point are present that is consistent to their five-band tight-binding model calculation. The flowerlike shape of the X -centered Fermi surface could be a consequence of the Fermi-surface reconstruction due to AFM correlations with the wave vector $\mathbf{Q}_{\text{Fe}_1} = (\pi, 0)$ [43]. Panel

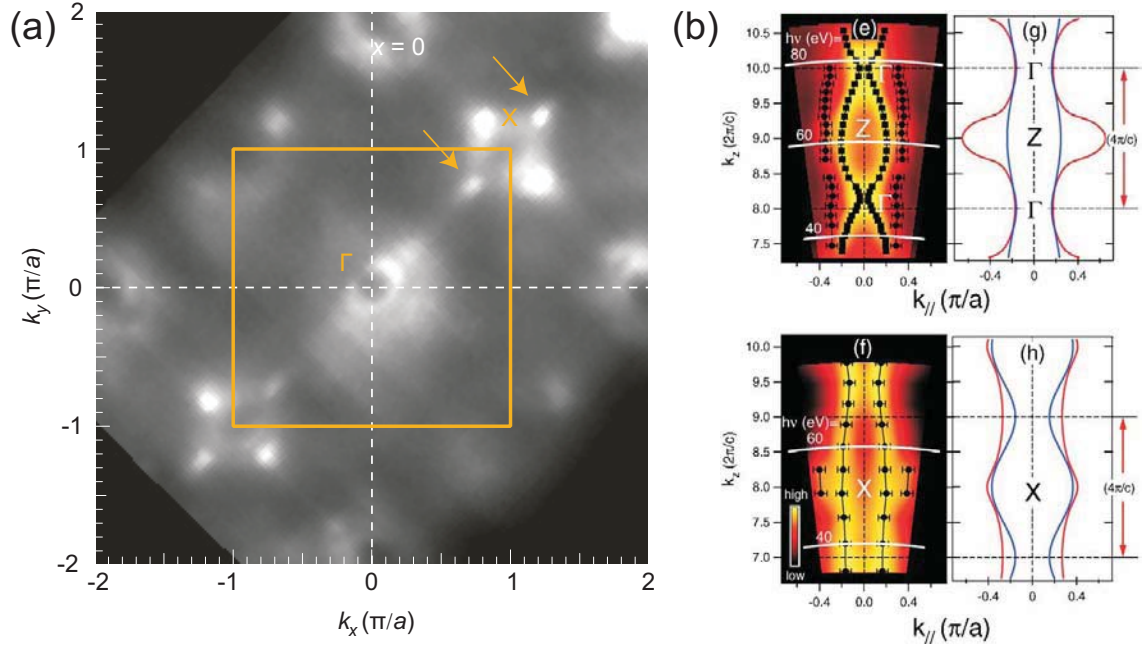


Figure 2.7: Experimental ARPES data on the parent BaFe_2As_2 from Ref. [44] and [59]. (a) Fermi surface topology integrated over 10 meV about the chemical potential. The hole Fermi pocket at Γ and electron pockets at X point are observed. A flower shape of electron Fermi surface could be due to the integration of Fermi surface along c axis. The data is taken in the magnetic state ($T = 20$ K) [44]. (b) The Fermi surface image in $k_{in-plane}$ - k_z plane acquired from photon-energy dependent ARPES data along fixed $k_{in-plane}$ cut ($T = 10$ K) [59]. Overall shape well matches to LDA band structure shown right next to the data, identifying a significant 3D character of electronic band structure of 122-ferropnictide.

(b) in the same figure shows k_z -dependence of hole (top panel) and electron (bottom panel) Fermi surfaces in $k_{in-plane}$ - k_z plane on the parent BaFe_2As_2 . For both Fermi barrels, a rather strong 3D corrugation has been observed. Although the Fermi surface reconstruction in the magnetic state ($T = 20$ K) [44] and renormalization factor have to be taken into account in those data, authors of this paper claimed that the overall shape of electronic band structure quite well matches their own calculations. However, other groups reported a strong deviations from the calculated band structure based on the similar experimental observations of propeller-shaped X -centered Fermi surface on the parent and K-doped BFA compounds [43].

2.2 Phase diagram

In this section, we shall discuss some physical properties of the FeSC systems based on their phase diagrams. A phase diagram provides an excellent overview how the system can be tuned by external parameters and also shows underlying physical phases. According to the generic phase diagram of FeSC (Fig. 2.8), it is important

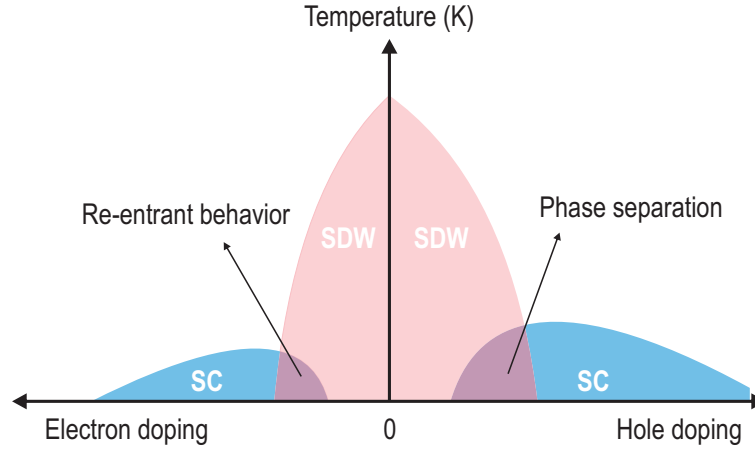


Figure 2.8: A generic phase diagram of FeSC under chemical doping. At the middle of phase diagram, the undoped parent compound shows a paramagnetic-metallic behavior in the normal state, and undergoes structural and magnetic phase transitions at low temperature (reddish area). The 122-parent system can be tuned either via replacing some alkaline metals within blocking layers (e.g. Ba in BaFe_2As_2) or substituting some transition metals (e.g. Co, Ni, etc.) into Fe layers. Gradually increasing amount of dopants suppresses structural and magnetic phase transitions, and eventually superconductivity emerges. The SC transition temperature is maximized at a certain doping level and slowly decrease upon further chemical doping.

to understand the magnetism in the parent compound of FeSC, since it is strongly related to superconductivity. For example, superconductivity slowly evolves as the static magnetism goes away, and the T_c is maximized at the point where the static magnetic order completely vanishes. Throughout this section, we will first discuss how the parent material behaves upon external parameters in terms of its electronic properties and ordered phases. At the end of this section, the magnetic dynamics in the parent compound will be discussed.

2.2.1 External parameters for modification of the system

Parent compound

The most important aspect in the phase diagram of FeSC is how superconductivity arises from the AFM metal compound. Fig. 2.8 shows a generic phase diagram of 122 ferropnictides versus chemical doping. The parent (undoped) compound of 122 system, AFe_2As_2 ($A = \text{Ca, Sr, Ba}$), has no superconductivity, but shows metallic behavior in the temperature-dependent resistivity curve [38, 72, 73]. However, the electrical resistivity value, ρ , at the room temperature is about $0.4 \text{ m}\Omega\cdot\text{cm}$ as shown in Fig. 2.11 (a) [73], which is two orders of magnitude higher than in pure elemental metals like copper, $\rho \sim 1.68 \mu\Omega\cdot\text{cm}$. This is why the parent compound is often

Compound	Optimal doping level	$T_{c,\text{optimum}}$ (K)	Type of charge carriers	Reference
$\text{Ba}_{1-x}\text{K}_x\text{Fe}_2\text{As}_2$	0.32	38.5	hole	[78]
$\text{Ba}(\text{Fe}_{1-x}\text{Co}_x)_2\text{As}_2$	0.125	25	electron	[79]
$\text{Ba}(\text{Fe}_{1-x}\text{Ni}_x)_2\text{As}_2$	0.1	20	electron	[80]
$\text{Ba}(\text{Fe}_{1-x}\text{Rh}_x)_2\text{As}_2$	0.057	23.2	electron	[81]
$\text{Ba}(\text{Fe}_{1-x}\text{Pd}_x)_2\text{As}_2$	0.053	19	electron	[81]
$\text{Ba}(\text{Fe}_{1-x}\text{Ru}_x)_2\text{As}_2$	0.35	20	isovalent	[82]
$\text{BaFe}_2(\text{As}_{1-x}\text{P}_x)_2$	0.32	30	isovalent	[83]

Table 2.1: A list of various 122-ferropnictides with their maximum SC transition temperature. Up to now, optimally-doped BKFA holds a record for the highest T_c among 122 materials.

called a “poor metal”. Such high electrical resistivity is understandable in terms of a semimetallic characteristic, where both hole and electron bands are partially filled simultaneously as shown in Fig. 2.5, since usually the charge concentration of semimetals is several orders of magnitude lower than typical metals [52]. Indeed, the first-principles calculations revealed the low charge-carrier density in the parent FeAs compound [41]. This metallic property of the parent compound is quite different from the well-known cooper-oxide high- T_c superconductors, where the undoped compound is a Mott insulator with localized electrons [74]. The tetragonal paramagnetic phase at room temperature experiences structural and magnetic phase transitions at 137 K for BaFe_2As_2 (BFA) [38], 173 K for CaFe_2As_2 (CFA) [75], and 198 K for SrFe_2As_2 (SFA) [76]. Across the phase transition temperature, the tetragonal $I4/mmm$ crystallographic symmetry is lowered to the orthorhombic $Fmmm$ symmetry. This structural transition seems not to be an abrupt transition, but rather a slight displacement of Fe and As atoms. At the same time, the static magnetic order (spin-density wave) sets in, aligning the spins at iron atoms with the AFM stripe order [77].

Aliovalent chemical substitution

Changing system’s environment by external parameters, such as chemical doping, suppresses those structural and magnetic transitions continuously, and above a certain amount of external parameter superconductivity emerges. Upon increasing the value of the external control parameter, the SC transition temperature reaches the maximum value, while structural and magnetic phase transitions completely vanish. Finally, after the maximum T_c , it gradually decreases [84, 32, 85, 86, 80, 87, 87] forming a dome-shaped SC phase. One of the easiest way to modify the 122 system is substituting dopants into the parent 122-compounds. There are several ways to introduce dopants as listed in Table 2.1. The first discovery of superconductivity in 122 system was the potassium-doped BFA (BKFA) with T_c of 38 K [88]. Barium atoms are partially replaced with potassium (or cesium [89]) atoms in the blocking layer, and according

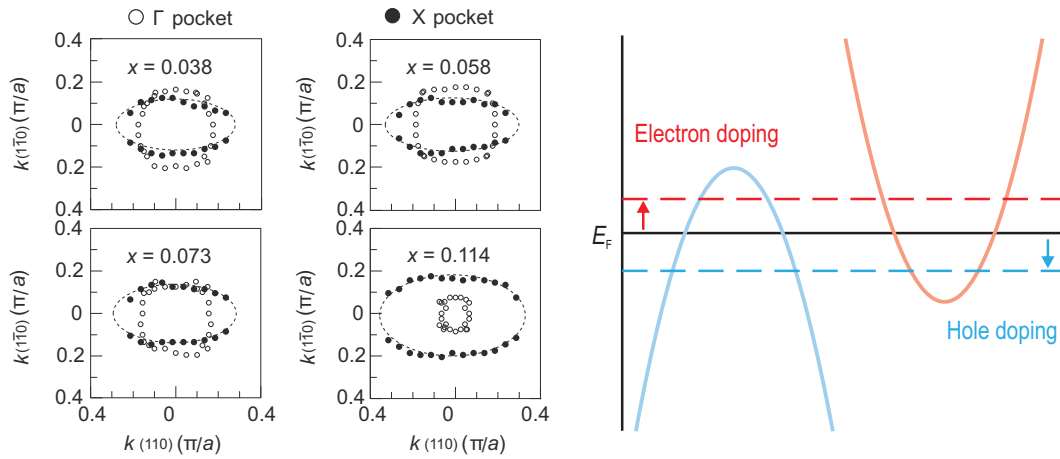


Figure 2.9: **Left.** Chemical doping dependence of hole and electron Fermi pocket size in Co-doped BaFe_2As_2 from Ref. [44]. Since substitution of Co into Fe layer generates extra electrons from an ionic point of view, hole Fermi pocket indeed shrinks upon chemical doing. On the other hand, the size of the electron Fermi pocket gradually increases as Co doping-level increases. **Right.** Schematic drawing of Fermi-energy-level shift depending on the type of doped charge carrier. When the hole is added to the system, Fermi energy shifts down, resulting in an expansion (contraction) of the hole (electron) Fermi pocket.

to the ionic point of view this aliovalent substitution should add an extra hole into the system. Such technique also can be applied to SrFe_2As_2 [89] and EuFe_2As_2 [90]. Up to now, the highest T_c for 122 system is recorded for 32% K-doped BaFe_2As_2 compound with a T_c of 38.5 K [78]. One notable thing in $\text{Ba}_{1-x}\text{K}_x\text{Fe}_2\text{As}_2$ (BKFA) is that superconductivity persists up to 100% K-doped BKFA, i. e., KFe_2As_2 (KFA), although its SC transition temperature remains at a quite low temperature ~ 3.8 K [89]. Yet, it is still controversial whether superconductivity in KFA shares the same origin with other ferropnictide systems [91, 92, 93]. In the regime where the SDW and superconductivity overlaps in the phase diagram for hole-(under)doped BKFA, two phases indeed coexist, but those are electronically phase separated as seen by muon-spin relaxation (μSR) [94, 95, 96] and nuclear-magnetic resonance (NMR) [97] experiments. We will come back to this issue later. Another possible way to dope the system is substituting transition metals (Co, Ni, Pd, Rh) into FeAs layers. In this way, dopants are directly substituted into the Fe layer, which can additionally stabilize the system [23]. The most commonly studied compound in the transition metal doped compound is Co-doped BFA (BFCA) since it is relatively easy to grow a sizable single crystal [79]. Other types of 122-ferropnictide systems are listed in Table 2.1 with the highest SC transition temperatures so far for every family.

It is quite obvious from ARPES measurements on BFCA [44] that such aliovalent chemical substitution indeed yields excess of electrons into the system. The left panel in Fig. 2.9 shows the size of hole (Γ -pocket in the legend) and electron (X -pocket in the

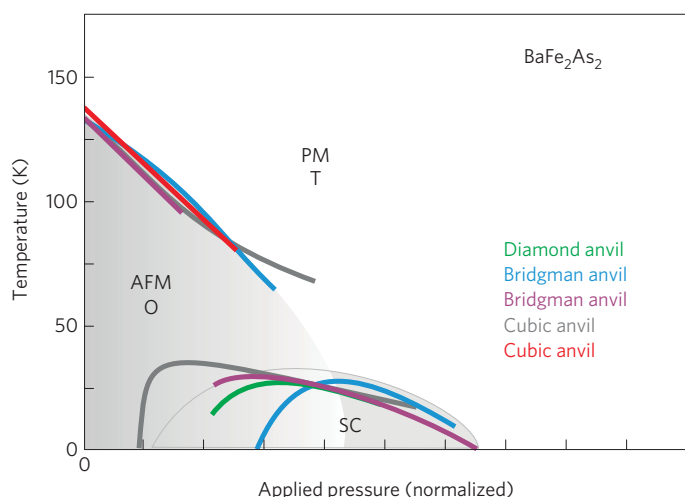


Figure 2.10: Pressure dependent phase diagram for Ba-based 122 compound from [20]. General behavior is very much alike to the one versus chemical doping in Fig. 2.8. Applying pressure to the parent compound also yields the gradual suppression of structural and SDW transitions, and SC dome appears.

legend) Fermi pockets at different doping levels in BFCA compound, where electrons are presumably doped. As the doping level [x in $\text{Ba}(\text{Fe}_{1-x}\text{Co}_x)_2\text{As}_2$] increases, the hole Fermi pocket continuously shrinks whereas the electron pocket becomes larger. In Ref. [44], authors further demonstrated that the hole pocket finally vanishes in heavily doped region, where superconductivity also disappears [98]. This can be understood within the framework of a rigid band shift. The right panel of Fig. 2.9 is a schematic drawing of hole and electron bands across the Fermi energy (E_F), shown as the black horizontal line. In the case of hole doping, the chemical potential shifts down (blue dashed line), resulting in expansion of hole-band radius at E_F while a size of electron pocket shrinks. Electron-doped case (red dashed line) also can be understood in the same manner, but *vice versa*.

Isovalent chemical substitution

There is another way to induce superconductivity in 122 ferropnictide: Isovalent chemical substitution, as in the phosphorus-doped BFA compound [83]. In $\text{BaFe}_2(\text{As}_{1-x}\text{P}_x)_2$ (BFAP), arsenic is partially replaced with phosphorus, and the quite similar phase diagram is demonstrated as in Fig. 2.8. In principle, P is located right above As in the element periodic table (belongs to the same group), thus such isovalent substitution, listed at the bottom of Tab. 2.1, is not supposed to introduce any extra charge carriers. Indeed, ARPES experiment reveals that the size and shape of the electron Fermi pocket does not change much even for high P concentration [99, 100]. Instead, the shape of the hole pocket becomes much more 3D (even more than in the parent BFA), and finally hole Fermi surface along k_z -direction becomes disconnected [99, 100]. What is remarkable in this compound is that the optimally doped BFAP shows comparable SC transition temperature (30 K) to optimally doped BKFA without any extra charge carrier doping [83]. This discovery apparently indicates that a charge carrier doping might not be a sole ingredient for superconductivity in the Fe-based

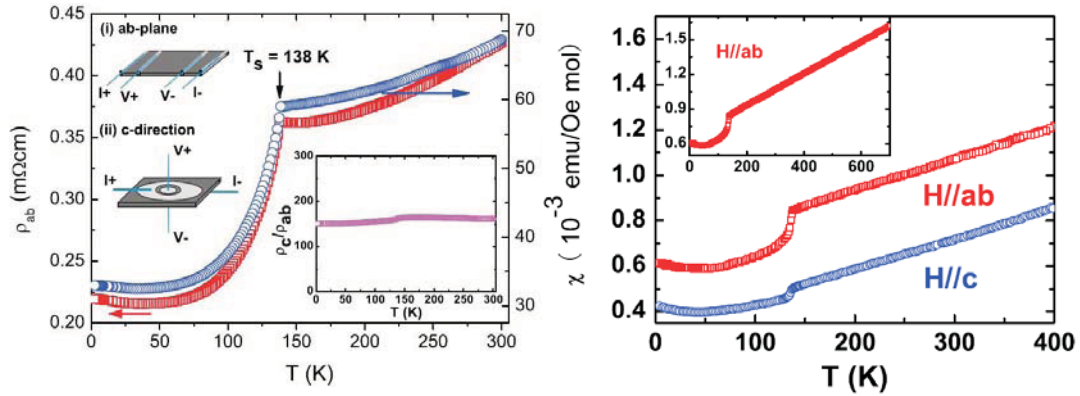


Figure 2.11: Resistivity and magnetic susceptibility characterization of the single-crystalline parent BFA compound reproduced from Ref. [73]. The left panel is the resistivity curve versus temperature measured along in-plane and out-of-plane directions. There is a sudden drop of resistivity at 138 K that is attributed to the coupled structural and magnetic transitions [73]. The right panel displays magnetization curves versus temperature in which the magnetic susceptibility suddenly falls down at the same temperature as seen in the resistivity curve [73].

materials. Since smaller atomic size of P as compared to As generates a “chemical pressure” effect, it was proposed that the unit-cell volume controls the physical phases in BFAP: As it shrinks, the SDW gets suppressed and superconductivity emerges at the corresponding unit-cell volume [83]. However, this scenario seems to be oversimplified because there are some compounds, for instance, $\text{Ba}_{1-x}\text{Sr}_x\text{Fe}_2\text{As}_2$ [101] that show comparable shrinking of the unit-cell, but no superconductivity has been observed in that system. Instead, Rotter *et al.* in Ref. [102] proposed that the variation of pnictogen height might be one of the main key parameters to host superconductivity. It is evident from the fact that the pnictogen height varies with the doping level [102], whereas there is no change in the pnictogen height for $\text{Ba}_{1-x}\text{Sr}_x\text{Fe}_2\text{As}_2$ [101]. This scenario is also consistent to what we discussed in Sec. 2.1.1 that the SC transition temperature is maximized at certain value of pnictogen height. Though, pnictogen height alone cannot be the fundamental origin of superconductivity in Fe-based compounds.

Application of uniaxial pressure

The other way to introduce superconductivity in 122 system is an application of uniaxial pressure to the parent compound [103]. This is a distinct physical property compared to cuprates, where oxygen doping is an essential ingredient for superconductivity [74]. In general, the phase diagram versus external pressure on the BFA compound (SFA exhibits almost the same behavior), shown in Fig. 2.10 reproduced from Ref. [20], is quite similar to that of the phase diagram versus chemical doping. Coupled structural and magnetic transitions in the parent phase are continuously suppressed by an applied uniaxial pressure, and the SC dome emerges. Analogous to the case of isovalent chemical substitution, the emergence of superconductivity under

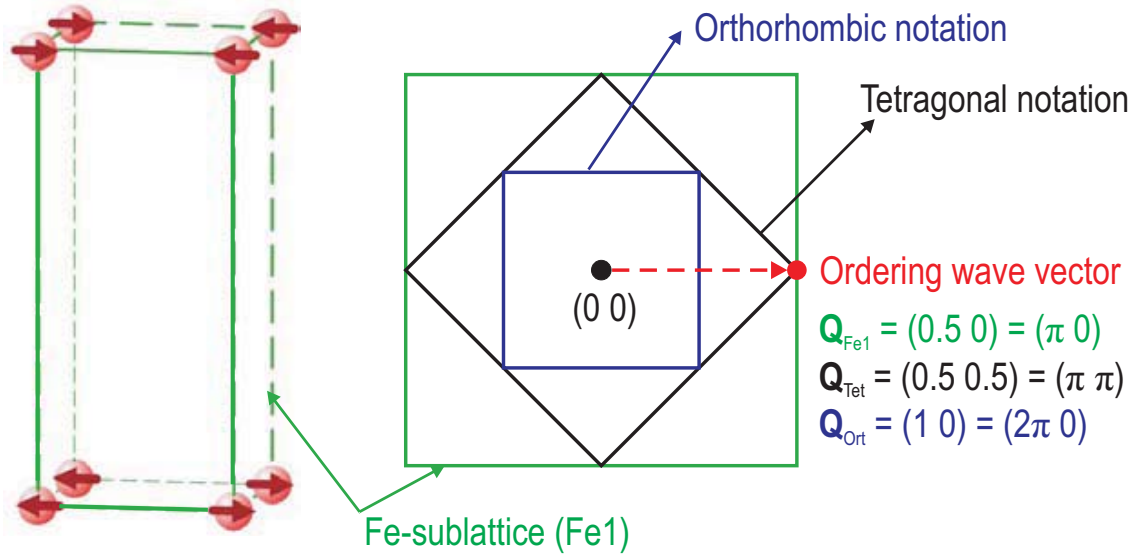


Figure 2.12: The spin configuration of collinear-AFM order is drawn in the direct space of iron-sublattice unit cell. Spins are aligned ferromagnetically along the shorter axis of iron square lattice and antiferromagnetically along the longer axis under orthorhombic lattice distortion. The propagation wave vector of SDW instability is drawn in the reciprocal space of Fe-sublattice, tetragonal, and orthorhombic unit cells of the 122 family. This vector (red dashed arrow) is coincided with the Fermi-surface nesting vector that connects hole and electron Fermi pockets in the electronic band structure.

uniaxial pressure without any doped charge carriers provides another serious evidence that superconductivity in Fe-based materials may not have strong correlation with extra holes or electrons in the system. Moreover, Kimber *et al.* found out remarkable similarities between structural distortion under pressure and chemical substitution in Ba-based 122 compounds, and showed that electronic band structure, calculated based on experimentally extracted structural data, similarly changes under both conditions [104]. As we will discuss later in more detail, this is an important aspect for superconductivity based on the Fermi-surface nesting condition of the system.

2.2.2 Long-range magnetic order and its spin dynamics

Magnetic long range order

As the parent 122 ferropnictide experiences the structural phase transition, unpaired spins of Fe atoms also develop AFM correlations, forming the SDW state. Such transition was first observed from the temperature-dependent resistivity and magnetic susceptibility measurements. Figure 2.11 shows the results of a representative electric and magnetic characterization on the single-crystalline BFA compound [73]. Both

temperature-dependent resistivity (left panel) and magnetic susceptibility (right panel) measurements show sudden drops around 137 K that are attributed to the coupled structural and magnetic phase transitions [73]. From a sudden drop of magnetic susceptibility below the magnetic transition temperature, one can naïvely guess that the type of spin ordering should be close to the AFM one. A remarkable thing in the magnetization curve is that the susceptibility shows an unusual linear behavior in the paramagnetic state up to very high temperature – 700 K in the inset of right panel – which can be explained neither by Pauli- nor Curie-Weiss-paramagnetism [73, 76]. Instead, there are several possible explanations for the linear dependence of susceptibility, such as attribution of the itinerant AFM spin fluctuations [105], strong thermal excitations of electrons in the electron bands near E_F [106], or a character of 3D two-band semimetallic band structures [107].

In early time of FeSC era, theoreticians have already predicted the presence of static magnetism from the first-principles calculations [54, 108, 109, 110, 111, 41, 112, 113]. Different theoretical works have calculated many different types of magnetic structures in FeSC systems – such as ferromagnetic (FM), checkerboard, or collinear AFM order – but they all ended up with the same result: collinear (or stripe) AFM spin-density-wave type instability. The configuration of collinear-AFM spin arrangement in the real space is depicted in Fig. 2.12. Spins are aligned ferromagnetically along the shorter axis of the iron square lattice and antiferromagnetically along the longer axis under orthorhombic lattice distortion, and spins are again antiferromagnetically arranged along the c -axis. At the right side of Fig. 2.12 we note the in-plane ordering wave vector in different notations (for the Fe-sublattice $\mathbf{Q}_{\text{Fe}_1} = (\pi, 0) = (0.5, 0)$ in r.l.u., tetragonal $\mathbf{Q}_{\text{Tet}} = (\pi, \pi) = (0.5, 0.5)$ in r.l.u., and orthorhombic $\mathbf{Q}_{\text{Ort}} = (2\pi, 0) = (1, 0)$ in r.l.u. unit cells of the 122 system) since in many publications such notations were mixed, which often led to confusions [24]. One interesting point is that the commensurate ordering wave vector coincides with the nesting vector $\mathbf{Q}_{F_1} = (\pi, 0)$ (red arrow depicted in Fig. 2.6), which connects the hole (at Γ) and electron (at X for 122 system) Fermi pockets [54, 108, 110, 41, 112, 113]. This fact strongly suggests that the static AFM order is apparently the spin-density wave state originated from the strong nesting between hole and electron Fermi surfaces of itinerant electrons rather than due to the localized spins. Already at the first-principles level, noninteracting static susceptibility $\chi_0(\mathbf{Q})$ shows the prominent peak centered at $\mathbf{Q}_{\text{Fe}_1} = (\pi, 0)$ as shown in Fig. 2.13 which firmly supports the Fermi-surface nesting scenario [113].

Another way to describe the magnetism in Fe-based superconductors is a localized moment picture [114, 115]. To set the collinear stripe order with this picture, one has to take two independent sublattices formed by the next-nearest-neighboring (NNN) sites depicted as red and blue dashed lines in Fig. 2.14, and the NNN exchange interaction (J_2) should be larger than a half of the nearest-neighboring (NN) exchange

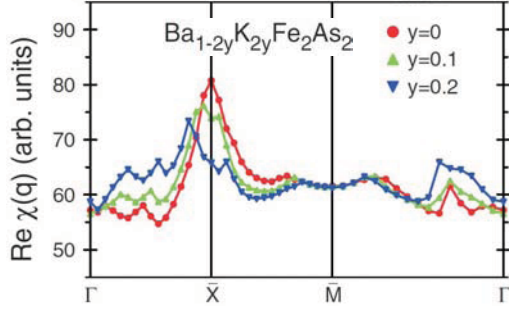


Figure 2.13: The real part of bare susceptibility for BFA family calculated within the LSDA approach [113]. The susceptibility is maximized at X point, that is the same vector for magnetic order in \mathbf{Q} -space.

interaction (J_1), i. e., $J_2 \geq J_1/2$. In this case, the NN interaction is frustrated since there must be both FM and AFM interactions between two sublattices. Therefore, each sublattice no longer interacts each other, and as a result, sublattice can be set in any arbitrary angle with respect to the other sublattice. To overcome such difficulty to describe magnetic order by localized model, one should consider to add an extra term in the Hamiltonian. For instance, anisotropic J_1 can be introduced by taking J_{1a} and J_{1b} separately [116], or the biquadratic term can be added in the Hamiltonian [117]. On the other hand, the local spin density approximation (LSDA) calculations revealed that the energy of BFA compound considerably depends on the angle between each sublattice, indicating that the simple $J_1 - J_2$ Heisenberg model is not applicable for the magnetism in pnictide systems [113].

Theoretically predicted collinear AFM spin structure of parent 122-compound has been experimentally proven using powder or single-crystal neutron-diffraction techniques [77, 118, 119, 75, 120, 121, 122]. The left panel of Fig. 2.15 is the two-dimensional magnetic Bragg peak intensity distribution measured on the Ca-122 parent compound below the magnetic transition temperature (T_N) [75]. Here, the orthorhombic notation has been used, thus the magnetic Bragg peak is placed at $\mathbf{Q}_{\text{ort}} = (10\bar{1})$ in the reciprocal lattice units. The temperature-dependent magnetic Bragg peak intensity is shown in the right panel of Fig. 2.15 measured on the BFA compound [77]. The magnetic intensity at $\mathbf{Q}_{\text{ort}} = (101)$ starts to develop right below 140 K and exhibits an order-parameter-like behavior toward the low temperature regime (*cf.* $T_N = 143$ K of BFA in Ref. [77] is somewhat higher than any other neutron diffraction works which reported $T_N = 137$ K on the same materials [123, 124], and latter value is more reliable in terms of sample quality and careful measurements), $T_N = 170$ K for CFA and $T_N = 200$ K for SFA). Other complementary experimental techniques, such as μSR [95, 96, 125] or Mössbauer spectroscopy [38, 126], also confirmed the existence of the static magnetic order in the parent 122 systems. By neutron diffraction measurements, the magnitude of ordered moment per iron atom had been determined: $\sim 0.9 \mu_B$ for Ba, Ca, Sr-based 122-parent compounds [77, 118, 119, 75, 120, 121, 122].

Although first-principles calculations fairly well describe the magnetic ground state and the behavior of noninteracting static susceptibility of the parent Fe-pnictide

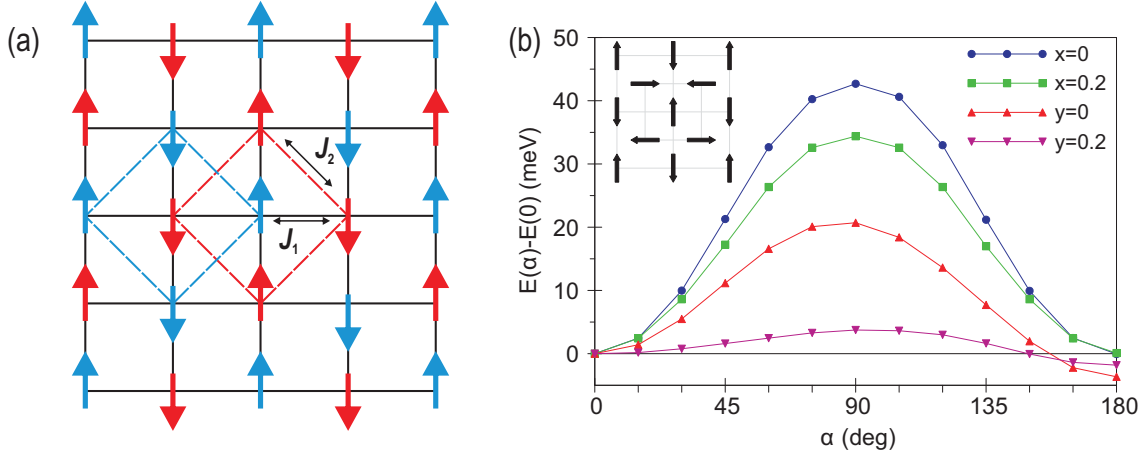


Figure 2.14: (a) Collinear AFM spin configuration is drawn with two independent sublattices (red and blue). Once $J_2 \geq J_1/2$ condition is satisfied, collinear AFM order can be constructed. (b) Angle between two sublattices dependent energy plot for BKFA reproduced from Ref. [113]. No matter what doping level is, the energy barrier is always presented with the maximum energy at 90° .

system [54, 113], a significant discrepancy remains between DFT calculations and experimental data until now. Within standard LDA calculations, much larger magnetic moment per Fe atom ($1.5 - 2 \mu_B$) was obtained from a numerous theoretical works [54, 108, 109, 110, 111, 41, 112, 113] than the experimentally determined magnetic moment per iron ($0.5 - 1 \mu_B$) [77, 118, 119, 75, 120, 121, 122, 95, 96, 125, 38, 126]. What is known about this inconsistency is that the calculated magnetic moment within the DFT approach is very much sensitive to the height of pnictogen (or chalcogen) from the Fe-layer [45]. In other words, to obtain the consistent magnetic moment from the calculation to the experimental value (note that the electronic band structures are also shifted significantly depending on the pnictogen height as seen in Fig. 2.5), one has to take theoretical position of As in the BFA case, but not the experimentally extracted value [45]. Such sensitivity of magnetic moment to the pnictogen height can be acceptable within the frame of itinerant electron system, but this still does not explain the main origin of discrepancy. Therefore, it is still under huge debate what is the exact origin of such inconsistency between *ab-initio* calculations and experiments. Mazin and Johannes proposed that assuming the fluctuating magnetic twin and antiphase domains within the experimental time scale can lead to a better agreement of magnetic moment in the first-principles level [56]. However, so far, such effect has not been observed by any experiments. Recently, on the other hand, Yin *et al.* reported that a combination of DFT and dynamical mean field theory (DMFT) describes the ferropnictide system better than a standard LDA in terms of the magnetic moment, effective masses, and Fermi surfaces [127].

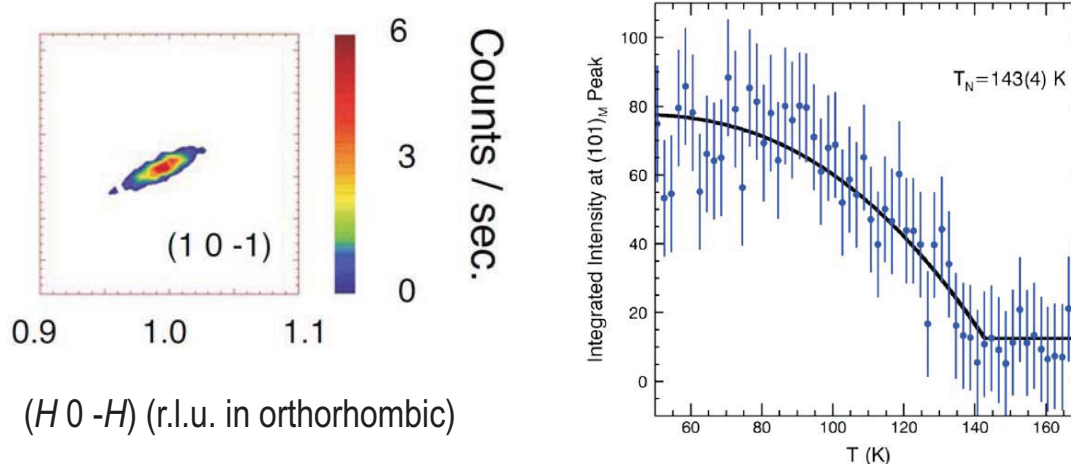


Figure 2.15: **Left.** The magnetic Bragg peak intensity distribution for the CFA compound below the SDW transition temperature in the two-dimensional momentum space [75]. The peak is well centered at $(10\bar{1})_{\text{Ort}}$ in the orthorhombic reciprocal lattice units. **Right.** An order-parameter-like temperature dependent behavior of magnetic Bragg peak intensity at $\mathbf{Q}_{\text{Ort}} = (101)$ in the BFA [77].

2.2.3 Coexistence of magnetic and superconducting phases

As shown in the phase diagram of 122-type ferropnictide systems (Fig. 2.8), there is the doping range where the magnetic and SC phases overlap in underdoped side. This regime is of particular interest since the interplay between the static magnetism and superconductivity can be investigated at the same time. There are two major ways to interpret this phenomenon, of coexisting magnetic and superconducting phases:

1. Mesoscopic phase separation: As the system experiences the magnetic transition, only some part of its volume becomes magnetically ordered, forming islands of the magnetic phase. The rest of the compound remains as paramagnetic and hosts superconductivity below T_c .
2. Competing ordered phases: If the magnetic ordering temperature is higher than T_c , the whole volume of compound becomes magnetically ordered below T_N , and then this phase competes with the SC phase below T_c .

Mesoscopic phase separation

For the BKFA family, it was first shown by Chen *et al.* that both the SDW and SC phases exist in the same compound confirmed by resistivity, magnetic susceptibility, and powder neutron diffraction measurements at $x = 0.2$ and 0.3 doping levels [128]. Although the neutron measurement provides an insight of bulk characteristic, it cannot tell whether two phases are coexisting microscopically or electronically separated.

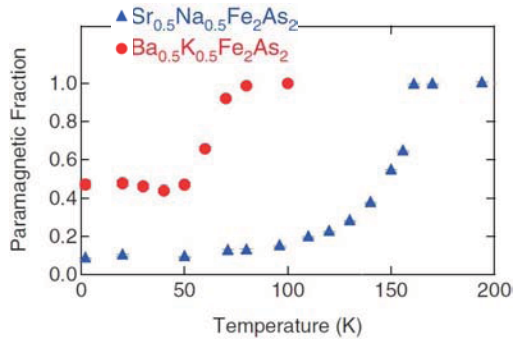


Figure 2.16: The paramagnetic volume fraction versus temperature extracted from the transversal-field μ SR profile in $\text{Ba}_{0.5}\text{K}_{0.5}\text{Fe}_2\text{As}_2$ and $\text{Sr}_{0.5}\text{Na}_{0.5}\text{Fe}_2\text{As}_2$ [96]. As the system crosses the magnetic transition temperature (80 K), approximately 50% volume of the sample becomes magnetic, whereas the remaining volume fraction can be regarded as SC phase ($T_c \sim 30$ K).

Soon thereafter, μ SR experiments were carried out on similar doping level BKFA compounds by different groups including ourselves [94, 95, 96]. In the zero-field μ SR (ZF- μ SR) measurements on underdoped BKFA compounds, the magnetic moment in the SDW state (~ 28 MHz) was deduced from the oscillation frequencies in asymmetry ratio of detected muons [94, 95, 96] which is inline with the neutron diffraction result on the similar doping level BKFA [128], indicating the same origin of the static magnetism. However, the transverse-field μ SR (TF- μ SR) measurements, where the paramagnetic volume fraction can be precisely extracted, revealed that below the magnetic transition temperature only some part of sample ($\sim 50\%$) becomes magnetically ordered [94, 95, 96]. Fig. 2.16 displays the how the paramagnetic volume fraction changes in temperature measured on $\text{Ba}_{0.5}\text{K}_{0.5}\text{Fe}_2\text{As}_2$ ($T_N \sim 80$ K, $T_c \sim 30$ K) by TF- μ SR [96]. About one half of the sample turns into the magnetic phase below 80 K, and the rest of its volume remains in the paramagnetic state down to the lowest temperature that is believed to host superconductivity [94, 95, 96]. We have further investigated with the magnetic-force microscope (MFM), and showed that AFM order phase forms an island-like patch surrounded by paramagnetic (and SC) phase with the characteristic length of 60 nm [94]. We will present relevant data in Sec. 4.1.4.

Although other complementary experiments also observed the mesoscopic phase separation in BKFA with such as NMR [97], neutron diffraction [129], and atom probe tomography, [29], there is a certain issue concerning the quality of those samples. All measurements supporting the mesoscopic phase separation scenario were made on Sn-flux grown BKFA single crystals, and it was argued that even a very small amount of Sn inclusion in samples can modify its physical properties significantly [130, 131, 97]. Recently it has been shown that polycrystalline BKFA samples show no evidence for electronic phase separations from elastic neutron and μ SR experiments, but rather exhibit similar behavior as in the Co-doped BFA (BFCA) case [30].

Competing magnetic and superconducting phases

In sharp contrast to the Sn-flux grown BKFA, underdoped BFCA compounds show no mesoscopic phase separation, but exhibit the microscopic coexistence of the SDW

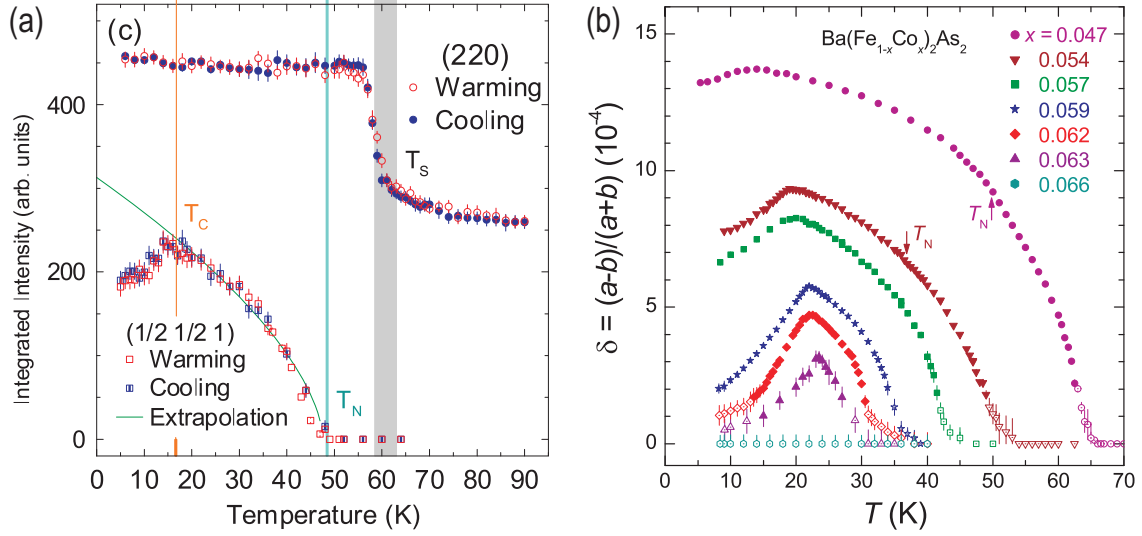


Figure 2.17: (a) The magnetic Bragg peak intensity suppression below T_c in the underdoped BFCA compound reproduced from Ref. [132]. (b) Suppression of the orthorhombicity, defined as $\delta = \frac{(a-b)}{(a+b)}$ where a and b are lattice constants in the orthorhombic notation, below T_c in several doping levels from [133].

and SC phases examined by μSR [134, 135], NMR [97, 136, 137], and tunneling spectroscopy experiments [138]. More remarkable aspect was reported from the neutron and high-resolution x-ray diffraction measurements on a series of underdoped BFCA compounds as shown in Fig. 2.17. Pratt and his co-workers observed an order-parameter-like behavior of the integrated magnetic Bragg intensity at $\mathbf{Q}_{\text{Tet,Fe}_4} = (0.5 \ 0.5 \ 1)$ below T_N [Fig. 2.17 (a)]. Then, right below T_c the magnetic Bragg reflection starts to decrease until the lowest temperature they have reached [132]. In addition, the structural transition becomes separated from the magnetic transition, occurring at slightly higher temperature than T_N . The orthorhombic distortion, defined as $\delta = \frac{(a-b)}{(a+b)}$ where a and b are lattice constants in orthorhombic notation, also gets suppressed across the SC transition [133] (i.e., the splitted nuclear Bragg peaks below the structural transition temperature become close each other below T_c). This effect has been observed in a series of underdoped BFCA as depicted in Fig. 2.17 (b) [133]. This, so-called “re-entrant behavior”, strongly indicates that superconductivity competes with the static magnetic order, that is partial electrons that were participating for the SDW might turn into the paired electrons (Cooper pairs) for the superconductivity. Fernandes *et al.* carried out the theoretical calculations for the phase diagram regarding the re-entrant behavior, and claimed that such peculiar coexistence of the SDW and SC phases can be well described under the assumption of s_{\pm} -wave pairing symmetry in the SC state [139].

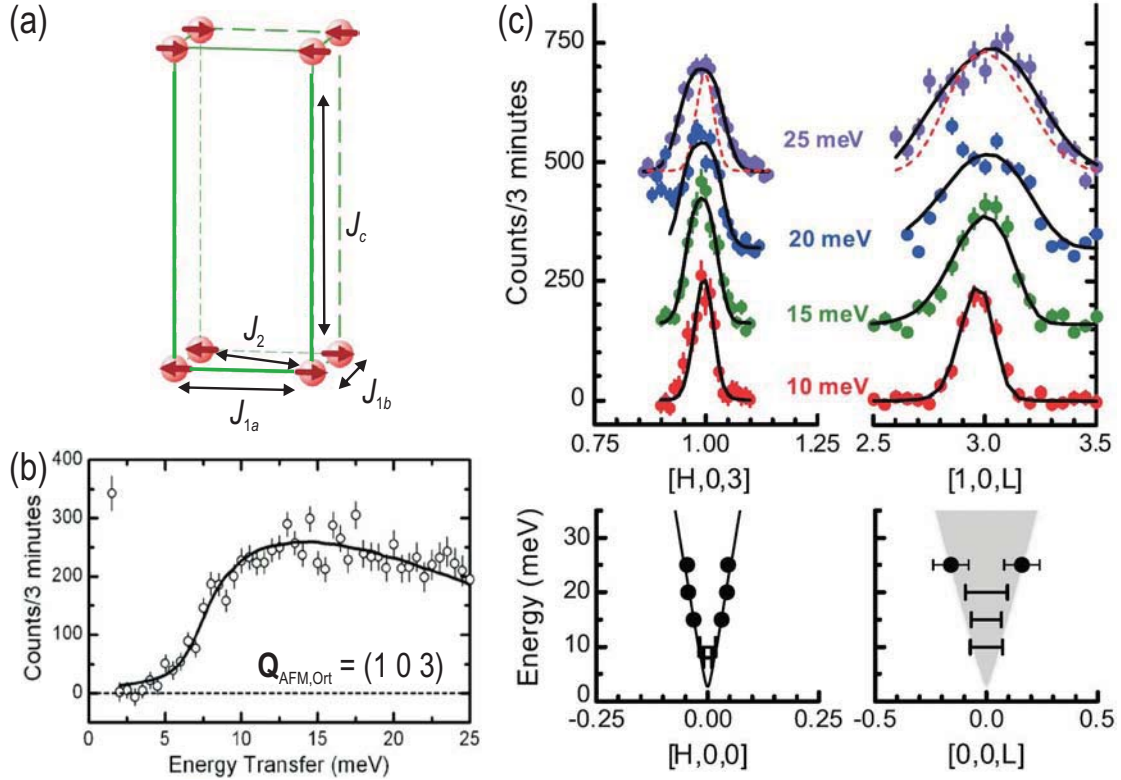


Figure 2.18: (a) NN, NNN, and interlayer exchange-interaction constants are drawn in the Fe-sublattice unit cell. Due to the orthorhombic distortion and AFM collinear order of spins, separated J_{1a} (along longer axis) and J_{1b} (along shorter axis) are introduced for spin-wave dispersion fitting in Ref. [116]. (b) Magnetically scattered neutron intensity versus energy at the ordering wave vector in the orthorhombic notation $\mathbf{Q}_{\text{AFM,Ort}} = (1\ 0\ 3)$ measured on the SFA compound in the SDW state [141]. (c) Some of representative momentum scans on the parent material along H and L direction in the vicinity of AFM wave vector at selective energies measured in the magnetically ordered state [141].

2.2.4 Spin dynamics in the parent compound

To elucidate the relationship between the magnetism and superconductivity, understanding of the magnetic ground state is required. Therefore, many of INS experiments were carried out to construct the overall spin-excitation spectra in the SDW state mostly on parent 122-ferropnictide and underdoped BFCA compounds (simply due to the availability of big enough size single crystal) with a triple-axis neutron spectroscopy (TAS) for low-energy regime [140, 141, 122, 142] and time-of-flight (TOF) neutron spectroscopy for high-energy magnetic excitations [143, 144, 116, 145, 146, 147]. By this, the dispersion of magnetic excitations can be mapped out throughout the whole BZ. Then, based on the dispersion, one can construct the effective Heisenberg model that would be useful to figure out the underlying physics of the magnetism in the FeSC.

Low-energy spin excitations in the SDW state

Compound	Spin gap (meV)	v_{ab} (meV·Å)	v_c (meV·Å)	v_c/v_{ab}	Reference
BaFe ₂ As ₂	9.8 ± 0.4	280 ± 150	57 ± 7	0.4	[122]
CaFe ₂ As ₂	6.9 ± 0.2	420 ± 70	270 ± 100	0.64	[141]
SrFe ₂ As ₂	≤ 6.5	560 ± 110	280 ± 56	0.5	[140]

Table 2.2: A list of fitted parameters based on linear approximation of spin-wave dispersions from Ref. [140, 141, 122]. v_{ab} is the spin-wave velocity along in-plane direction, whereas v_c is the out-of-plane spin-wave velocity in units of meV·Å. Rather higher value of ratio v_c/v_{ab} for all compounds indicates anisotropic 3D spin excitations.

Early investigations of magnetic-excitation spectra on three parent 122-compounds (Ba, Sr, Ca-based) were made by neutron-scattering TAS measurements [140, 141, 122], and revealed similar behavior of low-energy spin excitations in the vicinity of AFM ordering wave vector $\mathbf{Q}_{\text{AFM,Ort}} = (1\ 0\ 1)$ with slightly different physical quantities listed in Table 2.2. The INS data in Fig. 2.18 (b) and (c) are one of representative results from co-aligned single crystals of Sr-122 parent compound measured in the SDW state [141]. Fig. 2.18 (b) shows the magnetically scattered neutron intensity versus energy transfer at the fixed AFM ordering momentum position. The spin-excitation spectrum at \mathbf{Q}_{AFM} evolves smoothly from 7 meV and extends to the maximal reachable energy transfer. The spectrum is depleted of spectral weight from 0 to 7 meV which can be assigned to so-called the *spin gap*. The spin-gap phenomenon, which suppresses the spectral weight inside the spin-gap energy below T_N , has been also observed in the spectrum for the Ba- and Ca-based undoped compounds, but so far there is no good understanding of what is a physical origin of the gap. Above the spin-gap energy, prominent peaks can be seen centered at the AFM wave vector from the momentums scans both along orthorhombic H and L directions in $[HOL]$ scattering plane with the fixed energy transfer in between the energy range of 10 - 25 meV [Top panels in Fig. 2.18 (c)]. One remarkable thing is that the magnetic excitations are hardly dispersive up to 25 meV, indicating the quite steep spin-wave dispersion along the in-plane direction. Although the spin excitations along L -direction are less steep than in the plane, the magnetic intensity sharply peaks at the ordering wave vector which could be an evidence for the 3D nature of magnetism in ferropnictides [140, 141, 122]. Due to a technical limitation of TAS, it is challenging to reach high energy transfer (> 300 meV) within limited experiment time and size of samples. Nevertheless, fitting of spin-wave dispersion based on the available low-energy data points for parent materials has been conducted by using the empirical spin-wave dispersion relation:

$$\omega(q) = \sqrt{\Delta^2 + v_{ab}^2(q_a^2 + q_b^2) + v_c^2 q_c^2} \quad (2.1)$$

where Δ is the spin-gap energy (meV), v_{ab} and v_c are the spin-wave velocities along

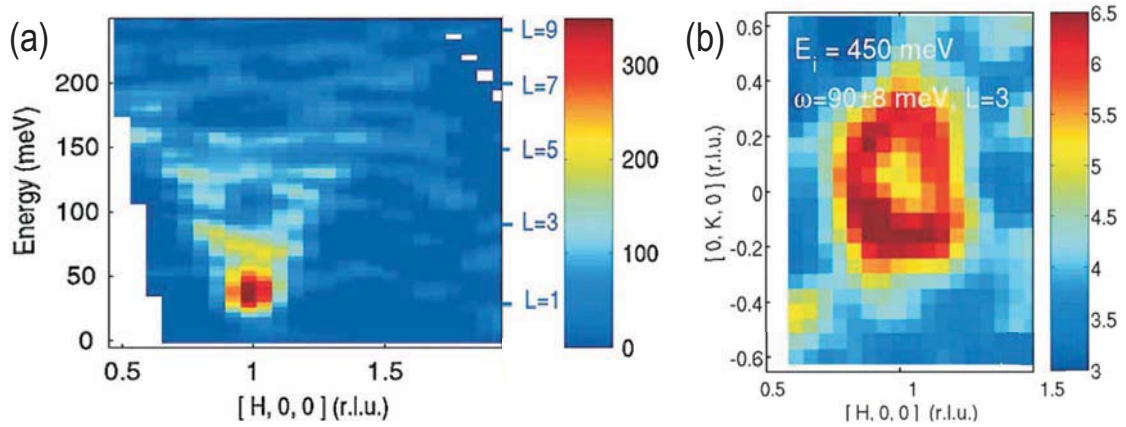


Figure 2.19: (a) A projection of magnetic intensity distribution in two dimensional map with energy (y-axis) and momentum space (x-axis) measured in the SDW data on the parent CFA [144]. The energy transfer is always coupled to the L component, thus L -value increase as the energy transfer increases. The strong signal is observed in the vicinity of AFM wave vector $\mathbf{Q}_{\text{AFM,Ort}}$ below 50 meV, then spin excitations disperse up to 200 meV. (b) Constant-energy slice ($\omega = 90 \pm 8$ meV) projected into the in-plane through the spin-wave in the same compound [144]. Intensities are more distributed along incommensurate positions away from $\mathbf{Q}_{\text{AFM,Ort}}$, confirming the clear dispersion of spin-wave at high energy. The width of excitation is different for each reciprocal axis; elongated along K -direction, forming an anisotropic in-plane cross section.

in-plane and out-of-plane directions, respectively, in units of $\text{meV}\cdot\text{\AA}$. The fitting results are shown in Table 2.2 for three 122-parent compounds. Albeit fitting errors are enormously large due to a lack of data points in the dispersion, one can find a trend in the ratio between in-plane and out-of-plane spin-wave velocities. This ratio, v_c/v_{ab} , is one of the most useful parameters determining whether the magnetic fluctuations in the system is more like two or three dimensional. The values of ratio vary from 0.4 to 0.6, indicating the 3D character of magnetic fluctuations in the parent 122-system. This fact is inline with the NMR results where the strong anisotropy of low-energy (lower than INS energy window) spin excitations in BFA, SFA, and CFA has been confirmed [148, 149, 150, 151].

High-energy spin excitations in the SDW state

As mentioned above, due to the infinitely steep spin-wave dispersion, the low-energy measurement with TAS is not enough to acquire a full spin-wave dispersion data. Instead, the TOF neutron spectrometer allows one to reach up very high energy transfer ($\omega \leq 300$ meV). Though, there are also some drawbacks in TOF method, for instance, the energy transfer is always coupled to one of the reciprocal orientation axes. In the ferropnictide case, all of TOF measurements on single crystalline samples were done in $[HOL]_{\text{Ort}}$ scattering plane, and usually L was fixed to be parallel to the incident neutron

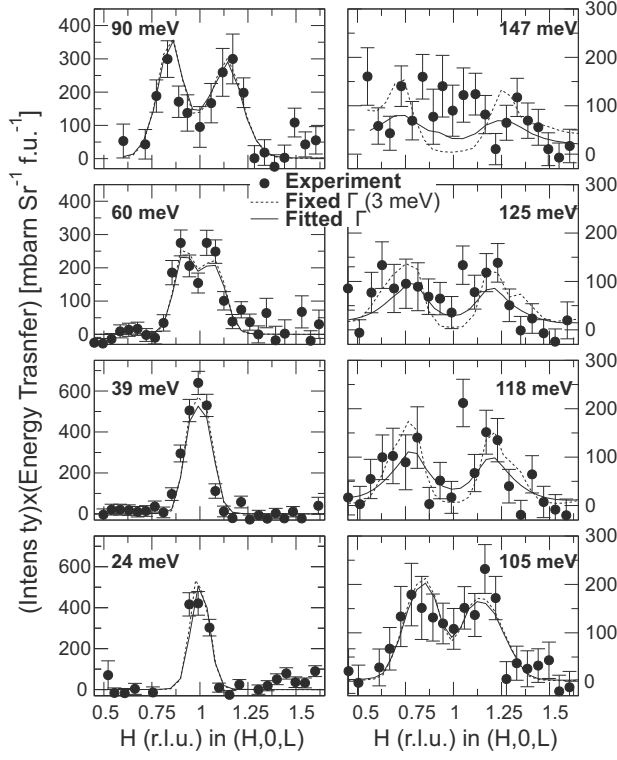


Figure 2.20: Constant-energy cuts along $[H00]_{\text{Ort}}$ direction at different energy transfers in CFA [144]. The single magnetic excitation peak starts to split already at 64 meV, and further goes away from AFM wave vector as the energy increases. Above 100 meV, excitations experience heavy damping that hinders to define the accurate dispersion data close to the BZ boundary [144].

beam, binding L -component with energy transfer [144, 116, 145, 146, 147, 152]. Figure 2.19 (a) shows a typical intensity-distribution map projected into $[H00]_{\text{Ort}}$ momentum direction together with the energy transfer dimension measured on co-aligned single crystalline CFA samples in the magnetically ordered state [144].

As consistent to the TAS low-energy measurements, intense magnetic excitations are accumulated around \mathbf{Q}_{AFM} below 50 meV, and as energy transfer increases, magnetic intensity disperses along $[H00]_{\text{Ort}}$ direction. Dispersive magnetic excitation can be seen more clearly in the constant-energy slice at $\omega = 90 \pm 8$ meV (Fig. 2.20) [144]. Spin excitation intensities in the two-dimensional in-plane momentum space are more distributed along incommensurate positions away from the \mathbf{Q}_{AFM} , confirming the clear dispersion of spin-wave excitations at high energies [144]. Notable thing is that the width of magnetic excitations is larger along K -direction, forming the anisotropic pattern of spin-wave dispersion (see Fig. 2.21) [144, 116]. Naïvely speaking, this phenomenon can be understood in the context of orthorhombic distortion, so that a little difference in the exchange interaction along longer (a in orthorhombic notation) and shorter (b) in-plane axes as drawn in Fig. 2.18 (a). However, theoretical calculations predicted that if J_{1a} is AFM while J_{1b} is FM, the magnetic interactions would be frustrated [111, 114, 153, 154].

For establishing the spin-wave dispersion, constant-energy cuts projected into one dimensional axis are quite useful as shown in Fig. 2.20 for the CFA compound [144]. Those data look quite similar to that of the TAS measurements, but those constant-energy cuts are apparently integrated over some energy and momentum transfer

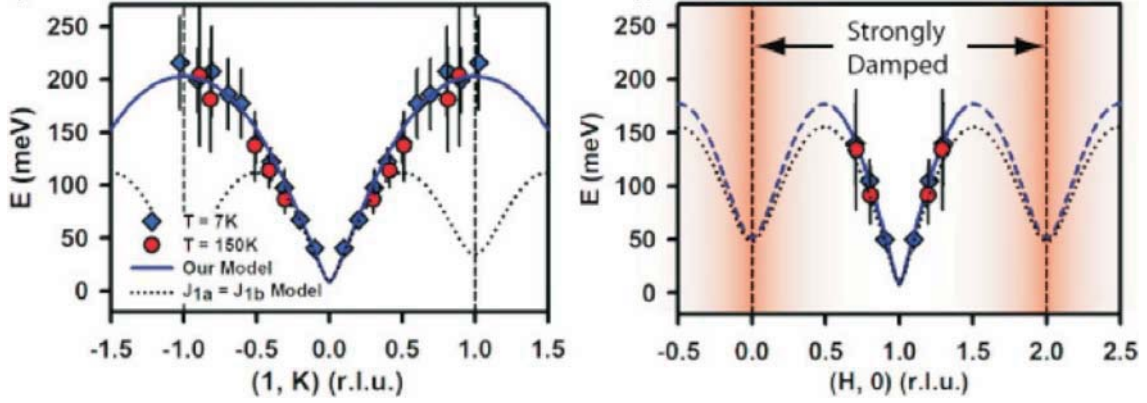


Figure 2.21: The dispersion relation of spin-wave excitations in the BFA compound over the wide range of in-plane momentum space in the magnetically ordered states [147]. The experimental data were fitted using Eq. 2.3, and fit results are listed in Table. 2.3.

Compound	SJ_{1a} (meV)	SJ_{1b} (meV)	SJ_2 (meV)	SJ_c (meV)	SD (meV)	Reference
BaFe ₂ As ₂	59.2 ± 2.0	-9.2 ± 1.2	13.6 ± 1.0	1.8 ± 0.3	0	[147]
CaFe ₂ As ₂	49.9 ± 9.9	-5.7 ± 4.5	18.9 ± 3.4	5.3 ± 1.3	0	[116]
CaFe ₂ As ₂	31.0 ± 7.0	13.0 ± 8.0	31.0 ± 3.0	4.5 ± 1.0	0.063	[144]
SrFe ₂ As ₂	38.7 ± 2.0	-5.0 ± 5.0	27.3 ± 0.7	2.3 ± 0.1	-	[152]

Table 2.3: A list of fitted exchange interaction constants from Ref. [147, 116, 144, 152].

windows. Nevertheless, the series of constant-energy cuts clearly reveals the trend of dispersive spin excitations: The sharp and intense single peak of magnetic excitation center at the ordering wave vector begins to split into two symmetric peaks around 60 meV, and disperses even further up to ~ 150 meV [144]. The similar dispersive spin-excitation spectrum was also observed in the nominally same CFA compound done by different group [116].

The complete spin-wave dispersion in the SDW state over a wide range of in-plane momentum space in the undoped BFA using TOF data is displayed in Fig. 2.21 [147]. As discussed above, the overall shape of spin-wave dispersion is quite distinct between H_{Ort} and K_{Ort} reciprocal axis directions which makes difficult to model the magnetic ground state based on a simple J_1 - J_2 Heisenberg model. Instead, the effective Heisenberg Hamiltonian proposed by Ref. [155] has been used for fitting of spin-wave dispersion:

$$H = J_{1a} \sum_{i,j} S_i \cdot S_j + J_{1b} \sum_{i,j} S_i^x \cdot S_j^x + J_2 \sum_{i,j} S_i \cdot S_j + J_c S_i \cdot S_j - DS_i^z \cdot S_j^z \quad (2.2)$$

where J_{1a} , J_{1b} , J_2 , J_c are the NN, NNN, and interlayer exchange interactions depicted in Fig. 2.18 (a), and D is the single ionic anisotropic gap, which is simply introduced to describe the spin-gap behavior in the excitation spectrum [140, 141]. Again, here

we note that the two NN exchange constants are artificially added for a convenient spin-wave dispersion fitting. Using Eq. 2.2, the spin-wave dispersion can be constructed as follows:

$$\omega(\mathbf{q}) = \sqrt{A_{\mathbf{q}}^2 - B_{\mathbf{q}}^2} \quad (2.3)$$

where

$$A_{\mathbf{q}} = 2S_{\text{eff}}J_{1b}[\cos\{\pi q_K\} - 1] + J_{1a} + 2J_2 + J_c + D \quad (2.4)$$

$$B_{\mathbf{q}} = 2S_{\text{eff}}[J_{1a} \cos(\pi q_H) + 2J_2 \cos(\pi q_H) \cos(\pi q_K) + J_c \cos(\pi q_L)] \quad (2.5)$$

where $\mathbf{q} = (q_H \ q_K \ q_L) = \mathbf{Q} - \mathbf{Q}_{\text{AFM}}$ is a reduced momentum transfer. Obtained fitting parameters from three INS experiments are listed in the Table 2.3. Strangely, J_{1b} turned out to be negative value in two experiments [116, 147]. This result is highly unexpected from the theoretical respect which predicted the magnetic frustration in such case [111, 114]. Until now, no conceivable physical explanation has been suggested for this unforeseen outcome. On the other hand, one of experiments in CFA yielded the positive J_{1b} value that makes all exchange interaction constants to be AFM [144]. The fitting result in Ref. [144] well satisfies the condition for the stripe AFM order, $J_2 \geq J_1/2$. However, their fitting was conducted under the assumption of $50 \text{ meV} < \omega(\mathbf{q}_K) < 150 \text{ meV}$ because they could not indisputably resolve the high-energy magnetic excitations near the BZ boundaries [144]. To resolve discrepancy between theoretically and experimentally extracted exchange interactions, an alternative effective Hamiltonian with a biquadratic term of NN and NNN exchange interactions has been proposed [156, 117, 157]. This model describes the spin-wave dispersion fairly well without requiring anisotropic J_{1a} and J_{1b} separately [117]. From the itinerant AFM point of view, it was also shown that the mean-field calculation with a random-phase approximation in a five-band model reproduces the observed spin-excitation spectra over whole BZ quite well [158]. Recently, Ewings *et al.* reported that a five-band itinerant mean-field model calculation fits better for their high-energy INS spectrum than J_1 - J_2 approach [152]. So far, there is no final consensus about which model best describes the spin dynamics in the magnetically ordered state.

Paramagnetic excitations in the normal state

Magnetic excitations around the AFM wave vector persist even in the tetragonal paramagnetic state of the parent compound [122, 159], or in the nearly optimally doped compound [160, 145, 146]. The paramagnetic spin excitations of parent system were observed in the BFA at 145 K ($T_N = 137 \text{ K}$) and in the CFA at 180 K ($T_N = 172 \text{ K}$) [122, 159]. Figure 2.23 displays a comparison of magnetic excitations below (left panels) and above (right panels) T_N in the CFA material. In the paramagnetic state, magnetic fluctuations become weaker and broader in the moment space, but still show well-centered peak at \mathbf{Q}_{AFM} even up to room temperature [159]. Moreover, the

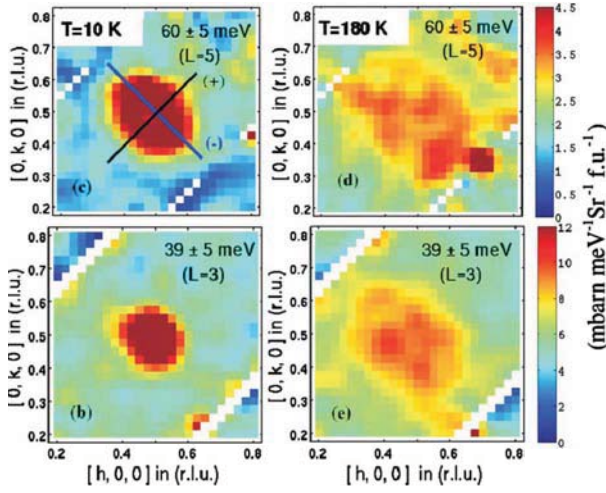


Figure 2.22: Constant-energy slices around the AFM wave vector $\mathbf{Q}_{\text{AFM,Tet}} = \left(\frac{1}{2}, \frac{1}{2}, L\right)_{\text{Fe}_4}$ below and above T_N measured by TOF neutron spectrometer on 122-parent CFA compound [159]. Spin excitations persist even in the paramagnetic state with weakened and broadened intensity distribution (right panels).

magnetic intensity along the L -direction keeps the 3D modulation (yet its modulation is somewhat weaker than in the SDW state), implying that the spin excitations share similar 3D character of electronic band structure in the parent 122 systems.

What is more astonishing is that magnetic fluctuations survive even in the optimally doped compound, where the static AFM order completely vanishes [160, 145, 146], indicating the importance of spin excitations for superconductivity. The normal-state spin dynamics of 122 FeSC is dominated by an intense branch of low-energy spin-fluctuations in the vicinity of the commensurate \mathbf{Q}_{AFM} wave vector which is very similar to that in the parent compound [160, 140, 141, 122]. On the other hand, not like a doubtful situation about the origin of magnetic fluctuation in the parent compound, characteristic low-energy spin-dynamics feature in the tetragonal paramagnetic state could be well reconciled within a nearly itinerant AFM metal framework [47, 161, 162]. We will discuss more details in Sec. 4.2.3. The magnetic intensity modulation along the L -direction is significantly reduced in doped materials, evidencing the crossover from 3D to quasi-2D spin-fluctuations upon chemical doping [50, 145, 146]. This effect (not only for the spin excitation spectra, but for a dimensionality of system upon doping) was already predicted from electronic band structure calculations, in which showed that 3D barrels of hole and electron Fermi surfaces translate to more cylindrical shape without pronounced ripples along the L -direction [163].

At higher energy transfer, the spin excitations generally exhibit a dispersive behavior along the in-plane momentum direction as shown in Fig. 2.23 and 2.24. Constant-energy slices measured on the nearly optimally doped BFCA by TOF revealed an anisotropic cross-section elongated along the transverse (TR) direction, which is the same elongated direction of magnetic in-plane cross-section in the parent compound [144, 116, 147], within every $L = \text{const}$ plane, and above 60 meV single spot of magnetic intensity became separated along TR direction. This in-plane anisotropic-pattern of spin excitations is naturally expected in a magnetically ordered state due to a or-

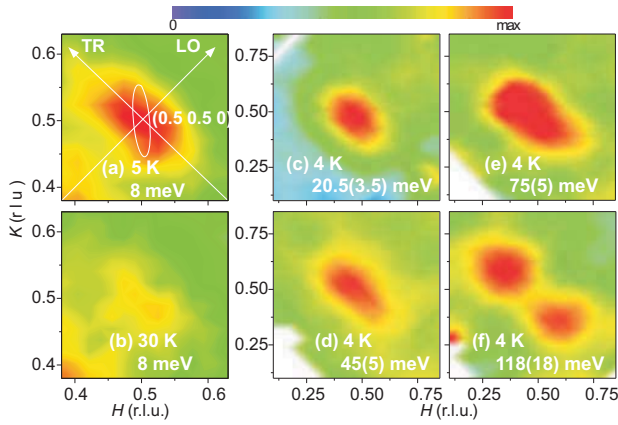


Figure 2.23: Constant-energy slices around the AFM wave vector $\mathbf{Q}_{\text{AFM,Tet}} = \left(\frac{1}{2}\frac{1}{2}L\right)_{\text{Fe}_4}$ in the paramagnetic state measured by TOF on nearly optimally doped BFCA [146]. Even though the static AFM order is completely suppressed at this doping level, substantial magnetic fluctuations centered at $\mathbf{Q}_{\text{AFM,Tet}}$ have been observed up to quite high energy transfer.

thorhombic lattice-distortion, which possesses a lower-symmetry operation than a tetragonal one. On the other hand, four-fold C_4 rotational symmetry has to be preserved in a paramagnetic tetragonal state, but the observed elliptical shape of in-plane magnetic cross-section in the paramagnetic tetragonal state for 122-ferropnictide seemed to violate above symmetry argument which served as a point for the proposed symmetry-broken (“electronic nematic”) ground state [159, 145, 146]. Normally, several mechanisms may lead to spontaneous breaking of the crystal symmetry as the system is driven by a change of some control parameter (e.g. temperature, electron doping, or pressure) towards an ordered ground state. For such symmetry breaking to occur, both electron and lattice degrees of freedom are often required [164], as in magneto-structural or charge-density-wave [165, 166] transitions. Occasionally, though, the electron degrees of freedom alone are sufficient to lead to an instability, while the lattice only adjusts itself to the new ground state, offering little contribution to the overall energy gain [164]. The most prominent examples of such electron-driven instabilities are SDW transitions [167, 168, 166], at which a magnetic ordering wave vector is spontaneously chosen out of several equivalent Fermi surface nesting vectors. In “electronic nematic” state, only the rotational symmetry of the electron subsystem is reduced, whereas the translational symmetry and, hence, the size of the BZ, are preserved. Such states have been extensively studied in quasi-two-dimensional compounds, such as $\text{Sr}_3\text{Ru}_2\text{O}_7$ [169] or underdoped $\text{YBa}_2\text{Cu}_3\text{O}_{6+y}$ [170, 171]. This electronic nematic phases for various iron-arsenide superconductors have been suggested not only from INS experiments [159, 145, 146] but also from theory [172, 173, 56, 174] and other experimental observations [175, 176, 133]. However, as a part of this thesis work [50], we have shown that at least the anisotropic pattern of in-plane spin-excitation spectra can be well described within the first-principles calculation level without invoking any symmetry-broken (or electronic nematic) ground state, and further proved that magnetic-excitation spectrum does not contain any finger-print for the nematicity that observed in underdoped $\text{YBa}_2\text{Cu}_3\text{O}_{6+y}$ [170]. We will present relevant INS data

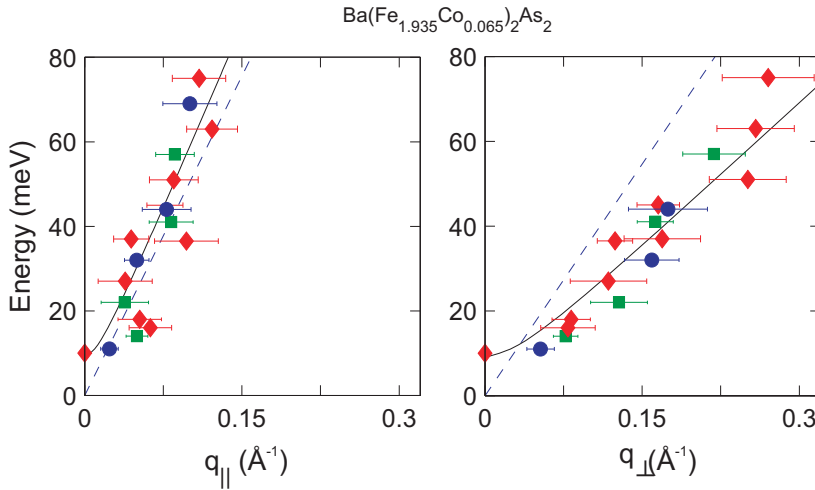


Figure 2.24: Dispersion of magnetic excitations in the paramagnetic state of nearly optimally doped BFCA compound [145].

for the anisotropic in-plane spin-fluctuation in the tetragonal paramagnetic state of optimally-doped BFCA in Sec. 4.2.3.

2.3 Superconducting properties

Superconductivity is phenomenologically characterized by zero resistance in electronic flow and expulsion of external magnetic-field (so called “Meißner effect”) [177]. Among the many FeSCs, representative experimental data for zero resistance and Meißner effect on the potassium-doped BKFA compound are shown in Fig. 2.25.

The microscopic model for superconductivity, known as BCS theory, explains the basic mechanism of resistanceless electrical flow based on phonon-mediated electron pairs (Cooper pairs), which occupy opposite momentum states and are bound within the SC energy gap, Δ [1]. Depending on the occupied spin states of Cooper pairs, the superconductivity can be categorized as singlet, where spins have opposite directions (*s*-wave or *d*-wave), or triplet Cooper-pairs, where spin states are the same direction (*p*-wave) [177]. Most well known conventional superconductors belong to phonon-mediated Cooper-pair type with *s*-wave spin-singlet symmetry, and SC behavior can be well described within the BCS theory. On the other hand, BCS theory has failed to explain the microscopic mechanism of the so-called *unconventional* superconductors, which are commonly defined by a different sign of SC gap ($\Delta_k = -\Delta_{k+q}$) and anisotropic pairing-symmetry. One of the main reasons for a failure of BCS theory in unconventional superconductors comes from the fact that the electron-electron interaction cannot be attractive due to the different signs of SC gap. Hence, alternative microscopic models for unconventional superconductors have been proposed such as magnetically mediated Cooper-pairs [178], but a final consensus remains has not been achieved. In this respect, studying electron-pairing symmetry and SC gap is essential to resolve the basic mechanism of unconventional superconductivity.

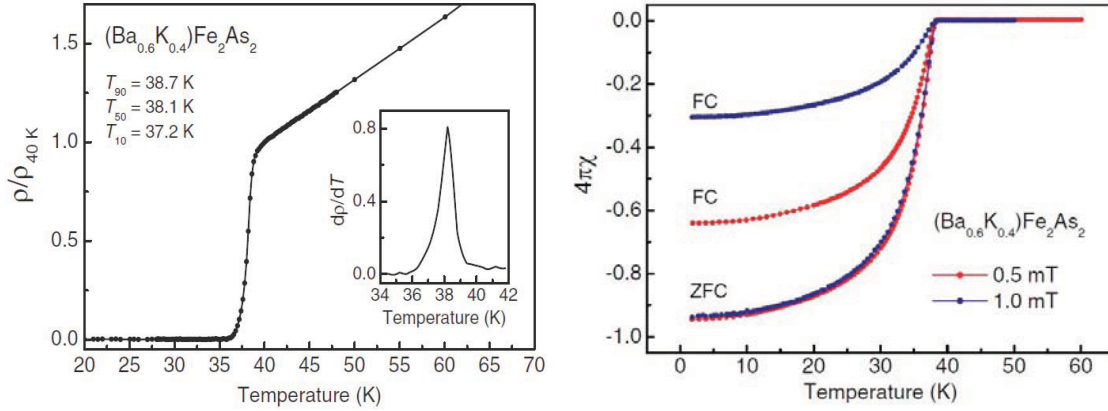


Figure 2.25: **Left.** Electrical resistivity curve versus temperature in the optimally doped BKFA [88]. The resistivity drops to zero below 38 K. **Right.** Magnetization curve versus temperature shows the diamagnetic response (Meißner effect) below T_c [88].

2.3.1 Pairing symmetry

In FeSC, the unconventional spin-singlet sign-reversal s -wave pairing symmetry, so-called s_{\pm} -wave, was theoretically predicted based on the circular shape of hole- and electron-like Fermi surfaces [54, 48, 179, 163, 180, 181, 182]. In addition, the nesting vector that connects these hole and electron Fermi surfaces at Γ and M positions in the unfolded BZ, creates strong interband particle-hole excitations that might be a key ingredient for superconductivity. Furthermore, the magnetically ordered state is also characterized by the same nesting vector, implying that magnetic collective excitations are a feasible candidate for the pairing mediator [54, 48, 179, 163, 180, 181, 182]. Thus, the SC energy gap on the hole Fermi surface at Γ and electron Fermi surface at M should have opposite signs of Δ , so that attractive electron-electron interaction becomes favorable within an assumption of spin-fluctuation mediated pairing [178]. Alternatively, s_{++} -wave symmetry, without no sign-change in the SC energy gap, has been proposed for FeSCs [183, 184, 185]. This scenario further suggested that the mediator of superconductivity might be the orbital fluctuations [183, 184, 185]. While the pairing mechanism in FeSCs has not been settled, most of experimental evidence is in favor of the magnetic-fluctuation mediated Cooper pairing scenario.

It was first shown by the NMR Knight-shift measurement in BKFA that Cooper pairs are in the spin-singlet state as expected from theoretical work [186]. The NMR Knight-shift (K) is sensitive to the paramagnetic response in the magnetic susceptibility, thus when two electrons are paired in the singlet state below the SC transition, $S = 0$, then the K should decrease and finally approach to zero. Figure 2.27 (a) shows one of representative NMR Knight shift data on BKFA, and K is indeed strongly reduced right below T_c , indicating the singlet Cooper-pairs [186]. On the other hand, ARPES technique can precisely measure the momentum-dependent

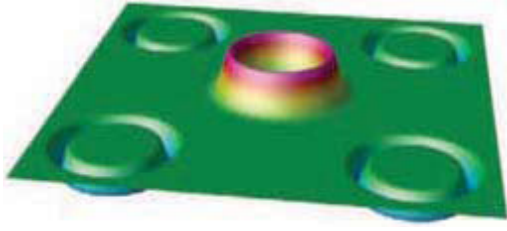


Figure 2.26: A schematic drawing of SC order-parameter for sign-reversal s_{\pm} -wave symmetry [21]. Each circle corresponds to 2D Fermi surface, and the sign of SC order-parameter along those Fermi surfaces changes between hole- and electron-like Fermi surfaces.

magnitude and structure of SC order-parameter [187]. Many ARPES experiments on 122 ferropnictides unambiguously revealed that the SC gap opens both at hole- and electron-like Fermi pockets as in Fig. 2.27 (b) [63] with slightly different magnitudes [63, 188, 66, 189, 190, 191, 192, 193]. Based on the nearly isotropic shape of SC order-parameter seen by ARPES and the strong reduction of the Knight-shift in the FeSC system, one can conclude that Cooper pairs should be in the spin-singlet state and their pairing symmetry should be isotropic. This fact is clearly inline with the theoretically predicted s_{++} and s_{\pm} -wave symmetry scenario, but this cannot determine which one is more preferable because both experimental techniques are not sensitive to a sign of SC order-parameter. Recently, some ARPES experimental works claimed the observation of orbital fluctuation as an alternative glue for Cooper pairs in FeSC, supporting s_{++} -wave symmetry [193], but it still remains a doubtful discussion.

A more direct examination for pairing-symmetry determination can be done by quasi-particle interference (QPI) pattern analysis in a scanning tunneling microscopy (STM) image. The STM measures the differential tunneling conductance, which is proportionally related to the density of states, in real space, and when impurities are present in a sample some electrons can be trapped in the local density of state due to the impurity scattering. Then, such electrons form a standing wave and produce a certain interference pattern in the Fourier-transformed STM images, known as a QPI pattern. Figure 2.27 (c) displays the QPI pattern in a 11-selenide compound where each spot corresponds to a \mathbf{q} -vector where it connects different electronic bands in the Fermi surface [194]. Under an applied external magnetic field, vortices are introduced, thus extra quasi-particle scattering arises. The coherence factor of extra scattering can be characterized by the sign of the order parameter, and as a result the intensity at some \mathbf{q} -vectors increases and some others decrease depending on whether the \mathbf{q} -vector connects the same sign of order-parameter or not. Such phenomenon was observed in a 11-FeSC, implying that s_{\pm} -wave symmetry is indeed favorable [194].

Another key experimental evidence of a sign-changing order parameter can be seen in the spin-excitation spectrum which will be discussed in Sec. 2.4.

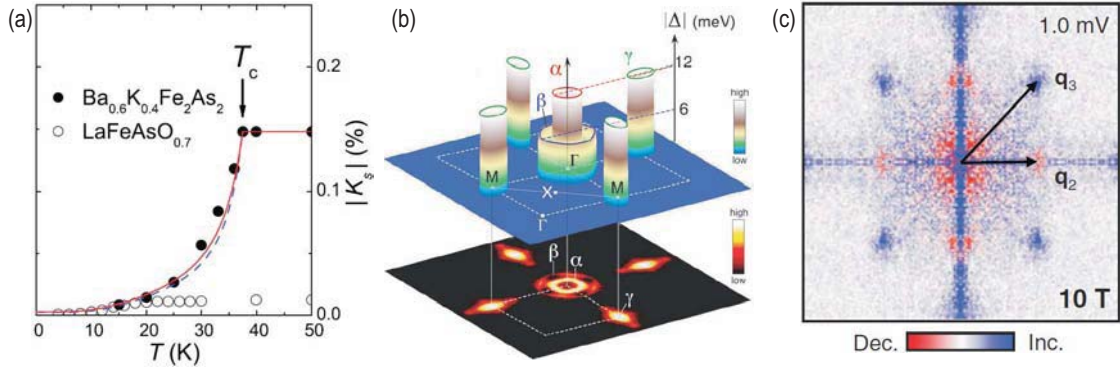


Figure 2.27: (a) The NMR Knight-shift versus temperature in BKFA [186]. The strong reduction of K indicates the spin-singlet state of Cooper pairs in the SC state. (b) 3D plot of the SC gap magnitude at different Fermi surfaces revealed by ARPES experiment in BKFA [63]. Nodeless SC gap along Fermi surfaces implies that the pairing symmetry should be a s -wave shape. (c) QPI patterns under the external magnetic field in the SC state for 11-compound [194]. Some patterns increase its intensity under the magnetic field whereas some other decreases. Such opposite behavior depending on electronic bands strongly suggests sign-changing in the SC order-parameter.

2.3.2 Coupling constant $2\Delta/k_B T_c$

Tied to the SC pairing-symmetry, the coupling constant, which is commonly characterized by the ratio of two times SC gap to the critical temperature $2\Delta/k_B T_c$, is another important physical quantity to determine the microscopic pairing-mechanism of superconductivity. For instance, conventional phonon-mediated superconductors are characterized by relatively weak pairing and low critical temperatures, whereas high- T_c layered copper-oxide-based ceramics typically exhibit stronger pairing with significant AFM correlations. Therefore, we are used to viewing these two classes of materials as clearly distinct. In FeSe, the results of the few existing systematic experimental studies of the pairing strength remain at odds with each other. Some report a more or less universal value of $2\Delta/k_B T_c$, either below [195] or well above [189] the weak-coupling limit of 3.53 predicted by the BCS theory, whereas others present evidence for a strongly doping-dependent coupling that reaches the BCS limit only as T_c decreases [196]. The reported values of $2\Delta/k_B T_c$ scatter from as low as ~ 3 , below the weak-coupling limit, [196, 197, 198, 199, 200] to 10 and above, [201] as summarized in the Appendix A.

In our recent paper [160] we have analyzed all the available energy-gap reports (either single, double, or multiple gaps) in various FeSC and their kin. We put these results into a broad context by comparing them to single- and multiband conventional superconductors, high- T_c cuprates, as well as heavy-Fermion compounds and a few other SC materials. In Fig. 2.28, the gap ratios, $2\Delta/k_B T_c$, are plotted vs. T_c . For

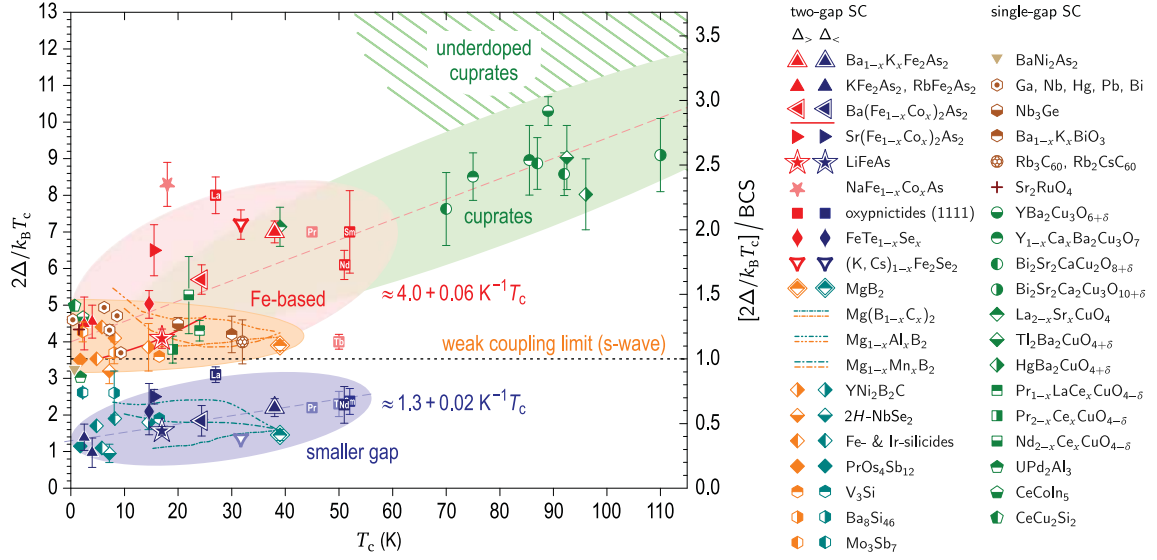


Figure 2.28: The coupling constants, $2\Delta/k_B T_c$, for different families of single- and two-gap superconductors versus their critical temperatures. The data points summarize most of the available measurements of the energy gaps in ferropnictides, high- T_c cuprates, and some conventional superconductors. Each data point is an average of all the available measurements of the corresponding compound by complementary techniques. The error bars represent the standard deviation of this average for repeatedly measured compounds or the experimental errors of single measurements, whenever averaging could not be performed. Such unconfirmed points are shown in lighter colors. Points confirmed in a considerable number of complementary measurements are additionally outlined. The weak-coupling limit, predicted for s-wave superconductors by the BCS theory, is shown by the dotted line. For weakly coupled d-wave superconductors, a slightly higher value of 4.12 is expected (not shown) [160].

multigap superconductors, we differentiate between the small ($\Delta_{<}$) and large ($\Delta_{>}$) energy gaps, which lie below and above the weak-coupling limit, respectively [202]. For Fe- and Cu-based materials, our analysis reveals a universal correlation between the coupling constant, $2\Delta/k_B T_c$, and T_c , which is not found in conventional superconductors. The best example comes from the juxtaposition of the stoichiometric conventional superconductor MgB_2 ($T_c = 39$ K) and the optimally hole-doped BKFA ($T_{c,\text{max}} = 38.5$ K) as shown in Fig. 2.28 (see Ref. [160] and references therein). Both are multiband superconductors with almost identical critical T_c temperatures, and their two well-separated SC gaps have been extensively measured by various experimental methods, such as ARPES [63, 188, 66, 189, 190, 191, 192, 193], scanning tunneling spectroscopy (STS) [203, 204, 205], point-contact Andreev reflection (PCAR) spectroscopy [206, 207], μSR [208, 209], calorimetry [78], and others (see the Appendix A).

By averaging these results, the gap ratios can be determined with a very small uncertainty. The larger gap in MgB_2 yields an average $2\Delta_{>}/k_B T_c$ ratio of 3.9 ± 0.13 , only 10% above the weak-coupling limit. The corresponding ratio for BKFA, however, is 7.0 ± 0.3 , almost twice the BCS value ~ 3.53 . On the other hand, the 100% doped

122-ferropnictides are stoichiometric low- T_c superconductors KFe_2As_2 ($T_c = 4$ K), RbFe_2As_2 ($T_c = 2.5$ K) and BaNi_2As_2 ($T_c = 0.68$ K), all characterized by weak coupling [197, 210, 93]. Moreover, BaNi_2As_2 appears to be a conventional phonon-mediated superconductor [197]. This implies that the $2\Delta_{>}/k_B T_c$ ratio must vary continuously with doping within the Ba-122 family — an effect that so far has been directly observed only in the Co-doped series [196]. Fig. 2.28 suggests this variation to be even stronger (almost twofold) in BKFA, where higher values of T_c can be reached. Indeed, the extensively studied optimally-doped BFCA ($T_c = 25$ K) has an average gap ratio of only 5.4 ± 0.4 , in the middle between those of optimally-doped BKFA and weakly coupled superconductors [211, 190, 212].

From our analysis, we found out that the SC pairing-strength in ferropnictides ranges from weak in low- T_c regime, near the limit predicted by the BCS theory, to strong in high- T_c , as in cuprates. Therefore, in contrast to the high- T_c cuprates, which can be generally classified as strong-coupling superconductors, Fe-based systems show a larger variability and fill in the wide gap between conventional and cuprate-like pairing strengths. The overall trend confirms that the superlinear increase of $\Delta_{>}$ with T_c , suggested in Ref. [196], remains qualitatively valid for all Fe-based compounds in general.

2.4 Magnetic resonant mode in the spin-excitation spectra

As discussed in the previous sections, spin fluctuations are the most likely mediator for the superconducting pairing in the FeSCs for the following two reasons: i) Persistence of AFM correlation throughout the phase diagram of FeAs-superconductors. ii) The electron-phonon coupling strength is too weak to explain the relatively high T_c in the FeSC system. The magnetically-driven Cooper-pairing scenario was also strongly supported by the experimental observation of a dramatic spectral-weight redistribution in the spin-excitation spectrum below the SC transition temperature [213]. As a result, a sharp peak, a so-called *magnetic resonant mode*, in the magnetic-fluctuation spectrum appears at the characteristic energy situated below $2\Delta_{\text{SC}}$. The magnetic resonant mode shows a strong correlation with superconductivity. For instance, resonance peak evolves at the SC critical temperature, and shows an order-parameter-like behavior with decreasing temperature. Moreover, the energy of the magnetic resonant mode is correlated with the SC transition temperature and the magnitude of SC energy gap. In this section, we will discuss how the resonance mode emerges as collective magnetic excitations in the SC state within in a Fermi-liquid framework under an assumption of BCS-like SC gap and what the magnetic resonant mode implicates about the SC

pairing symmetry. Then, experimental observations of the magnetic resonant mode in FeSCs will be introduced.

2.4.1 Theoretical approach

Let us start by showing how one can describe the magnetic dynamics in a weakly-interacting Fermi-liquid system. While the single-particle Green's function accurately describes the single-particle excitation property within a linear response region, more complicated response function would be needed to describe a higher-order response function, also known as a *two-particle correlation function*¹. This function is defined as

$$\chi_0(\mathbf{q}, t) = \langle [\rho_\sigma(\mathbf{q}, t), \rho_\sigma(\mathbf{q}', 0)] \rangle, \quad (2.6)$$

where ρ_σ is the spin-density operator and \mathbf{q} is the momentum of occupied or unoccupied electron states. The time-dependent spin-density operator can be defined as,

$$\rho_\sigma(\mathbf{q}, t) = \frac{1}{(2\pi)^3} \int d\mathbf{k} c_{\mathbf{k},\sigma}^\dagger c_{\mathbf{k}+\mathbf{q},-\sigma} e^{i(\epsilon_{\mathbf{k}} - \epsilon_{\mathbf{k}+\mathbf{q}})t}. \quad (2.7)$$

By substituting it into Eq. 2.6 and taking a Fourier transformation, we get the bare susceptibility, also known as the *Lindhard function*.

$$\chi_0(\mathbf{q}, \omega) = -\frac{1}{(2\pi)^3} \int d\mathbf{k} \frac{f_{\mathbf{k}+\mathbf{q}} - f_{\mathbf{k}}}{\epsilon_{\mathbf{k}+\mathbf{q},\sigma} - \epsilon_{\mathbf{k},-\sigma} - \omega - i\delta}, \quad (2.8)$$

where $f_{\mathbf{k}}$ is the Fermi-function. The Lindhard function is a good starting point to calculate the two-particle correlation functions of interacting electron systems, if the interactions are small enough to be considered as perturbations. Indeed, this Lindhard function describes the normal-state magnetic-dynamic response very well for the FeAs-superconductors [113]. The imaginary part of the bare susceptibility shows a gapless particle-hole continuum down to zero energy, but this channel would be gapped out up to 2Δ when the SC gap opens on the Fermi surface. Hence, the bare susceptibility with the SC energy gap, Δ has to be normalized as [214, 215, 216],

$$\chi_0^{\text{SC}}(\mathbf{q}, \omega) = -\frac{1}{(2\pi)^3} \int d\mathbf{k} \sum_{\alpha,\beta=\pm} (A_{\mathbf{k}}^\alpha A_{\mathbf{k}+\mathbf{q}}^\beta + C_{\mathbf{k}}^\alpha C_{\mathbf{k}+\mathbf{q}}^\beta) \frac{f(E_{\mathbf{k}+\mathbf{q}}^\alpha) - f(E_{\mathbf{k}}^\beta)}{E_{\mathbf{k}+\mathbf{q}}^\alpha - E_{\mathbf{k}}^\beta - \omega - i\delta}, \quad (2.9)$$

where the quasi-particle dispersion relation is given by $E_{\mathbf{k}}^\pm = \pm \sqrt{\epsilon_{\mathbf{k}}^2 + \Delta_{\mathbf{k}}^2}$, and $\epsilon_{\mathbf{k}}^\nu$ is the electronic band energy measured relative to the Fermi level. Pre-factors $A_{\mathbf{k}}^\pm$ and $C_{\mathbf{k}}^\pm$, generated by the exchange of operators during a diagonalization, are defined as,

$$A_{\mathbf{k}}^\pm = \frac{1}{2} \pm \frac{\epsilon_{\mathbf{k}}}{E_{\mathbf{k}}^+ - E_{\mathbf{k}}^-} \quad C_{\mathbf{k}}^\pm = \pm \frac{\Delta_{\mathbf{k}}}{E_{\mathbf{k}}^+ - E_{\mathbf{k}}^-}. \quad (2.10)$$

¹This is an essential approach for calculating magnetic neutron scattering function which is extensively discussed in Sec. 3.2.1.

The random-phase approximation (PRA) provides a simple way to introduce the interaction onto the bare susceptibility by summing up multi-order pair-correlations. Then, the RPA susceptibility can be written as [214, 215, 217],

$$\chi_{\text{RPA}}(\mathbf{q}, \omega) = \frac{\chi_0(\mathbf{q}, \omega)}{1 - U(\mathbf{q})\chi_0(\mathbf{q}, \omega)}, \quad (2.11)$$

where $U(\mathbf{q})$ represents an arbitrary interaction. Finally, the imaginary part of the RPA susceptibility will diverge when $\text{Re}\chi_0^{\text{SC}}(\mathbf{q}, \omega) = 1/U(\mathbf{q})$ and at the characteristic energy, ω_{res} , where the $\text{Im}\chi_0^{\text{SC}}(\mathbf{q}, \omega) = 0$, that is below the particle-hole continuum. Such divergence of the imaginary part of RPA spin susceptibility can be referred to as a bound state of spin-1 exciton in the particle-hole channel, and is called the magnetic resonant mode. More importantly, however, the divergence of the imaginary part of $\text{Im}\chi_{\text{RPA}}(\mathbf{q}, \omega)$ will appear when the coherence factor which entered in Eq. 2.9 becomes non-zero. The coherence factor, the multiplier in Eq. 2.9, can be rewritten as [215, 217],

$$\begin{aligned} & A_{\mathbf{k}}^+ A_{\mathbf{k}+\mathbf{q}}^- + C_{\mathbf{k}}^+ C_{\mathbf{k}+\mathbf{q}}^- + A_{\mathbf{k}}^- A_{\mathbf{k}+\mathbf{q}}^+ + C_{\mathbf{k}}^- C_{\mathbf{k}+\mathbf{q}}^+ \\ &= \frac{1}{2} - \frac{2\epsilon_{\mathbf{k}}\epsilon_{\mathbf{k}+\mathbf{q}} + 2\Delta_{\mathbf{k}}\Delta_{\mathbf{k}+\mathbf{q}}}{(E_{\mathbf{k}}^+ - E_{\mathbf{k}}^-)(E_{\mathbf{k}+\mathbf{q}}^+ - E_{\mathbf{k}+\mathbf{q}}^-)} \\ &= \frac{1}{2} \left(1 - \frac{\epsilon_{\mathbf{k}}\epsilon_{\mathbf{k}+\mathbf{q}} + \Delta_{\mathbf{k}}\Delta_{\mathbf{k}+\mathbf{q}}}{E_{\mathbf{k}}E_{\mathbf{k}+\mathbf{q}}} \right). \end{aligned} \quad (2.12)$$

Therefore, the coherence factor becomes finite only if $\Delta_{\mathbf{k}}\Delta_{\mathbf{k}+\mathbf{q}} < 0$, i.e., when the SC order parameters on two Fermi surfaces connected by \mathbf{q} has a different sign. After all, the presence of the magnetic resonant mode is taken as undoubtable evidence for sign-changing SC pairing-symmetry such as d -wave in cuprates or s_{\pm} -wave in the pnictide superconductors. The other aspect of the resonance mode is that its characteristic energy is related to the strength of the interaction in the system as well as the magnitude of SC energy gap.

2.4.2 Experimental observations

The magnetic resonant mode in the magnetic spectrum can be observed by INS measurements due to its wide momentum-transfer range and relevant energy-transfer range, which is about a milli-electron-volt. The first experimental finding of a magnetic resonant mode in the spin-excitation spectrum was made in $\text{YBa}_2\text{Cu}_3\text{O}_{6+y}$, where the SC order parameter possesses a $d_{x^2-y^2}$ -wave symmetry in momentum space [218]. Subsequent observations of the resonance mode in many other cuprates and heavy Fermions have been reported [219, 220, 221, 222, 6]. In the iron-arsenide system, the magnetic resonant mode was first observed from an INS study on polycrystalline $\text{Ba}_{1-x}\text{K}_x\text{Fe}_2\text{As}_2$ [213]. Since then the magnetic resonant mode has been observed not

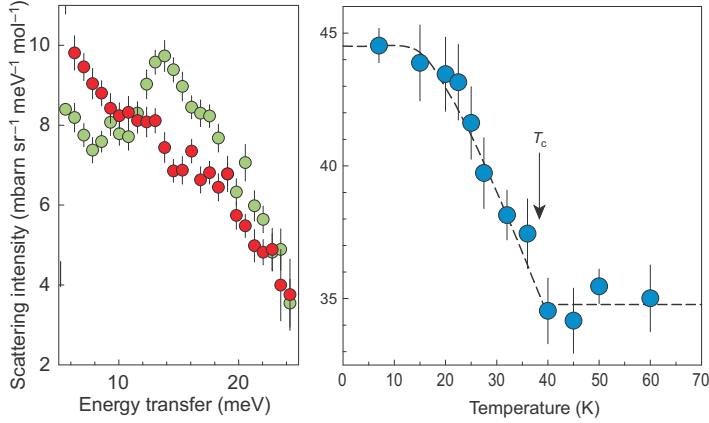


Figure 2.29: Reproduced from Ref. [213]. **Left.** The redistribution of spectral weight across T_c in the optimally-doped $\text{Ba}_{1-x}\text{K}_x\text{Fe}_2\text{As}_2$. **Right.** The temperature dependence of magnetic resonant peak intensity shows an order-parameter-like behavior starting from T_c .

only in the 122-ferropnictides, but also in numerous Fe-based superconductors (for a summary, see the table in Appendix. A.2) [223, 224, 225, 226, 160, 227, 228, 229, 230, 231, 232, 233, 234, 50, 235, 236, 237, 238, 239, 240, 241, 242, 243, 244]. The magnetic resonant mode is manifested in the spin-fluctuation spectrum by a strong enhancement of the magnetic neutron-scattering intensity at characteristic energy and momentum positions in the SC state. The onset temperature of such an enhancement of magnetic intensity generally coincides with the SC transition temperature, and the temperature-dependent resonance peak exhibits an order-parameter-like behavior towards the zero temperature as shown in Fig. 2.29. This signature implies that the magnetic resonant mode is strongly correlated to superconductivity. The momentum position of the magnetic resonant mode, \mathbf{q}_{res} , in the FeSC is situated at the nesting vector, which connects hole and electron Fermi surfaces. As we already discussed based on the theory, the presence of magnetic resonant mode unquestionably indicates a sign difference with the SC order-parameters, thus confirming the s_{\pm} -wave pairing symmetry in the FeSC system.

The main work of this thesis is focused on the magnetic resonant mode. Hence, we will continue to discuss further physical implications of the resonant mode, such as a distinct resonant mode in the newly discovered iron-selenides and scaling relationships of the resonance energy in Chap. 4 and 5.

Chapter 3

Experimental methods

3.1 Preparation of single crystalline samples

3.1.1 Flux method for single crystal growth

The samples used in this thesis were grown either by the flux or Bridgman method in the group of Dr. C. T. Lin at the MPI-FKF and Prof. A. Loidl at Augsburg University. A detailed description of growth procedure can be found in Ref. [79, 245]. In short, starting materials in a mole ratio of Ba:Fe:Co:As = 1:4.5:0.5:5 (all elements are from Alfa Aesar, 4-5 N purity) were used for self-flux growth. Usually, ~ 20 g of mixture were ground and then loaded in a ZrO₂ crucible covered with a lid to minimize arsenic volatilization. An Al₂O₃ stick of $\varnothing 2 \times 50$ mm is inserted to a hole drilled through the lid and dips into the mixture to serve as a nucleation pole. All preparation procedures were carried out in a glove box containing Ar gas. The loaded crucible was then sealed in a quartz ampoule filled with 250 mbar argon atmosphere. The ampoule was placed in a furnace and heated up to 1190 °C for 10 hours. The temperature of the melt was then lowered to 1090 °C at a rate of $\sim 2^\circ\text{C}/\text{h}$, and this was followed by decanting of the residual flux. Finally, the furnace was cooled down to room temperature at 100 °C/h. The whole procedure of crystal growth was carried out in a sealed system with a specially designed apparatus shown in Fig. 3.1.

A nucleation center is crucial for the growth of a large and high-quality single crystal. In our growth experiment, we used an alumina stick which served as a seed to play a role of a nucleation pole in the melt during the growth procedure. The alumina stick was positioned at the bottom of the crucible. This allows for the heat to flow from the hotter melt T_1 to the colder end T_2 of the stick, creating a temperature gradient of 3 – 8 °C/cm when the heating temperature ranges between 1190 and 1090 °C. A schematic drawing of the experimental setup is shown in Fig. 3.1. By using this “seeding” method together with a low cooling rate of $\sim 2^\circ\text{C}/\text{h}$ applied, spontaneous and numerous nuclei can be minimized during growth. The process of crystallization

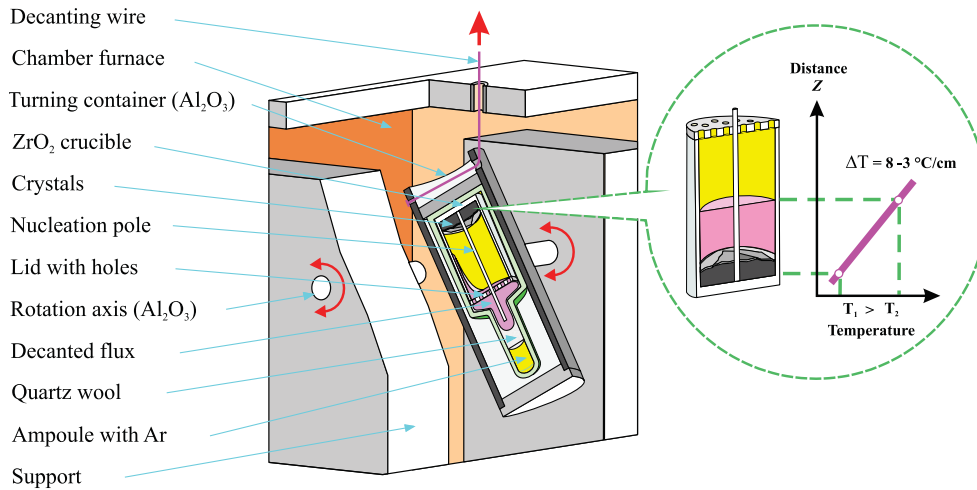


Figure 3.1: Schematic drawing of the apparatus used to grow single crystals of 122-ferropnictides [79]. The inset shows a temperature gradient of 3 – 8 °C/cm distributed from the bottom to the upper part of the solution.

takes place around the seed, which is the colder pole of the stick. With cooling the crystals gradually grow, resulting in a large crystal, together with some small crystals being formed around the big one. We demonstrate that a crystal can be grown as large as $\varnothing 40 \times 5$ mm where the thickness depends on the amount of the source material. Fig. 3.2 (left) shows a seed rod located in the center of a crystal disk and a broken part of a crystal sized $20 \times 10 \times 2$ mm³, one third of the disk. It has been noticed that to minimize the amount of residual flux in the sample a temperature of $\sim 1090^\circ\text{C}$ had to be maintained for ~ 2 h after decanting before cooling to room temperature. This allows most of residual flux to flow out while leaving free-standing crystals inside the crucible. It should be emphasized that the decanting device is specially equipped with a movable nickel wire of the top, used for tilting the crucible to remove the residual flux from the furnace at high decanting temperatures. This can avoid possible poisoning from arsenic in case a crack of the quartz tube occurs.

As-grown single-crystalline samples already show layers, which one can see even with a naked eye, perpendicular to a disk-like plane and such well-distributed layers can be easily seen in an X-ray single-crystal diffraction measurement. Figure 3.2 (right) displays a typical X-ray single-crystal diffraction pattern along the c -axis. Sharp peaks of $(00L)$ nuclear Bragg reflections were recorded for the parent and Co-doped BFA compounds, which confirms their high quality.

In spite of good crystallinity of samples grown by flux method, a piece of a single crystal can often contain an excess FeAs phase forming a natural eutectic alloy with the main phase according to the chemical phase diagram of FeAs/BaFe₂As₂ [246]. Such alloys typically coexist with the main superconducting phase in large single crystals grown either by self-flux or Bridgman methods. SEM images (Fig. 3.3), Energy-

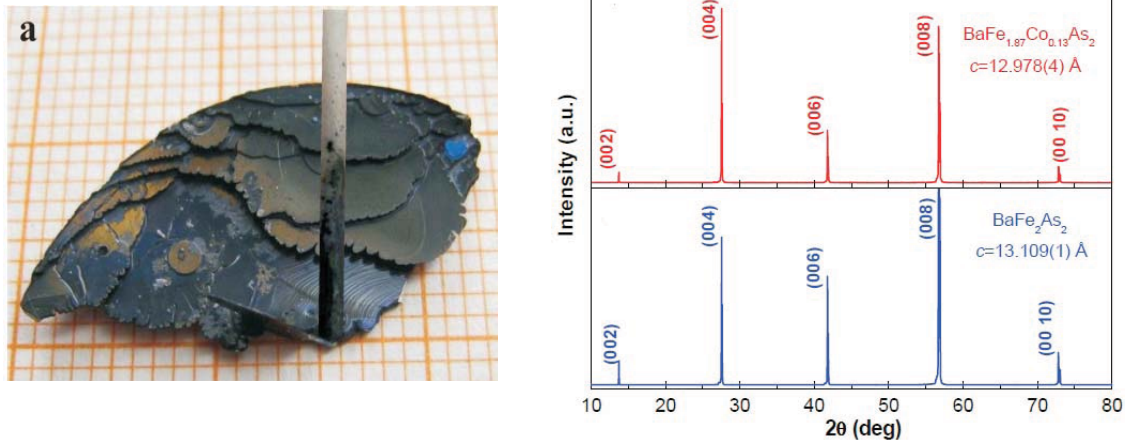


Figure 3.2: **Left.** A photo of $\text{BaFe}_{1.85}\text{Co}_{0.15}\text{As}_2$ single crystal with a mass of ~ 1 g. The alumina “seed” is located in the center of the disk-shaped single crystal. **Right.** X-ray single-crystal diffraction pattern of the parent BFA and optimally doped BFCA materials. Sharp and clean $(00l)$ Bragg reflections were recorded and showed slight difference in 2θ positions due to c -lattice parameter contraction under chemical substitution.

dispersive X-ray (EDX) measurements, and elastic neutron scattering data indicate that our samples are also partially contaminated by the eutectic mixture of Fig. 3.3. In the backscattered-electron (BSE) image of the $\text{BaFe}_{1.85}\text{Co}_{0.15}\text{As}_2$ single crystal ($T_c = 25$ K) grown in self-flux, bright areas represent the homogeneous phase of $\text{BaFe}_{1.85}\text{Co}_{0.15}\text{As}_2$, meanwhile dark areas contain a eutectic mixture of the Ba-free flux phase with the main phase. $\text{Fe}_{1-x}\text{Co}_x\text{As}$ with the main phase. A neutron elastic θ - 2θ scan measured with a triple axis neutron spectrometer on one of the most contaminated samples is shown in Fig. 3.3. It shows a number of additional peaks next to the main (110) structural Bragg reflection, which we associate with the impurity phase. The rocking curve measured on the strongest of impurity peaks has a well-developed peak structure (inset), indicating that some part of the Ba-free phase is single crystalline and co-oriented with the main phase. The other peaks, however, are consistent with the powder diffraction peaks of the polycrystalline phase of the same compound. From our experience, the fraction of such impurity phases can vary from 5–10% in the highest-quality samples to ~ 30 –40% in lower-quality samples, and usually increases with the sample mass. In principle, such impurity phases can influence the results of INS measurements by introducing spurious peaks into the spectra. Thus, we have mapped out not only the nuclear Bragg reflections of the real phase, but also the complicated nuclear Bragg reflections from the mixture of eutectic phases by using the E2 flat-cone diffractometer at HMI. Indeed, powder lines coming from the trace of the $(\text{Fe,Co})\text{As}$ flux have been observed in Fig. 3.6 (c), but their intensity is quite small, so that possible spurious effects related to the impurity phase are negligible in our INS measurements.

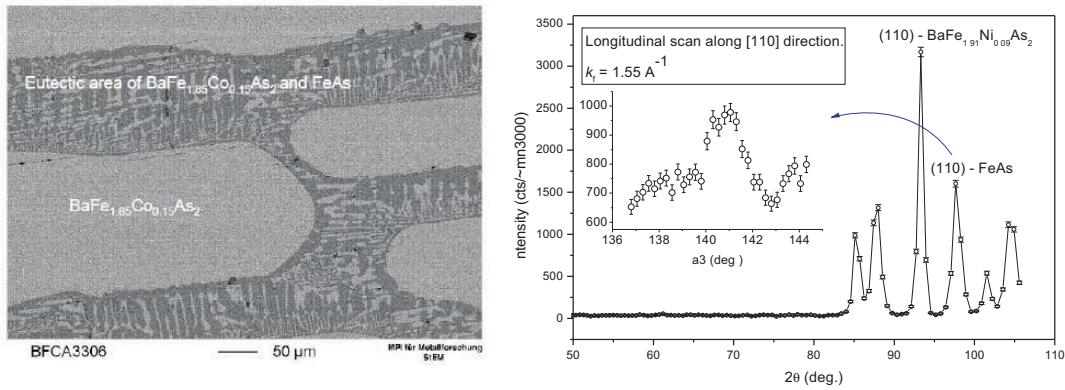


Figure 3.3: **Left.** Backscattered-electron image of the BaFe_{1.85}Co_{0.15}As₂ single crystal grown in self-flux. Bright areas represent the homogeneous phase of BaFe_{1.85}Co_{0.15}As₂, while the dark areas contain a eutectic mixture of the Ba-free flux phase with the main phase. **Right.** Longitudinal q-scan along the [110]_{Fe₂} direction of BaFe_{1.91}Ni_{0.09}As₂. The strongest main peak represents the (110) Bragg reflection from the real phase. On the other hand, smaller peaks can be attributed to the mixed eutectic phase. Inset shows a rocking curve on the (110) Bragg reflection in the FeAs phase.

3.1.2 Sample characterization

Before studying the physical properties of target materials by means of a spectroscopic method, the quality of a sample has to be assured for successful spectroscopic experiments. For example, if one wants to study a single-crystalline superconductor with triple-axis neutron-scattering spectroscopy, proper characterization of the superconducting properties and single-crystallinity of samples should be performed in advance. In following, several basic characterization methods are listed.

Magnetization measurements

One of the most commonly used ways to characterize physical properties of samples is a magnetization measurement. In the case of superconductors, it allows one to determine the SC transition temperature and estimate the SC volume fraction by means of “Meißner-Ochsenfeld” effect, which was already discussed in Sec.2.3. In a perfectly clean material, this effect should be independent of whether a magnetic field is applied after the sample was been cooled below T_c or the sample is cooled into the SC state already in a field, as long as the applied field is smaller than H_{c1} . That is, no matter how one measures the magnetic moment of a superconductor, the external magnetic field will be expelled or excluded in the SC state, which would result in the same diamagnetic signal. However, in practice, samples always possess at least some amount of impurities, which act as magnetic vortex pinning centers. As a result, the actual diamagnetic response in a field-cooled (FC) measurement is smaller than a zero-field-cooled (ZFC) measurement, and the signal difference between ZFC and

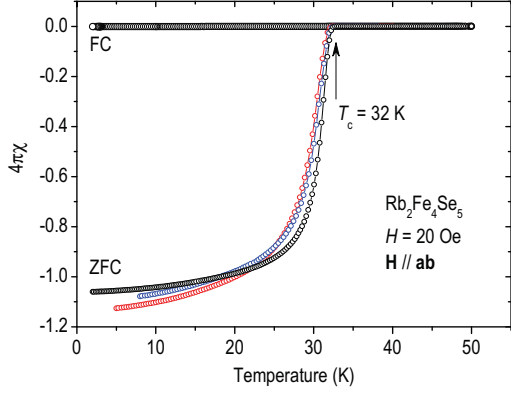


Figure 3.4: The dc magnetic susceptibility measurements on three representative single-crystalline $\text{Rb}_2\text{Fe}_4\text{Se}_5$ samples from the same batch. A sharp diamagnetic response is observed in the ZFC measurement right below 32 K, indicating 100% exclusion of the external magnetic field. However, a full shielding effect does not prove 100% SC volume fraction in the sample.

FC measurements will strongly depend on the amount of impurities or disorder in a compound. In FeSC, most SC compounds contain a substantial amount of dopants (or isovalent chemical substitutions), thus ZFC is a better test to determine the SC transition temperature and SC volume fraction of samples than FC measurements.

As an example of how a magnetization curve characterizes the SC properties, Fig. 3.5 displays a set of ZFC magnetization curves in the SC state for many different samples from the same batch measured by superconducting quantum interference device (SQUID)-vibrating sample magnetometry (VSM) (Quantum Design). The nominal composition of the batch is 24% Co-doped BFA compound with T_c of 10 K according to its phase diagram [32]. Indeed, most of the samples exhibit a sharp drop in the magnetic response around 10 K. However, some of the samples show diamagnetic response originating from a shielding effect already at 25 K, which is close to the optimal SC transition temperature in the BFCA system. Such observation indicates that those samples should contain the areas where the Co concentration is nearly optimal (7.5% of Co). In this case, optimally-doped regions in the sample should be regarded as an impurity phase, so that once should exclude such inhomogeneous samples from further investigations. The optimally-doped BFCA and BFNA compounds that we have intensively studied by INS experiments in this thesis, were characterized in the same manner, and all showed a very clean and strong SC response in the magnetization curves as shown in Fig. 3.6 (a), indicating a bulk nature of superconductivity in both materials. In addition, one can extract a rough estimation of the SC volume fraction using the signal of the shielding effect. If a superconductor expels or excludes an applied magnetic field completely in the SC state, then its magnetic susceptibility χ_m should be -1. Hence, χ_m in the SC state should vary between 0 and -1 depending on the fraction of superconducting phase in a sample. In a SQUID measurement, one obtains the magnetic moment (m) and can convert it to χ_m using a simple relation,

$$\mathbf{M} = \chi_m \mathbf{H} \quad (3.1)$$

$$\chi_{m, \text{SI}} = 4\pi \frac{m}{V\mathbf{H}}. \quad (3.2)$$

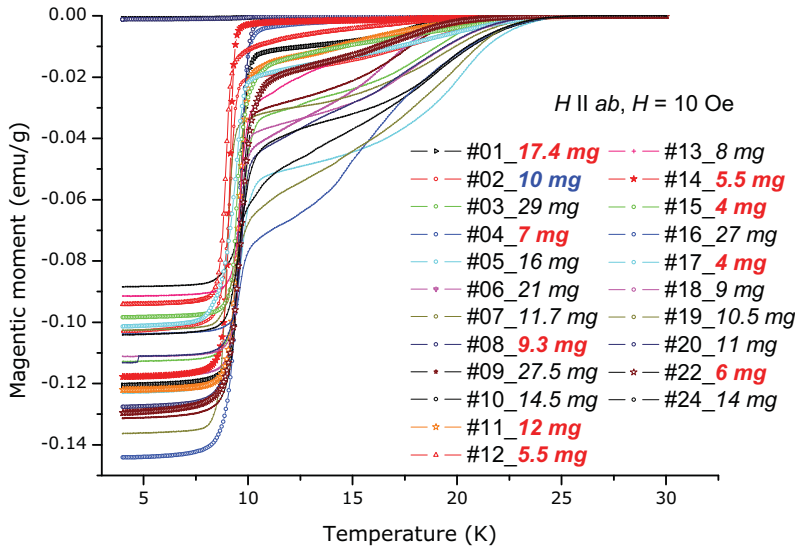


Figure 3.5: Magnetic moments versus temperature in an external magnetic field of 10 Oe measured in the zero-field cooled (ZFC) configuration for many different pieces of one overdoped BFCa batch. Some pieces show a sharp and clean SC transition, whereas some others exhibit a broad or multiple SC transition due to inhomogeneous distribution of Co concentration in the sample.

where \mathbf{M} is the magnetization of materials, V is volume of the sample, and \mathbf{H} is the applied field in Gauss. 4π is multiplied to convert to the dimensionless SI magnetic susceptibility value [247]. Yet, one has to bear in mind that there could be a non-negligible demagnetization effect, which is related to the sample shape [247]. To minimize such side-effects in deducing shielding fraction, it is recommended to always measure a slab-shaped sample with applied magnetic field along plane direction in which a demagnetization factor should be close to zero.

There is also a special case for 100% shielding effect without actual 100% of SC volume fraction. Imagine a spherical shape of a material with a thin SC layer on the surface with a thickness of tens of nanometers. In the SC state, supercurrent would be generated on the surface to prevent a magnetic field from penetrating into the sphere. As a result, in the ZFC case, it will show a full diamagnetic response ($\chi_{m,SI} = -1$) even though only tiny fraction of material is superconducting. On the other hand, in a FC measurement, a certain amount of field will be trapped inside the sphere, resulting in a small diamagnetic response compared to that of ZFC measurement. Unfortunately, it is difficult to distinguish whether the trapped flux inside the sample is due to pinning centers or a non-SC phase. Thus, to estimate the SC volume fraction with a high precision, other complementary experiments have to be carried out, for instance, μ SR. Recently discovered 122-type FeSCs (245-selenides) seem to manifest the surface superconductivity. Fig. 3.4 shows several ZFC magnetization measurements on Rb-245 superconductors, and indeed, the diamagnetic signal reaches -1 at low temperatures which could be an indication of 100% SC volume fraction in the sample. However, it is now reported that the SC volume fraction of this compound is only about 20%, as

determined by many different experimental methods [248, 249, 250, 251, 252]. In summary, the magnetization data for superconductors give useful information about the SC properties of the sample, but one should keep in mind the difference between the shielding fraction and the actual SC phase volume fraction.

X-ray and neutron diffraction

Investigating single-crystalline compounds is essential for the condensed matter research field. This is because investigation of the directional dependence of various physical properties only can be done only in single crystals. One example of such a property is the anisotropic ratio of electrical resistivity along different crystallographic directions. It is more important to measure high-quality single-crystalline samples when performing momentum-resolved spectroscopic studies, for instance ARPES or INS. Therefore, characterization for single-crystallinity has to be done beforehand.

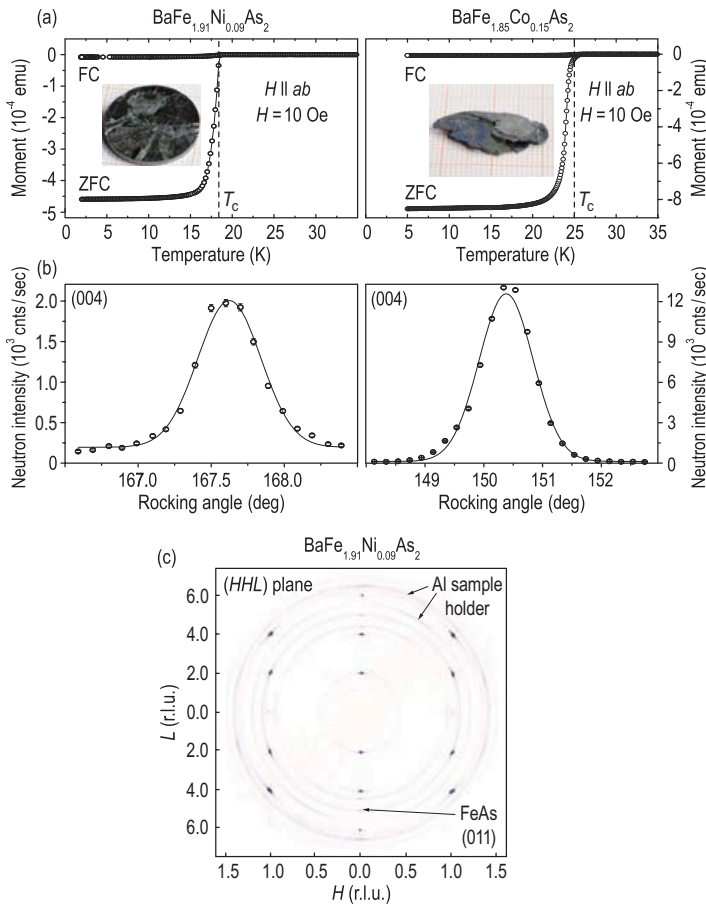


Figure 3.6: (a) Magnetization curves measured in the magnetic field of 10 Oe, applied in plane, after cooling in the field (FC) and in zero field (ZFC). Insets show photos of the samples. (b) Rocking curves measured on the (004) reflection in the (HHL) scattering plane with a triple-axis spectrometer. (c) Neutron-diffraction pattern of a $\text{BaFe}_{1.91}\text{Ni}_{0.09}\text{As}_2$ sample in the (HHL) scattering plane. Powder lines coming from the Al sample holder and traces of the $(\text{Fe},\text{Co})\text{As}$ flux are marked by arrows.

X-ray diffraction using conventional laboratory equipment is one of the most common and standard methods to test sample's crystallinity. First of all, it provides about information whether the sample is a single-crystalline phase by observing allowed Bragg reflections from a given scattering plane. If additional Bragg reflections showed up, then one might suspect the existence of other multiple grains with different



Figure 3.7: Photo of a mosaic of co-aligned Mn-doped BFCA samples. The orientation of each sample was checked by X-ray Laue diffraction.

crystallographic orientations in the sample. Moreover, by analyzing the width of each Bragg reflection, one can determine either the angular spread of mis-oriented domains or the homogeneity of lattice constants in the sample depending on which type of measurement is done.

However, this tool is not sufficient if a sample is quite bulky and massive because the X-ray diffraction is a surface-sensitive probe. In particular, samples for INS experiments must be large due to a lower neutron flux and scattering probability compared to the photon scattering. Thus, in such a case, other bulk probes, complementary to X-ray diffraction, such as neutron diffraction, should be carried out. Panel (b) in Fig. 3.6 displays sample-rotating neutron-diffraction scans on the (004) nuclear Bragg reflection in Ni- and Co-doped BFA compounds. In spite of the centimeter size of the samples, as shown in the insets of panel (a), the mosaicity of samples is less than 1° with no signature of multiple single-crystalline grains, which confirms the excellent quality of INS measurements. As mentioned above, some polycrystalline contamination originating both from the main phase and to a lesser extent from traces of the (Fe,Co)As flux was detected [see Fig. 3.6 (c)].

Thanks to the single-crystal-growth group led by Dr. C. T. Lin within our institute (MPI-FKF), we got big single crystals of BFNA and BFCA, although usually it is extremely challenging to grow big enough single-crystalline samples for INS measurements. To overcome this difficulty, we have prepared a couple of sample mosaics, usually consisting of a few tens of small single-crystal pieces, using a back-scattered X-ray Laue diffractometer (see Fig. 3.7 as an example). The total mass of each sample mosaic is about ~ 1 g with its mosaicity of approximately 2 – 3 degrees, as characterized by a neutron diffractometer, which is sufficient for INS experiments.

3.2 Neutron scattering technique

Neutron scattering is constantly used in condensed-matter research to understand the structural and dynamical properties of materials. The uniqueness of neutron scattering as an experimental probe originates from the fundamental properties of neutrons. First of all, neutrons are charge-neutral particles which means that they do not interact with charged particles inside a material via the long-range Coulomb interactions. Instead, neutrons scatter off by experiencing the short-range strong force interaction ($\sim 10^{-15}$ m) with nuclei in matter. Additionally, neutrons carry the magnetic moment of spin $\frac{1}{2}$, which allows it to interact with an electron's magnetic moment (spin or orbital) in matter through the magnetic dipole-dipole interaction. Both fundamental ways of interacting with matter are much weaker than the Coulomb force. As a result, most neutrons penetrate into the bulk of a compound on a centimeter scale¹. Therefore, neutron scattering can probe bulk properties of materials. Another characteristic of neutron scattering is related to the energy and length scale of neutrons. Since a typical inter-atomic distance in the solid is about a few angstroms, the ideal tool for studying structure and dynamics on atomic scales is the one that has a wavelength in the range of a few angstroms. Electrons with a wavelength of a few Å have energies of tens of electron volts (eV) which corresponds to the energy scales of charge or plasmonic excitations in the matters. On the other hand, neutrons with a wavelength of a few Å have energies of tens of milli-electron volts (meV) - they are usually called thermal ($10 \text{ meV} < E < 100 \text{ meV}$) or cold ($E < 10 \text{ meV}$) neutrons - which is comparable to collective modes such as lattice vibrations (phonons) or spin-wave excitations (magnons). Hence, neutron scattering is an excellent probe of low-energy excitations in solids.

Neutrons can be produced in two different ways, either in a fission nuclear reactor or spallation source. A research reactor uses uranium metals enriched with ^{235}U as a fuel for nuclear fission. When a neutron collides with a ^{235}U atom, the latter decays into two different fission fragments emitting on average 2.3 neutrons per one decay process. Some part of those emitted neutrons will cause other nuclear fission reactions by colliding with other ^{235}U atoms, which results in a chain reaction until ^{235}U atoms are exhausted. The neutrons that do not participate in the chain reaction can be utilized for neutron scattering experiments after passing through a light-atom composite (also called *moderator*), which assembles neutrons into a Maxwellian flux distribution with the maximum in the desired energy range². Then, continuous and moderated neutrons will be guided from the reactor core to the

¹On the other hand, some materials easily capture neutrons such as boron, and those materials can be used as a shielding component.

²Most common moderator is heavy water (D_2O) at the room temperature for thermal neutrons, and liquid helium at 20 K is used for cold neutrons.

spectrometer for neutron-scattering experiments. For a continuous neutron flux, a triple-axis spectrometer (TAS) is suitable to conduct scattering measurements as a function of momentum- and energy transfer, and all of the neutron-scattering data in this thesis have been collected using a spectrometer of this kind. Further details about this technique can be found in Sec. 3.2.2³. Most frequently used research reactors for the work in the thesis are FRM-II (Garching, Germany), ILL (Grenoble, France), and LLB (Saclay, France). The other way of producing neutrons is using a proton-accelerator source, where a target material (e.g. lead or tungsten) is bombarded with highly accelerated protons. In this case, neutrons are produced in a form of a pulse, and usually the total neutron flux is much lower than the continuous neutron flux at research reactors. The big advantage of using a spallation source is that the radiation hazard is easier to handle than the nuclear chain-reaction process. A spallation event is caused by the external injection of high-energy protons, while the nuclear fission reaction is internally induced within the fuel. Thus, there is no danger to close control over the nuclear reaction at a spallation source. For neutron-scattering measurements with spallation source, a pulsed flux of neutron is used in a time-resolved technique, such as time-of-flight (TOF) neutron spectroscopy. Instead of using a monochromator to select a specific energy of incident neutrons at TAS, the TOF spectrometer uses a high-frequency chopper to modify the incident neutron energy. Then, neutrons scattered from a sample will fly to a position-sensitive two-dimensional detector array, which covers a few steradian. The time of flight of the scattered neutrons from the sample to the detectors will be measured and the transferred momentum and energy of neutrons can be deduced.

Both TAS and TOF spectrometers are very useful especially for inelastic-neutron-scattering measurements and are complementary depending on a specific purpose of studies. The TAS is suitable for measuring in a narrow momentum and energy range with higher intensity per unit time; for instance, for spin-fluctuation measurements in the vicinity of an antiferromagnetic wave vector. On the other hand, TOF data show an overview of scattered neutrons in a wide range of energy and momentum transfer. However, due to much lower neutron flux at the spallation source, it requires three to four times bigger sample amounts and longer measurement time than a TAS experiment.

3.2.1 Scattering formulae

A measurable quantity in actual neutron-scattering experiments is the number of scattered neutrons from a sample that arrive at a finite size of the detector over given

³There are several books illustrating the triple-axis spectrometer and implementation of neutron-scattering experiments in great detail [253, 254, 255].

time. Using the knowledge of scattering physics, one can formulate the scattering theory. Consider an incident neutron flux on a sample per unit area and time, ϕ_{incident} , scattering off with a certain rate. Then, the total number of scattered neutrons per unit time will be

$$\text{number of scattered neutrons into all directions} = \phi_{\text{incident}} \cdot \sigma \quad (3.3)$$

where, σ is the scattering cross-section which is a material-specific and experimental-condition dependent quantity. However, since detectors have a finite spatial size, we are more interested in the rate of scattered neutrons into a given solid angle $d\Omega = \sin\theta d\theta d\phi$ covered by detectors. One can define the differential scattering cross-section as follows

$$\left(\frac{d\sigma}{d\Omega}\right) = \frac{\text{number of detected neutrons}}{d\Omega \cdot \text{unit time}}. \quad (3.4)$$

As one can see that the differential ($d\sigma/d\Omega$) and total (σ) cross-section have a dimension of area since the solid angle element ($\Delta\Omega$) is dimensionless. In the case of an inelastic-scattering process, where the energy of outgoing neutrons is different from that of incoming neutrons, the double-differential scattering cross-section $\left(\frac{d^2\sigma}{d\Omega dE_f}\right)$, where E_f denotes the final neutron energy, has to be used. In general, the differential cross-section can be divided into a coherent and an incoherent scattering parts

$$\left(\frac{d^2\sigma}{d\Omega dE_f}\right) = \left(\frac{d^2\sigma}{d\Omega dE_f}\right)_{\text{coherent}} + \left(\frac{d^2\sigma}{d\Omega dE_f}\right)_{\text{incoherent}}. \quad (3.5)$$

The coherent scattering gives information about interference effect among different atoms, such as Bragg reflection or collective excitations of lattice/spin. On the other hand, incoherent scattering provides information about the self-correlation of an atom, which is distributed randomly in the solid and thus has no momentum dependence (or angular dependence in the real space). The distinction between the two processes will be clarified below.

Since neutrons generally interact with matter very weakly, they do not perturb the inherent properties of the scattering system. Therefore, the double-differential scattering cross-section can be calculated based on the Fermi's Golden rule, which describes the transition rate (probability of transition per unit time) from one quantum state to another

$$W_{i \rightarrow f} = \frac{2\pi}{\hbar} |\langle f | V | i \rangle|^2 \rho_f \quad (3.6)$$

where V is the interaction potential operator. $|i\rangle$, $\langle f|$, and ρ_f denote the initial state, final state, and density of final states. After expanding density of final state, the differential cross-section can be written as follows:

$$\frac{d^2\sigma}{d\Omega dE_f} = \frac{k_f}{k_i} \left(\frac{m_n}{2\pi\hbar^2}\right)^2 |\langle \mathbf{k}_f, \lambda_f | V | \mathbf{k}_i, \lambda_i \rangle|^2 \delta(\hbar\omega + E_i - E_f). \quad (3.7)$$

where V , in this case, represents the interaction between a neutron and matter. m_n , \mathbf{k}_i , \mathbf{k}_f , λ_i , and λ_f denote the mass of the neutron, the initial wave vector, the final wave vector of neutrons, initial quantum state, and the final quantum state of the sample. The amount of energy transfer between scattered neutrons and matter, $\hbar\omega$, is defined by

$$\hbar\omega \equiv E_i - E_f = \frac{\hbar^2}{2m_n} (k_i^2 - k_f^2). \quad (3.8)$$

Nuclear scattering

As mentioned above, neutrons are a weakly-interacting probe, therefore, incoming and outgoing neutron states can be expressed as plane waves. In this stage, the first-order Born approximation is adequate for evaluating the matrix element with the neutron scattering potential operator:

$$|\langle \mathbf{k}_f, \lambda_f | V | \mathbf{k}_i, \lambda_i \rangle| = V(\mathbf{Q}) |\langle \lambda_f | \sum_l e^{i\mathbf{Q}\cdot\mathbf{r}} | \lambda_i \rangle|, \quad (3.9)$$

where

$$V(\mathbf{Q}) \equiv \int d\mathbf{r} e^{i\mathbf{Q}\cdot\mathbf{r}} V(\mathbf{r}), \quad (3.10)$$

which is simply a Fourier transform of the scattering potential. Here, $\mathbf{Q} = \mathbf{k}_i - \mathbf{k}_f$ is the momentum transfer during the scattering process as shown in Fig. 3.8 (a). Let's consider that scattering events occur from a single nucleus. The interaction between a neutron and a nucleus is short-range strong force, so one can assume a point-like interaction potential. That is,

$$V(\mathbf{r}) = \frac{2\pi\hbar^2}{m_n} b \delta(\mathbf{r} - \mathbf{R}) \quad (3.11)$$

where \mathbf{R} is the fixed position of a nucleus, and b is the nuclear scattering length. b varies dramatically among different elements and isotopes. This is because a typical de Broglie wavelength of a nucleus is much smaller than usual neutron wave-length, hence the outgoing wave of neutrons only has the lowest-order spherical symmetry, known as s -wave ($l = 0$) scattering. The nuclear scattering length is extremely small, about $\sim 10^{-13}$ m = 1 fm. If you consider the elastic scattering process only, i.e., $E_i = E_f$, then the differential cross section for a single nucleus would be

$$\frac{d\sigma}{d\Omega} = |b|^2. \quad (3.12)$$

Then, the integrated total elastic cross-section over all directions is

$$\sigma_{\text{coherent}} = \int \frac{d\sigma}{d\Omega} d\Omega = 4\pi|b|^2. \quad (3.13)$$

Now, the general expression for the interaction potential in the solid would be

$$V(\mathbf{r}) = \frac{2\pi\hbar^2}{m_n} \sum_{\mathbf{R}} b_{\mathbf{R}} \delta(\mathbf{r} - \mathbf{R}). \quad (3.14)$$

Finally, rewrite Eq. 3.7 for the elastic scattering from a sample containing N unit cells

$$\frac{d\sigma}{d\Omega_{\text{elastic}}} = N \frac{(2\pi)^3}{v_0} \sum_{\mathbf{G}} \delta(\mathbf{Q} - \mathbf{G}) |F_{\mathbf{N}}(\mathbf{G})|^2 \quad (3.15)$$

where v_0 is the unit cell volume and vector \mathbf{G} is a reciprocal-lattice vector. The nuclear structure factor $F_{\mathbf{N}}(\mathbf{G})$, is defined as

$$F_{\mathbf{N}}(\mathbf{G}) = \sum_{\mathbf{d}} e^{i\mathbf{G}\cdot\mathbf{d}} b_{\mathbf{d}}, \quad (3.16)$$

where \mathbf{d} is the basis vector for a unit cell with several atoms. The δ -function in Eq. 3.15 indicates that nuclear scattering will be allowed only if $\mathbf{Q} = \mathbf{G}$, which is also known to be the Bragg's condition. The relationship between the scattering angle θ (a half of the angle between the incident and the scattered neutron) and the reciprocal lattice vector is found to be

$$\sin \theta = \frac{Q}{2k} = \frac{1}{2} \frac{2\pi n}{d} \frac{\lambda}{2\pi} 2d \sin \theta = n\lambda \quad (3.17)$$

where n and d represent an integer number and a lattice constant. Thus, the lattice structure of samples can be determined by measuring the nuclear Bragg reflections via the elastic neutron-scattering process. So far, the calculation for differential cross-section was based on the case of an identical isotope with zero nuclear spin, $I = 0$. However, as discussed above, most elements exist as a random mixture of different isotopes, and those have different scattering lengths. Moreover, b also varies depending on where the spin states of a nucleus and a neutron are parallel or antiparallel, that is either $I + \frac{1}{2}$ or $I - \frac{1}{2}$. Therefore, for a given element, one should use averaged scattering length over different isotope and spin states. Then, the average elastic nuclear scattering cross-section would be

$$\sigma_{\text{coherent}} = 4\pi (\bar{b})^2. \quad (3.18)$$

This means that any deviation of the scattering length from the average among different nuclei will not contribute to the collective behavior such as Bragg reflections. Thus, the incoherent cross-section will be given as

$$\sigma_{\text{incoherent}} = 4\pi \overline{(b - \bar{b})^2}. \quad (3.19)$$

Most of the time during neutron scattering measurements, the incoherent scattering gives \mathbf{Q} -independent intensities, which reduce the signal-to-noise ratio. Hence, it is

always desirable to have a single isotope with zero nuclear spin materials, such as ^{58}Ni , for use as a monochromator or analyzer in neutron spectrometers to minimize the background signal due to incoherent scattering. On the other hand, a few elements which have a very large incoherent scattering length, such as vanadium, are useful for spectrometer alignment, especially for components placed after the sample stage.

To interpret neutron scattering data, especially inelastic scattering data, based on the differential scattering cross-section, it is convenient to describe the scattering formulae in terms of *correlation functions*. This is because these functions well express the scattering phenomena as a function of time and position, and, more importantly, they provide physical information about what is actually happening during the scattering process. Recalling the double-differential scattering cross-section in Eq. 3.7 and scattering potential in Eq. 3.14, one can rewrite the double-differential scattering cross-section as

$$\frac{d^2\sigma}{d\Omega dE_f} = \frac{k_f}{k_i} \sum_j b_j |\langle \lambda_f | e^{i\mathbf{Q}\cdot\mathbf{R}_j} | \lambda_i \rangle|^2 \delta(\hbar\omega + E_i - E_f). \quad (3.20)$$

Now we express the energy δ -function in terms of an integral over time, and apply the standard mathematical transformation of angle brackets to arrive at [254].

$$\frac{d^2\sigma}{d\Omega dE_f} = \frac{k_f}{k_i} \frac{1}{2\pi\hbar} |\bar{b}|^2 \int \sum_{jj'} \langle e^{-i\mathbf{Q}\cdot\mathbf{R}_{j'}(0)} e^{i\mathbf{Q}\cdot\mathbf{R}_j(t)} \rangle \times e^{-iEt} dt. \quad (3.21)$$

Then, we define the *time-dependent pair correlation function* $G(\mathbf{r}, t)$:

$$G(\mathbf{r}, t) = \frac{1}{N} \int \langle \rho(\mathbf{r}', 0) \rho(\mathbf{r}' + \mathbf{r}, t) \rangle d\mathbf{r}' \quad (3.22)$$

where N is the number of nuclei in the scattering system. The pair-correlation function, $G(\mathbf{r}, t)$, represents the spontaneous excitations of the density of particles in the scattering system. The density operator ρ is defined as

$$\rho(\mathbf{r}, t) = \sum_j \delta\{\mathbf{r} - \mathbf{R}_j(t)\} \quad (3.23)$$

where $\{\mathbf{r} - \mathbf{R}_j(t)\}$ is the time-dependent position of nuclei as a function of time. The Fourier transformation of Eq. 3.22 is known to be the *intermediate function*:

$$I(\mathbf{Q}, t) = \int e^{i\mathbf{Q}\cdot\mathbf{r}} G(\mathbf{r}, t) d\mathbf{r} = \frac{1}{N} \sum_{jj'} \langle e^{-i\mathbf{Q}\cdot\mathbf{R}_{j'}(0)} e^{i\mathbf{Q}\cdot\mathbf{R}_j(t)} \rangle. \quad (3.24)$$

By Fourier transforming the pair-correlation function $G(\mathbf{r}, t)$, an exponential term $\exp\{-2W(\mathbf{Q})\}$ would be obtained, which is known to be the Debye-Waller factor. The Debye-Waller factor is defined as

$$e^{-2W(\mathbf{Q})} = e^{-\langle (\mathbf{Q}\cdot\mathbf{u})^2 \rangle} \quad (3.25)$$

where \mathbf{u} is the displacement of a nuclei, and $\langle \dots \rangle$ denotes thermal averaging. $W(\mathbf{Q})$ tends to increase as the absolute values of \mathbf{Q} increase. Thus, this factor acts as a form factor for nuclear elastic and inelastic scattering along $|\mathbf{Q}|$ and temperature, suppressing the scattering cross-section when the displacement of nuclei becomes large. Within our experimental uncertainty, the Debye-Waller factor is negligible.

Finally, here we define the *scattering function* (or *response function*) $S(\mathbf{Q}, \omega)$, which is the time Fourier transformation of the intermediate function:

$$S(\mathbf{Q}, \omega) = \frac{1}{2\pi\hbar} \int e^{-i\omega t} I(\mathbf{Q}, \omega) dt = \frac{1}{2\pi\hbar} \int e^{i(\mathbf{Q}\cdot\mathbf{r}-\omega t)} d\mathbf{r} dt. \quad (3.26)$$

That is,

$$S(\mathbf{Q}, \omega) = \frac{1}{2\pi\hbar N} \int e^{-i\omega t} dt \int e^{i\mathbf{Q}\cdot\mathbf{r}} \int \langle \rho(\mathbf{r}', 0) \rho(\mathbf{r}' + \mathbf{r}, t) \rangle d\mathbf{r}' \quad (3.27)$$

which is, after all, the space-time Fourier transform of the density-density correlation function in the scattering system. Using these correlation functions, the partial differential cross-section can be rewritten as

$$\frac{d^2\sigma}{d\Omega dE_f} = N \frac{k_f}{k_i} |\bar{b}|^2 S(\mathbf{Q}, \omega). \quad (3.28)$$

From here, one can see that the partial differential cross-section is basically the product of the scattering length b , which is mainly related to specific material properties, and the scattering function $S(\mathbf{Q}, \omega)$ (or the dynamical structure factor), which describes the dynamical properties of a sample. Therefore, for the elastic neutron scattering, where the position of nuclei is the central information, the first term in the cross-section, $N \frac{k_f}{k_i} |\bar{b}|^2$ should be dominant during the scattering process. On the other hand, for inelastic neutron scattering events, $S(\mathbf{Q}, \omega)$ should give a physical insight into the elementary collective excitations such as phonons.

According to the scattering function, incident neutrons in principle can either lose (creation of excitations) or gain (annihilation of excitations) energy during the scattering events. The ratio between energy loss and gain shows obvious temperature dependence through the so called *principle of detailed balance*.

$$S(-\mathbf{Q}, -\omega) = e^{-\hbar\omega/k_B T} S(+\mathbf{Q}, +\omega). \quad (3.29)$$

This formula implies that at low temperatures there is a higher population-probability that neutrons will lose energy when colliding with slowly moving nuclei. On the other hand, at high temperatures nuclei already move very fast, thus there is a higher probability that neutrons will gain energy in a collision. As a result, there would be no neutrons which gain energy from nuclei during the scattering event at the $T = 0$. Therefore, it makes sense to measure neutron energy-loss spectrum at low temperatures. Most of measurements in this thesis have been carried out in this regime.

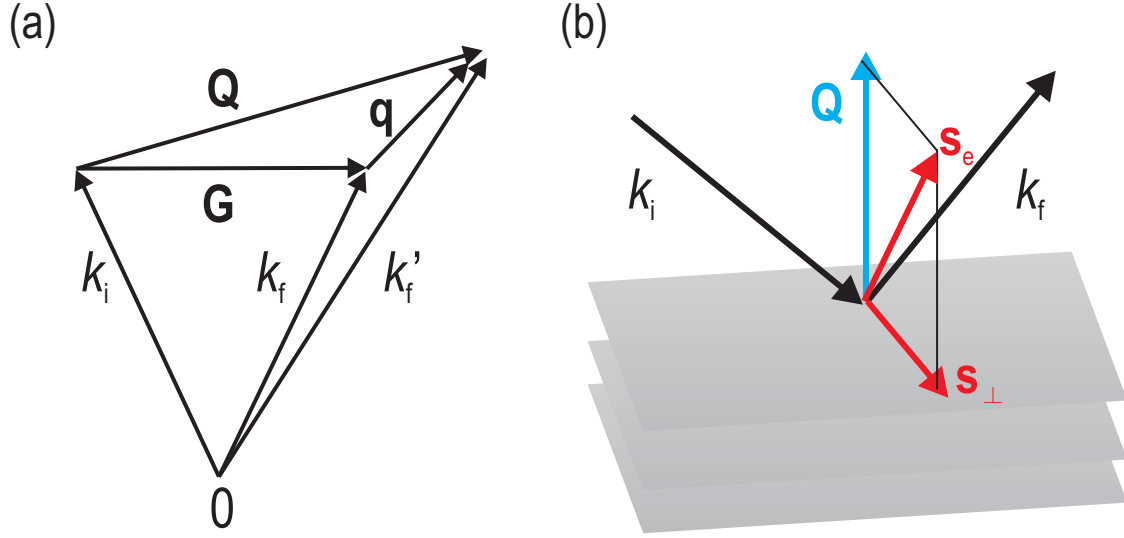


Figure 3.8: (a) The reciprocal-space vectors for elastic ($|k_i| = |k_f|$) and inelastic ($|k_i| \neq |k_f|$) scattering events. \mathbf{G} denotes the reciprocal-lattice vectors, and $\mathbf{q} = \mathbf{Q} - \mathbf{G}$ is the neutron-momentum transfer. (b) Schematic scattering geometry representation in case for the magnetic neutron scattering. Only the magnetic moment component which is perpendicular to the momentum transfer will contribute to the scattering intensity due to the relation between \mathbf{Q} , \mathbf{s}_e , \mathbf{s}_\perp given as Eq. 3.35.

There is another quite important characteristic related to $S(\mathbf{Q}, \omega)$. The scattering function is closely connected to the imaginary, i.e. dissipative part of the dynamic susceptibility, $\chi''(\mathbf{Q}, \omega)$, of a scattering system through the fluctuation-dissipation theorem

$$S(\mathbf{Q}, \omega) = \frac{\chi''(\mathbf{Q}, \omega)}{1 - e^{-\hbar\omega/k_B T}} \quad (3.30)$$

where $1/(1 - e^{-\hbar\omega/k_B T})$ is the thermal-population factor for neutron energy-loss (also called the Bose factor) which is applied only for bosonic excitations. $\chi''(\mathbf{Q}, \omega)$ also represents the spectrum of fluctuations in the scattering system, and this physical quantity is most commonly used in the theoretical calculations for the spectral function of the system. This makes neutron scattering one of the most powerful experimental techniques since the neutron-scattering intensity can be directly compared with theoretical calculations without any complicated model-based data analysis.

Magnetic scattering

Magnetic neutron scattering originates from the interaction between the magnetic dipole moment of neutrons and the magnetic field generated by spin and orbital moments of electrons in the scattering system. Although the magnetic scattering cross-sections share some of similarities with nuclear scattering cross-section, the magnetic scattering event requires more complex approximation due to a vector tensor

of magnetic field potential and spin operators. We can start from the double-differential cross-section in Eq. 3.7:

$$\frac{d^2\sigma}{d\Omega dE_f} = \frac{k_f}{k_i} \left(\frac{m_n}{2\pi\hbar^2} \right)^2 |\langle \mathbf{k}_f, \lambda_f, m_f | H | \mathbf{k}_i, \lambda_i, m_i \rangle|^2 \delta(\hbar\omega + E_i - E_f). \quad (3.31)$$

where H is the scattering potential between neutrons and electrons, and m stands for the neutron spin state whose eigenstates are either +1 or -1. The scattering potential can be defined as product of the neutron magnetic moment and magnetic field generated by the motion of electrons:

$$H = -\boldsymbol{\mu}_n \cdot \mathbf{H}_e \quad (3.32)$$

where $\boldsymbol{\mu}_n$ and \mathbf{H}_e denote the magnetic moment of a neutron and the magnetic field due to an electron spin⁴. $\boldsymbol{\mu}_n$ and H_e are given as

$$\boldsymbol{\mu}_n = -\gamma\mu_N\boldsymbol{\sigma}_n$$

and

$$\mathbf{H}_e = \frac{\mu_0}{4\pi} \nabla \times (\boldsymbol{\mu}_e \times \nabla \frac{1}{|\mathbf{r}|}),$$

where $\mu_N = \frac{e\hbar}{2m_n}$, the gyromagnetic ratio $\gamma = 1.91$, and $\boldsymbol{\mu}_e = -2\mu_B\mathbf{s}_e$ with $\mu_B = \frac{e\hbar}{2m_e}$. Inserting these terms into Eq. 3.31 leads to

$$\frac{d^2\sigma}{d\Omega dE_f} = \frac{k_f}{k_i} \left(\frac{m_n}{2\pi\hbar^2} \right)^2 (2\gamma\mu_N\mu_B)^2 \left| \left\langle \mathbf{k}_f, \lambda_f, m_f \left| \boldsymbol{\sigma}_n \cdot \nabla \times \left(\mathbf{s}_e \times \nabla \frac{1}{|\mathbf{r}|} \right) \right| \mathbf{k}_i, \lambda_i, m_i \right\rangle \right|^2 \delta(\hbar\omega + E_i - E_f). \quad (3.33)$$

Using the well-known identity

$$\frac{1}{|\mathbf{r}|} = \frac{1}{2\pi^2} \int d\mathbf{u} \frac{1}{u^2} \exp(i\mathbf{u} \cdot \mathbf{r})$$

where u is a dummy variable. Then,

$$\nabla \times \left(\mathbf{s}_e \times \nabla \frac{1}{|\mathbf{r}|} \right) = \frac{1}{2\pi^2} \int d\mathbf{u} \{ \hat{\mathbf{u}} \times (\mathbf{s}_e \times \hat{\mathbf{u}}) \} \exp(i\mathbf{u} \cdot \mathbf{r})$$

Using the \mathbf{r} -integrated relation below

$$\int d\mathbf{r} \exp\{i(\mathbf{u} - \mathbf{Q}) \cdot \mathbf{r}\} = (2\pi)^3 \delta(\mathbf{u} - \mathbf{Q})$$

we find,

$$\left| \left\langle \mathbf{k}_f \left| \nabla \times \left(\mathbf{s}_e \times \nabla \frac{1}{|\mathbf{r}|} \right) \right| \mathbf{k}_i \right\rangle \right| = 4\pi \{ \hat{\mathbf{Q}} \times (\mathbf{s}_e \times \hat{\mathbf{Q}}) \}. \quad (3.34)$$

⁴For simplicity, from here we consider the spin component for electron magnetic field. In general, the orbital contribution also plays a role for the magnetic neutron scattering, and detail description can be found in Ref. [253, 254, 255]

Here, we can define the so-called magnetic interaction vector

$$\mathbf{s}_\perp = \hat{\mathbf{Q}} \times (\mathbf{s}_e \times \hat{\mathbf{Q}}), \quad (3.35)$$

where $\hat{\mathbf{Q}}$ is the unit vector of \mathbf{Q} . This equation implies that only the magnetic moment of the scattering system which is perpendicular to the momentum transfer will contribute to the scattering intensity. Then the differential cross-section can be written as,

$$\frac{d^2\sigma}{d\Omega dE_f} = \frac{k_f}{k_i} (\gamma r_0)^2 \left| \langle \mathbf{k}_f, m_f | \sigma_n \cdot \mathbf{s}_\perp | \mathbf{k}_i, m_i \rangle \right|^2 \delta(\hbar\omega + E_i - E_f). \quad (3.36)$$

Here, all pre-factors are collected into

$$r_0^2 = \left(\frac{m_n}{2\pi\hbar^2} 2\mu_N\mu_B \right)^2 (4\pi)^2 = 5.4 \times 10^{-15} m,$$

which is known as the classical electron radius. For unpolarized neutron scattering, one has to average over the random neutron spin states, and

$$\langle m_f | \sigma_\alpha \sigma_\beta | m_i \rangle = \delta_{\alpha,\beta}.$$

In the meantime, Eq. 3.35 can be rewritten as [253, 254, 255]

$$\mathbf{s}_\perp^* \cdot \mathbf{s}_\perp = \sum_{\alpha\beta} (\delta_{\alpha\beta} - \hat{Q}_\alpha \hat{Q}_\beta) s_\alpha^* \cdot s_\beta. \quad (3.37)$$

Finally, the generalized partial-differential magnetic scattering cross-section becomes

$$\frac{d^2\sigma}{d\Omega dE_f} = N \frac{k_f}{k_i} (\gamma r_0)^2 |F_M(\mathbf{Q})|^2 \sum_{\alpha,\beta} (\delta_{\alpha\beta} - \hat{Q}_\alpha \hat{Q}_\beta) \mathbf{s}^{\alpha\beta}(\mathbf{Q}, \omega) \quad (3.38)$$

where $F_M(\mathbf{Q})$ is the magnetic form factor defined as the Fourier transformation of the normalized spin density on the magnetic ion.

From Eq. 3.31, one can see that there are three components that contribute to the magnetic neutron scattering. First of all, the product of the pre-factor and the magnetic form factor, $(\gamma r_0)^2 |F_M(\mathbf{Q})|^2$, gives the scattering intensity due to the interaction between neutrons and magnetic ions. Unlike the $|\mathbf{Q}|$ -independent scattering length in the nuclear scattering, the magnetic form factor tends to decrease quite rapidly as $|\mathbf{Q}|$ increases. This is because in the case of the nuclear scattering, the density of nuclei is quite sharp so that neutrons scatter off nuclei as from point-like particles, whereas the density of electrons is distributed over regimes comparable to the flying incident neutrons. Such differences can be seen in neutron diffraction data. Figure 3.9 is a sketch of scattered-neutron intensity as a function of the scattering angle, θ , below and above the magnetic transition temperature in a simple cubic lattice where each atom orders antiferromagnetically. Nuclear Bragg reflections are separated depending on the distances between inter-scattering-layers, whereas magnetic Bragg peaks are placed at

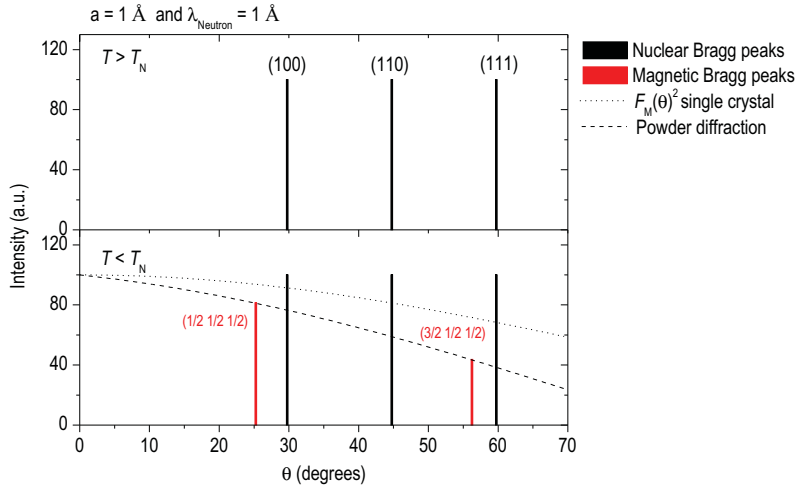


Figure 3.9: A sketch of diffraction patterns in the simple cubic lattice with AFM order below and above the magnetic transition temperature.

different scattering angles from nuclear Bragg peaks since the AFM unit cell is twice larger than the nuclear unit cell. Moreover, the scattering amplitude of the nuclear Bragg peaks does not change with \mathbf{Q} , whereas the magnetic Bragg peak intensity falls off quickly with \mathbf{Q} . After all, the magnetic form factor limits the experimental range by accessible momentum space to low Brillouin zones (BZ) for magnetic excitations. During an actual measurement it is quite useful to confirm the magnetic origin of observed signal by checking whether the scattering intensity follows the magnetic form factor or not.

Secondly, there is a contribution from the so-called *orientation factor* given as $(\delta_{\alpha\beta} - \hat{Q}_\alpha \hat{Q}_\beta)$. This term indicates that the magnetic scattering intensity depends on the relative orientation between the scattering vector [\mathbf{Q} in Fig. 3.8 (b)] and the magnetic moment of electrons in the scattering system [\mathbf{s}_e in Fig. 3.8 (b)]. This factor enables the magnetic neutron scattering to determine the structure of a static magnetic order or the direction of a fluctuating moment⁵.

Finally and most importantly, the term $\mathbf{S}^{\alpha\beta}(\mathbf{Q}, \omega)$, the so-called the magnetic response function, provides physical insight into magnetic dynamics in the scattering system. The magnetic response function can be described by the space and time Fourier transform of the spin-spin density correlation function. For a localized spin system,

$$\mathbf{S}^{\alpha\beta}(\mathbf{Q}, \omega) = \frac{1}{2\pi\hbar} \int \sum_l e^{i\mathbf{Q}\cdot\mathbf{r}_l} \langle \mathbf{s}_0^\alpha(0) \mathbf{s}_l^\beta(t) \rangle dt e^{-i\omega t} \quad (3.39)$$

where $\mathbf{s}_l^\beta(t)$ represents the β spin operator placed at l at a given time t . Analogous to the dynamical structure factor in the nuclear scattering, the magnetic response function is the physical quantity which can be measured directly. So far, the calculation for magnetic scattering is only concerned about localized spin systems, but the magnetic

⁵For unpolarized neutron scattering measurements, one needs to measure multiple \mathbf{Q} -positions, or polarized neutrons are needed to determine the complete spin correlations in the system.

response function can be generalized to the case of an itinerant system or magneto-vibrational scattering. A detailed description of those can be found in Ref. [253].

Since our study in this thesis is mainly about the magnetic dynamics in superconductors, it is worthwhile to mention some characteristics of the magnetic response function. First, upon integrating $\mathbf{S}^{\alpha\beta}(\mathbf{Q}, \omega)$ over all frequencies and momenta in the BZ of the reciprocal space, one obtains the following relation:

$$\int_{-\infty}^{\infty} d\omega \int_{BZ} d\mathbf{Q} \mathbf{S}^{\alpha\beta}(\mathbf{Q}, \omega) = \frac{(2\pi)^3}{3v_0} S(S+1) \delta_{\alpha,\beta}, \quad (3.40)$$

where S represents the total spin. This simple sum rule is completely independent of external parameters, such as temperature. It is, therefore, useful to study a possible spectral-weight transfer in a spin-dynamics spectrum below and above a phase transition temperature.

Second, the fluctuation-dissipation theorem can be applied similarly to the nuclear scattering to convert the magnetic response function to the imaginary part of spin susceptibility:

$$\mathbf{S}^{\alpha\beta}(\mathbf{Q}, \omega) = \frac{\chi''_{\alpha\beta}(\mathbf{Q}, \omega)}{1 - e^{-\hbar\omega/k_B T}}. \quad (3.41)$$

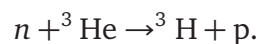
Again, the imaginary part of susceptibility shows how the magnetic energy dissipates during the scattering process and reveals the energy spectrum of the magnetic dynamics.

3.2.2 Triple-axis neutron spectrometer

So far, we have described the partial differential cross section for nuclear and magnetic neutron scattering in terms of structural and magnetic response functions as functions of momentum and energy transfer. In this section, we shall discuss how an actual measurement of the neutron scattering cross-section can be performed using the so-called “triple-axis spectrometer”(TAS). As the name of spectrometer already indicates, TAS consists of three main components, which are the central rotating axes of spectrometer’s movement. Three axes are *monochromator*, *analyzer*, and *sample stage*. Of course, there are still many other important instrumental components in TAS experiment. Let us first start by showing how scattered neutrons can be detected.

Detector

As mentioned at the beginning of this chapter, neutrons are charge-neutral particles, thus conventional methods of detecting are not applicable. One possible way to detect a neutron is to use a nuclear reaction to produce additional charged particles. For instance, neutrons would react with ${}^3\text{He}$,



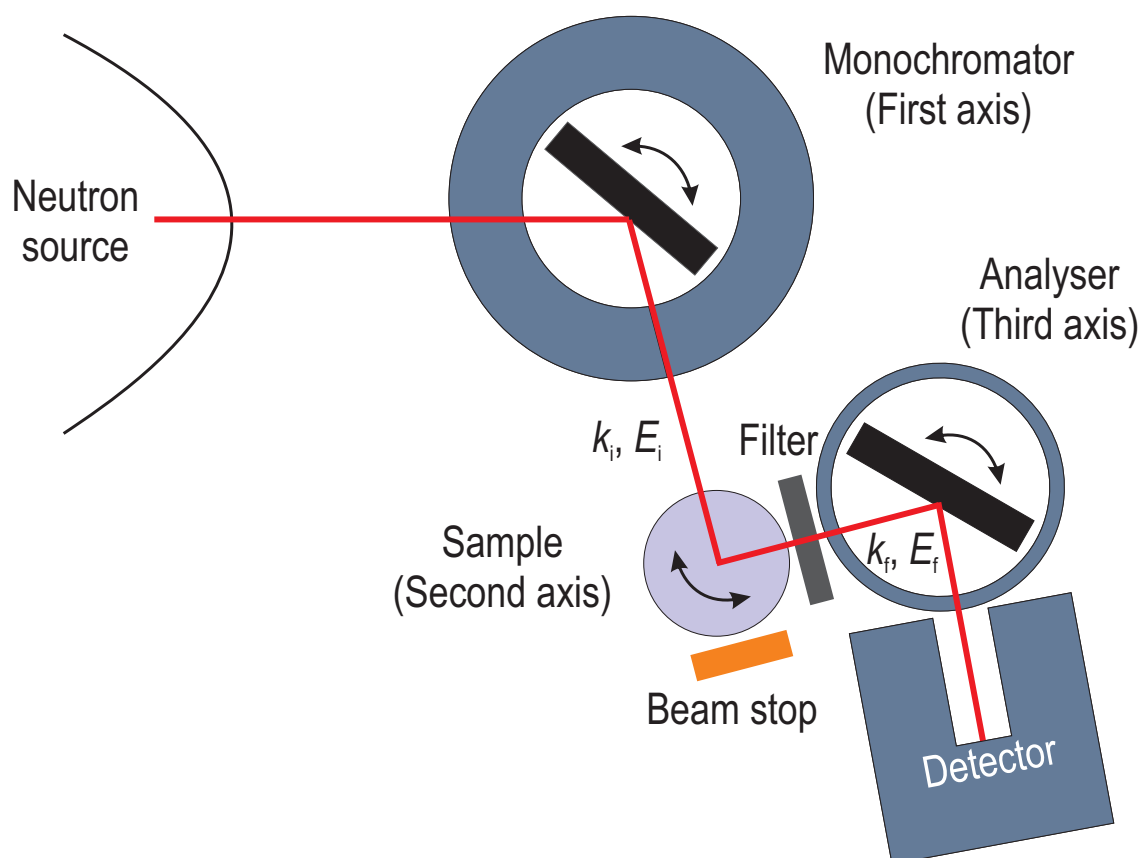


Figure 3.10: Schematic drawing of a typical TAS configuration. The neutron beam path resembles a letter “W”, hence such a setup is commonly called a “W”-configuration. There are three axes for rotating motion at the monochromator, sample, and analyser. Combining the movements of the three components properly enables one to set desirable scans as a function of Q and E .

Such converted protons will be collected under a high electric field, and the current flow can be easily detected. Some other heavy elements can also be used as a gas in the detector chamber, such as $^{10}\text{BF}_3$. In this case, ionized gas molecules will be produced after the nuclear reaction, and generate a measurable electric current. The detector is placed at the end of the spectrometer as shown in Fig. 3.10.

Monochromator

Neutrons that are produced from the reactor core have no characteristic energy distribution, but after being moderated, their energy distribution follows the Maxwellian distribution spanning the energy range from 0 to 200 meV. However, for an actual neutron scattering measurement, one needs to have a well-defined energy of neutrons to correctly measure the neutron scattering cross-section at given Q and E . Selecting particular energy of neutrons from the polychromatic neutron beam is done using a *monochromator*. In TAS, the monochromator is placed right after the neutron beam

tube connected to the reactor core (the first axis of TAS). Usually, the monochromator is made of a mosaic of small single crystals, which have proper lattice constants and small incoherent scattering cross-section. By choosing a corresponding angle between the incident and outgoing neutrons for the Bragg reflection from the material used for the monochromator, only the neutrons with a proper wavelength (λ), which satisfies the Bragg condition, are selected. This indicates that some characteristics of the monochromatized neutron beam are varied depending on the monochromator material properties, such as reflectivity, neutron absorption, Debye temperature, and incoherent cross-section. Of course, the ideal monochromator should have large reflectivity independent of the chosen neutron energy, a very low neutron-absorption rate, high Debye temperature to avoid phonon excitations from neutron collisions, and a low incoherent scattering length to minimize the background. Isotopically pure ^{58}Ni is a good candidate for the perfect monochromator since it shows large reflectivity with no incoherent scattering, but it is extremely difficult to manufacture to the realistic size. Therefore, depending on the aim of a neutron experiment, one has to correctly choose the most suitable monochromator considering between more neutron flux at the sample or better resolution. One of the most popular monochromator material is a pyrolytic-graphite (PG) which has a preferable crystallographic orientation along (00 l) directions. Since other ($hk0$) scattering planes are almost randomly oriented, most of unwanted harmonic Bragg reflections would show up as a powder pattern, which can be easily avoided during a TAS experiment. PG (002) reflection also shows relatively high reflectivity without serious fluctuations in the neutron energy ⁶[255]. In addition, owing to the medium size of the unit cell in PG, the reciprocal-lattice vectors can be tuned from small to large values which is suitable for a broad energy range in inelastic neutron measurements. In practice, a small amount of mis-alignment of monochromator crystals is adopted to gain more neutron flux by opening a broad path for incoming neutrons through the monochromator, whereas the energy resolution of the spectrometer is sacrificed by a little amount ⁷. Such a mis-alignment can be introduced either by mechanical bending of the monochromator followed by a thermal treatment or reassembling small pieces of single crystals with intended degree of mis-alignment.

⁶The reflectivity of PG (002) reflection varies between 60 – 80% versus energy of neutrons.

⁷Typical distribution of mosaic is about the order of 30'.

Sample stage

Finally, monochromatized neutrons now can be referred to as the incident neutrons with k_i and E_i for the sample. The sample stage also rotates for the measurements of scattering cross-section, and this is placed on the second axis of the spectrometer as shown in Fig. 3.10. Most of incident neutrons will pass through the sample and arrive at the so-called *beam stop* (orange color in Fig. 3.10), which is situated right after the sample stage along the same direction as the incident neutron beam to prevent transmitted neutrons from reaching the detector. Some of incident neutrons will elastically scatter as Bragg reflections into various directions, carrying nuclear and magnetic structural information about the sample. Inelastically-scattered neutrons also fly into all directions, carrying physical information about the dynamic properties of the scattering system, which can be interpreted through the correlation function as described in Sec. 3.2.1. In practice, incoherently scattered neutrons from the sample will also go into various directions which can be detected.

Analyzer

After interacting with the sample, scattered neutrons are heading in all directions, with either the same or different energies compared to that of the incident neutrons. However, we are interested only in a neutron scattering range at a certain momentum and energy transfer, $S(\mathbf{Q}, \omega)$. In order to select only desirable information out of all the scattered neutrons, they must be analyzed to select a well-defined momentum and energy. Such a task can be done using the nuclear Bragg reflections in single-crystalline materials, so-called *analyzers*, in a similar manner to the monochromator. The analyzer crystal is situated at the third axis of the spectrometer as displayed in Fig. 3.10. Adjusting the angle of the analyzer enables fulfilling the Bragg condition for the chosen neutron energy, then the neutron intensity can be measured by a detector which is placed at the end of spectrometer. Since the analyzer works in exactly the same way as the monochromator, analyzer materials are basically the same as those used for the monochromator⁸. It is common to use the same materials for both monochromator and analyzer (symmetric configuration), but sometimes it is useful take different compounds for the monochromator and analyzer to have a better energy resolution (asymmetric configuration).

The above mentioned three axes are very heavy due to massive shielding for radiation protection, thus one uses air pressure to lift those components, which allows them to move smoothly and continuously on the *dance floor*. Movement for each axis can be controlled by computer. For INS measurements, either incident or final neutron energy can be fixed, but fixed- k_f mode is more popular in practice.

⁸Hence, requirements for “good” analyzer are also same: A large reflectivity, a low neutron absorption rate, a high Debye temperature, and a small incoherent scattering-length.

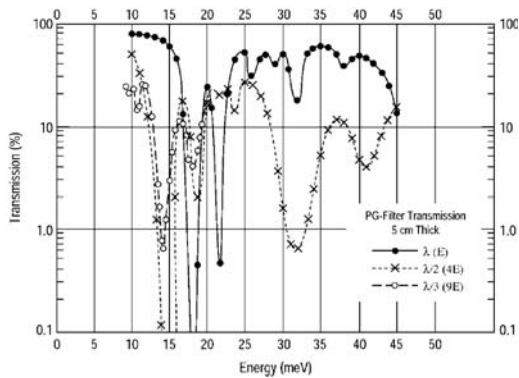


Figure 3.11: Taken from Ref. [255]. Transmission characteristics of a typical PG-filter with a thickness of 5 cm. $k_f = 2.662 \text{ \AA}^{-1}$ ($E = 14.6 \text{ meV}$) is by far the most promising value for the final-neutron wave vector.

Focusing monochromator and analyzer

To gain more neutron flux at the sample and detector, one can use a focusing monochromator and analyzer by bending an array of single crystals vertically or sometimes horizontally. It works in the same manner as a concave mirror for light. Usually, a vertical Q resolution (perpendicular to the scattering plane) is not crucial for neutron experiments, so a vertically bent monochromator and analyzer are commonly used. On the other hand, good Q resolution within the scattering plane is required, thus one needs to consider carefully the balance between more neutron flux and better momentum resolution. This trade-off can be understood as follows: the momentum resolution is decided in the spread of magnitude and direction of the incident- and final-neutron wave vectors, whereas the energy resolution originates solely from the spread in the magnitude of k_i and k_f . The variation in the magnitude of k is caused by a divergence of the beam that is reflected from the monochromator and sample since those distributed neutrons also have a corresponding k for the Bragg reflections. Ultimately, more scattered neutrons will be counted at the detector, but the momentum distribution would be quite broad. For a flat monochromator and analyzer, the momentum resolution is better, but neutron intensity drops significantly. Moreover, the typical sample size for a neutron experiment is not as large as the monochromator plate, so most of the neutrons scattered from the monochromator would not hit the sample.

Filter

As you can see, the monochromator and analyzer are the most important components for TAS. However, utilizing Bragg reflections as a source of monochromatization and analysis also causes some unwanted neutrons in the scattering path. According to Bragg's law, at a given angle, not only the desired neutron wave length λ , but also higher order Bragg reflections ($\lambda/2$, $\lambda/3$, $\lambda/4$, ...) are allowed. Of course, such higher-harmonic neutrons will pass the analyzer through other Bragg reflections before finally ending up at the detector. To prevent higher-order neutrons from being counted,

a filter can be installed right after the sample (especially useful for the k_f -fixed mode). The most commonly-used filter for thermal neutron measurements is a PG-filter. If the c -axis of the PG-filter lies along the neutron path, the filter will scatter off neutrons at certain Bragg conditions. Hence, as long as the PG-filter has an order of 1° mosaicity and enough thickness, the first of the Bragg reflections will pass the filter whereas second (or higher) order Bragg reflected neutron-intensity would be suppressed by the filter. Fig. 3.11 displays the transmission of a 5-cm-thick PG filter as a function of the first three neutron harmonics [255]. For instance, at $k_f = 2.662 \text{ \AA}^{-1}$ ($E = 14.6 \text{ meV}$), the first order neutron λ shows a transmission rate around 100% whereas second and third ($\lambda/2$ and $\lambda/3$ respectively) neutrons hardly pass the PG-filter. Therefore, $k_f = 2.662 \text{ \AA}^{-1}$ ($E = 14.6 \text{ meV}$) is by far the most frequently used wave number for thermal-neutron scattering experiments. Alternatively, $k_f = 3.84 \text{ \AA}^{-1}$ ($E = 30.4 \text{ meV}$) or $k_f = 4.1 \text{ \AA}^{-1}$ ($E = 34.6 \text{ meV}$) can be chosen depending on the experimental condition. For a cold-neutron source, polycrystalline Be-filters are commonly used. Be possesses a minimal cut-off wave length for Bragg reflection, about $4 - 8 \text{ \AA}$. Hence, if one uses lower k_f for the measurement, scattered neutrons with higher k_f would be suppressed effectively. The best choice of k_f for Be-filter is about 1.58 \AA^{-1} .

Monitor counts

The TAS measures the neutron-scattering rate at a given \mathbf{Q} -, E -position, and time. To combine a set of different \mathbf{Q} - and E -positioned data points, either the number of incident neutrons or the counting time has to be monitored. To do this, a counter with low efficiency is placed in the neutron beam path between monochromator and sample, and each data point is weighted by the number of incident neutrons. One important point is that as the energy of the incident neutron beam decreases, the monitor rate would be perturbed because a substantial number of higher-order neutrons would hit the fission monitor as well. As a consequence, the low-energy transfer scattering rate would be underestimated due to a lack of incident neutrons at the desired energy. Thus, a significant correction is required to understand the relative intensities as a function of energy transfer. Fig. 3.12 displays the monitor correction factor as a function of incident-neutron energy measured at three different thermal-neutron TAS, IN8 at ILL, and 1T and 2T at LLB. A complete characterization and correction of such contamination can be performed by dividing the measured intensities by the monitor correction factor. There is another monitor situated immediately after the analyzer, which helps to discriminate spurious signals from neutrons with undesired k_f which scattered from the analyzer.

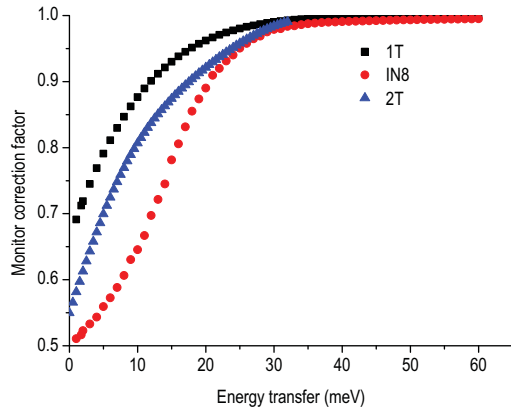


Figure 3.12: Monitor correction factor for different thermal-neutron spectrometers, IN8 at ILL, 1T and 2T at LLB, taking into account higher harmonic neutrons recorded by the monitor counter. Measured neutron intensity has to be divided by the correction factor, hence it mostly affects to the low-energy transferred neutrons.

3.2.3 Spurions

Although several protective elements against unwanted neutrons are already installed in the TAS, it is inevitable that spurious signals or called *Spurion*, will be detected. One of the main issues for the three-axis neutron experiment is thus how to discriminate true signals from spurions. There are several ways to check the origin of a signal based on the underlying physical behavior. For instance, a magnetic excitation intensity should decrease as temperature and $|\mathbf{Q}|$ increase, whereas a phonon's intensity should behave the opposite way. It is almost mandatory to check such physical behavior, if one wants to prove the origin of an observed signal. However, sometimes such a test is not sufficient to rule out any possible spurious effect, and a number of other methods (mostly related to the instrumental tricks) can be used to avoid any misleading interpretation of neutron scattering data.

1. **Incoherent scattering on the analyzer:** This causes one of the most frequently occurred spurions. Even if the scattering geometry is meant to be inelastic, some elastically scattered neutrons from the sample might arrive at the detector after incoherently scattering from the analyzer. This can happen because elastically scattered neutrons from the sample are sometimes very strong, so they can act as an incident neutron beam on the analyzer. Of course, most scattered neutrons from the sample would not reach the detector through the Bragg reflections, but still a small portion of neutrons could pass the analyzer through incoherent scattering. In this case,

$$|k_i| = |k_{f,\text{actual}}| \neq |k_f|$$

and

$$\mathbf{Q}_{\text{actual}} = k_i - k_{f,\text{actual}}.$$

Therefore, $\mathbf{Q}_{\text{actual}}$ is not the correct momentum transfer for the measurement. Possible sources of this spurious signal at $\mathbf{Q}_{\text{actual}}$ are the accidental Bragg peaks from the sample or from mis-aligned grains in the sample, or Bragg reflections

from the sample holder or plate (most commonly Al). An easy way to check for this kind of spurions is to do exactly the same scan but with “analyzer-off”. What this means is that if the spurion comes from incoherent scattering from the analyzer, then it should be present under the same scan condition with a different rotation angle for the analyzer. On the other hand, all the meaningful signals which previously satisfied the inelastic scattering condition would be completely eliminated. To eliminate or avoid such spurions due to accidental Bragg reflections, the same scan can be performed at a physically equivalent \mathbf{Q} -positions which is set to be a different scattering geometry.

2. **Incoherent scattering on the monochromator:** This is basically the same problem as for the analyzer. However, it happens with much lower probability since it needs to pass many other instrumental components. To check for this kind of spurions, one can repeat the scan with “monochromator-off”.
3. $2k_i = 3k_f$: The mechanism underlying this problem shares the same origin as the filter-related higher-harmonic neutrons. When the energy of second-order neutrons from the monochromator is nearly the same as the energy of third-order neutrons at the analyzer, second-order incident neutrons will pass through the analyzer. In such a case, all elastically scattered neutrons from the sample will scatter in the same way as inelastic scattering for the first-order neutrons. To avoid this effect, a different k_f can be used for the measurement at the desired energy.
4. $k_i = 2k_f$: A similar problems to the previous one. However, this effect is stronger than above-mentioned spurion, thus an additional PG-filter should be installed to eliminate this spurion.
5. **Bisecting the scattering angle in the high-symmetric axis of the sample:** Clearly accidental or unwanted Bragg reflections from the sample are dangerous. When the high-symmetry line of the sample is placed at the scattering angle, many Bragg conditions can be fulfilled. However, this process requires two incoherent scattering from both the monochromator and the analyzer, making it unlikely to occur. Nevertheless, when it does occur, a sizable signal can be generated.
6. **Direct beam:** When the scattering angle is quite small at small \mathbf{Q} , the monochromator arm and analyzer arm are nearly parallel. In this geometry, a huge number of neutrons which did not interact with the sample will directly hit the detector. Usually, this effect is obvious due to its significant intensity. To avoid, one should keep the scattering angle above some critical value.

7. **Epithermal neutrons:** Sometimes, very fast neutrons with energy higher than 1 eV, so-called *epithermal neutrons*, pass the monochromator drum and reach the detector directly through a path where the shielding is relatively weak. This rarely happens, but still could contribute a bumpy base line. To reduce contamination of the primary beam by epithermal neutrons, a sapphire filter can be installed right before the monochromator.

There are still many other types of spurious peaks, and an extensive discussion about spurions can be found in Ref. [255].

Chapter 4

Results and discussion

4.1 Hole-doped $\text{Ba}_{1-x}\text{K}_x\text{Fe}_2\text{As}_2$

In this section, a combined study of the hole-doped pnictide superconductor $\text{Ba}_{1-x}\text{K}_x\text{Fe}_2\text{As}_2$ ($T_c = 32$ K) is presented, using X-ray powder diffraction (XRPD), neutron scattering, muon spin rotation (μSR), and magnetic force microscopy (MFM). Commensurate static magnetic order sets in below $T_m \approx 70$ K as inferred from the emergence of the magnetic $(1\ 0\ 3)_{\text{ort}}$ reflection observed using neutron scattering and from the observation of damped oscillations in the zero-field- μSR asymmetry. The detail analysis on XRPD data reveals that below the magnetic transition temperature $T_m = 70$ K there is an additional broadening of the nuclear Bragg peaks, suggesting a weak structural phase transition. However, macroscopically the system does not break its tetragonal symmetry down to 15 K. Instead, XRPD patterns at low temperature reveal an increase of the anisotropic microstrain proportionally in all directions.

Transverse-field μSR below T_c shows a coexistence of magnetically ordered and non-magnetic states, which is also confirmed by MFM imaging analysis. Combining these experimental observations with the effect of lattice softening below the magnetic phase transition, we explain such coexistence by electronic phase separation into antiferromagnetic (AFM) and superconducting/normal state regions. Experimental evidence indicates that such phase separation can be considered as the unique property of iron-pnictide superconductors which are grown by the Sn-flux method. These results are published in Ref. [94, 129], and part of the following figures and text are reproduced from those publications.

4.1.1 Characterization of physical properties

It is noteworthy to mention that the single crystals of $\text{Ba}_{1-x}\text{K}_x\text{Fe}_2\text{As}_2$ (BKFA) subjected to the current research were grown using Sn as flux in a zirconia crucible sealed in a quartz ampoule filled with Ar. From an energy-dispersive X-ray spectroscopy (EDX)

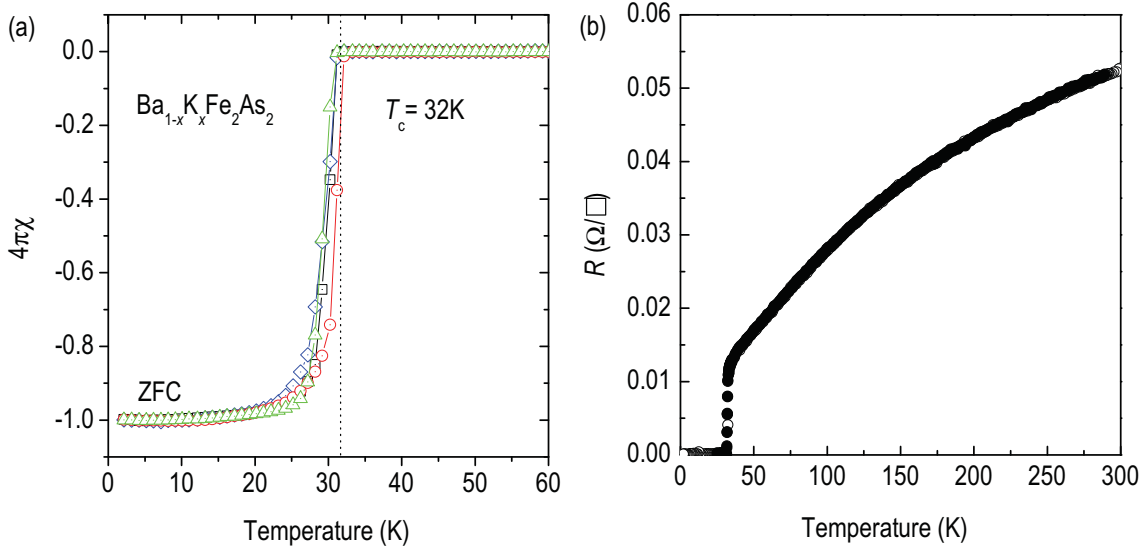


Figure 4.1: (a) The dc susceptibility data measured by PPMS on four randomly selected single-crystalline BKFA samples. The sharp and reproducible SC transition at 32 K is observed in the ZFC measurements, indicating $\sim 100\%$ Meißner fraction. (b) The dc resistance curve measurement also confirms a sharp drop of sheet resistance (assuming as two-dimensional system) at 32 K which is perfectly in-line with the magnetization measurements.

measurement, the potassium concentration was determined to be 30 % that is a slightly underdoped region. A tiny amount (less than 1%) of Sn was also detected. Sample characterization of physical properties by resistivity and dc susceptibility measurements (Fig. 4.1) revealed a sharp SC transition at $T_{c,\text{onset}} = (32 \pm 1)$ K, which was reproducible. Close to 100% external magnetic exclusion was observed in the zero-field-cooled (ZFC) magnetization measurement, clearly indicating the bulk superconductivity in this sample. To exclude a possible inhomogeneity in potassium distribution, randomly selected several pieces were examined by the magnetization measurements, and they showed sharp and reproducible SC transition at 32 K as shown in Fig. 4.1 (a). X-ray powder diffraction data confirmed that our crystals consist of a single phase fitted well by a tetragonal $I4/mmm$ space group symmetry, both at room temperature and at $T = 15\text{ K}$. On the other hand, slight broadening of the diffraction peaks by $\sim 20\%$ below T_m was realized which might indicate the tendency towards weak orthorhombicity at low temperature. The room-temperature lattice parameters of the sample, as determined from XRPD by the Rietveld refinement [256] [see Fig. 4.3 (a)], are $a = b = 3.911\text{ \AA}$ and $c = 13.339\text{ \AA}$ at room temperature, whereas the quality of the fit lets us conclude that the potassium distribution in the sample is homogeneous within a few atomic % in agreement with the results of our EDX analysis.

4.1.2 Neutron and X-ray diffraction

The neutron diffraction measurements were performed at the *Morpheus* diffractometer (two-axis diffractometer) and RITA-II spectrometer (TAS), both at the Swiss spallation source SINQ, Paul Scherrer Institut (PSI), Villigen, Switzerland. The X-ray powder diffraction measurement was performed at the X16C beamline at the National Synchrotron Light Source, Brookhaven National Laboratory, USA.

Fig. 4.2 shows neutron scattering intensity measured in the vicinity of the $(\frac{1}{2} \frac{1}{2} \bar{3})_{\text{Tet}}$ magnetic Bragg peak on a ~ 30 mg sample [see the inset in Fig. 4.2 (b)] with in-plane and out-of plane mosaicities $< 1.5^\circ$ and $< 2.5^\circ$ respectively. The final neutron wave vector was set to $k_f = 1.55 \text{ \AA}^{-1}$, and a Be-filter was used to extinguish contamination from higher-order neutrons. The sample was mounted with the tetragonal [110] and [001] crystallographic directions in the scattering plane in a 15 T cryomagnet. Panel (a) shows $(hh\bar{3})_{\text{Tet}}$ scans at three different temperatures. While within the error bar there is no intensity at 100 K, a clear magnetic peak starts to evolve at low temperatures. From the width of the magnetic Bragg peaks, the lower estimate for the correlation length of the AFM phase can be estimated: $\zeta > 100 \text{ \AA}$. This is quite larger than in $\text{YBa}_2\text{Cu}_3\text{O}_{6+y}$ compound, where the correlation length does not exceed 20 \AA [170]. Panel (b) reveals the longitudinal width of the $(110)_{\text{Tet}}$ nuclear Bragg reflection as a function of temperature, which is plotted together with the intensity of the $(\frac{1}{2} \frac{1}{2} \bar{3})_{\text{Tet}}$ magnetic Bragg peak. The temperature-dependent magnetic Bragg intensity lets us estimate the magnetic transition temperature $T_m \approx 70$ K. One can clearly see the broadening of the nuclear Bragg peak at low temperatures, with an onset at T_m , which perfectly follows the magnetic intensity, and amounts to $\sim 20\%$ as $T \rightarrow 0$. The most straightforward explanation for such broadening would be a weak orthorhombic distortion that leads to a splitting of the peak that is masked by the experimental resolution, as was also previously observed whenever the AFM order was suppressed either by doping, as in $\text{CeFeAsO}_{0.94}\text{F}_{0.06}$ at low temperature [257], or by temperature, as in the parent compound LaFeAsO at $T = 138$ K [57].

To check this interpretation, we have performed XRPD measurements of the same samples, with subsequent analysis of the microstrain anisotropy, which is known to be helpful in detecting minute structural distortions related to possible phase transitions.

The XRPD data for the structure refinement were collected at room temperature and at 15 K, as shown in Fig. 4.3 (a) and (b). X-rays of 0.7 \AA wavelength were selected by a double Si(111) monochromator. The wavelength and zero-point error were calibrated using eight precisely measured peaks of the NBS1976 flat plate alumina standard. The diffracted beam was analyzed by reflection from a Ge(111) crystal before a NaI scintillation detector. Data were taken at each 2Θ step of 0.005° from 3° to 38.6° at room temperature and 2° to 52° at 15 K. XRPD data were analyzed

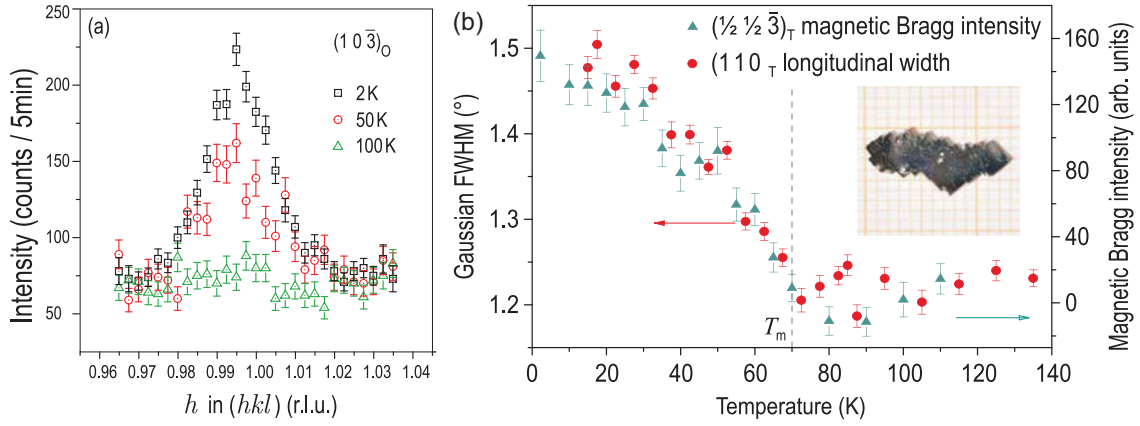


Figure 4.2: (a) Elastic neutron scattering data measured in the vicinity of the $(\frac{1}{2} \frac{1}{2} \bar{3})_{\text{Tet}}$, where T represents the tetragonal notation, magnetic Bragg peak. Scans along $(hh\bar{3})_{\text{Tet}}$ at three different temperatures. (b) The temperature dependent longitudinal broadening of the $(110)_{\text{Tet}}$ nuclear Bragg reflection (circles) overlaid with the intensity of the $(\frac{1}{2} \frac{1}{2} \bar{3})_{\text{Tet}}$ magnetic Bragg peak. Both effect sets in around 70 K which is attributed to the magnetic transition temperature. The inset in panel (b) is a photo of the sample which was used for the neutron diffraction measurements.

using the program TOPAS (*Bruker-AXS*). Again, both high- and low-temperature data could be interpreted in terms of a tetragonal $I4/mmm$ space group symmetry both at room temperature and at $T = 15$ K (see Fig. 4.3). As impurity phases, a few wt. % of tetragonal β -tin from the flux and some reflections of the brass sample holder were included in the refinement. The analysis of the anisotropic peak broadening in the powder pattern due to a microstrain distribution was performed using the Cartesian parametrization by Dr. A. Leineweber at MPI-IS [258, 259].

The lattice parameters of the sample, as determined from XRPD are $a = b = 3.9111(1)$ Å and $c = 13.3392(6)$ Å at room temperature and $a = b = 3.90075(7)$ Å and $c = 13.2476(3)$ Å at 15 K, which corresponds to a 1.2 % decrease in the unit cell volume at low temperature. From the dependence of the lattice parameters on doping [37], the average potassium content of $x = 0.3$ could be determined which is inline with our EDX result. No clear evidence was found for an orthorhombic distortion of the tetragonal lattice at low temperature. This conclusion is based on the absence of any orthorhombic splitting of the Bragg reflections and the refinement of the lattice parameters. The isotropic microstrain distribution in the ab -plane also does not hint at an orthorhombic distortion.

The microstrain distribution represents the statistics of the deviations Δd of the interplanar spacings from their average values, normalized by the average spacings d , i.e. of the strain $\varepsilon = \Delta d/d$, over the investigated specimen as a function of the crystallographic direction. Tensor surfaces representing the squared FWHM of the anisotropic microstrain distribution B_ε^2 along different crystallographic directions are

shown as insets in Fig. 4.3 (a) and (b), whereas panel (c) shows the x - z [tetragonal (ac) plane] and x - y [tetragonal (ab) plane] cross-sections of both surfaces. The largest microstrains of the crystalline lattice both at 300 K and at 15 K are found in the c -direction ($|B_\varepsilon|_\perp = 0.9\%$ and 1.1% , respectively) as compared to the average in-plane values of $|B_\varepsilon|_\parallel = 0.65\%$ and 0.82% . The flowerlike shape of the x - z cross-section indicates a negative correlation between the in-plane ($hk0$) and the out-of-plane ($00l$) directions, which agrees with the opposite changes of the a and c lattice constants upon the variation of doping [37]. The low-temperature increase of the microstrain amounts to $\sim 20\%$ relative to the corresponding values at room temperature both in the c -direction and in-plane. In other words, to a good approximation the two tensor surfaces are geometrically similar to each other, which would not be expected in the case of a weak orthorhombic distortion, as it should instead broaden only the in-plane peaks. Moreover, at both temperatures no considerable in-plane anisotropy is observed [i.e. anisotropy in the x - y plane, see Fig. 2(c)], which would be a sign for the onset of an orthorhombic phase transition, e.g. for an incomplete orthorhombic reflection splitting.

This lets us conclude that the origin of the microstrain at both temperatures is not related to a macroscopic structural transition to orthorhombic symmetry, but rather should be attributed to an increase of the microscopic distortions of the lattice. The microstrain distribution quantitatively represents the response of the lattice to structural defects, such as chemical inhomogeneities or dislocations, which are unavoidable in any real material. Therefore an increase of the microstrain below the magnetic transition can either indicate that the lattice becomes softer, i.e. increases its response to the local stresses upon entering the AFM state, or that the local stresses themselves increase, causing a proportional increase of the microstrain. In the studied compound, both mechanisms could be important. On the one hand, in the case of lattice softening, one would expect its direct influence on the phonon mode frequencies. Indeed, such an effect has been reported in the phonon spectra of two similar 122-compounds: polycrystalline $\text{Sr}_{0.6}\text{K}_{0.4}\text{Fe}_2\text{As}_2$ and $\text{Ca}_{0.6}\text{Na}_{0.4}\text{Fe}_2\text{As}_2$ [260]. There, softening of phonon modes below 10 meV has been observed by inelastic neutron scattering upon cooling from 300 K to 140 K, despite the decrease of the unit cell volume at low temperature. More recently, softening and narrowing of several phonon modes below the spin density wave transition was also observed by Raman scattering in underdoped $\text{Sr}_{1-x}\text{K}_x\text{Fe}_2\text{As}_2$ and in the parent BaFe_2As_2 single crystals [261]. On the other hand, possibly phase-separated coexistence of AFM and paramagnetic phases or the presence of twin AFM domain boundaries could lead to an increase of local stresses below T_m due to the magnetic anisotropy of individual AFM domains.

In our BKFA compound, we have already shown that superconductivity and AFM order coexist at the same time, but neutron or X-ray diffraction measurement do

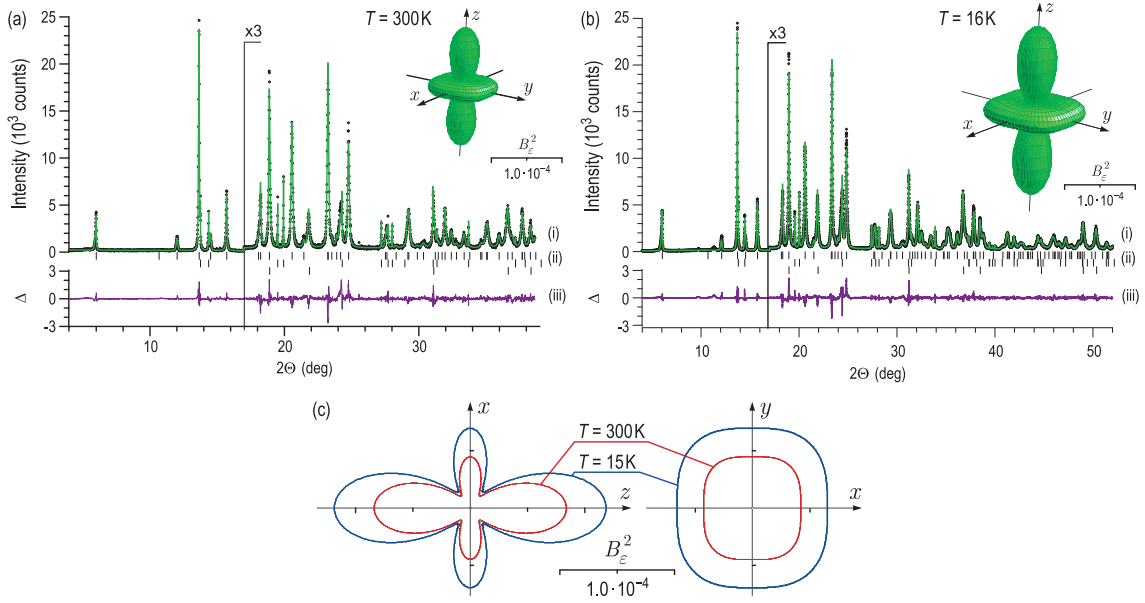


Figure 4.3: Panels (a) and (b) present XRPD data measured at 300 K and 15 K, respectively. (i) Scattered x-ray intensity as a function of the diffraction angle 2Θ ($\lambda = 0.7 \text{ \AA}$) fitted to the tetragonal $I4/mmm$ space group. For $2\Theta > 17^\circ$ the plots are enlarged by a factor of three. The fit includes a few wt. % of tetragonal β -tin from the flux as an impurity phase and some reflections of the brass sample holder as indicated by the reflection markers in (ii). (iii) The difference Δ between the experimental points and the fitting curve. The insets show tensor surfaces representing the normalized anisotropic microstrain distribution along different crystallographic directions. The distance of the surface from the origin corresponds to the squared full width at half maximum (FWHM) of the microstrain B_ϵ^2 along the corresponding directions in real space. The x - z and x - y cross-sections of both surfaces are shown in panel (c) for comparison.

not provide information about a spatial distribution of different phases in the sample. Therefore, a magnetic-volume sensitive, μ SR, and real-space resolved, MFM, spectroscopy studies were carried out.

4.1.3 μ SR and magnetic force microscopy measurements

To gain further insight into the nature of the magnetic ordering—in particular the magnitude of the ordered moment and the magnetic volume fraction—we performed zero-field (ZF) and transverse-field (TF) μ SR measurements using 100 % spin polarized muons, which corresponds to the full muon spin asymmetry of 21 % [262]. The results of our μ SR measurements are illustrated by Fig. 4.4. Panel (a) shows the time dependence of the asymmetry, which is a measure for the spin polarization of the muon ensemble. In principle, the oscillation frequency ν_{ZF} is determined by the ordered Fe moment m_{Fe} . Since the stopping position of the muon in the lattice is not known precisely, we resort to a comparison with BaFe_2As_2 , where m_{Fe} was determined

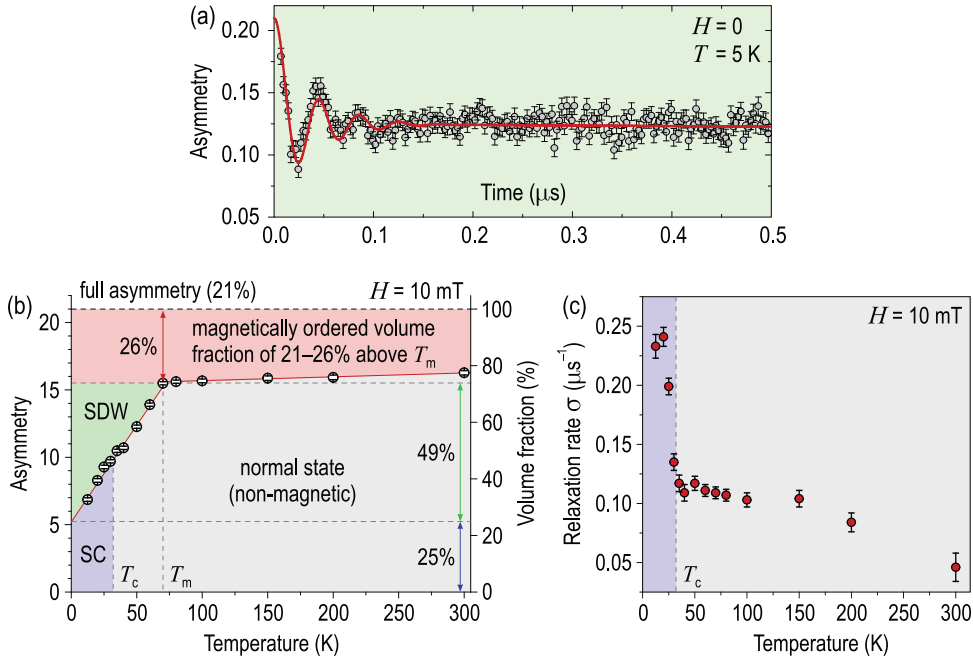


Figure 4.4: μ SR data. (a) Time dependence of the muon spin asymmetry in zero field. (b) Temperature dependence of the asymmetry in a weak transverse field, showing coexistence of magnetic and non-magnetic phases. (c) Temperature dependence of the relaxation rate in a transverse field.

to be $0.4\mu_B$ [38]. The zero-field frequency for BaFe_2As_2 has been established to be $\nu_{ZF} = 28$ MHz. In comparison, for our sample $\nu_{ZF} = 24.7(5)$ MHz, so we estimate the ordered moment to be only slightly reduced to $\sim 0.35\mu_B$. This is remarkable, since simultaneously T_m is reduced by a factor of two from 140 K to 70 K.

By applying a weak field of $H = 10$ mT transverse to the original muon spin polarization, we can determine the non-magnetic volume fraction, in which the muons precess around \mathbf{H} conserving the asymmetry, and the magnetically ordered fraction, in which a superposition of external and internal fields depolarizes the beam. Fig. 4.4 (b) shows the temperature dependence of the asymmetry in the transverse field. Surprisingly, already at 300 K we observe a $\sim 21\%$ loss of asymmetry that might be an indication of a disordered magnetic phase. A straightforward explanation for it would be the presence of a magnetic impurity phase in our sample, such as Fe_2As ($T_N = 353$ K), but such an explanation can be ruled out, since XRPD performed on several pieces of samples from the same batch, ground into powder, indicated no presence of parasitic phases, as discussed above. Additionally, angle-resolved photoemission spectroscopy (ARPES) indicates the presence of some kind of density-wave-like order above T_m in the same samples, which is weakly temperature-dependent [43]. Assuming its magnetic character, it could be speculated that such “hidden” order is possibly responsible for the high-temperature loss of asymmetry observed by μ SR, which also decreases slightly with temperature above T_m . Below ~ 70 K—the onset temperature of the magnetic

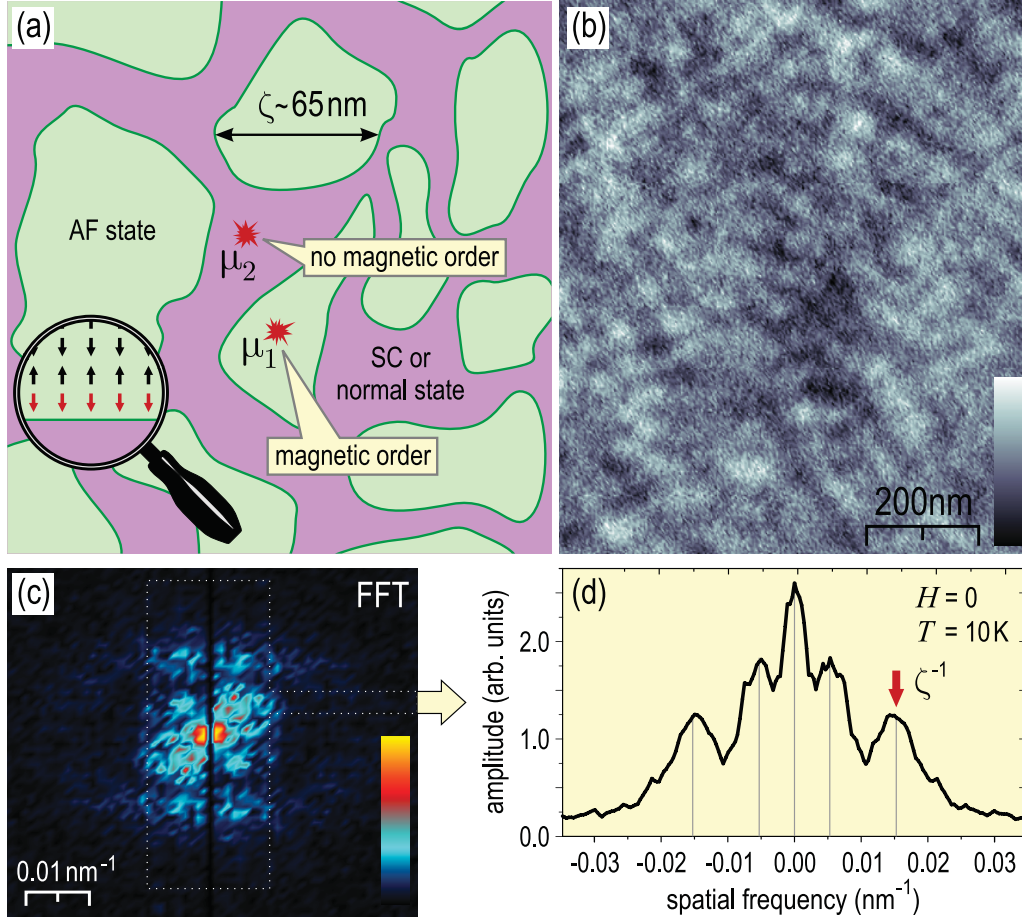


Figure 4.5: (a) Cartoonish representation of the phase-separated coexistence of AFM and SC/normal states. (b) MFM image measured at 10 K in the absence of external field reveals weak magnetic contrast on the lateral scale of $\sim 65 \text{ nm}$, as can be estimated from the Fourier transformed image in panel (c). Panel (d) shows the corresponding spatial frequency profile integrated within the dotted rectangle. The arrow marks the highest-frequency peak in the spectrum, responsible for the 65 nm modulations.

intensity at the $(\frac{1}{2}, \frac{1}{2}, \bar{3})_{\text{Tet}}$ position — the asymmetry further decreases gradually from 15.5% at T_m to 5.2% at $T \rightarrow 0$, indicating that the volume fraction of the SDW state is $\sim 49\%$ in the low-temperature limit.

The remaining 25% of the volume phase which remains non-magnetic at low temperature can be associated with the SC phase. For comparison, in nearly optimally doped BKFA with $x = 0.5$, the low-temperature non-magnetic volume fraction constitutes almost 50% [96], in-line with the increased $T_c = 37 \text{ K}$. The SC volume fraction in our samples was also independently estimated from ARPES [66], which yielded $23 \pm 3\%$ in agreement with our μSR result. Note that the decrease in asymmetry below T_m is gradual, indicating that we are dealing with a crossover rather than a sharp phase transition. This agrees with the absence of any appreciable anomalies at T_m in susceptibility and resistivity measurements.

The μ SR relaxation rate was also measured in the same transverse field. The weak magnetic field penetrates the sample through the AFM islands, creating an inhomogeneous field distribution within the SC phase, which results in a rapid increase of muon depolarization below T_c , as seen in Fig. 4.4 (c). Thus, the AFM islands act as pre-formed vortex cores, precluding the formation of an ordered vortex lattice. At $T \rightarrow 0$ the relaxation rate, which in a homogeneous superconductor is expected to be proportional to the superfluid density according to the Uemura relation [263], extrapolates to $\sigma = 0.9 \pm 0.1 \mu\text{s}^{-1}$. Surprisingly, this value follows the Uemura relation reasonably well, despite the phase separation. It is noteworthy that our value of σ is higher than that reported for the $x = 0.45$ sample in Ref. [95], but still somewhat lower than in the optimally-doped $x = 0.5$ sample from Ref. [96].

At this point, we can already conclude that our sample simultaneously exhibits bulk SC with a sharp transition temperature of 32 K and SDW order with a large correlation length $> 100 \text{ \AA}$, which are spatially separated and change their volume ratio as a function of temperature. This resembles the situation in underdoped cuprates, where SC coexists with a short-range AFM-correlated magnetic state with albeit strongly reduced ordered magnetic moment [264]. There, however, the magnetic volume fraction seen by μ SR is nearly 100% [264], indicating a more homogeneous coexistence of the two phases. On the other hand, scanning tunneling spectroscopy measurements provide numerous evidence for nano-scale inhomogeneities in the electronic density of states. In contrast to the cuprates, in BKFA we rather observe a mesoscopic phase-separated coexistence [96], as we schematically illustrate in Fig. 4.5 (a), with an ordered moment which is hardly suppressed as compared to the parent compound exhibiting long-range SDW order.

To get a better understanding of the real-space distribution of the magnetically ordered domains, a zero-field magnetic force microscopy (MFM) measurements was performed in the SC state on a cleaved surface of a BKFA sample with a somewhat reduced T_c of 26 K using an *Omicron Cryogenic SFM* scanning force microscope supplied with a commercial *Nanoworld MFMR* magnetic tip possessing a force constant of $\sim 2.8 \text{ N/m}$ and a resonance frequency of 72 kHz. Magnetic contrast was imaged with the lateral resolution $< 50 \text{ nm}$ by measuring the frequency shift at a scan height of 10 nm above the sample surface. As shown in Fig. 4.5 (b), weak static magnetic contrast is clearly seen below T_m , which would not be expected for a magnetically homogeneous sample. Successive scanning of the same area of the sample confirmed the reproducibility of the magnetic contrast at temperatures below T_m . The contrast is weakened above T_m , though does not disappear completely. We associate this contrast with AFM domain boundaries like those sketched in the inset in Fig. 4.5 (a), as the stray field produced by uncompensated magnetic moments at such a boundary is likely to result in a magnetic contrast detectable by MFM. To estimate the characteristic

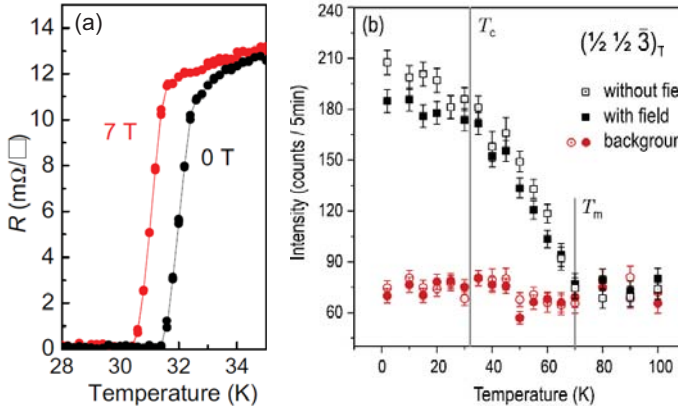


Figure 4.6: (a) Resistance measurement on the slightly underdoped BKFA in a magnetic field. (b) Temperature evolution of the magnetic Bragg peak intensity in a magnetic field of 13.5 T.

spatial scale of the observed inhomogeneities, we performed a Fourier transform of the MFM signal [see Fig. 4.5 (c) and (d)]. The highest-frequency peak in the spectrum corresponds to the characteristic scale of the inhomogeneities of the order of $\zeta = 65 \pm 10$ nm. A peak corresponding to larger-scale modulations can also be seen in some of the spectra.

To summarize, we have observed mesoscopic phase-separated coexistence of magnetically ordered and non-magnetic states on the lateral scale of ~ 65 nm in a slightly underdoped iron pnictide superconductor, as estimated from MFM imaging in agreement with the μ SR measurements. However, as already discussed in Sec. 2.2.3, based on the improvements made in the single-crystal-growth technique, recent literature on both electron- or hole-doped 122-ferropnictide points toward the microscopic coexistence, leading to a competition between magnetic and SC phases. One possible explanation of such an inconsistency is that the electronic phase separation might be a unique property of Sn-flux-grown FeAs superconductors.

4.1.4 Magnetic field effect

We have also studied the magnetic field effect on the SC phase by means of electrical transport and elastic magnetic neutron scattering measurement. Figure 4.6 (a) is the resistance data measured in zero field (black curve) and 7 T (red curve) applied along the in-plane. The SC transition temperature shifted down to 28 K from 32 K in the magnetic field of 7 T, indicating the slight suppression of superconductivity under the external magnetic field. However, the width of the SC transition in the resistance curve remains unchanged. To investigate the magnetic field effect on the magnetic Bragg reflection, an external field of $H = 13.5$ T was applied perpendicular to the scattering plane and thus parallel to the FeAs-layers. The magnetic intensity was suppressed by $\sim 10\%$, as shown by solid symbols in Fig. 4.6 (b). However, the onset temperature of the magnetic Bragg reflection did not change.

Recently, similar neutron diffraction work was performed on the FeAs-flux-grown

underdoped BKFA by Rotundu *et al.* [265], and their data showed that T_c was reduced by a factor of two while the magnetic Bragg peak intensity at 1.2 K was somewhat increased. The authors interpreted these observations as an evidence for the competition between superconductivity and magnetism [265].

4.2 Electron-doped $\text{BaFe}_{1.85}\text{Co}_{0.15}\text{As}_2$ and $\text{BaFe}_{1.91}\text{Ni}_{0.09}\text{As}_2$

In this section, we will present spin-excitation spectrum measurements on both cobalt and nickel substituted BaFe_2As_2 compounds by means of inelastic neutron scattering (INS). Both compounds show no static magnetism down to the lowest temperature, but present a bulk SC phase transition at 25 K in optimally-doped $\text{BaFe}_{2-x}\text{Co}_x\text{As}_2$ and at 18 K in nearly optimally-doped $\text{BaFe}_{2-x}\text{Ni}_x\text{As}_2$ compounds. Initially, the magnetic dynamics in the SC state will be discussed in terms of the spin-1 collective mode as well as its L -dependence property. Then, the normal-state spin-fluctuations will be discussed based on existing theoretical model, which describes the AFM excitations in a metal, and its in-plane cross-section. To obtain a better physical insight of the normal-state magnetic response, we employed the first-principles calculations. This research is now available as peer-reviewed papers in Ref. [160, 50, 266], and part of the figures and text are reproduced from the publications.

4.2.1 Sample characterization and experimental details

The single crystals of $\text{BaFe}_{1.91}\text{Ni}_{0.09}\text{As}_2$ ($T_c = 18$ K, $m \approx 4$ g) and $\text{BaFe}_{1.85}\text{Co}_{0.15}\text{As}_2$ ($T_c = 25$ K, $m \approx 1$ g) were grown by the FeAs-flux method [79] as described in Sec. 3.1.1 in details, and characterized by EDX, SQUID magnetometry, and single-crystal neutron diffraction using the E2 flat-cone diffractometer at the Helmholtz-Zentrum Berlin für Materialien und Energie. Magnetization measurements on several small pieces of each sample revealed sharp SC transitions at $T_c = 18$ K and 25 K, respectively, as shown in Fig. 3.6 (a). In both the $(HHL)_{\text{Fe}_4}$ and $(HK0)_{\text{Fe}_4}$ planes, the neutron diffraction patterns exhibit well defined Bragg spots with narrow mosaicity $< 1^\circ$ [Fig. 3.6 (b)], with no signature of multiple single-crystalline grains, but with some polycrystalline contamination originating both from the main phase and to a lesser extent from traces of the (Fe,Co)As flux [see Fig. 3.6 (c)]. We therefore had to optimize the scattering conditions in our INS measurements by avoiding the appearance of spurious inelastic peaks caused by such contamination. No structural or SDW transitions were detected down to 2 K in both samples, consistent with the known phase diagrams [32, 267, 268, 81].

The INS measurements were performed at the triple-axis spectrometers PANDA and PUMA (FRM-II, Garching), IN8 (ILL, Grenoble), and 1T and 2T (LLB, Saclay).

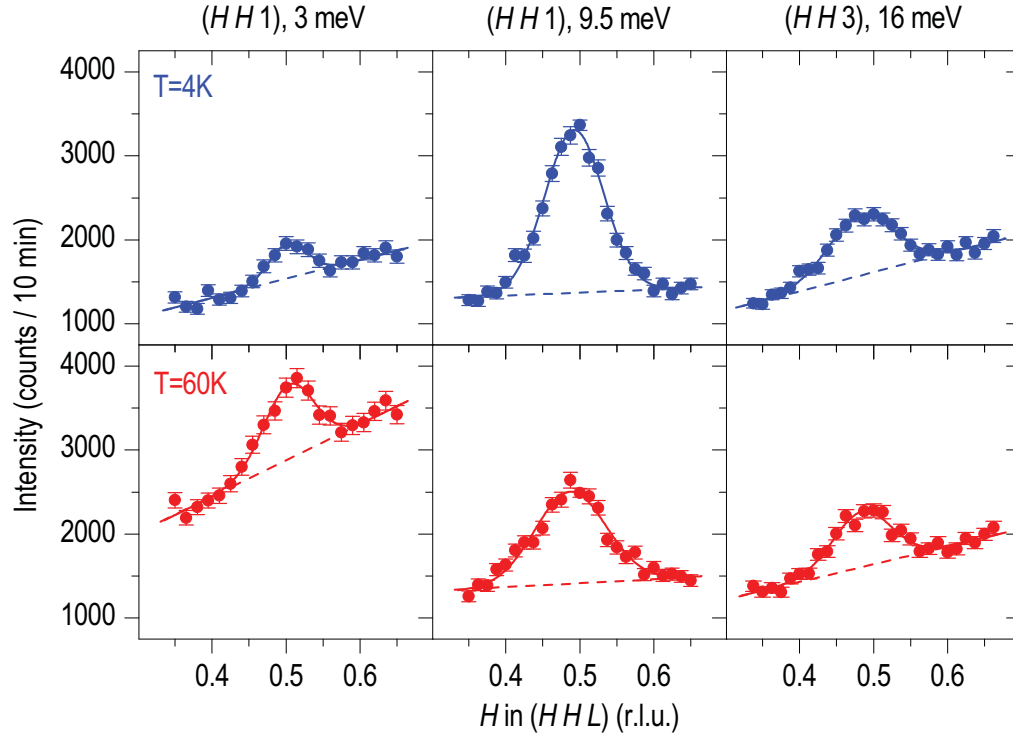


Figure 4.7: Several raw \mathbf{Q} -scans in the vicinity of AFM wave vector for $\text{BaFe}_{1.85}\text{Co}_{0.15}\text{As}_2$, measured along the longitudinal direction in the SC state (top row, $T = 4\text{ K}$) and in the normal state (bottom row, $T = 60\text{ K}$) at three different energies: 3 meV, 9.5 meV, and 16 meV. The solid lines represent Gaussian fits with a linear background. The background is indicated by dashed lines.

The instruments were operated in their high-flux setup without collimators, using focussed pyrolytic-graphite (002) monochromator and analyzers. Measurements were done in the constant- k_f mode, with $k_f = 1.55\text{ \AA}^{-1}$ ($E_f = 4.98\text{ meV}$) or $k_f = 2.662\text{ \AA}^{-1}$ ($E_f = 14.7\text{ meV}$). Correspondingly, either a cold Be-filter or two pyrolytic-graphite filters were used for higher-order neutron elimination.

The INS data for the present work were collected both in the (HHL) and $(HK [H + K])$ scattering planes. Throughout this section we are using back-folded tetragonal notation [see Fig. 2.3 (e)], in which $\mathbf{Q}_{\text{AFM}} = \left(\frac{1}{2}\frac{1}{2}1\right)_{\text{Fe}_4}$ corresponds to the AFM ordering wave vector of the parent compound. Wherever applicable, the background was subtracted from the data, and corrections for the magnetic structure factor for the measurements at several physically equivalent \mathbf{Q} positions and for the energy-dependent fraction of higher-order neutrons were applied. The imaginary part of the dynamical spin susceptibility $\chi''(\mathbf{Q}, \omega)$ was obtained from the scattering function $S(\mathbf{Q}, \omega)$ by the fluctuation-dissipation relation, which is described in Sec. 3.2.1. The data sets measured at different spectrometers or with different experimental settings were scaled by using overlapping energy regions as a reference. The error bars in all figures correspond to one standard deviation of the count rate and do not include the

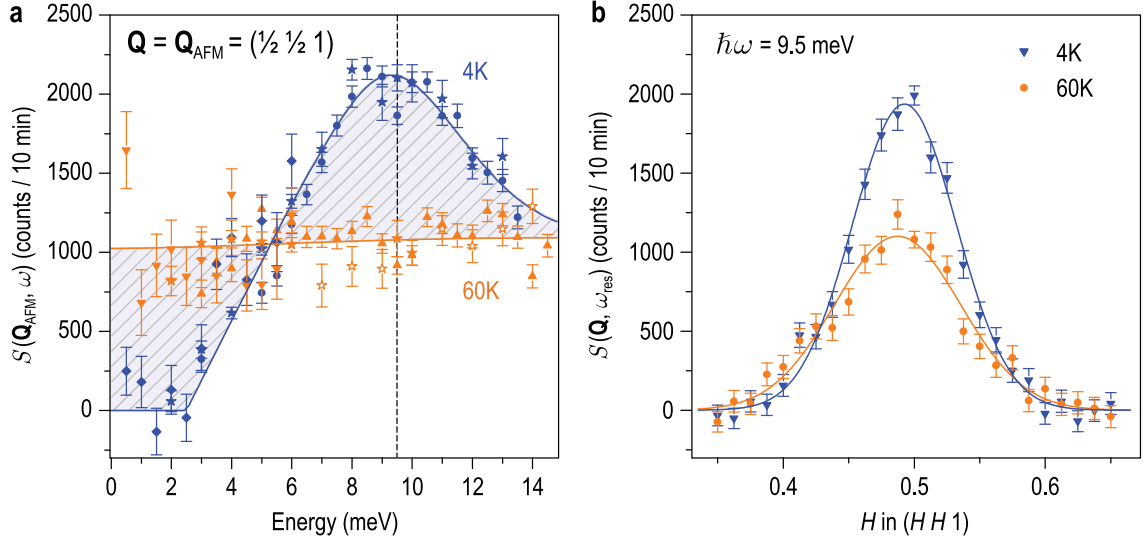


Figure 4.8: Spin excitations in the vicinity of the AFM wave vector, \mathbf{Q} , in the SC ($T = 4$ K) and the normal state ($T = 60$ K). (a) Energy evolution of the magnetic scattering function $S(\mathbf{Q}_{\text{AFM}}, \omega)$ after a background correction. The different symbol shapes represent measurements at different spectrometers. The solid lines are guided to eyes. (b) Momentum dependence of $S(\mathbf{Q}, \omega)$ measured at the magnetic resonant energy [dashed line in (a)]. A linear background has been subtracted from the fit. The lines are Gaussian fits. The error bars represent the statistical error of measured points.

normalization errors. We quote the wave vector $\mathbf{Q} = (HKL)$ in reciprocal lattice units (r.l.u.), i. e. in units of the conventional reciprocal lattice vectors \mathbf{a}^* , \mathbf{b}^* , and \mathbf{c}^* ($a^* = b^* = 2\pi/a$, $c^* = 2\pi/c$) that would correspond to a simple tetragonal unit cell with the same dimensions. The room-temperature lattice constants are $a = b = 3.94 \text{ \AA}$, $c = 12.86 \text{ \AA}$ for $\text{BaFe}_{1.91}\text{Ni}_{0.09}\text{As}_2$ and $a = b = 3.92 \text{ \AA}$, $c = 12.84 \text{ \AA}$ for $\text{BaFe}_{1.85}\text{Co}_{0.15}\text{As}_2$. For the sake of a compact notation we will set $\hbar = 1$ in the following and quote the energy transfer ω in meV.

4.2.2 The spin-excitation spectrum in the SC state

The magnetic resonant mode

Generally, the spin dynamics of 122 Fe-based superconductors are dominated by an intense branch of low-energy spin fluctuations in the vicinity of the commensurate $\mathbf{Q} = \left(\frac{1}{2} \frac{1}{2} L\right)_{\text{Fe}_4}$ wave vector. In Fig. 4.7, several representative longitudinal Q -scans across the AFM wave vector are shown. One can see that both in the normal and SC states, the signal is well fitted by a single Gaussian peak with a linear background, showing no signatures of incommensurability along this reciprocal-space direction within the low-energy range of up to $\sim 2\Delta$.

Let us begin by showing in Fig. 4.8 the scattering function $S(\mathbf{Q}, \omega)$ at the antiferromagnetic wave vector $\mathbf{Q}_{\text{AFM}} = \left(\frac{1}{2} \frac{1}{2} 1\right)_{\text{Fe}_4}$ for $\hbar\omega \leq 15$ meV in the SC state (4 K) and in the normal state (60 K). The data were obtained by collecting a series of \mathbf{Q} -scans at fixed ω , and ω -scans at fixed \mathbf{Q}_{AFM} as shown in Fig. 4.7, supplemented by points appropriately offset from \mathbf{Q}_{AFM} to allow an accurate background subtraction. In the SC state, the spectrum shows very prominent peak situated around 9.5 meV while the normal-state spectrum shows almost flat behavior down to the lowest energy transfer. By this, we determine ω_{res} to be 9.5 meV, which is attributed to the magnetic resonant mode, in agreement with the first investigations on samples of similar doping levels [223]. The enhancement of magnetic scattering intensity can be also seen in the momentum scan in Fig. 4.8 (b). The peak amplitude is about twice stronger in the SC state compared to that in the normal state. This feature is again in-line with the experimental feature of the resonance mode. At this stage, we present $S(\mathbf{Q}, \omega)$ instead of the dynamical susceptibility $\chi''(\mathbf{Q}, \omega)$, since a sum rule holds, stipulating that $\int_{-\infty}^{\infty} d\omega \int d\mathbf{Q} S(\mathbf{Q}, \omega)$ is T -independent. An important result is that within the experimental error the resonant spectral-weight gain is compensated by a depletion at low energies, and that the superconductivity-induced effects are limited to $\hbar\omega \lesssim 2\Delta_{\text{SC}}$. The \mathbf{Q} -integration can be neglected here, since within the shown energy range of up to 2Δ the spectrum remains commensurate and the measured \mathbf{Q} -width does not change appreciably: Its value of ~ 0.1 r.l.u. is much broader than the resolution and thus represents the intrinsic \mathbf{Q} -width to a good approximation.

$\chi''(\mathbf{Q}_{\text{AFM}}, \omega)$ can be obtained by correcting $S(\mathbf{Q}_{\text{AFM}}, \omega)$ for the thermal population factor (Bose factor), which is largest at low ω and high T (Fig. 4.9). Performing this correction, we now clearly establish that the low- ω depletion represents a real spin gap (not to be confused with the superconducting gap Δ_{SC}) and not a trivial thermal population effect. One of the central results of this work is that we can present $S(\mathbf{Q}, \omega)$ in absolute units by comparing the magnetic scattering intensity to the intensity of acoustic phonons as well as nuclear Bragg peaks after taking care of resolution corrections. This approach is extensively discussed in Ref. [269] and references therein, from which here the definition of χ'' as $\text{Tr}\chi''_{\alpha\beta}/3$ is also adopted, where $\chi''_{\alpha\beta}$ is the imaginary part of the generalized susceptibility tensor. Apart from its importance for theoretical work, this allows us to extract the weight of the spectral features to be discussed later.

From Fig. 4.9, we can define three energy intervals: The spin gap below ~ 3 meV, the magnetic resonant mode region between ~ 3 and ~ 15 meV, and the region above ~ 15 meV with no superconductivity-induced changes. In Fig. 4.10 we show the evolution of $\chi''(\mathbf{Q}_{\text{AFM}}, \omega)$ at the representative energies 3, 9.5 and 16 meV for temperatures up to 280 K. We observe a smooth increase upon cooling down to T_c at all three energies. While at 16 meV the intensity also evolves smoothly across T_c , there are

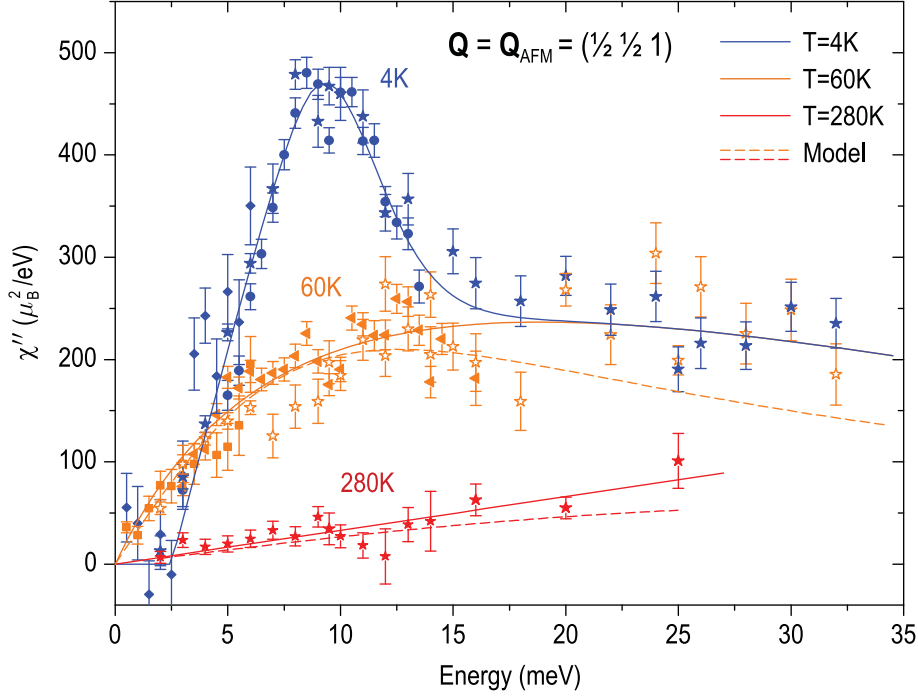


Figure 4.9: Imaginary part of the spin susceptibility $\chi(\mathbf{Q}_{\text{AFM}}, \omega)$ in the superconducting ($T=4\text{K}$) and the normal state ($T=60$ and 280K). The data were obtained from $S(\mathbf{Q}_{\text{AFM}}, \omega)$ by correcting for the thermal population factor and were put on an absolute scale as described in the text. The solid lines are guides to the eye. The dashed lines represent global fits which we are going to discuss in the next section for the normal state data.

pronounced anomalies at 3 and 9.5 meV, indicating the abrupt gap opening. We note that there is no indication of a pseudogap opening above T_c , which is consistent with the linear behavior of $\chi''(\mathbf{Q}, \omega)$ at small ω (Fig. 4.9). However, since the SC gap decreases upon heating to T_c [66, 190], it does not suffice to study the T -dependence of $\chi''(\mathbf{Q}, \omega)$ at a fixed energy. Hence, we investigated the evolution of the resonance peak by performing energy scans at several temperatures below T_c (Fig. 3b). An important result is that ω_{res} decreases upon heating as well, and it follows the same functional dependence as Δ_{SC} with remarkable precision, that is $\omega_{\text{res}}(T) \propto \Delta_{\text{SC}}(T)$ (Fig. 4.10).

A comprehensive summary of our data in the ω - T plane is shown in Fig. 4.10 (d). As indicated by the vertical bar, the resonance maximum always remains inside the $2\Delta_{\text{SC}}$ gap, while its tail might extend beyond. Here we note that the impact of superconductivity on the spin excitations can be fully accounted for by the opening of Δ_{SC} and the appearance of the resonant mode, without qualitative changes to the excitation geometry. Considering the resonant excitation as a bound state within the SC gap, as discussed in Sec. 2.4.1, $\omega_{\text{res}} < 2\Delta_{\text{SC}}$ is required, and our value of $\omega_{\text{res}} = (1.6 \pm 0.3)\Delta_{\text{SC}}$ is in good agreement with the predictions for a sign-reversed s_{\pm} -wave gap [47, 161]. Furthermore, we have shown that ω_{res} follows the same trend as $\Delta_{\text{SC}}(T)$ when the gap closes upon heating, as expected from conventional Fermi liquid based

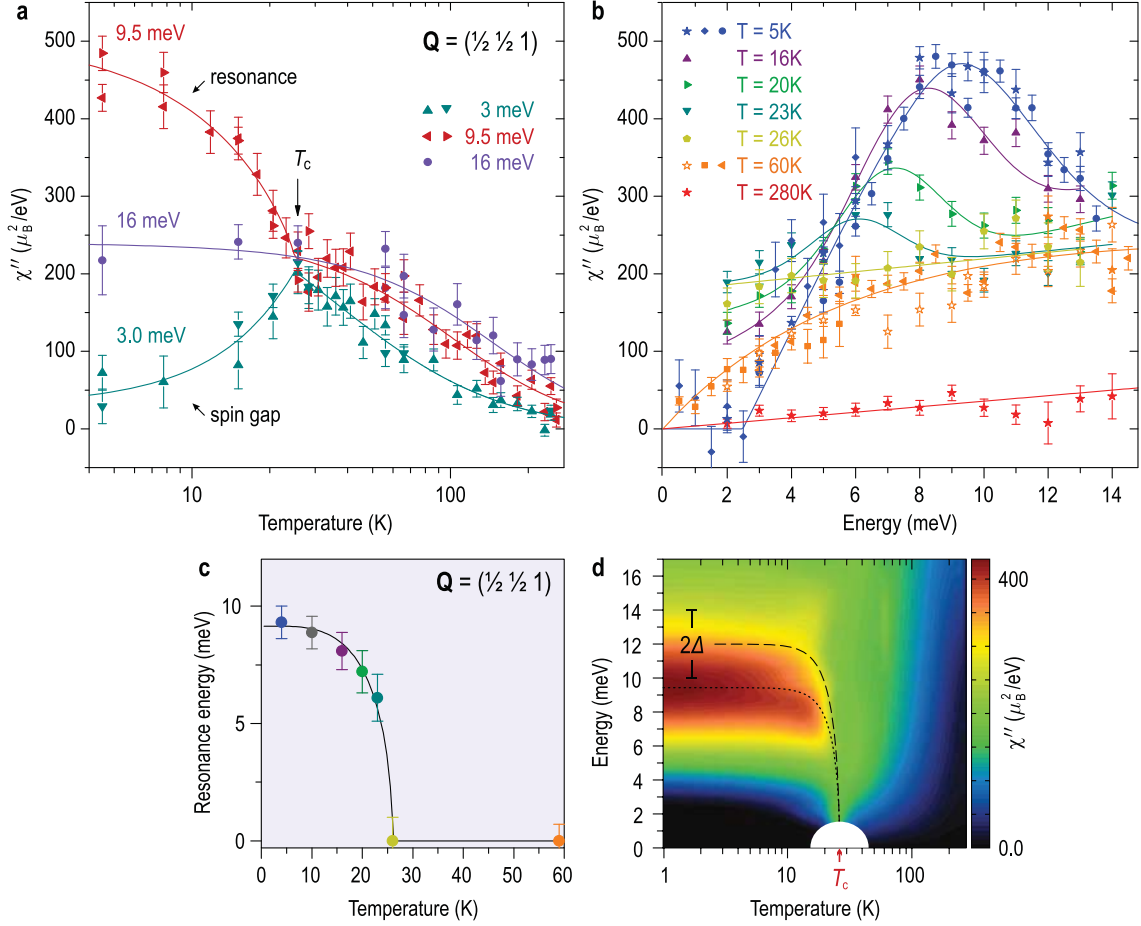


Figure 4.10: Energy and temperature dependence of $\chi''(\mathbf{Q}_{\text{AFM}}, \omega)$ and evolution of the resonance peak below T_c . (a) Temperature dependence of $\chi''(\mathbf{Q}_{\text{AFM}}, \omega)$ at three different energies: within the spin gap (3 meV), at ω_{res} (9.5 meV) and above $2\Delta_{\text{SC}}$ (16 meV). (b) Energy scans at \mathbf{Q}_{AFM} showing $\chi''(\mathbf{Q}, \omega)$ at different temperatures. The lines in panel (a) and (b) are guides to the eye. (c) Temperature evolution of the resonance energy $\omega_{\text{res}}(T)$ defined by the maxima in panel (b). The line has the same functional dependence as the SC gap Δ_{SC} obtained by ARPES [66, 190], that is $\omega_{\text{res}}(T) \propto \Delta_{\text{SC}}(T)$. (d) Interpolation of the data in panels (a) and (b) showing $\chi''(\mathbf{Q}_{\text{AFM}}, \omega)$ in the ω - T plane for T up to 280 K. The vertical bar shows the interval of the reported $2\Delta_{\text{SC}}$ values [211, 212, 190]. The dotted line is the same as the fit in (c). The dashed line has the same functional dependence and tracks the average value of $2\Delta_{\text{SC}}(T)$ as a function of T . Note the logarithmic T -scale in panels (a) and (d).

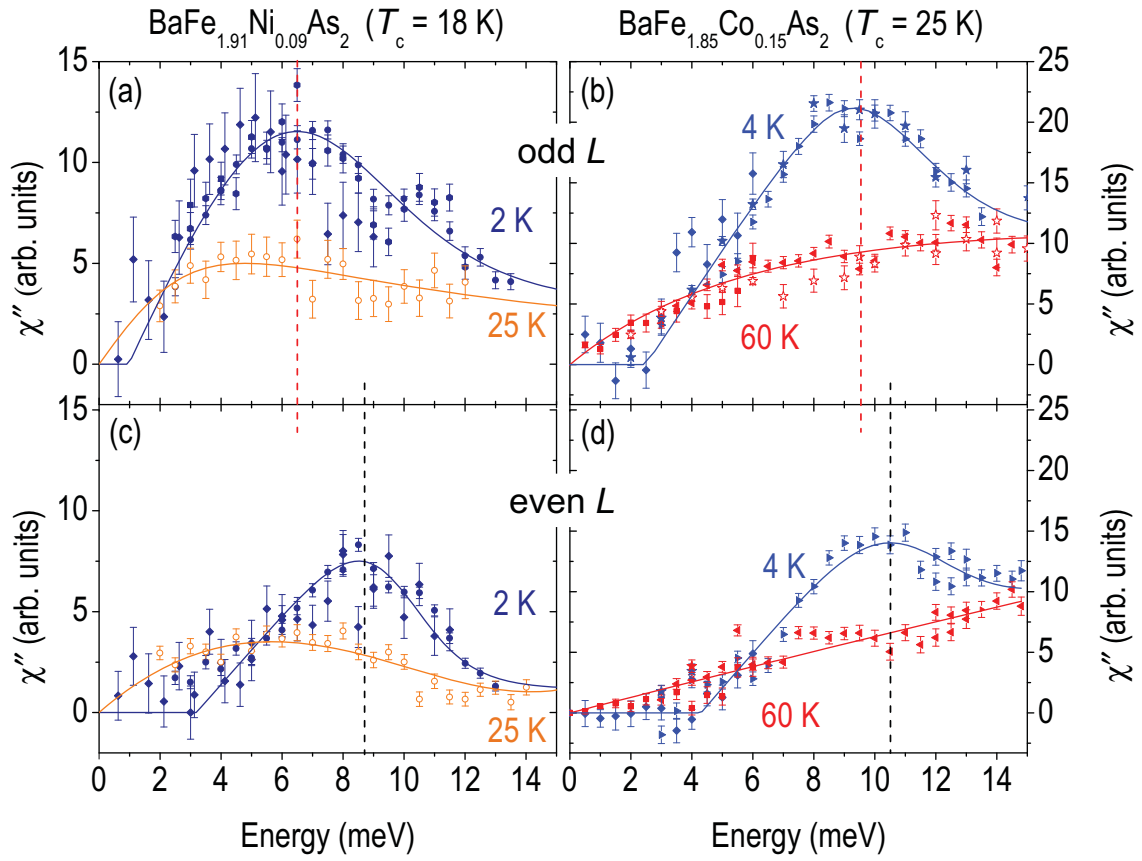


Figure 4.11: Imaginary part of the spin susceptibility at odd (top) and even (bottom) L in the normal and SC states. The left column shows data for $\text{BaFe}_{1.91}\text{Ni}_{0.09}\text{As}_2$ at $\mathbf{Q} = \left(\frac{1}{2} \frac{1}{2} 1\right)_{\text{Fe}_4}$ and $\left(\frac{1}{2} \frac{1}{2} 3\right)_{\text{Fe}_4}$ in (a) and at $\left(\frac{1}{2} \frac{1}{2} 2\right)_{\text{Fe}_4}$ in (c). The right column shows corresponding data for $\text{BaFe}_{1.85}\text{Co}_{0.15}\text{As}_2$. The data points were obtained from constant- ω scans and constant- \mathbf{Q} scans, as described in the text. The solid lines are guides to the eye. Different symbol shapes represent data obtained in different measurements.

approaches. Such simple behavior of the magnetic resonant mode versus T or Δ_{SC} is in notable contrast to its counterpart in the cuprates [219], where the temperature insensitivity of ω_{res} has inspired theories that attribute the magnetic resonant mode to a particle-particle bound state [270] or a collective mode characteristic of a state competing with superconductivity [271].

As discussed in Sec. 2.1.3, the iron-arsenide superconductors maintain their multi-band character across the different materials and doping levels. Thus, this property should be kept in mind especially when discussing the resonance energy since it can contribute to the intrinsic width of the resonance peak.

L - and doping-dependence of magnetic resonant mode

The magnetic resonance mode in FeSC shares various common aspects with cuprates, such as its abrupt intensity evolution below T_c , and the fact that it is always observed at an energy ω_{res} below the particle-hole continuum that sets in at twice the

SC gap Δ [272, 273]. However, there are also differences: In BFCA, the temperature evolution of ω_{res} is BCS-gap-like, and no signature of a pseudogap has been found [160] as we just discussed in the previous section. Here, we will compare two further aspects of the spin resonant features in both systems. First, due to the intra-bilayer coupling, bilayer cuprates exhibit two resonant modes characterized by odd and even symmetries with respect to the exchange of CuO_2 layers within a bilayer unit, as reported for the $\text{YBa}_2\text{Cu}_3\text{O}_{6+x}$ and $\text{Bi}_2\text{Sr}_2\text{CaCu}_2\text{O}_{8+\delta}$ families [272, 273]. These modes show intensity modulations with L , anti-phase with respect to each other, as well as different but L -independent resonance energies. Although distinct resonance energies for even and odd L were already observed in BFNA [224, 229], a comparison to the cuprates has not yet been drawn conclusively, because due to the equally-spaced FeAs layers, two distinct resonant modes are not expected.

In Fig. 4.11, we show the energy dependence of the experimentally measured imaginary part of the spin susceptibility $\chi''(\mathbf{Q}, \omega)$ which is the similar plot for Fig. 4.9, at $\mathbf{Q}_{\text{Fe}_4} = \left(\frac{1}{2} \frac{1}{2} L\right)_{\text{Fe}_4}$ for both samples at even and odd L , obtained from the raw INS data after background subtraction and Bose-factor correction. The measured signal has also been corrected to account for the energy-dependent fraction of higher-order neutrons. The data were acquired by performing a series of full \mathbf{Q} -scans similar to those shown in Fig. 4.7 at different fixed energies and an energy scan at $\mathbf{Q}_{\text{Fe}_4} = \left(\frac{1}{2} \frac{1}{2} L\right)_{\text{Fe}_4}$. To estimate the background for the latter, we used a linear interpolation for the background obtained from Gaussian fits to the full \mathbf{Q} -scans, or measured points appropriately offset to both sides from $\left(\frac{1}{2} \frac{1}{2} L\right)_{\text{Fe}_4}$. The error bars correspond to one standard deviation of the neutron count and do not include the normalization errors. The two left panels of Fig. 4.11 show data on $\text{BaFe}_{1.91}\text{Ni}_{0.09}\text{As}_2$, measured in the SC and normal states at $L = 1$ and 3 [panel (a)] and at $L = 2$ [panel (c)]. The respective data for $\text{BaFe}_{1.85}\text{Co}_{0.15}\text{As}_2$ are shown at the right.

Already in the normal state, a difference between odd and even L values can be observed. For both samples, the normal-state spectral weight, integrated over \mathbf{Q} and ω up to 14 meV, is $\sim 60\%$ larger at odd than at even L . Such a difference cannot be a consequence of the magnetic form factor, which would be smaller at $L = 1$ than at $L = 0$, producing the opposite effect. On the other hand, this difference is reminiscent of the SDW phase of the parent compounds, where low-energy magnon branches are present only near magnetic Bragg peaks at odd L , whereas spin waves at even L are gapped and thus yield zero intensity at low energy [141, 140, 122, 116, 144]. However, in the paramagnetic state, the normal-state intensity at even L is only moderately suppressed. Here we note that the absence of any magnetic Bragg intensity at $\left(\frac{1}{2} - \frac{1}{2} 0\right)$ or $\left(-\frac{1}{2} \frac{1}{2} 0\right)$ in the SDW state is fully consistent with the unfolded-BZ scheme [see Fig. 2.3 (a)]. Indeed, as can be seen from Fig. 2.3, these two X points correspond to the zone center in the doubly-folded magnetic BZ, which means that the

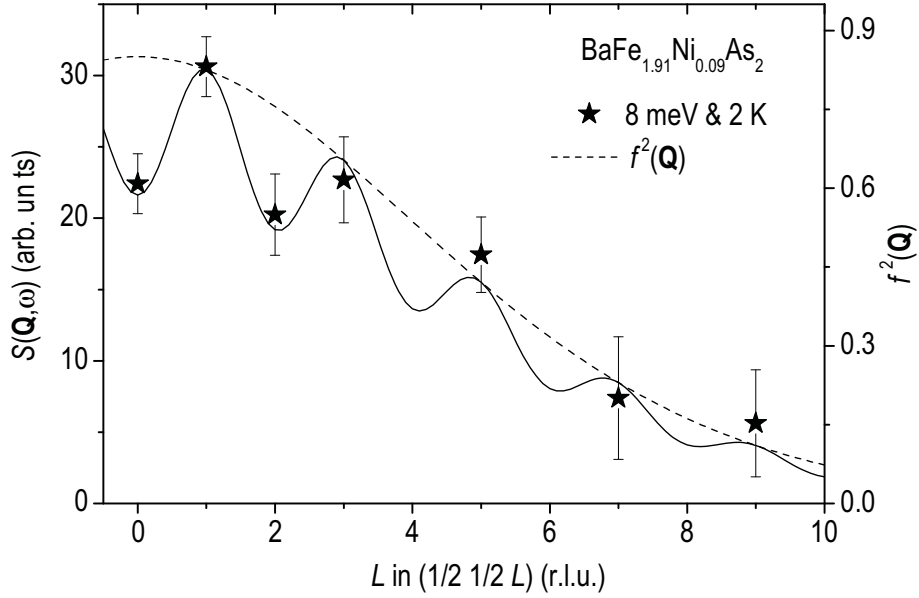


Figure 4.12: L -dependent magnetic intensity of $\text{BaFe}_{1.91}\text{Ni}_{0.09}\text{As}_2$ in the SC state at $\mathbf{Q} = \left(\frac{1}{2} \frac{1}{2} L\right)_{\text{Fe}_4}$ and 8 meV (close to the resonance energy). The dashed line shows the Fe^{2+} spin-only magnetic form factor.

influence of the As superstructure would lead to an appearance of magnetic Bragg-peak replicas at these points. In a twinned crystal, this would imply equivalency of all the $(\pm \frac{1}{2} \pm \frac{1}{2} L)$ points up to the magnetic structure factor. The fact that these replicas have not been observed by neutron diffraction indicates that the structure factor for the As-superstructure reflections is negligibly small or zero. In other words, no folding of the magnetic signal occurs due to the As sublattice, and hence the unfolded-BZ scheme is perfectly justified. Our results presented in this and the following sections serve to generalize these arguments to the inelastic magnetic signal.

At first, we consider the low-temperature spectra that exhibit the SC resonant mode in both compounds at both L -positions. We define the resonance energy ω_{res} as the maximum of $\chi''(\mathbf{Q}, \omega)$ in the SC state and discriminate between its value at even and odd L , $\omega_{\text{res,even}}$ and $\omega_{\text{res,odd}}$, where necessary. The dashed vertical lines mark these positions for odd and even L in the upper and lower panels of Fig. 4.11, respectively. We note that the resonance energies at odd and even L differ by more than 2 meV in $\text{BaFe}_{1.91}\text{Ni}_{0.09}\text{As}_2$, in agreement with Ref. [224]. In contrast, this difference is only about 1 meV in optimally doped $\text{BaFe}_{1.85}\text{Co}_{0.15}\text{As}_2$, as seen in Fig. 4.11 (c) and (d).

Fig. 4.12 shows the magnetic intensity evolution near the resonance energy along L , obtained from Gaussian fits of full constant-energy scans around $\mathbf{Q} = \left(\frac{1}{2} \frac{1}{2} L\right)_{\text{Fe}_4}$ at 8 meV. Similarly to the normal-state intensity, it is modulated periodically in L (on the top of the magnetic form factor), analogous to the magnons in the parent compound. Two factors can be responsible for the observed modulation. First, as the normal-state intensity is already lower at even L , it will preserve this modulation

after redistribution of the spectral weight due to the opening of the SC gap below T_c . Second, the higher energy of the resonance at even L is closer to (or even within) the particle-hole continuum, which may result in stronger damping and additional intensity reduction.

In addition to ω_{res} and the spectral weight of the resonance, the energy range below the resonance peak that is depleted upon entering the SC state (which we refer to as the *SC spin gap*) also depends on L . We define the spin-gap energy ω_{sg} as the intersection of the low-energy linear extrapolation of $\chi''(\mathbf{Q}, \omega)$ at 2 or 4 K with the $\chi'' = 0$ line (Fig. 4.11). Inspection of Fig. 4.13, where we compare constant-energy scans at even and odd L for both samples, clearly shows that ω_{sg} is larger at even L . We remark that the SC spin gap should not be mistaken for the SC gap Δ to which it is only indirectly related: ω_{sg} is determined by the energy, ω_{res} , and the width of the resonant mode.

Recalling that the X points in the BZ for odd and even L values are equivalent due to the $4/m$ screw symmetry described in Sec. 2.1.2, we can now conclude that this symmetry is absent in the spin-excitation spectra of both samples based on the following evidence observed in the out-of-plane direction: (i) different normal-state intensities at odd and even L ; (ii) different resonance energies $\omega_{\text{res,odd}}$ and $\omega_{\text{res,even}}$; (iii) periodic L -dependent intensity of the resonance; (iv) the corresponding difference of the spin gaps $\omega_{\text{sg,odd}}$ vs. $\omega_{\text{sg,even}}$.

In order to investigate the doping dependence of the resonance and its L -modulation, we summarize in Fig. 4.14 (a) our results together with other studies of electron-doped BaFe_2As_2 [223, 224, 233, 235, 50]. To put the ω_{res} values from different compounds and doping levels on the same scale, we divided ω_{res} by the optimal $k_B T_{c,\text{opt}}$ and normalized the doping level by the optimal doping level, respectively. While $\omega_{\text{res,odd}}$ values (blue symbols) in $\mathbf{Q} = \left(\frac{1}{2} \frac{1}{2} L\right)_{\text{Fe}_4}$ fall onto the blue dotted line which follows the average T_c in the phase diagrams from Refs. [32, 267, 268, 81], $\omega_{\text{res,even}}$ values (red symbols) do not follow T_c , but rather stay at higher energies than $\omega_{\text{res,odd}}$ in the underdoped region, in agreement with a similar recent study [235]. As a consequence, the difference between $\omega_{\text{res,odd}}$ and $\omega_{\text{res,even}}$ increases with underdoping (as can also be seen in Fig. 4.11).

The integrated intensity of the resonance is influenced, in particular, by its proximity to the particle-hole continuum with an onset at 2Δ . As a consistency check, we therefore plot in Fig. 4.14 (b) the Q - and ω -integrated intensities of the resonance at odd and even L versus its energy. Since in an RPA description the spectral weight of the resonant mode is roughly proportional to its excitonic binding energy [272], under the assumption of L -independent onset of the particle-hole continuum, a linear extrapolation of the two intensities onto the energy axis gives us a rough lower estimate of 2Δ —the point where the resonance intensity is fully suppressed by

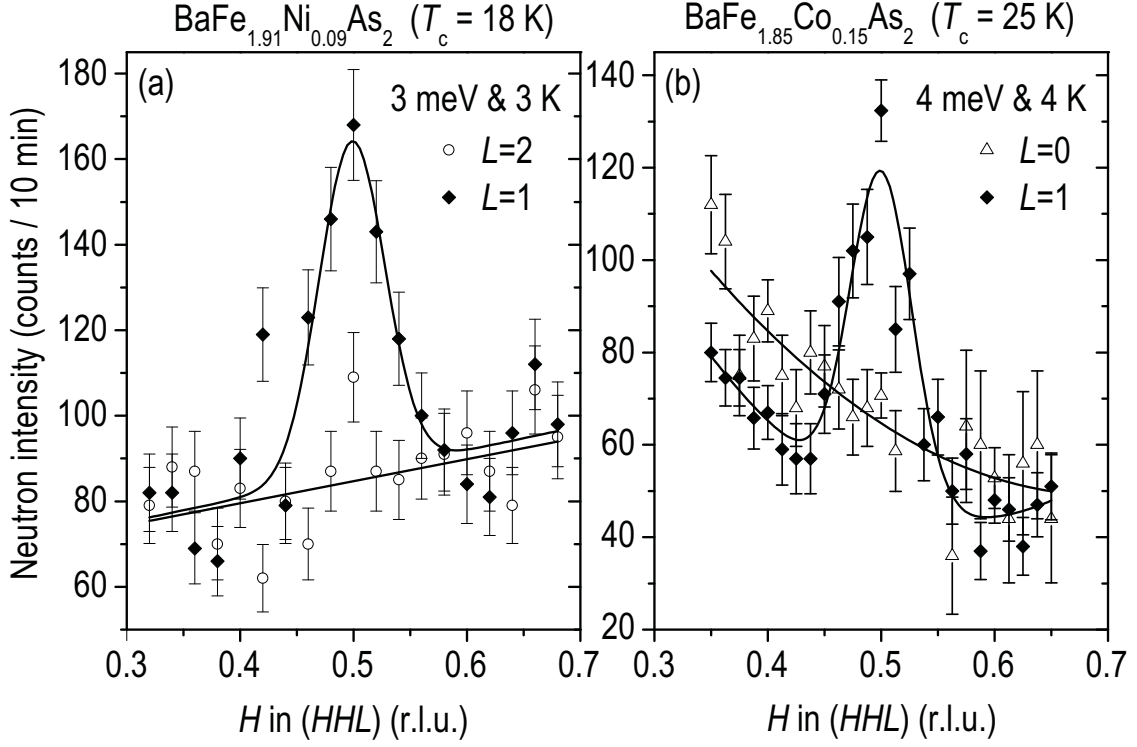


Figure 4.13: Comparison of momentum profiles at even and odd L at fixed energies that are below ω_{sg} for even L , but above it for odd L . (a) BaFe_{1.91}Ni_{0.09}As₂, $T = 3$ K and $\omega = 3$ meV. (b) BaFe_{1.85}Co_{0.15}As₂, $T = 4$ K and $\omega = 4$ meV.

particle-hole scattering (for similar analysis in cuprates, see Ref. [272]). For the Co-doped compound, such an extrapolation results in $2\Delta_{\text{BFCA}} \approx 11.8$ meV, which indeed falls in the middle of the range of values reported from direct measurements [190, 211, 212, 274, 196] (hatched region). Since SC gap measurements for the Ni-doped compound are scarce, we resort to calculating the coupling constant $2\Delta/k_{\text{B}}T_{\text{c}} = 6.8$ that results from the extrapolated gap of $2\Delta_{\text{BFNA}} \approx 10.6$ meV. On the one hand, it agrees with the universal value of 7 ± 2 that was reported for the larger gap in various two-gap ferropnictides [189] and coincides with that of 6.8 (or 6.6) derived from combined ARPES and μSR [189, 209] and specific-heat [78] measurements on Ba_{1-x}K_xFe₂As₂, respectively. On the other hand, it exceeds the maximum coupling constant of $2\Delta/k_{\text{B}}T_{\text{c}} \approx 5.0$ that was recently inferred [274, 196] from specific-heat measurements on BFCA. The non-linear dependence of the larger gap on T_{c} , reported in Ref. [196], would result in a much lower estimate for $2\Delta_{\text{BFNA}} \approx 6.9$ meV in the Ni-doped sample, under the assumption that this dependence is universal among 122-compounds. Such low value would imply a considerable overlap of the resonance peak with the particle-hole continuum, which could explain its broad width in energy.

The successful application of the simple scaling relation with L -independent particle-hole continuum indicates that the distance between the resonance and the continuum $2\Delta - \omega_{\text{res}}$ is L -dependent, as otherwise the agreement with directly mea-

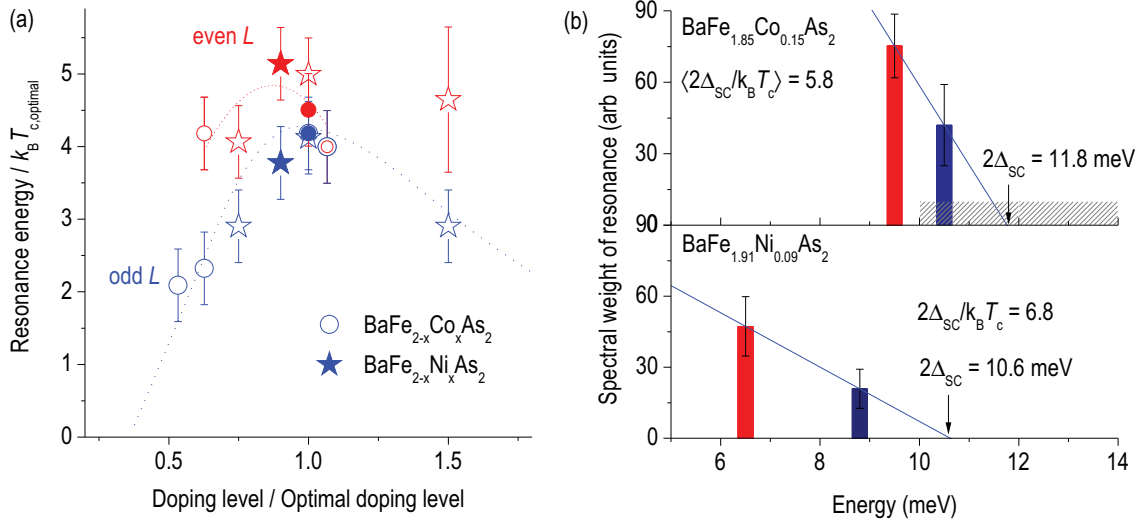


Figure 4.14: (a) Doping dependence of ω_{res} at odd and even L in BFNA and BFCA studied here (full symbols) and in previous works (empty symbols) [223, 224, 233, 235, 50]. The blue line follows the average T_c , rescaled to 4.3 at its optimum [32, 267, 268, 81]. The red line is a guide to the eye. (b) Linear extrapolation of the resonance intensities to the energy axis, as compared to the onset of particle-hole continuum. The hatched region covers the range of directly measured 2Δ values for the larger gap in nearly optimally doped BFCA, estimated by various experimental techniques [190, 211, 212, 274, 196].

sured gap values would be coincidental. In other words, the L -dependence of the resonance energy and intensity alone does not necessarily imply a k_z -dependent energy gap, as suggested previously [224], but more likely is a natural consequence of the normal-state intensity modulation. While a SC order parameter that differs at odd and even L values is conceivable and was even supported by experimental evidence [191, 275], it can only result from the normal-state properties of the “pairing glue”, and thus does not appear to be the primary reason for the dispersing resonant mode.

Now, let us consider the SC state properties and discuss the implications of our results for the SC pairing mechanism. First, we note that while the conventional unit cell contains two FeAs layers, the primitive cell, from which the BZ is constructed, contains only one. Thus, in contrast to cuprates only one resonant mode is expected; the different resonance energies at even and odd L are therefore to be attributed to an L -dispersion rather than to a mode splitting, in agreement with a recent report [229]. This dispersion signals the non-negligible 3D character of the electronic band structure and its importance for the description of the SC state. Indeed, there is compelling evidence for such three-dimensionality both from ARPES [276, 61, 59, 42] and band structure calculations [41, 275]. In view of the normal-state L -modulation, already a minimal model like RPA is expected to capture the L -dispersion of ω_{res} : By virtue of the magnetic resonant condition, namely the vanishing denominator in Eq. 2.11, the modulation is carried over into the SC state. Here both the bare susceptibility χ_0

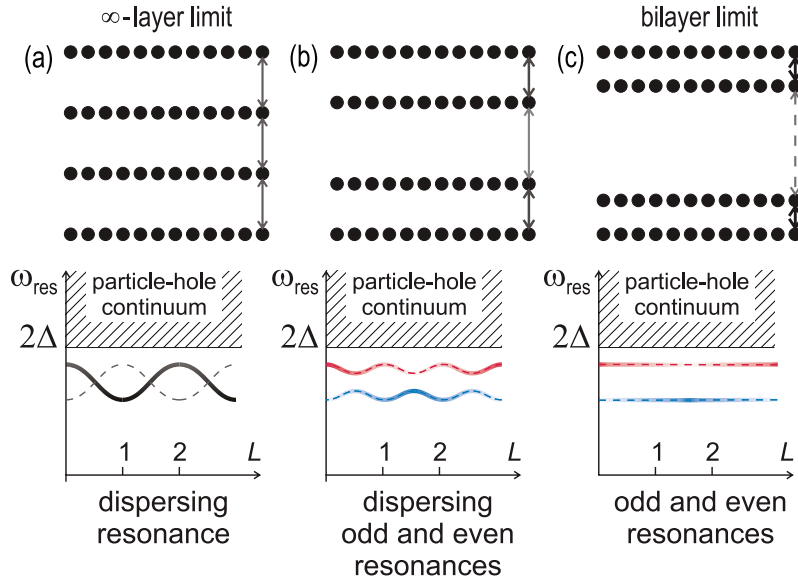


Figure 4.15: Illustration of the evolution from an ∞ -layer system like BFCa to a bilayer system like YBCO in terms of inter- and intra-bilayer distances and effective interactions. For the equidistant limit (left), a single dispersing resonant mode is observed, whose intensity modulation (shown here by the brightness of the curve) is mainly governed by the closeness to the particle-hole continuum with an onset at 2Δ . The dashed line depicts the replica that gains intensity only after the equivalency of the layers is broken (middle panel). For alternating interlayer coupling, the resonance splits into odd and even modes, which become non-dispersive for the case of $\text{YBa}_2\text{Cu}_3\text{O}_{6+y}$ with nearly independent bilayers (right).

and the interaction I can depend on L . We keep U deliberately general — there is no need to refer, for instance, to a t - J model [224, 229], whose applicability to the iron arsenides is being disputed.

We now put our considerations into a broader context by comparing our results to the resonant phenomena in $\text{YBa}_2\text{Cu}_3\text{O}_{6+y}$ (Fig. 4.15). The latter consists of nearly independent CuO_2 bilayers and exhibits manifestly 2D electronic structure and SC gap. One observes two distinct, non-degenerate resonances due to the difference in both the bare susceptibility χ_0 and the interaction I between the even and odd channels [277, 278], which can be ultimately tracked back to the contrast between the intra- and inter-bilayer hopping and interaction terms. On the contrary, in our iron-arsenide samples, this contrast vanishes and we observe a single resonance, which in addition disperses for the reasons described above. Thus, both systems represent different limiting cases of a more general model with coupled bilayers and possibly 3D electronic structure, Fig. 4.15 (b), where we expect two resonant modes which both disperse and exhibit an intensity modulation along L , depending on the effective coupling.

The similarity between the doping dependence of the out-of-plane dispersion bandwidth in the 122-family of iron arsenides [Fig. 4.14 (a)] and the even-odd resonant-

mode splitting in bilayer cuprates [272] supports our juxtaposition of the two systems: In both cases, the even-odd difference increases when moving towards the magnetic quantum critical point. Whereas the vanishing difference in Fig. 4.14 (a) around optimal T_c suggests that it is determined by the proximity to the magnetic instability, emphasizing the importance of the out-of-plane magnetic coupling in the arsenides, other measurements suggest a persistent even-odd difference even beyond optimal doping level [235], indicating that it rather scales with T_c . More detailed experimental and theoretical work is necessary to settle this point.

4.2.3 The spin-excitation spectrum in the normal state

To discuss the spin-excitations spectrum in the normal state, we first go back to the $\chi''(\mathbf{Q}, \omega)$ plot depicted in Fig. 4.9. In the normal state at 60 K we observe a broad spectrum of gapless excitations with a maximum around 20 meV and a linear ω -dependence for $\omega \rightarrow 0$. Increasing T to 280 K suppresses the magnetic intensity, which confirms the magnetic neutron-scattering origin, and presumably shifts the maximum to higher energies, while the low-energy linearity is preserved. This behavior and the absence of complications by incommensurate modulations or a pseudogap (see also Fig. 4.10) first motivates an analysis of the normal-state spin dynamics within the framework of the theory of nearly antiferromagnetic Fermi liquids [31], for which

$$\chi''_T(\mathbf{Q}, \omega) = \frac{\chi_T \Gamma_T \omega}{\omega^2 + \Gamma_T^2 (1 + \xi_T^2 |\mathbf{Q} - \mathbf{Q}_{\text{AFM}}|^2)^2}. \quad (4.1)$$

Here $\chi_T = \chi_0 (T + \Theta)^{-1}$ represents the strength of the AFM correlations in the normal state, $\Gamma_T = \Gamma_0 (T + \Theta)$ is the damping constant, $\xi_T = \xi_0 (T + \Theta)^{-1/2}$ is the magnetic correlation length, and Θ is the Curie-Weiss temperature. We obtain the best fit to all the normal-state data (Figs. 1b, 2, and 3) for $\chi_0 = (3.8 \pm 1.0) \cdot 10^4 \mu_B^2 \text{ K/eV}$, $\Gamma_0 = (0.14 \pm 0.04) \text{ meV/K}$, $\Theta = (30 \pm 10) \text{ K}$, and $\xi_0 = (163 \pm 20) \text{ \AA K}^{1/2}$, shown as dashed lines in Fig. 4.9. The deviation of the model from the experimental data at high energies can possibly be explained by the presence of multiple bands in the system, which shifts the maximum of $\chi''_{60\text{K}}(\mathbf{Q}_{\text{AFM}}, \omega)$ to a higher value of $\sim 20 \text{ meV}$. The total spectral weight at 60 K, integrated over \mathbf{Q} and ω up to 35 meV is $\chi''_{60\text{K}} = 0.17 \mu_B^2/\text{f.u.}$, and is thus comparable to underdoped $\text{YBa}_2\text{Cu}_3\text{O}_{6+y}$ [269]. The net resonance intensity, on the other hand, amounts to $\chi''_{\text{res}} = \chi''_{4\text{K}} - \chi''_{60\text{K}} = 0.013 \mu_B^2/\text{f.u.}$, which is 3–5 times smaller than in $\text{YBa}_2\text{Cu}_3\text{O}_{6+y}$ [269]. What is remarkable here is that the overall magnitude of $\chi''(\mathbf{Q}, \omega)$ is similar in both pnictides and cuprates families [269]. However, the spin-excitations spectra in cuprates show anomalous feature known as a ‘pseudogap’ and a broad peak reminiscent of the resonant mode in the normal state. In contrast, we have shown that the normal-state spin-dynamics of $\text{BaFe}_{1.85}\text{Co}_{0.15}\text{As}_2$ is gapless and can be well described by a simple formula for the nearly AFM metals [31]. We

note that despite the comparable normal-state magnitude of $\chi''(\mathbf{Q}, \omega)$ in the iron-arsenides and cuprates, T_c and the resonant enhancement of $\chi''(\mathbf{Q}, \omega)$ below the SC transition temperature are significantly lower in the former, which is an indication the spin-Fermion coupling is weaker in arsenides than in cuprates, resulting in universally lower T_c of FeSC [266].

4.2.4 Asymmetric spin-excitation spectrum

As we already discussed in Sec. 2.2.4, electronic nematic phases have been suggested for various iron-arsenide superconductors based on the anisotropic resistivity curve in detwinned single crystals, elliptical shape of in-plane spin excitations, and stripe pattern in topology [172, 56, 279, 174, 175, 145, 146, 159, 176, 234, 133] (for the latest reviews, see Refs. [24, 280, 281]). Here, we present the results of the INS measurements of the spin excitation spectra in the normal of slightly underdoped BFNA and optimally doped BFCA single crystals. Combining INS data and the first-principles calculations, we successfully demonstrate that the absence of any appreciable magnetic moment on the pnictogen atoms allows for a much simpler description of the dynamical spin susceptibility, which experiences no structural folding and hence does not acquire the additional reciprocal-space symmetry expected in the backfolded tetragonal (structural, nonmagnetic) BZ. Therefore, as far as the magnetic fluctuations in the paramagnetic state of ferropnictides are concerned, the unfolded description of the spectrum becomes physically justified. Moreover, we discuss the origin of anisotropic pattern of in-plane spin-excitation spectrum.

Due to the 3D character of the 122 systems, manifest both in their electronic structure (see Sec. 2.1.3) and in the substantial out-of-plane magnetic coupling in their undoped compounds, the missing symmetry operation which causes the symmetry-broken state should be essentially three-dimensional, involving all three crystallographic coordinates. It corresponds to the $4_2/m$ screw symmetry around the $\left(\frac{1}{2}\frac{1}{2}L\right)_{\text{Fe}_4}$ axis, as discussed in relation to Fig. 2.4, and is equivalent to a product of a 90° in-plane rotation around the Γ point and a translation by the reciprocal lattice vector $\mathbf{G} = \overline{\Gamma\Gamma} = (101)$. We will show that the clear absence of such screw symmetry — a conjectured 3D analog of the electronic nematicity — can indeed be observed in the spin-excitation spectrum already in the normal (paramagnetic) state, both along the out-of-plane and along the in-plane directions of the reciprocal space. In this respect, our experimental data are in qualitative agreement with recent reports of anisotropic in-plane excitations seen both in the magnetically ordered [116, 144] and paramagnetic [159, 145, 146] states. The latter excitations were previously associated with “spin nematic correlations”. However, a comparison with normal-state density-functional-theory (DFT) calculations shows good agreement between the calculated and measured susceptibilities, leading us to an

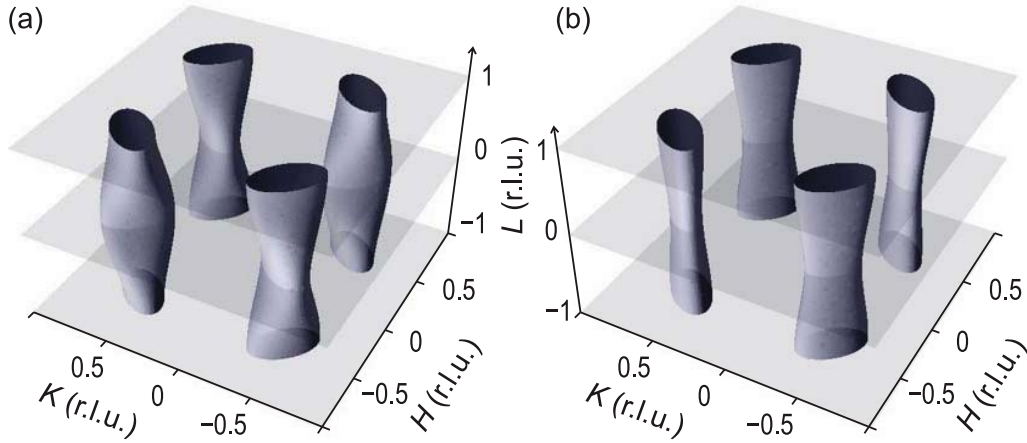


Figure 4.16: A sketch illustrating the symmetry of spin excitations: (a) as expected from the BZ symmetry in the absence of matrix elements; (b) as actually observed experimentally in doped 122-compounds. The surfaces schematically represent constant-intensity contours of the magnetic INS response. The center of each panel corresponds to the Γ point. Note that despite the lower symmetry in (b) due to the absence of the $4_2/m$ screw around $(\frac{1}{2}\frac{1}{2}L)_{\text{Fe}_4}$, the four-fold ($4/m$) rotational symmetry around $(00L)$ is preserved.

alternative explanation for the lowered symmetry of the spin-excitation spectrum that does not require a symmetry-broken ground state or proximity to a quantum critical point. Instead, it turns out to be a direct consequence of the crystal structure with two Fe atoms per primitive unit cell, in which the crystalline lattice that determines the BZ geometry has a lower symmetry than its Fe-sublattice, which is responsible for the magnetism [282, 283].

Before we show our INS data, we would like to point out that the INS data presented here were measured in the vicinity of two $\overline{\Gamma X}$ wave vectors that are shown by dashed arrows in Fig. 2.4: The magnetic ordering wave vector of the parent compound $\mathbf{Q}_{\text{AFM}} = (\frac{1}{2}\frac{1}{2}1)_{\text{Fe}_4}$ and its in-plane projection $\mathbf{Q}_{\parallel} = (\frac{1}{2}\frac{1}{2}0)_{\text{Fe}_4}$. Note that the two vectors are equivalent in a tetragonal system modulo the reciprocal lattice vector $\mathbf{G} = \overline{\Gamma\Gamma} = (101)$, because $\mathbf{Q}_{\text{AFM}} - \mathbf{G} = (-\frac{1}{2}\frac{1}{2}0)_{\text{Fe}_4} \simeq (\frac{1}{2}\frac{1}{2}0)_{\text{Fe}_4}$. This equivalency is obliterated, however, by the magnetic order in the orthorhombic phase that selects \mathbf{Q}_{AFM} as the preferred SDW vector. It is difficult to understand the out-of-plane component of this SDW ordering wave vector in a simple (geometric) nesting picture because of the equal nesting conditions at \mathbf{Q}_{AFM} and \mathbf{Q}_{\parallel} , imposed by the $4_2/m$ screw symmetry. But as we will subsequently show that a more rigorous calculation of the Lindhard function, taking into account the orbital matrix elements, is sufficient to resolve this dilemma.

The crystal symmetry axes are shown in Fig. 2.4 by dash-dotted lines. In particular, the $4_2/m$ screw symmetry along the XPX axis appears only in the bct BZ with 2 Fe atoms per primitive cell as a result of folding, but is found neither in the unfolded

BZ corresponding to the Fe-sublattice because of the missing (1 0 1) translation, nor in the magnetic BZ because of the spontaneously broken 4-fold rotational symmetry in the SDW or orthorhombic phases (see Fig. 2.3). The fact that this screw axis is only found in the bct BZ will be especially important for our discussion because of its insensitivity to electronic twinning of the crystal, i.e. the presence of domains with different orientations of the spontaneously symmetry-broken electron states in samples with in-plane anisotropy or under the assumption of electronic nematicity. In contrast, the breaking of the 4-fold rotational symmetry around the $\Gamma\Lambda Z$ axis cannot be directly observed, unless the sample is electronically detwinned, which can be achieved by the application of uniaxial pressure [176]. It is also essential that the $4_2/m$ symmetry axis coincides with the \mathbf{Q} -space location of the spin excitations found in INS experiments, which allows us to compare the magnetic intensities along this direction. These excitations, which constitute the subject of the present study, originate from the nested hole- and electron-like Fermi surfaces [45, 46, 41, 47, 48, 49, 42] and survive even in the overdoped regime [284], i.e. well above the onset of the static SDW order in the phase diagram.

As shown above, these excitations are characteristic of a nearly AFM metal [160] and can be well described within an itinerant framework [47, 284, 162, 174]. At higher energy transfers, the spin excitations exhibit a dispersion that has an anisotropic cross-section within every $L = \text{const}$ plane. This has been evidenced in time-of-flight (TOF) experiments covering odd, even, or half-integer L values [145, 146]. The observed similarity to the magnetic parent compound [116, 144, 159] served as a starting point for the proposed symmetry-broken (“electronic nematic”) ground state. Caution has to be taken, however, since in the structural BZ (Fig. 2.4) the orthogonal $\overline{X}\overline{T}$ and $\overline{X}\overline{Z}$ vectors lying in the $k_x k_y$ plane (which for $L = 0$ correspond to the maximal and minimal spin-wave velocities, respectively) are not equivalent. Indeed, the different shapes of the hole-like barrels that alternate in a checkerboard manner, as seen in ARPES maps at a fixed excitation energy, confirm the significance of this difference. Moreover, electronic band structure calculations within the tetragonal phase yield elliptical in-plane cross-sections of the electron-like Fermi surface sheets around the X point [41], which obviously do not by themselves imply any anisotropy between the (110) and (1 $\overline{1}$ 0) directions, because the ellipse rotates by 90° when shifting to the next X point. Therefore, discussions of the in-plane anisotropy in 122-compounds necessarily require consideration of the full 3D band structure, including the out-of-plane dispersion of the spin response along L . If the observed ellipticity followed the $I4/mmm$ symmetry of the crystal, then the X -centered intensity pattern in the spin susceptibility would be rotated by 90° at odd L with respect to even L values because of the $4_2/m$ screw symmetry, as illustrated in Fig. 4.16 (a). On the contrary, the absence of this symmetry in the spin-excitation spectrum may lead to the same orientation of

the ellipse at all L and to the doubling of the period of intensity modulation along $\left(\frac{1}{2}\frac{1}{2}L\right)_{\text{Fe}_4}$, as shown in Fig. 4.16 (b).

In order to discriminate between these two possibilities, we made a direct comparison of the transverse and longitudinal scans around the $\left(\frac{1}{2}\frac{1}{2}1\right)_{\text{Fe}_4}$ and $\left(-\frac{1}{2}\frac{1}{2}0\right)_{\text{Fe}_4}$ wave vectors, and shows that the excitation spectrum indeed does not fully follow the crystal symmetry, but inherits it only from the magnetically active Fe-sublattice. This consequence of the material's crystallography *per se* does not imply any spontaneously symmetry-broken states in direct space. Moreover, the vanishing L -dependence of the anisotropy ratio indicates that the structural contribution to the ellipticity (originating from the folded Fermi surface geometry) is not detectable within our experimental accuracy.

We start by presenting DFT calculations of the Lindhard function done by A. Yaresko in Abt. Andersen at MPI-FKF [285, 286, 287]

$$\chi_0(\mathbf{Q}, \omega) = -\frac{1}{V} \sum_{\mathbf{k}, n, n'} \frac{f_{n'}(\mathbf{k} + \mathbf{Q}) - f_n(\mathbf{k})}{\varepsilon_{n'}(\mathbf{k} + \mathbf{Q}) - \varepsilon_n(\mathbf{k}) + \omega + i\delta} \times \langle \mathbf{k}, n | \hat{\sigma}_+ e^{-i\mathbf{Q}\cdot\mathbf{r}} | \mathbf{k} + \mathbf{Q}, n' \rangle \langle \mathbf{k} + \mathbf{Q}, n' | \hat{\sigma}_- e^{i\mathbf{Q}\cdot\mathbf{r}} | \mathbf{k}, n \rangle, \quad (4.2)$$

where $\varepsilon_n(\mathbf{k})$ is the energy of the n -th band, $|\mathbf{k}, n\rangle$ is the corresponding wave function, $f_n(\mathbf{k})$ is the Fermi function, and $\hat{\sigma}_\pm$ are Pauli matrices. These calculations were performed starting from the tetragonal non-magnetic state for the experimentally determined atomic positions [38]. The chemical doping was included in the virtual crystal approximation. Further details of the calculations can be found in Ref. [113].

The surface plots of the static susceptibility $\chi_0(\mathbf{Q}, \omega \rightarrow 0)$ in the undoped BaFe_2As_2 , 10% Co-doped (electron-overdoped), and 40% K-doped (optimally hole-doped) compounds are shown in Fig. 4.17 for $L = 0$ and $L = 1$ together with the respective profiles along high-symmetry directions. Already in the parent compound, despite the commensurability of the nesting, a significant in-plane anisotropy of the AFM peak is observed both in the real and imaginary parts of χ_0 , preserving its transverse elongation at all L . This clearly indicates that the $4_2/m$ screw symmetry is not to be expected in the spin-fluctuation spectrum. In other words, our calculations are consistent with the lowered symmetry of the spin response that corresponds to the unfolded BZ of the Fe-sublattice, as sketched in Fig. 4.16 (b). It should be emphasized that the asymmetry of the calculated Lindhard function along the $X\Gamma$ and XZ lines appears only if the matrix elements of the perturbation are properly taken into account in Eq. 4.2. If the matrix elements are neglected, $\chi_0(\mathbf{Q})$ becomes four-fold symmetric with respect to the rotation around the $\left(\frac{1}{2}\frac{1}{2}L\right)_{\text{Fe}_4}$ axis.

The stronger response along the transverse direction is present at all L values, resulting in an almost vanishing L -dependence, except for the weak intensity modulation that is best seen in Fig. 4.17 (c). Due to this modulation, $\text{Re}\chi_0(\mathbf{Q}, \omega)$ — the function

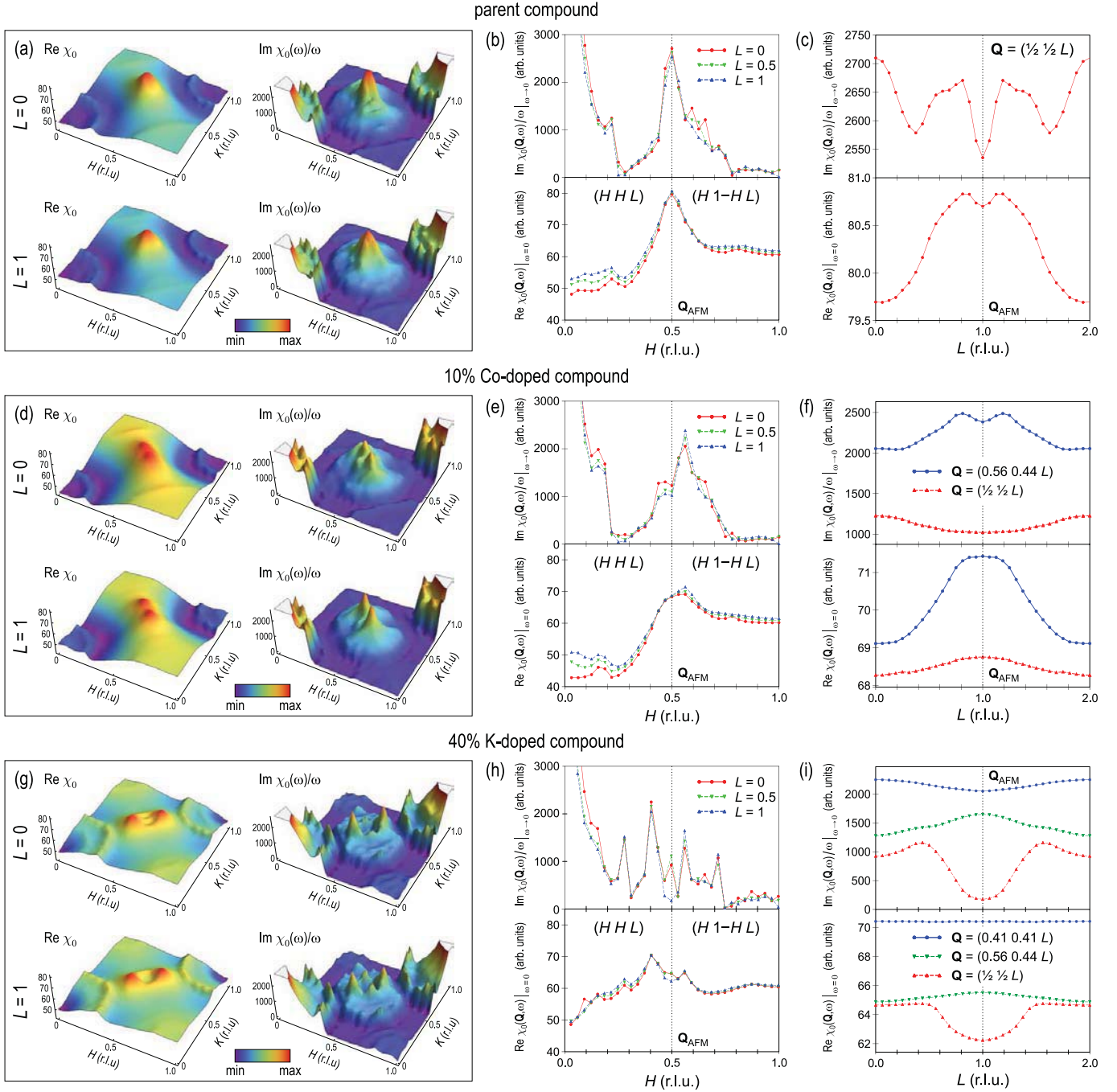


Figure 4.17: The Lindhard function $\chi_0(\mathbf{Q}, \omega)$, resulting from DFT calculations in the undoped (top), 10% Co-doped (electron-overdoped, middle), and 40% K-doped (optimally hole-doped, bottom) BaFe_2As_2 compounds. (a, d, g) Surface plots of the real (left) and imaginary (right) parts of the Lindhard susceptibility within the $L = 0$ and $L = 1$ planes. (b, e, h) Respective profiles of $\chi_0(\mathbf{Q}, \omega)$ along the high-symmetry directions, plotted at $L = 0, 1/2$, and 1 . (c, f, i) L -dependence of $\chi_0(\mathbf{Q}, \omega)$ along the $\left(\frac{1}{2} \frac{1}{2} L\right)_{\text{Fe}_4}$ symmetry axis and at the incommensurate peak positions (for doped compounds only).

that is responsible for the SDW instability—is $\sim 1.4\%$ larger at $L = 1$ than at $L = 0$ in undoped BaFe_2As_2 , which is sufficient to explain the out-of-plane component of the 3D AFM ordering wave vector $\left(\frac{1}{2}\frac{1}{2}1\right)_{\text{Fe}_4}$ that otherwise cannot be understood using simple geometrical nesting considerations.

As the system is doped by either electrons [Fig. 4.17 (d–f)] or holes [Fig. 4.17 (g–i)], the in-plane anisotropy of the $\left(\frac{1}{2}\frac{1}{2}L\right)_{\text{Fe}_4}$ peak and, consequently, the absence of the $4_2/m$ symmetry become even more apparent. The nesting peaks in the Lindhard function develop an incommensurability along the directions transverse or longitudinal to \mathbf{Q} , respectively, which becomes well resolved only at sufficiently high doping levels. In the Co-doped compounds below or at the optimal doping, where most of the available INS experiments were performed, the incommensurability only leads to an additional broadening of the peak in the transverse direction, and to an increase in the anisotropy ratio as compared to the undoped compound.

The L -dependence of $\text{Re}\chi_0$ at the wave vector $\left(\frac{1}{2}\frac{1}{2}L\right)_{\text{Fe}_4}$ corresponding to stripe-like AFM correlations in the ab plane is strongly affected by doping. In undoped BaFe_2As_2 , the maximum of $\text{Re}\chi_0$ is found close to $L=1$, indicating that AFM correlations between Fe layers are favorable [Fig. 4.17 (c)]. Electron doping suppresses the variation of the susceptibility along the $\left(\frac{1}{2}\frac{1}{2}L\right)_{\text{Fe}_4}$ line. Figure 4.17 (f) shows, however, that the L -dependence at the maximum of $\text{Re}\chi_0$, i.e., along the $(0.56, 0.44, L)$ line, becomes more pronounced. Hole doping [Fig. 4.17 (i)] leads to even stronger suppression of spin correlations with \mathbf{Q}_{AFM} so that $\text{Re}\chi_0$ at $\left(\frac{1}{2}\frac{1}{2}1\right)_{\text{Fe}_4}$ becomes lower than at $\left(\frac{1}{2}\frac{1}{2}0\right)_{\text{Fe}_4}$. The L dependence at the maximum of $\text{Re}\chi_0$ at $\mathbf{Q} = (0.41, 0.41, L)$ is negligible, and only at the local maximum $\mathbf{Q} = (0.56, 0.44, L)$, AFM correlations between the layers are still preferable.

In order to go beyond the bare spin susceptibility and account for electronic interactions, we apply the random phase approximation (RPA) to the 3D tight-binding (TB) model done by Dr. S. Graser in University of Augsburg introduced in Ref. [288], which effectively parameterizes the unfolded DFT band structure calculated for the experimental atomic positions [38]. Here the Lindhard function is calculated from the multiorbital susceptibility [289, 288]

$$(\chi_0)_{st}^{pq}(\mathbf{Q}, \omega) = -\frac{1}{N} \sum_{\mathbf{k}, \mu, \nu} \frac{a_\mu^s(\mathbf{k}) a_\mu^{p*}(\mathbf{k}) a_\nu^q(\mathbf{k} + \mathbf{Q}) a_\nu^{t*}(\mathbf{k} + \mathbf{Q})}{\omega + E_\nu(\mathbf{k} + \mathbf{Q}) - E_\mu(\mathbf{k}) + i0^+} \times [f(E_\nu(\mathbf{k} + \mathbf{Q})) - f(E_\mu(\mathbf{k}))], \quad (4.3)$$

where p, q, s and t are orbital indices, μ and ν label the energy dispersion $E_\nu(\mathbf{k})$, and $f(E)$ is the Fermi function. With the summation over all momenta in the first BZ, the full 3D dispersion is taken into account. The underlying symmetry of the crystal (including the orbital composition of the bands) is reflected both in the TB band dispersions $E_\nu(\mathbf{k})$ and in the matrix elements $a_\mu^s(\mathbf{k})$, connecting the band and

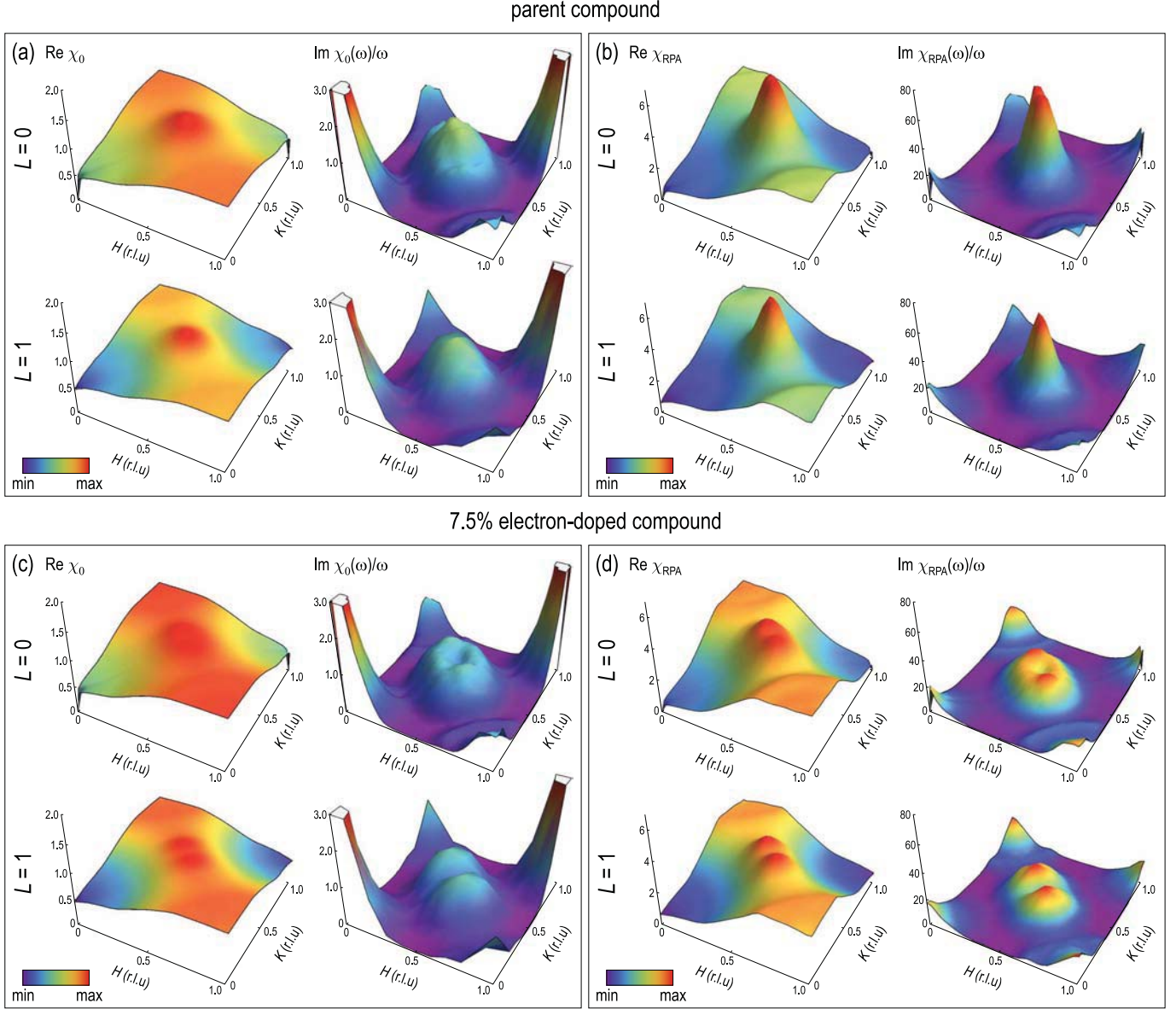


Figure 4.18: Lindhard function (left) and renormalized RPA spin susceptibility (right) in the static limit ($\omega \rightarrow 0$), calculated from a 3D tight-binding model [288]. (a) Lindhard function $\chi_0(H, K, 0)$ and $\chi_0(H, K, 1)$ for the parent (undoped) compound; (b) Corresponding renormalized RPA spin susceptibilities $\chi_{\text{RPA}}(H, K, 0)$ and $\chi_{\text{RPA}}(H, K, 1)$ calculated for $\bar{U} = 0.8$ and $\bar{J} = 0.25\bar{U}$. (c, d) The same for 7.5% electron-doped compound within rigid-band approximation.

orbital spaces [289]. Since there are indications that electronic correlations in the iron arsenide systems are moderate, as compared to the high- T_c cuprates [290], we have included the Coulomb repulsion U and the exchange splitting J on the Fe sites in the framework of the RPA. Here the multiorbital susceptibility of the interacting system is given by [289]

$$(\chi_1^{\text{RPA}})_{st}^{pq} = (\chi_0)_{st}^{pq} + (\chi_1^{\text{RPA}})_{uv}^{pq} (\hat{U}_{\text{spin}})_{wz}^{uv} (\chi_0)_{st}^{wz}, \quad (4.4)$$

where \hat{U}_{spin} is the interaction matrix in orbital space as defined in Ref. [288]. In Fig. 4.18, the Lindhard function

$$\chi_0(\mathbf{Q}, \omega) = \frac{1}{2} \sum_{s=t, p=q} (\chi_0)_{st}^{pq}(\mathbf{Q}, \omega) \quad (4.5)$$

and the total RPA spin susceptibility

$$\chi_{\text{RPA}}(\mathbf{Q}, \omega) = \frac{1}{2} \sum_{s=t, p=q} (\chi_1^{\text{RPA}})_{st}^{pq}(\mathbf{Q}, \omega), \quad (4.6)$$

calculated for $\bar{U}=0.8$ and $\bar{J} = 0.25\bar{U}$, are shown in the static limit within $\mathbf{Q} = (HK0)$ and $\mathbf{Q} = (HK1)$ planes both for the electron-compensated parent compound and for the 7.5% electron doping that results from a rigid-band shift of the TB bands by 33.5 meV. The Lindhard functions presented here are not strictly equivalent to those in Fig. 4.17, as they are derived from independent DFT band structures and are calculated from a TB fit to the unfolded electronic bands, whereas those in Fig. 4.17 originate directly from DFT calculations performed in the backfolded (bct) unit cell. This results in subtle differences, such as a sharper nesting peak in Fig. 4.17, that are not essential for the purpose of the present discussion. We also note that in contrast to Ref. [288], we have determined the doping level from the electron count within the tight-binding model to ensure internal consistency. The notation in Fig. 4.18 corresponds to the backfolded tetragonal BZ and therefore also differs from that of Ref. [288]. The RPA approach allows for a qualitative analysis of the \mathbf{Q} -dependence of the measured susceptibility and correctly reproduces the location of the signal in the phase space and its anisotropy. For a quantitative comparison approximations going beyond a standard RPA with momentum-independent interactions might be necessary.

At both doping levels, the dominant feature in χ_{RPA} is located around the \mathbf{Q}_{AFM} wave vector, originating from the nesting of hole- and electron-like Fermi surface sheets. Its maximum appears at a nearly commensurate position in the parent compound, but the incommensurability increases drastically upon doping as a natural consequence of the rigid-band approximation. This is at variance with experiments that found a commensurate spin response in a wide range of electron doping levels [160, 284]. This lack of correspondence indicates that the rigid-band approximation cannot fully account for the doping effects in iron arsenides, as suggested earlier in several theoretical works [41, 291].

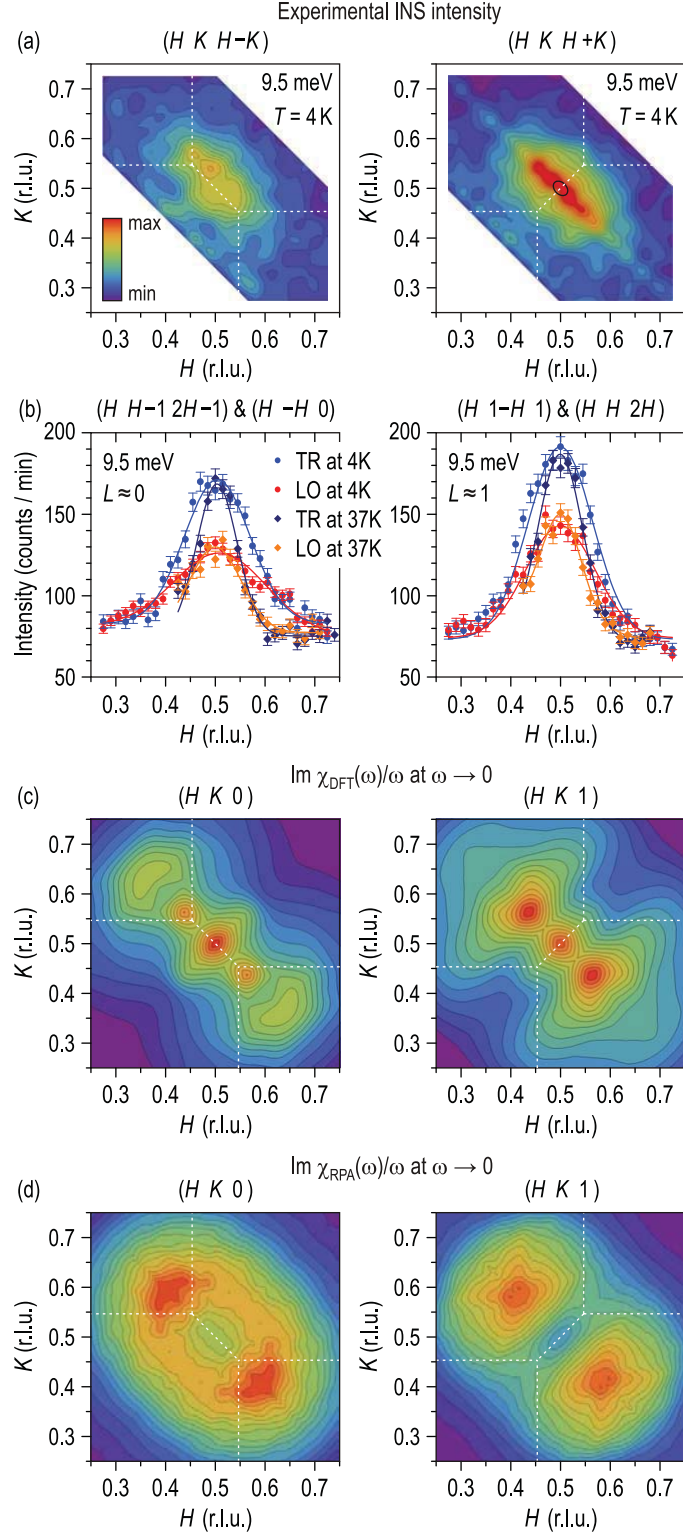


Figure 4.19: (a) Experimental intensity distributions for $\text{BaFe}_{1.85}\text{Co}_{0.15}\text{As}_2$ near \mathbf{Q}_{\parallel} (left) and \mathbf{Q}_{AFM} (right), measured in the $(HK [H+K])$ scattering plane in the SC state ($T = 4\text{ K}$) at the resonance energy (9.5 meV). The small black ellipse around $(\frac{1}{2} \frac{1}{2} 1)_{\text{Fe}_4}$ is a 9.5 meV cross-section of the spin wave dispersion for the CaFe_2As_2 parent compound [116, 144], shown for comparison. The white dotted lines are BZ boundaries. (b) Comparison of the longitudinal (LO) and transverse (TR) cross-sections of the data from panel (a) around $L = 0$ (left) and $L = 1$ (right). (c) The Lindhard function $\text{Im}\chi_{\text{DFT}}(\omega)/\omega$ at 7.5% Co-doping, calculated by DFT in the same reciprocal space regions. (d) The same for the RPA-renormalized low-energy spin susceptibility $\text{Im}\chi_{\text{RPA}}(\omega)/\omega$ [same as in Fig. 4.18 (d)], calculated from a TB model in the rigid-band approximation.

On the other hand, the symmetry of the magnetic spectrum, as well as the tendency to larger anisotropy with increased doping, are well captured by the TB model. The Lindhard function shows good qualitative agreement with the directly calculated one from DFT calculations. The susceptibility patterns are incommensurate along the transverse direction both at $L = 0$ and $L = 1$, and therefore do not possess the $4_2/m$ symmetry. The RPA renormalization considerably enhances $\text{Im } \chi_0(\mathbf{Q}, \omega)/\omega$ around the nesting vector, whereas the strong peak at the Γ point is considerably suppressed due to a much smaller Stoner factor. As a result, the overall agreement with experimental spectra that consist of a single pronounced feature centered at $\left(\frac{1}{2} \frac{1}{2} L\right)_{\text{Fe}_4}$ is further improved.

In summary, the results of our theoretical calculations indicate that the normal-state spin susceptibility contains all essential ingredients that are necessary to understand the symmetry of the measured INS spectra, both in the normal and SC states, on a qualitative level. These include both the out-of-plane modulation of the Lindhard function, peaked at the \mathbf{Q}_{AFM} wave vector, and the in-plane anisotropy of the nesting-driven peak, which preserves its transverse elongation at all L values. Both effects lead to the absence of the $4_2/m$ screw symmetry in the spin-excitation spectrum.

Turning now to the experimental data, we first present in-plane anisotropy of the measured INS intensity. In Fig. 4.19 (a), we show experimental constant-energy maps, interpolated from a series of triple-axis \mathbf{Q} -scans in the vicinity of $\left(\frac{1}{2} \frac{1}{2} 1\right)_{\text{Fe}_4}$ and $\left(-\frac{1}{2} \frac{1}{2} 0\right)_{\text{Fe}_4}$ wave vectors, measured in the $(HK [H+K])$ scattering plane. We compare them with the calculated dynamic spin susceptibilities of the paramagnetic tetragonal phase, plotted in the equivalent regions of \mathbf{Q} -space surrounding the X points. Panel (c) shows the imaginary part of the Lindhard function $\text{Im } \chi_0(H, K, 0)_{\text{Fe}_4}$ (left) and $\text{Im } \chi_0(H, K, 1)_{\text{Fe}_4}$ (right) in the vicinity of \mathbf{Q}_{\parallel} and \mathbf{Q}_{AFM} , respectively, for 7.5% Co-substitution, as calculated by DFT in the virtual crystal approximation. Panel (d) displays the respective results for the RPA-enhanced susceptibility $\text{Im } \chi_{\text{RPA}}(+q_x, +q_y, 0)$ and $\text{Im } \chi_{\text{RPA}}(+q_x, +q_y, 1)$ [same as in Fig. 4.18 (d)], calculated in the rigid-band approximation from the TB model [288] at 7.5% electron doping. Notably, the transverse elongation of the susceptibility pattern is preserved at all L values [This is the case for Fig. 4.16 (b)] both in the measured INS signal and in the results of both calculations, meaning that the longer axis of the ellipse is oriented either along \overline{XZ} or along $\overline{X\Gamma}$ directions for even and odd L , respectively. This anisotropy is insensitive to the SC transition and persists also in the normal state. Neither the widths of the peaks nor their anisotropy experience any change across T_c within our experimental accuracy, as evidenced by Fig. 4.19 (b).

In comparison to the magnetically ordered parent compound, which exhibits a steep spin wave dispersion cone around \mathbf{Q}_{AFM} , as shown by a small black ellipse in Fig. 4.19 (a), electron doping tends to increase the transverse incommensurability

[cf. Fig. 4.17 (c, d)] and, in addition, leads to softening of spin excitations predominantly in the transverse direction [145]. This results in a rapid increase of the anisotropy ratio with increasing doping. The emerging pattern resembles the “unusual quasi-propagating excitations” observed at higher energies in a similar compound by Li *et al.* [146], as well as the pair of incommensurate peaks seen in $\text{FeTe}_{1-x}\text{Se}_x$ (Refs. [236, 228, 234, 292]). In the light of our present results, the former can be understood as two incommensurate branches of itinerant Stoner-like excitations, driven by Fermi surface nesting, as in the case of iron chalcogenides [228, 234, 293]. The fact that such incommensurability has not been resolved experimentally at low energies is not surprising, because for sufficiently small doping levels at which the overwhelming majority of INS experiments was performed, the two incommensurate peaks merge into one due to their finite width, resulting in a broad commensurate peak elongated in the transverse direction. Similar measurements of strongly overdoped samples are therefore necessary to confirm this scenario and the emerging similarity to the 11-compounds.

In order to quantify the observed in-plane anisotropy and compare it with previous experiments, in Fig. 4.20 we plot the temperature and energy dependence of the measured full width at half maximum (FWHM) of the commensurate inelastic peak along the longitudinal (LO) and transverse (TR) directions for $L = 0$ and $L = 1$. In the longitudinal direction, the resolution-corrected width of the peaks w_{LO} (dashed line) was already quantified for the same sample by a fit to the Moriya formula in Eq. 4.1. To extract the anisotropy ratio $A = (w_{\text{TR}} - w_{\text{LO}})/(w_{\text{TR}} + w_{\text{LO}})$, we have fitted the experimentally measured FWHM of the peaks in the longitudinal (W_{LO}) and transverse (W_{TR}) directions (solid lines in Fig. 4.20) using the following equations:

$$W_{\text{LO}}(\omega, T) = \sqrt{w_{\text{LO}}^2(\omega, T) + R^2}; \quad (4.7)$$

$$W_{\text{TR}}(\omega, T) = \sqrt{\left[\frac{1+A}{1-A} w_{\text{LO}}(\omega, T) \right]^2 + R^2}. \quad (4.8)$$

The fitted value of the effective resolution, $R = 0.066 \pm 0.004$ r.l.u., was used to perform resolution correction of the experimental data and calculate the anisotropy ratio that is presented in panels (c) and (d). By setting the resolution to a constant, we relied on the fact that the calculated instrumental resolution is nearly isotropic and does not vary within our region of interest by more than $\sim 10\%$. The effective momentum-space resolution resulting from our fit (hatched region in Fig. 4.20) is somewhat lower than the calculated instrumental resolution ($R_{\text{min}} \approx 0.04$ r.l.u.). The difference may indicate a finite-size limit on the fluctuating domains imposed by the random distribution of dopant atoms and/or a slight inhomogeneous broadening due to variations of the doping level across the sample. With this reasonable assumption,

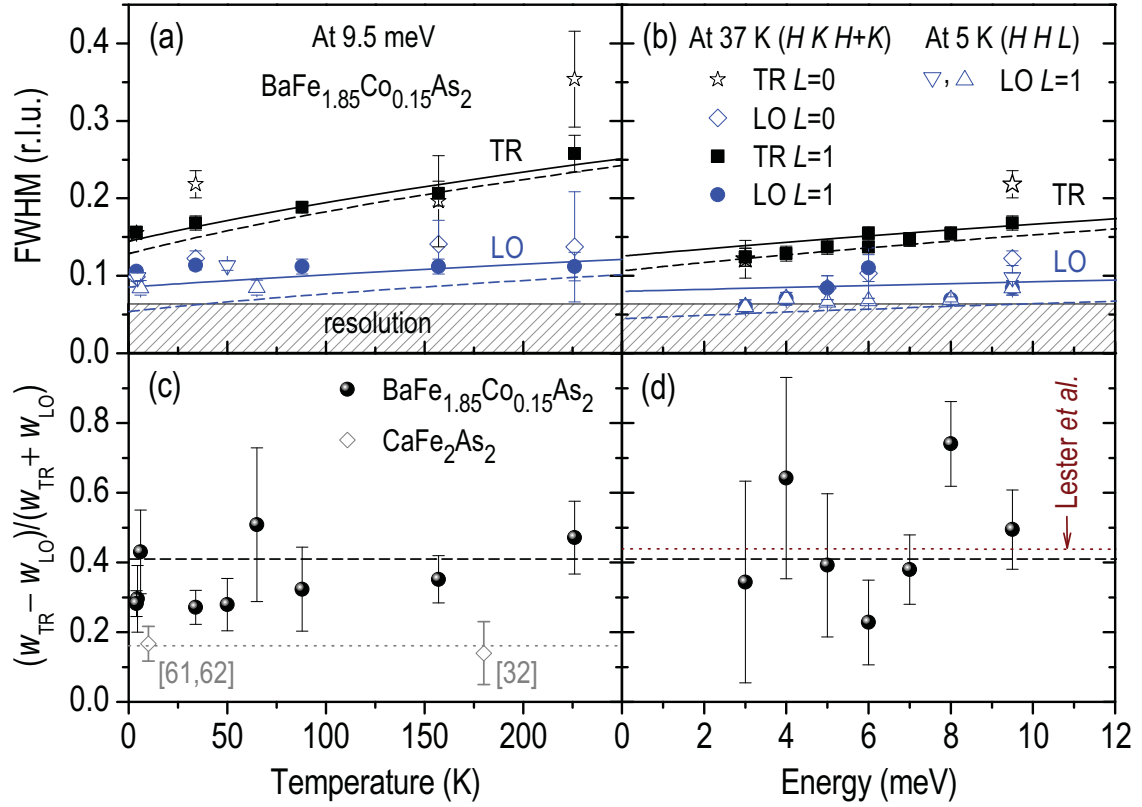


Figure 4.20: (a) Longitudinal (LO) and transverse (TR) widths of the commensurate peaks around Q_{AFM} ($L = 1$) and Q_{\parallel} ($L = 0$) at 9.5 meV versus temperature. (b) The same widths versus energy transfer at low temperatures. Solid lines are results of a global fit to the data in both panels (see text) using Eq. (4.8). Resolution-corrected dependencies are shown by dashed lines. (c) The resolution-corrected anisotropy ratio $A = (w_{\text{TR}} - w_{\text{LO}})/(w_{\text{TR}} + w_{\text{LO}})$ as a function of temperature, compared to the respective values for the magnetically ordered [116, 144] and paramagnetic [159] states of CaFe_2As_2 . (d) The same ratio as a function of energy transfer. The dashed line gives the anisotropy from the global fit. The dotted line is derived from the high-energy dispersion reported for $\text{BaFe}_{1.87}\text{Co}_{0.13}\text{As}_2$ in Ref. [145].

the entire data set can be described by a single, temperature- and energy-independent anisotropy parameter. A similar fit based on the instrumental resolution alone (without finite-size or inhomogeneous broadening) would yield an anisotropy parameter that increases with temperature, which would be highly unusual.

The anisotropy ratio $A = 0.41 \pm 0.02$ that results from the global fit to our data is shown in Fig. 4.20 (c) and (d) by the dashed line. This value corresponds to the aspect ratio $w_{\text{TR}}/w_{\text{LO}} = 2.4 \pm 0.1$, which is nearly a factor of 2 larger than the respective ratio of spin wave velocities (~ 1.4) in the undoped CaFe_2As_2 , according to Refs. [116] and [144]. The dotted line in Fig. 4.20 (c) shows that the anisotropy ratio remains nearly constant across the SDW transition, as estimated from the paramagnetic-state data measured at $T = 180$ K by Diallo *et al* [159]. On the other hand, the anisotropy ratio of 0.44 extracted from the high-energy TOF data on a similarly doped

BaFe_{1.87}Co_{0.13}As₂ compound [145] [dotted line in Fig. 4.20 (d)] perfectly coincides with our value. This agreement confirms the energy independence of the anisotropy and indicates that the difference in the peak widths originates mainly from two unresolved incommensurate peaks, in agreement with our DFT calculations, rather than from an anisotropic broadening caused by the finite correlation lengths of the spin excitations [146, 159]. Despite the present lack of \mathbf{Q} -resolved INS data on hole-doped compounds, the results of our DFT susceptibility calculations allow us to predict that the anisotropy of the spin-excitation spectrum should vanish and subsequently switch to the longitudinal orientation as the system is doped with more holes.

As we have demonstrated, the elliptical shape of the spin excitations within the $L = \text{const}$ planes shows no measurable L -dependence (apart from an intensity modulation) and is insensitive to the SC transition. Therefore, the origins of this anisotropy are to be found in the properties of the normal (paramagnetic) state. An anisotropic spin correlation length that is larger in the direction parallel to the AFM propagation vector than in the transverse (ferromagnetic) direction has been proposed as a possible explanation [146, 159]. Although such description is successful in the low-energy region, where the two spin wave branches are not resolved, it clearly fails to describe the anisotropic spin wave velocities that become evident at higher energies in the paramagnetic state [145, 146], mimicking the behavior of the parent compounds [144]. This implies that the larger momentum width of the spectrum in the transverse direction is more likely to be a result either of two unresolved spin-wave branches that are less steep than the longitudinal ones, or of the incommensurability of the nesting peaks at $\omega = 0$. The results of our DFT calculations support the incommensurate nesting scenario, similar to that inferred earlier from nuclear-magnetic-resonance measurements [136] and to the one proposed for the iron chalcogenide [228, 234, 293]. In such a case, the anisotropy results from Fermi surface nesting, and not from an “electronic liquid-crystal state” that arises spontaneously from electron-electron interactions [145, 175, 174, 176]. The latter state has been invoked for the cuprates based in part on the strong temperature dependence of the in-plane anisotropy of the spin excitations [170], which is not observed in the 122-iron-arsenide system (Fig. 4.20). If our prediction of the rotated (longitudinally elongated) susceptibility profile in the hole-doped compounds were confirmed experimentally, it would provide additional support for this scenario. Indeed, recently, in the optimally doped BKFA compounds, longitudinally elongated spin-excitations have been observed by INS, in perfect agreement with our DFT calculations [240]. Figure 4.21 shows in-plane cross-sections of magnetic excitations in 122-ferropnictides for various dopants and doping levels [147, 240]. Panel (a) in Fig. 4.21 is the vertically elongated spin-excitation spectrum in the optimally electron-doped BFCA compound, (b) and (c) are nearly isotropic shape of in-plane magnetic excitation in Ba(Fe_{1.88}Mn_{0.12})₂As₂ and the parent

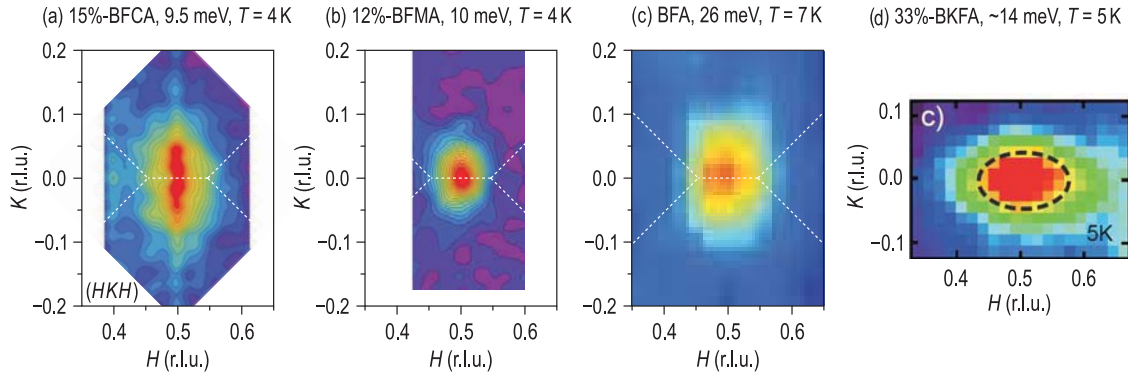


Figure 4.21: In-plane cross-sections for magnetic excitations in various doping level 122-ferropnictide: (a) Optimally electron-doped BFCA compound measured at 9.5 meV and 4 K. (b) 12%-Mn doped BFA compound (no superconductivity) measured at 10 meV and 4 K. (c) The parent BFA compound measured at 26 meV and 7 K [147]. (d) Optimally hole-doped BKFA compound measured at 14 meV and 5 K [240]. Vertically elongated magnetic-excitation profiles in the electron-doped regime gradually shrinks when approaching to the parent compound, where the in-plane cross-section is nearly isotropic. In optimally hole-doped regime, the elongated axis of spin excitations turns to the horizontal direction which is perfect agreement with our LDA calculations in Sec. 4.2.3.

BFA compounds, respectively. Panel (d) in Fig. 4.21 displays 90° rotated anisotropic cross-sections observed in the optimally hole-doped BKFA compound [240]. Although measured energies are not identical each other, we have already shown that the anisotropy ratio is nearly energy and temperature independent (see Fig.4.20) which justifies such comparison. In addition, the independent INS work revealed that 100% K-doped BFA compound, KFe_2As_2 , shows more dramatic elongation, ultimately leading incommensurate peaks along longitudinal direction [294]. Such agreement between DFT calculations and experimental data sharply opposes the nematic scenario, as any symmetry breaking of magnetic origin would be expected to behave similarly on both sides of the phase diagram in systems with equivalent magnetic structures.

As we have demonstrated, the spin-fluctuation spectrum possesses considerable anisotropy and does not fully follow the crystallographic symmetry even in the normal (paramagnetic and tetragonal) state, when no electronic nematicity is assumed. Therefore, the observed in-plane anisotropy in the doped compounds does not necessarily imply a symmetry-broken ground state, but has a more trivial structural origin. As the primitive structural unit cell of the 122-compounds contains two Fe atoms, its size is twice larger, as compared to that of the Fe-sublattice. Because the magnetic INS signal originates predominantly from the latter, with no magnetic moment being induced on the As sites [282, 283], the symmetry of the spectrum is determined by the unfolded BZ. In the real bct BZ, both the electronic bands and the spin susceptibility are folded, but the matrix elements that are responsible for the intensities of the primary features

and their replica (an analog of the dynamic structure factors) are such that no abrupt change in the magnetic spectrum can be seen as long as the folding potential remains sufficiently weak.

The periodic modulation of the magnetic spectral weight with L (see Fig. 4.11 and 4.12) can also be explained by the L -dependence of the spin susceptibility observed in our normal-state DFT calculations. Although the variation of the Lindhard function between $L = 0$ and $L = 1$ is weak in the parent compound, it can possibly be enhanced by the Stoner-like renormalization effects to an amplitude comparable with experimental observations. The maximum of $\text{Re } \chi_0(\mathbf{Q}, 0)$ in the parent compound occurs at $\mathbf{Q}_{\text{AFM}} = \left(\frac{1}{2} \frac{1}{2} 1\right)_{\text{Fe}_4}$ and thus determines the AFM ordering wave vector. In the SDW state, excitations at even L correspond to zone-boundary magnons which, due to a combination of intra- and interlayer coupling parameters, have a substantial gap of ~ 80 meV [141, 140, 122, 116, 144]. In contrast, at high doping levels the magnetic response is virtually L -independent [223]. Two mechanisms are likely to provide the connection between these two limiting cases: First, when approaching the magnetically ordered state from higher doping levels, the paramagnon mode softens at \mathbf{Q}_{AFM} , and the in-plane magnetic correlation length increases [295]. As a consequence, one can expect the out-of-plane magnetic correlations to become more efficient in stabilizing the mode and its gapped response at even L . Second, when starting from the ordered state, the increasing damping of the mode with doping will progressively redistribute spectral weight towards lower energies, including the gapped region around even L [229]. At our intermediate doping levels we thus observe a moderate L -modulation in the normal state [Figs. 4.11 and 4.14 (a)].

Starting from the paramagnetic state, one sees that the similarity of excitation spectra in the magnetically ordered and normal states does not imply that the anisotropy of the SDW state survives above the structural transition in the form of “spin nematic correlations”. On the contrary, the symmetry-breaking L -modulation is present in the tetragonal phase for reasons not related to magnetic ordering, whereas the SDW instability that occurs on top of the paramagnetic state upon cooling or decreasing the doping is predetermined by this modulation, so that the AFM propagation vector coincides with the strongest nesting-driven peak in $\text{Re } \chi_0(\mathbf{Q}, 0)$. An electronic nematic state also appears implausible in view of the temperature independence of the in-plane anisotropy (Fig. 4.20), which is in sharp contrast to the strongly temperature dependent, order-parameter-like behavior observed in $\text{YBa}_2\text{Cu}_3\text{O}_{6+y}$ (Ref. [170]). Our conclusions about the nonmagnetic origin of the missing symmetry are additionally supported by the following evidence: (i) experimentally observed enhancement of the anisotropy in the doped compound with respect to a magnetically ordered parent, which agrees with the increased transverse incommensurability seen in the DFT calculations; (ii) temperature-independence of the anisotropy even in the parent compound,

including its insensitivity to the presence of static AFM order. Independently of its origins, the symmetry of the normal-state spin-fluctuation spectrum may have important implications for the SC order parameter under the assumption of spin-fluctuation-driven superconductivity. It was argued, for example, that the transverse elongation of the spin-fluctuation profile stabilizes the s_{\pm} pairing state [296].

4.3 Superconducting $\text{Rb}_{0.8}\text{Fe}_{1.6}\text{Se}_2$ compound

So far, our discussion was focused on the iron-arsenide superconductors. In this section, we present the latest INS study on newly discovered arsenic-free iron-selenide superconductors $A_2\text{Fe}_4\text{Se}_5$ ($A = \text{K}, \text{Rb}, \text{Cs}$), also known as 245-compounds. Soon after the discovery of 245-FeSC [34, 35, 36], their unprecedented physical properties came to light, such as the coexistence of high- T_c superconductivity with strong antiferromagnetism [297, 298, 299]. The pairing mechanism and the symmetry of the superconducting (SC) order parameter in this family of compounds still remain among the major open questions. In the majority of other FeSC, it is widely accepted that the strong nesting between the hole-like Fermi surface at the Brillouin zone (BZ) center and electron-like Fermi surface at the BZ boundary leads to the sign-changing s -wave (s_{\pm} -wave) pairing symmetry, as we have constantly discussed through this thesis. This scenario has been supported by different experimental methods, such as ARPES, quasi-particle interference [194], and INS. On the other hand, recent theoretical calculations [300, 301, 302] and ARPES experiments [303, 304, 305, 306] on the 245-system revealed the absence of hole-like Fermi surface at the BZ center in the electronic structure, implying that the nesting between the hole- and electron-like Fermi surface sheets is no longer present. Hence, several theoretical studies proposed alternative pairing instabilities, such as d -wave or another type of s_{\pm} -wave symmetry with sign-changing order parameter between bonding and anti-bonding states [307, 308, 309, 310, 311]. As a hallmark of sign-changing SC order parameter, several authors theoretically predicted a resonant mode in the magnetic excitation spectrum below the SC transition, yet its precise position in momentum space still remains controversial [307, 308, 309].

A major complication in treating the 245-compounds theoretically arises from the presence of a crystallographic superstructure of Fe vacancies that has been consistently reported both from x-ray and neutron diffraction experiments [312, 313]. This $\sqrt{5} \times \sqrt{5}$ superstructure is closely related to the static antiferromagnetic (AFM) order persisting up to the Néel temperature, $T_N \approx 540 \text{ K}$ [314, 315]. Although most of the existing band structure calculations have so far neglected the superstructure, several others have pointed out that it may have a strong influence on the Fermi surface shape [316, 317, 318, 319]. However, these pronounced Fermi surface reconstruction

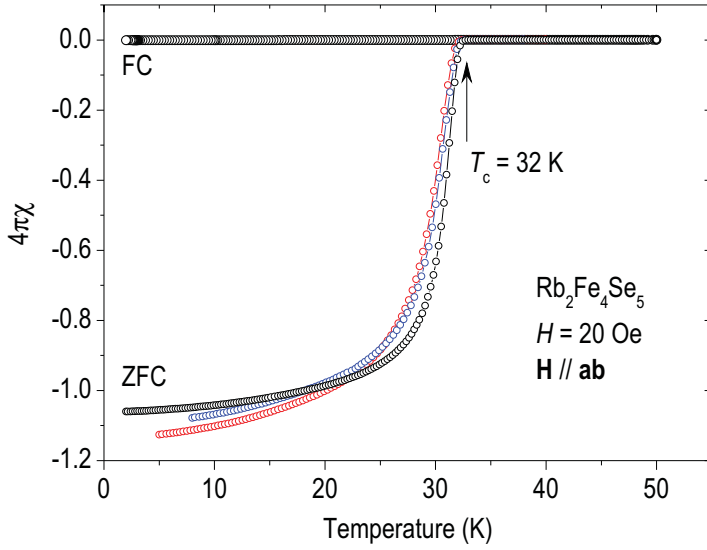


Figure 4.22: The dc magnetic susceptibility measurements on three representative single-crystalline $\text{Rb}_{0.8}\text{Fe}_{1.6}\text{Se}_2$ samples from the same batch. A sharp diamagnetic response is observed in the ZFC measurement right below 32 K, indicating $\sim 100\%$ exclusion of the external magnetic field.

effects have not been experimentally confirmed so far [299, 303, 304, 305, 306]. Such an uncertainty in the Fermi surface geometry and its nesting properties makes it hard to predict the exact location of itinerant spin fluctuations in reciprocal space. Moreover, band structure calculations in the vacancy-ordered magnetic state result in insulating solutions for the stoichiometric 245-compound [316, 317, 318, 319]. A possible way to reconcile these apparently contradictory observations is to assume a nanoscale phase separation of (i) insulating vacancy-ordered magnetic domains and (ii) metallic non-magnetic phase domains with effective electron doping that could host superconductivity at low temperature. Such kind of electronic phase segregation, resembling the situation in hole-doped 122-pnictides [94], found recent support from ARPES [299], scanning nano-focus single-crystal x-ray diffraction imaging [320], scanning-tunneling microscopy [321], optical spectroscopy [252], and NMR [322] experiments. Here we provide experimental insight by using INS to directly probe the elementary magnetic excitations in superconducting $\text{Rb}_{0.8}\text{Fe}_{1.6}\text{Se}_2$ (RFS).

In the following, some of the figures and text are reproduced from Ref. [243, 244].

4.3.1 Sample characterization

For the present study, we used a mosaic of RFS single crystals with a total mass of ~ 1 g, grown by the Bridgman method [245]. The nearly stoichiometric and homogeneous composition with $\text{Rb}:\text{Fe}:\text{Se} = 0.796:1.596:2.000$ (1.99:3.99:5) has been determined by wave-length dispersive x-ray electron-probe microanalysis using a *Camebax SX50* analyzer with an accuracy of 0.5% for Fe and up to 1% for Se. The SC properties of the sample were characterized by magnetometry, where $\sim 100\%$ flux exclusion was observed in the zero-field-cooled (ZFC) measurement for temperatures up to $T_c = 32$ K [Fig. 4.22 (a)]. The INS experiment was performed at the thermal-neutron

triple-axis spectrometer IN8 (ILL, Grenoble), with the sample mosaic mounted in the $(HH0)/(00L)$ or $(H00)/(00L)$ scattering planes. The wave vectors $\mathbf{Q} = (0.5 \ 0.5 \ L)_{\text{Fe}_1}$ and $(0.5 \ 0 \ L)_{\text{Fe}_1}$ were directly accessible in our scattering planes, and the spectrometer further allowed us to tilt the sample in order to access \mathbf{Q} -vectors in a certain range out of the scattering planes. Here and henceforth, we are using unfolded reciprocal-space notation corresponding to the Fe sublattice, which we denote as Fe_1 , because of its simplicity and the natural correspondence to the symmetry of the observed signal [50]. We quote the wave vector $\mathbf{Q} = (HKL)$ in reciprocal-lattice units (r.l.u.), i.e. in units of the reciprocal-lattice vectors \mathbf{a}^* , \mathbf{b}^* , \mathbf{c}^* of the Fe sublattice ($a^* = 2\pi/a$, etc.). Here $a = b = 2.76 \text{ \AA}$ is the room-temperature distance between the nearest-neighbor Fe atoms, and $c = 7.25 \text{ \AA}$ is the distance between Fe layers. All INS measurements were done in the fixed- k_f ($k_f = 2.662 \text{ \AA}^{-1}$) mode, using double-focused PG(002) monochromator and analyzer. A 5 cm thick oriented PG filter was installed before the analyzer to eliminate higher-order neutron contamination, and no collimation was applied, thereby maximizing the intensity.

4.3.2 $\sqrt{5} \times \sqrt{5}$ magnetic order

We start with the magnetic Bragg peak patterns arising from the $\sqrt{5} \times \sqrt{5}$ Fe-vacancy superstructure. Panel (a) in Fig. 4.23 is a sketch of magnetic and nuclear superstructure Bragg reflections, projected on to the two-dimensional $\mathbf{Q}_{\parallel} = (H \ K)$ plane. Black dots and the large dashed rectangle correspond to the center and boundaries of the unfolded Fe_1 BZ, respectively. The solid dots represent magnetic Bragg reflections from two twin domains, and the corresponding dashed lines, rotated clockwise and counterclockwise with respect to the Fe_1 BZ, are magnetic zone boundaries of the two twin domains. Forbidden magnetic Bragg peaks, which coincide with the nuclear Fe-vacancy superstructure reflections seen by x-ray diffraction [312, 313], are shown by empty circles. Figure 4.23 (b) shows elastic scans crossing two magnetic Bragg peaks at $(0.7 \pm 0.1 \ 0.5)_{\text{Fe}_1}$, as shown by the arrow in panel (a), and along equivalent reciprocal-space directions in higher BZs. Note that the two magnetic Bragg peaks at $K = \pm 0.1$ originate from different twin domains, so that their similar intensity indicates almost equal population of both twins in our sample. The magnetic Bragg peak intensity decreases more rapidly when moving to a higher BZ along the out-of-plane direction than in-plane, indicating that the magnetic moment is oriented predominantly along the L -direction in this system. This is consistent with the reported spin configuration in the magnetically ordered phase, in which spins are alternatively pointing up and down along the c -axis [324]. Figure 4.23 (c) shows inelastic magnetic intensity in the vicinity of the AFM ordering wave vector $\mathbf{Q} = (1.3 \ 0.1 \ 0.5)_{\text{Fe}_1}$ at 11.5 meV, measured at low temperature, $T = 1.5 \text{ K}$. The intense spin-wave peak is consistent with recent

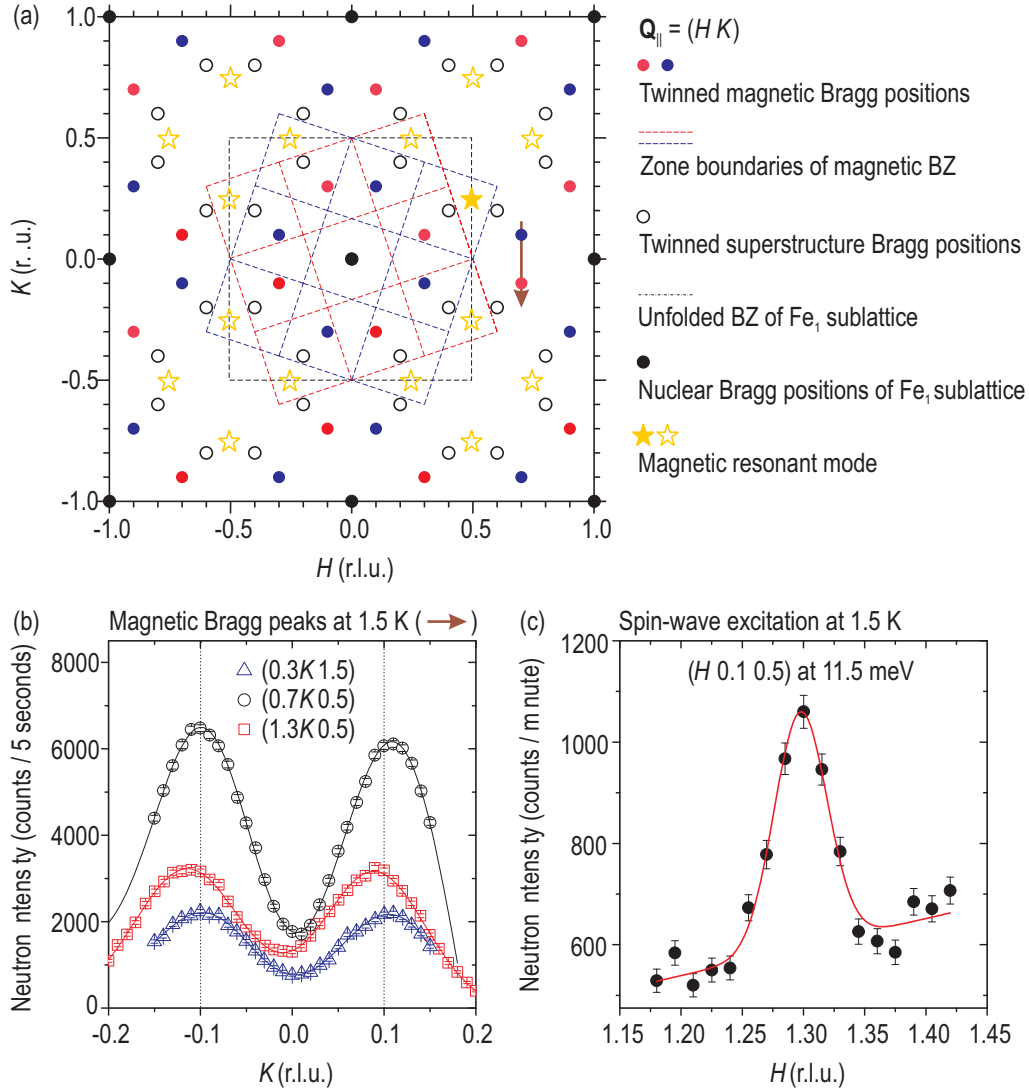


Figure 4.23: (a) The in-plane projection of twinned magnetic and nuclear Bragg peak positions arising from the $\sqrt{5} \times \sqrt{5}$ Fe-vacancy superstructure. The two sets of dots and the corresponding dashed lines (red and blue) denote magnetic superstructure Bragg reflections and the magnetic BZ boundaries for the right and left twin domains, respectively. Black dotted lines represent the Fe₁ unfolded BZ boundary. The arrow shows the trajectory of elastic momentum scans. (b) Elastic scans along the K direction [arrow in panel (a) and equivalent scans] measured at 1.5 K. The almost identical neutron intensities of two symmetric magnetic Bragg peaks indicate the nearly equal population of the two twin domains in the sample. (c) INS intensity at 11.5 meV in the vicinity of the magnetic ordering wave vector $(1.3\ 0.1\ 0.5)_{\text{Fe}_1}$. The intense spin-wave excitation peak is consistent with recent time-of-flight INS measurements on an insulating $\text{Rb}_{2+\delta}\text{Fe}_4\text{Se}_5$ compound [323].

time-of-flight INS measurements on an insulating $\text{Rb}_{2+\delta}\text{Fe}_4\text{Se}_5$ compound [323].

4.3.3 Magnetic resonance mode

Now we turn to the INS measurements across T_c near a few candidate \mathbf{Q} -vectors, where the magnetic resonant mode could be expected. Figure 4.24, (a) and (b), displays raw energy-scan spectra recorded above and below T_c at $\mathbf{Q} = (0.5 \ 0.3125 \ 0.5)_{\text{Fe}_1}$, where the resonance has been theoretically predicted [307], and at $(0.5 \ 0 \ 0.5)_{\text{Fe}_1}$, where it is usually found in other FeSC (see the previous section). In the absence of any resonant enhancement, the intensity is expected to be higher in the normal state due to the influence of the Bose factor at low energies. Already in the raw data, one can see that this is the case for all data points except a narrow energy region around 14 meV at $\mathbf{Q} = (0.5 \ 0.3125 \ 0.5)_{\text{Fe}_1}$.

To emphasize this effect and to eliminate the energy-dependent background, we plot temperature differences of the same data sets in Figs. 4.24 (c) and (d). Also shown are the difference spectra for $\mathbf{Q} = (0.5 \ 0.5 \ 0.5)_{\text{Fe}_1}$, $(0.5 \ 0.25 \ 0.5)_{\text{Fe}_1}$, and $(0.5 \ 0 \ 0)_{\text{Fe}_1}$. As seen in Fig. 4.24 (c), a prominent peak (shaded region) is found at $\hbar\omega_{\text{res}} \approx 14$ meV for $\mathbf{Q} = (0.5 \ 0.3125 \ 0.5)_{\text{Fe}_1}$ and $\mathbf{Q} = (0.5 \ 0.25 \ 0.5)_{\text{Fe}_1}$, which we attribute to the magnetic resonant mode. However, no such peak is observed at $\mathbf{Q} = (0.5 \ 0.5 \ 0.5)_{\text{Fe}_1}$, in contrast to some alternative predictions based on the d -wave pairing symmetry [307, 308, 309]. Figure 4.24 (d) also demonstrates the absence of any resonant mode at $\mathbf{Q} = (0.5 \ 0 \ 0.5)_{\text{Fe}_1}$ and $(0.5 \ 0 \ 0)_{\text{Fe}_1}$, where it is usually found in iron pnictides. At these wave vectors, the data simply follow the solid line, which is the Bose-factor difference between 1.5 K and 35 K.

To verify whether the observed redistribution of spectral weight at low temperatures is related to the SC transition, we have measured the temperature dependence of the resonance intensity at $\mathbf{Q} = (0.5 \ 0.3125 \ 0.5)_{\text{Fe}_1}$, which is shown in Fig. 4.25 (a). Indeed, an order-parameter-like increase of intensity below T_c is found, which is accepted as the hallmark of the magnetic resonant mode.

To pin down the exact location of the resonance in \mathbf{Q} -space, we have measured momentum scans along the BZ boundary at both temperatures. Their difference is presented in Fig. 4.25 (b) and suggests a maximum at the commensurate nesting wave vector $\mathbf{Q}_{\text{res}} = (0.5 \ 0.25 \ 0.5)_{\text{Fe}_1}$ shown by the star symbols in Fig. 4.23 (a), close to the predicted resonance position, $\mathbf{Q} = (0.5 \ 0.3125 \ 0.5)_{\text{Fe}_1}$ [307]. Yet, the disagreement is small compared to the \mathbf{Q} width of the peak, which explains the similar INS response at both \mathbf{Q} -vectors, as seen from Fig. 4.24 (c). Because the position of the nesting vector is strongly doping dependent, and the calculations in Ref. [307] were done for the arbitrary doping of 0.1 electrons per Fe, a quantitative agreement with our results is not expected. The observed wave vector suggests an even higher level of

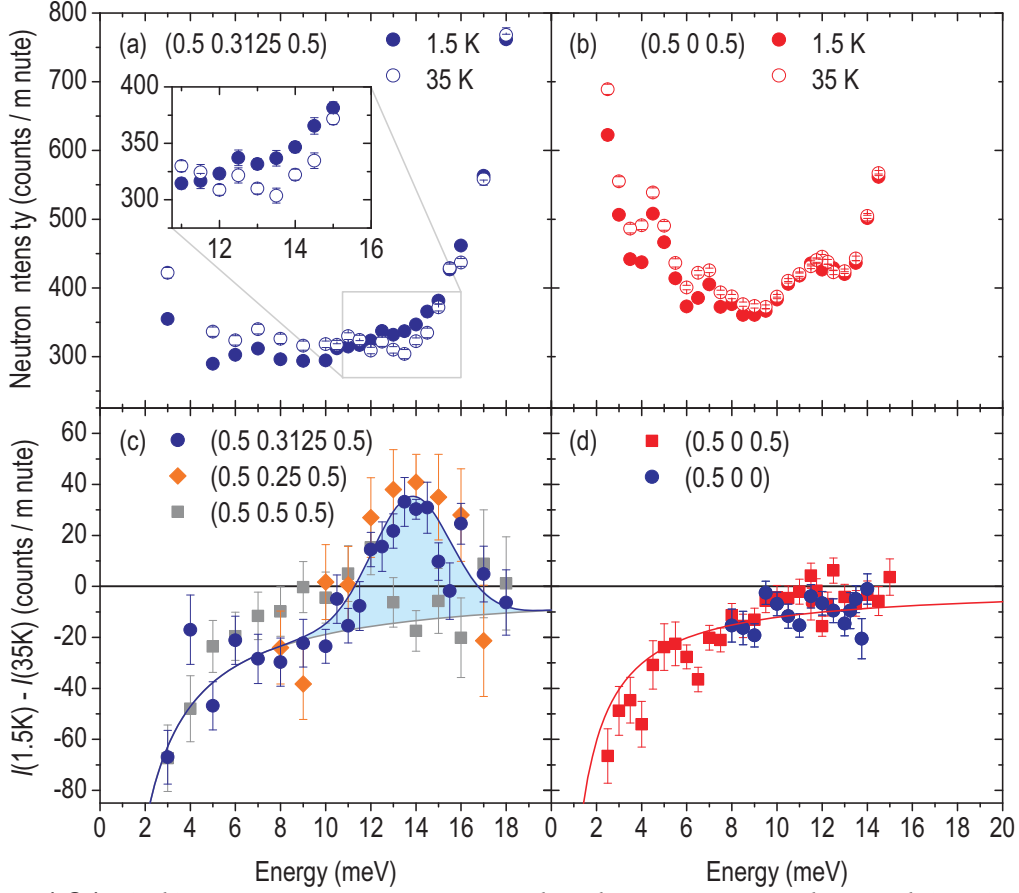


Figure 4.24: (a, b) Raw energy scans measured in the SC (1.5 K) and normal (35 K) states at $\mathbf{Q} = (0.5 \ 0.3125 \ 0.5)_{\text{Fe}_1}$ and $(0.5 \ 0 \ 0.5)_{\text{Fe}_1}$, respectively. The inset in panel (a) shows the zoomed-in part of the resonant peak in the raw data. (c) Intensity difference between the SC state and the normal state at three \mathbf{Q} -vectors: $(0.5 \ 0.25 \ 0.5)_{\text{Fe}_1}$, $(0.5 \ 0.3125 \ 0.5)_{\text{Fe}_1}$, and $(0.5 \ 0.5 \ 0.5)_{\text{Fe}_1}$. While there is no positive intensity at $(0.5 \ 0.5 \ 0.5)$, a clear resonance peak (shaded region) is observed around 14 meV both at $(0.5 \ 0.25 \ 0.5)_{\text{Fe}_1}$ and $(0.5 \ 0.3125 \ 0.5)_{\text{Fe}_1}$. (d) The same plot as in panel (c), but for $\mathbf{Q} = (0.5 \ 0 \ 0.5)_{\text{Fe}_1}$ and $(0.5 \ 0 \ 0)_{\text{Fe}_1}$, where the magnetic resonant mode has been found in other Fe-based superconductors, but is absent here. The base line in (c) and (d) is the difference of the Bose factors.

the effective electron doping in the metallic phase of the sample, which is difficult to reconcile with the stoichiometric chemical composition unless we assume electronic phase segregation into electron-rich and electron-poor regions of the kind discussed in Ref. [320] and [325]. Such a high doping level of the metallic regions would also agree qualitatively with the ARPES results [299, 303, 304, 305, 306].

Furthermore, we have also mapped out the resonant enhancement of spin excitations at $E = 15$ meV in the $(HK0)$ scattering plane by means of the *FlatCone* multi-analyzer. Figure 4.26 (a) shows the difference of intensity maps, after re-binning the raw data, measured around the BZ corner in the SC and normal states. In this experiment, we have observed resonant intensity at all four symmetric positions equivalent to $\mathbf{Q} = (0.5 \ 0.25 \ 0)_{\text{Fe}_1}$. One sees that the in-plane shape of the resonant intensity

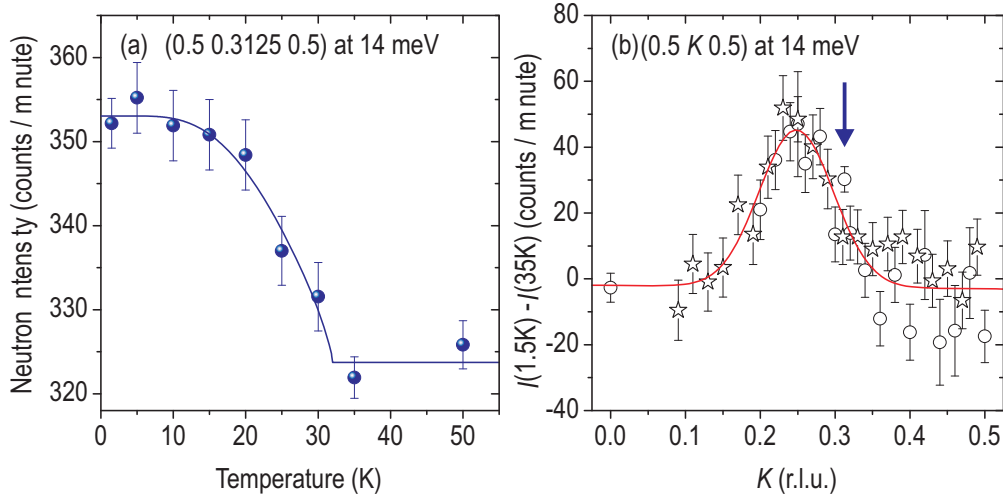


Figure 4.25: (a) Temperature dependence of the raw INS intensity at 14 meV and $\mathbf{Q} = (0.5 \ 0.3125 \ 0.5)_{\text{Fe}_1}$ that demonstrates an order-parameter-like behavior with an onset at T_c . (b) Intensity difference of momentum scans along the BZ boundary, measured below and above T_c , with a maximum at the commensurate wave vector $\mathbf{Q}_{\text{res}} = (0.5 \ 0.25 \ 0.5)_{\text{Fe}_1}$. The solid line is a Gaussian fit with a linear background. Different symbols represent identical momentum scans measured in different experiments, rescaled to the (002) nuclear Bragg peak intensity. The position of the resonant mode predicted by Maier *et al.* [307] is shown by the arrow.

takes an elliptical form, elongated transversely with respect to the vector connecting it to $\mathbf{Q} = (0.5 \ 0.5 \ 0)_{\text{Fe}_1}$. The ratio of the peak widths in the transverse and longitudinal directions results in an aspect ratio of $\sim 2:1$ for the magnetic resonant feature.

As shown in Fig. 4.26 (b), this complicated pattern of resonant intensity in \mathbf{Q} -space could be successfully reproduced by a theoretical calculation of the spin susceptibility based on a d -wave symmetry of the SC order parameter and a tight-binding model that was introduced in Ref. [307] to describe the electronic structure of an electron-doped $A_x\text{Fe}_2\text{Se}_2$. The chemical potential has been adjusted by a rigid-band shift of the bands to match the positions of the magnetic resonant peaks in the calculated susceptibility with the experimental data. This resulted in a doping level of ~ 0.18 electrons/Fe. Such an agreement between the two \mathbf{Q} -space patterns strongly supports the itinerant origin of the observed magnetic response, which can be traced back to the nesting of electron-like Fermi pockets, as indicated in Fig. 4.26 (c) by black arrows.

By comparing the normalized resonance intensity in RFS with that in the nearly optimally doped $\text{Ba}(\text{Fe}_{1-x}\text{Ni}_x)_2\text{As}_2$, measured in a similar experimental configuration at the same spectrometer [50], we find that the intensity at the resonance energy in RFS is approximately a factor of three smaller than in BFNA. Because we expect four nonequivalent resonant peaks in the BZ of RFS from symmetry considerations, as opposed to only two such peaks [$\mathbf{Q}_{\text{res}} = (0.5 \ 0)_{\text{Fe}_1}$ and $(0 \ 0.5)_{\text{Fe}_1}$] in the 122 system, the total resonant spectral weight in both compounds turns out to be comparable.

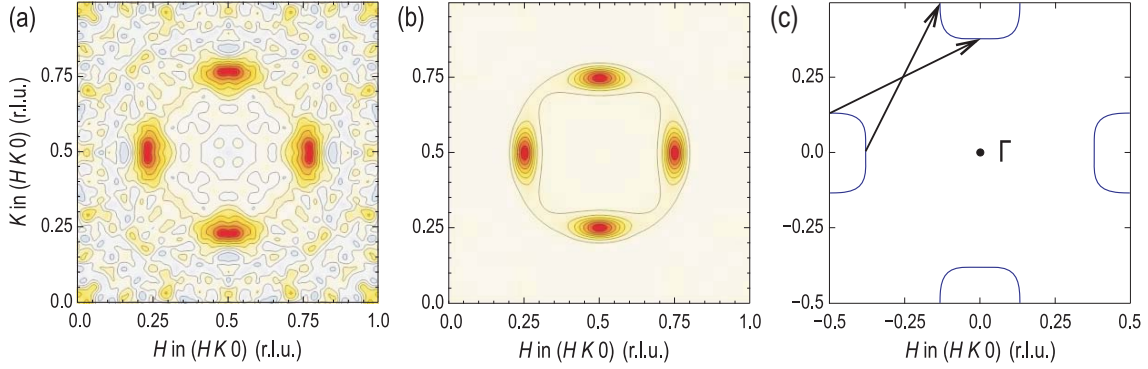


Figure 4.26: (a) Color map of the reciprocal space after re-binning on a 81×81 grid symmetrized with respect to the mirror plane, showing intensity difference between the SC and normal states at $E = 15$ meV, measured by the *FlatCone* detector. (b) The difference of the calculated imaginary parts of the dynamic spin susceptibility for the SC and normal states, taken at the resonance energy. (c) The Fermi surface in the $(HK0)$ plane corresponds to the doping level of 0.18 electrons/Fe. The black arrows are the in-plane nesting vectors responsible for the resonance peaks revealed in our study.

It has been shown that the resonance energy scales linearly with T_c in FeSC, with a ratio of $\hbar\omega_{\text{res}}/k_B T_c$ that slightly varies between different families [231, 50, 235], but is generally lower than the respective ratio of ~ 5.3 measured in high- T_c cuprates [217]. In Fig. 4.27, we compare this ratio in all Fe-based superconductors, in which the resonant mode has been found (we will discuss more about the resonance energy scaling in Chap. 5.). The value for RFS, $\hbar\omega_{\text{res}}/k_B T_c \approx 5.1 \pm 0.4$, lies slightly above the nearly universal ratio of 4.3 estimated for 122-compounds (solid line) [50], but is close to that in $\text{FeTe}_{1-x}\text{Se}_x$, LiFeAs , La-1111 , and cuprates superconductors.

Another important dimensionless parameter that allows an assessment of the pairing strength in unconventional superconductors is the $\hbar\omega_{\text{res}}/2\Delta$ ratio, where Δ is the superconducting gap. In the 245-systems, the SC gap has been measured by ARPES and NMR [304, 305, 306, 326], producing the average $2\Delta/k_B T_c$ ratio of $\sim 7.2 \pm 0.4$

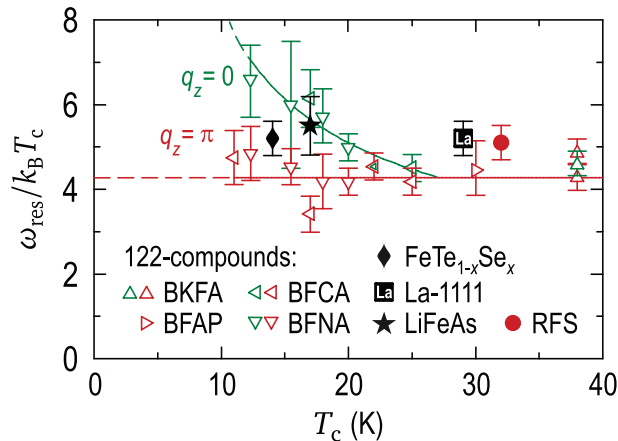


Figure 4.27: Normalized resonance energy, $\hbar\omega_{\text{res}}/k_B T_c$, in Fe-based superconductors for $q_z = 0$ and $q_z = \pi$ [266]. This ratio for RFS is slightly higher than for 122-compounds, but comparable to 11-, 111-, and 1111-type superconductors.

[266]. It corresponds to the $\hbar\omega_{\text{res}}/2\Delta$ ratio of $\sim 0.7 \pm 0.1$ in RFS, slightly above the strong-coupling limit [266].

Chapter 5

Summary

A substantial amount of INS data on 122 and 245 iron-based superconductors has been presented and discussed throughout the previous chapter. In this chapter, we summarize the most important physical implications of our INS results.

5.1 Spin-dynamics in Fe-based superconductors within the itinerant framework

Here we address point by point the physical insight that we have gained thanks to our experimental observations of the spin-excitation spectrum.

- 1. Magnetic resonant mode in FeAs superconductors:** In the SC state, a strong enhancement of magnetic intensity at the characteristic energy and AFM wave vector in the spin-excitation spectrum of 122-ferroplnictide has been observed. The onset temperature of the intensity enhancement coincides with the SC transition temperature. This feature is known as the magnetic resonant mode (see Sec. 4.2.2). Such drastic spectral weight redistribution could induce a positive feedback effect, stabilizing the formation of Cooper pairs in the SC state. This magnetic resonant mode also carries information about the symmetry of the SC gap. Due to the coherence factor which enters the bare susceptibility in the RPA formalism, the magnetic resonant mode appears only if the SC order parameter possesses different signs on different Fermi surfaces, that is, $\Delta(\mathbf{k}) = -\Delta(\mathbf{k} + \mathbf{q})$ (see Sec. 2.4.1). Therefore, the existence of a resonant mode in FeSCs strongly supports s_{\pm} -wave pairing symmetry. Finally, the temperature evolution of ω_{res} is BCS-gap-like, and no signature of complex physics such as the pseudogap in cuprates has been found.
- 2. Simple description of normal-state magnetic response by the Moriya formula:** The normal-state magnetic dynamics are dominated by an intense branch

of low-energy spin excitations in the vicinity of the commensurate AFM wave vector. In Fig. 4.9, we have shown that the energy spectrum of the spin fluctuations is characteristic of a nearly AFM metal and can be well described by the simple Moriya formula given in Eq. 4.1. Experimental observations of the magnetic resonant mode and Moriya-like normal-state response imply that the magnetic dynamics in the FeSC can be understood within the itinerant framework.

3. **Comprehensive understanding of magnetic-fluctuation spectra by first-principles calculations:** In Sec. 4.2.3, we presented a wealth of INS data which revealed detailed structure in the spin-excitation spectra of $\text{BaFe}_{1.85}\text{Co}_{0.15}\text{As}_2$ and $\text{BaFe}_{1.91}\text{Ni}_{0.09}\text{As}_2$, such as L -dependent magnetic intensity modulations, a dispersive resonance energy along the L -direction, and the elliptical shape of the in-plane magnetic excitations. Interestingly, first-principles calculations (DFT and RPA) capture these rather elaborate patterns quite well without having to invoke strong correlation effects between electrons.
4. **Physical justification to describe the spin dynamics in the *unfolded* BZ of the 122 system:** We have determined that the spin-fluctuation spectrum lacks the 3D screw symmetry ($4_2/m$) around the $\left(\frac{1}{2}0L\right)_{\text{Fe}_1}$ axis that is implied by the $I4/mmm$ space group. Combining the experimental evidence of the temperature and energy independent in-plane anisotropy ratio and the first-principle calculations, we proved that this effect originates from the higher symmetry of the magnetic Fe sublattice with respect to the crystal itself. Therefore, the magnetic neutron-scattering signal inherits the symmetry of the *unfolded* BZ of the Fe sublattice.
5. **Magnetic resonant mode in $\text{Rb}_{0.8}\text{Fe}_{1.6}\text{Se}_2$ superconductors:** Without a hole Fermi pocket in this system, the s_{\pm} -wave pairing-symmetry becomes questionable. Our observation of a magnetic resonant mode at an unusual wave vector $\left(\frac{1}{2}\frac{1}{4}\frac{1}{2}\right)_{\text{Fe}_1}$ clearly indicates unconventional pairing with a sign-changing order parameter in the 245-systems, qualitatively consistent with theoretical predictions, made under the assumption of finite electron doping in the metallic phase volume. By tuning the chemical potential in band structure calculations, the exact momentum position of the resonant mode can be reproduced within the RPA formalism. The estimated ratios of $\hbar\omega_{\text{res}}/k_{\text{B}}T_c \approx 5.1 \pm 0.4$ and $\hbar\omega_{\text{res}}/2\Delta \approx 0.7 \pm 0.1$ in this compound indicate moderately strong pairing, similar to other FeSCs.

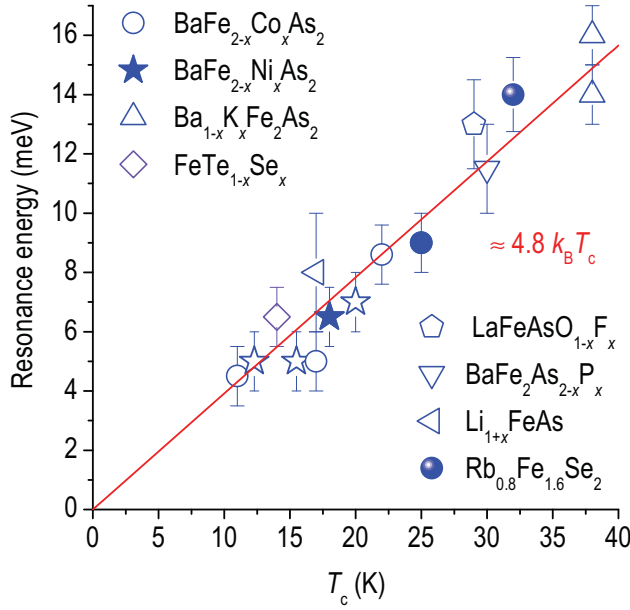


Figure 5.1: Resonance energy versus T_c for different iron-based superconductors. Filled symbols are taken from our work [160, 50, 243, 244] and empty symbols are from previous works [223, 224, 225, 226, 227, 228, 229, 230, 231, 232, 233, 234, 235, 236, 237, 238, 239, 240, 241, 242]. A universal linear relationship $\omega_{\text{res}} \approx 4.8k_B T_c$ holds for all the studied FeSC, independent of their structure or carrier type. For the compounds with dispersing resonant modes, only ω_{res} at $q_z = \pi$ is shown.

5.2 The magnetic resonant mode: Scaling relationships

Owing to the rapid improvement in growing single crystals of FeSC systems, a number of INS results have been reported on the magnetic resonant mode for various materials and doping levels, as discussed in Sec. 2.4.2. All available resonant mode data in FeSC from the literature are summarized to identify correlations among the resonance energy, SC transition temperature, and SC energy gaps. See the table in Appendix A.2 for values for particular materials or doping levels.

In Fig. 5.1, We combine our resonant mode data in 122- and 245-FeSC data with all the previously reported data [223, 224, 225, 226, 227, 228, 229, 230, 231, 232, 233, 234, 235, 236, 237, 238, 239, 240, 241, 242] to show how the resonance energy ω_{res} at $q_z = \pi$ depends on the SC transition temperature. A linear relationship between ω_{res} and T_c has been extensively discussed for cuprates, and a ratio of $\omega_{\text{res}}/k_B T_c \approx 5.3$ has been established for the odd resonance, for doping levels not too far from optimal [273]. However, progressive deviations have been noted with underdoping [327], a violation was reported for single-layer HgBa₂CuO_{4+y} [328], and there is an ongoing controversy about the situation in electron-doped cuprates [328]. In contrast to this, as seen in Fig. 5.1, a similar linear relationship $\omega_{\text{res}}/k_B T_c \approx 4.8$ is universal among all the studied FeSC, over the entire phase diagram and independent of their structure or carrier type, and holds down to the lowest doping levels. This means that the coupling strength (as opposed to ω_{res}) depends only very weakly on doping. Here we address the implications of the linear relationship between ω_{res} and T_c . First, the lower value of this ratio, as compared to that of 5.3 for cuprates, supports the notion of a weaker SC pairing in FeSC [160]. Second, the validity of the linear relationship for all FeSC hitherto studied (independent of the doping carrier type and over the entire studied

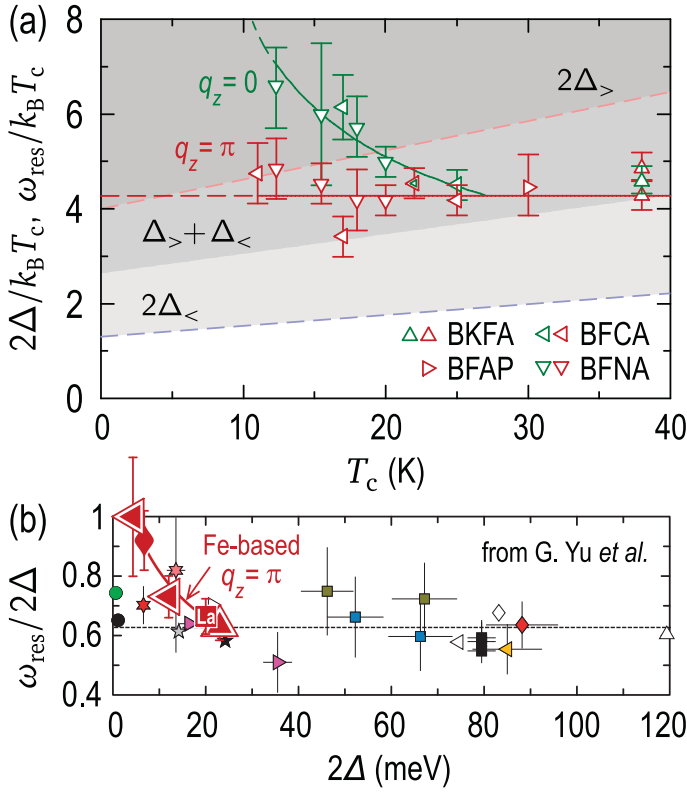


Figure 5.2: (a) Normalized spin-resonance energy, $\omega_{\text{res}}/k_{\text{B}}T_{\text{c}}$, in the Ba-122 iron arsenides for $q_z = \pi$ and $q_z = 0$ [160, 235, 50, 231, 240], plotted vs. T_{c} (see Table A.2). The gray shading shows the particle-hole continuum with a three-step onset at $2\Delta_{<}$, $\Delta_{<} + \Delta_{>}$ and $2\Delta_{>}$. (b) Ratios of the spin-resonance energy at $q_z = \pi$ to the SC gap, $\omega_{\text{res}}/2\Delta$, in Fe-based superconductors (large symbols) in comparison to the universal ratio of 0.64 proposed for other unconventional superconductors [329].

doping range [213, 223, 224, 233, 227, 230, 236, 228, 160]) suggests that models that attribute the resonant mode to an excitonic bound state within the $2\Delta_{\text{SC}}$ may be more straightforwardly applicable to the iron-based superconductors than they are to the cuprates. Whereas in the cuprates, deviations from the linear relationship accompany the increasingly anomalous physical properties at underdoping [327], the resonance in FeSC is remarkably insensitive to the proximity of the magnetic state and even coexists with it at very low doping [229].

The proximity of the magnetic resonant mode to 2Δ determines its damping by particle-hole scattering [272], hence the behavior of the energy gap discussed in Sec. 2.3.2 has important consequences for the SC resonant mode. In 122-compounds, its energy ω_{res} varies with the out-of-plane component of the momentum q_z so that its minimum, found at $q_z = \pi$, scales linearly with T_{c} , whereas the maximal value at $q_z = 0$ always stays above 4 meV, if extrapolated down to $T_{\text{c}} \rightarrow 0$ [160, 235, 50, 231, 240]. This results in $\omega_{\text{res}}/k_{\text{B}}T_{\text{c}}$ ratios that are plotted in Fig. 5.2 (a). The ratio stays constant for $q_z = \pi$, but diverges for $q_z = 0$ as $T_{\text{c}} \rightarrow 0$. Because $2\Delta/k_{\text{B}}T_{\text{c}}$ remains finite at all temperatures, such behavior must increasingly suppress the resonance intensity for $q_z = 0$ as its energy enters the particle-hole continuum [shaded regions in Fig. 5.2 (a)] with decreasing T_{c} . So far, direct experimental evidence for such a suppression [229] remain scarce. A systematic investigation of the resonant peak intensity and shape for doping levels with $T_{\text{c}} < 11$ K is therefore warranted.

For $q_z = \pi$, the situation concerning resonance damping is more speculative, as it

depends on the detailed q_z -dispersion of the continuum and the exact T_c -dependence of the gap ratios. Generally for a two-gap superconductor, the particle-hole continuum has a three-step onset at $2\Delta_<$, $\Delta_< + \Delta_>$ and $2\Delta_>$. In 122-superconductors, however, the smaller gap typically resides only on one of the Γ -centered hole-like bands [63, 66, 188, 192], rendering $2\Delta_<$ onset irrelevant for interband scattering close to the nesting vector. In electron-doped 122-compounds with optimal T_c , the resonance mode appears below $2\Delta_>$, but has a significant overlap with $\Delta_< + \Delta_>$, which possibly contributes to its unusually large energy width [160, 235, 50, 231, 240]. This situation would not change with doping under the assumption of constant $2\Delta_>/k_B T_c$ ratios. However, if one assumes them to follow the average linear trends implied by Fig. 2.28 (dashed lines), the resonance would approach $2\Delta_>$ even at $q_z = \pi$, leading to its further broadening and suppression. This possibility is consistent with the fact that resonant modes have not so far been reported in either under- or overdoped samples with $T_c < 11$ K.

The described behavior of the gap implies that FeSC violate the universality of the $\omega_{\text{res}}/2\Delta$ ratio proposed in Ref. [?, 329]. Indeed, according to the gap values in Fig. 2.28 and the proportionality $\omega_{\text{res}} \approx (4.6 \pm 0.4)k_B T_c$, established in Ref. [160, 235, 50, 231, 240], this ratio continuously increases from ~ 0.65 in the optimally doped BKFA to ~ 0.8 in the optimally doped BFCA. Then it approaches unity in compounds with even lower T_c , such as underdoped BFCA or the 11-family, as illustrated by the large red symbols in Fig. 5.2 (b). The universal ratio of $\omega_{\text{res}}/2\Delta = 0.64$ has been interpreted as the result of a fundamental spin-mediated pairing mechanism in unconventional superconductors [329]. Therefore, its breakdown in Fe-based systems, which becomes increasingly pronounced for low- T_c compounds (see the Table A.2), might be indicative of a variation in the role played by spin fluctuations. One suggestion would be that they become increasingly less important to the SC pairing as T_c decreases (e.g. due to an interplay with conventional phononic pairing), which could explain the simultaneous increase in $\omega_{\text{res}}/2\Delta$ and the reduction of the gap ratio.

Appendix A

TABLES

Doping level	sample	T_c (K)	$\Delta_<$ (meV)	$2\Delta_</k_B T_c$	$\Delta_>$ (meV)	$2\Delta_>/k_B T_c$	Experiment	Method	Reference	
122-family of ferropnictides										
Ba_{1-x}K_xFe₂As₂, hole-doped (BKFA)										
$x = 25\%$ (UD)	FeAs-flux	26	4.0 ± 0.8	3.6 ± 0.7	7.8 ± 0.9	7.0 ± 0.8	ARPES	symmetrization	[330]	
$x = 40\%$ (OP)	\	37	5.8 ± 0.8	3.6 ± 0.5	12.3 ± 0.8	7.7 ± 0.5	\	\	\	
$x = 70\%$ (OD)	\	22	4.4 ± 0.8	4.6 ± 0.9	7.9 ± 0.8	8.3 ± 0.9	\	\	\	
$x = 29\%$ (UD)	Sn-flux	28	$3.7 \pm 0.5^*$	$3.1 \pm 0.4^*$	—	—	PCAR	<i>c</i> -axis Au junction	[195]	
$x = 28\%$	\	31.5	2.3	1.7	9.8	7.2	⁷⁵ As-NMR	spin-lattice relax.	[331]	
$x = 32\%$ (OP)	FeAs-flux	38.5	3.5	2.2	11	6.6	calorimetry	specific heat	[78]	
$x = 40\%$	\	38	3.6 ± 0.5	2.2 ± 0.3	8.2 ± 0.9	5.1 ± 0.5	STS	peak-to-peak	[204]	
\	\	37	3.5 ± 0.5	2.3 ± 0.3	—	—	PCAR	single-gap BTK-fit	[206]	
\	\	\	$3.3 \pm 1.1^*$	$2.1 \pm 0.7^*$	$7.6 \pm 0.9^*$	$4.8 \pm 0.6^*$	STS	two-band model	[203]	
\	\	\	6.4 ± 0.5	4.0 ± 0.3	11.3 ± 1.0	7.0 ± 0.6	ARPES	symmetrization	[192]	
\	\	\	6.0 ± 1.0	3.7 ± 0.6	12.0 ± 1.0	7.5 ± 0.6	ARPES	symmetrization	[63]	
\	\	\	6.0 ± 1.5	3.7 ± 1.0	13 ± 2	8.1 ± 1.2	ARPES + STS	\	[205]	
\	\	\	5.8 ± 0.8	3.6 ± 0.5	12.0 ± 0.8	7.5 ± 0.4	ARPES	\	[188]	
\	\	\	—	—	12.5 ± 2.0	7.8 ± 1.2	optics	reflectance	[332]	
\	\	36.2	2.0 ± 0.3	1.3 ± 0.2	8.9 ± 0.4	5.7 ± 0.3	magnetization	lower critical field	[333]	
\	\	35	7.5 ± 1.5	5.0 ± 1.0	11 ± 1.5	7.3 ± 1.0	ARPES	symmetrization	[334]	
\	\	Sn-flux	< 4	< 3	9.2 ± 1.0	6.7 ± 0.7	\	Dynes-function fit	[66]	
\	\	\	1.5 ± 1.0	1.1 ± 0.7	9.1 ± 1.0	6.6 ± 0.7	ARPES + μ SR	penetration depth	[209]	
\	\	Bridgman	3.5	2.3	12	7.7	optics	optical conductivity	[335]	
\	\	polycryst.	38	6.8 ± 0.3	4.1 ± 0.2	12	7.3	μ SR	penetration depth	[208]
$x = 45\%$ (OD)	Sn-flux	27	$2.7 \pm 0.7^*$	$2.3 \pm 0.6^*$	$9.2 \pm 0.5^*$	$7.9 \pm 0.4^*$	PCAR	<i>ab</i> -plane junction	[207]	
$x = 49\%$	\	25.5	$3.1 \pm 0.7^*$	$2.8 \pm 0.6^*$	—	—	\	<i>c</i> -axis Pb junction	[195]	
$x = 55\%$	\	FeAs-flux	32.7	3.3	2.3	6.8	4.8	MSI	penetration depth	[336]
$x = 77\%$	\	Sn-flux	21	$2.7 \pm 0.3^*$	$3.0 \pm 0.4^*$	—	—	PCAR	<i>c</i> -axis Pb junction	[195]
KFe₂As₂, 100 % hole-doped (K-122 or KFA)										
N/A	FeAs-flux	4.0	—	—	0.93 ± 0.12	5.4 ± 0.7	TDR	nodal-gap model	[92]	
	\	3.6	0.23 ± 0.03	1.5 ± 0.2	0.55 ± 0.02	3.55 ± 0.13	SANS	3-gap model	[93]	
	polycryst.	3.5	0.07	0.46	0.73	4.84	⁷⁵ As-NQR	fully gapped s^\pm	[91]	
RbFe₂As₂, 100 % hole-doped (Rb-122)										
N/A	polycryst.	2.5	0.15 ± 0.02	1.4 ± 0.2	0.49 ± 0.04	4.5 ± 0.4	μ SR	penetration depth	[210]	

Continued on next page

Doping level	sample	T_c (K)	$\Delta_<$ (meV)	$2\Delta_</k_B T_c$	$\Delta_>$ (meV)	$2\Delta_>/k_B T_c$	Experiment	Method	Reference	
Ba(Fe_{1-x}Co_x)₂As₂, electron-doped (BFCA)										
$x = 7.0\%$	(OP)	FeAs-flux	22	—	—	$7.0 \pm 2.4^*$	$7.4 \pm 2.5^*$	STS	peak-to-peak	[138]
∖	∖	∖	23	—	—	$5.5 \pm 0.5^*$	$5.5 \pm 0.5^*$	PCAR	<i>c</i> -axis Pt junction	[211]
∖	∖	∖	24.5	—	—	7.3	6.9	STS	peak-to-peak	[337]
$x = 7.5\%$	∖	∖	25.5	4.5 ± 1.0	4.1 ± 0.9	6.7 ± 1.0	6.1 ± 0.9	ARPES	symmetrization	[190]
∖	∖	∖	25	3.1 ± 0.2	2.9 ± 0.2	7.4 ± 0.3	6.9 ± 0.3	optics	optical conductivity	[338]
$x = 10\%$	∖	∖	24.5	4.4 ± 0.6	4.2 ± 0.6	9.9 ± 1.2	9.4 ± 1.1	PCAR	<i>ab</i> -plane, BTK-fit	[339]
∖	∖	∖	25.3	—	—	$6.3 \pm 1.7^*$	$5.8 \pm 1.6^*$	STS	peak-to-peak	[212]
$x = 7.4\%$	(OD)	∖	22.5	1.5	1.6	3.7	3.8	μ SR	penetration depth	[340]
$x = 7.5\%$	∖	∖	21.4	1.75	1.9	4.1	4.4	calorimetry	specific heat	[341]
$x = 4.0\%$	(UD)	∖	5.8	0.38	1.5	0.86	3.4	∖	∖	[196]
$x = 4.5\%$	∖	∖	13.3	0.89	1.5	2.2	3.8	∖	∖	∖
$x = 5.0\%$	∖	∖	19.5	1.36	1.6	3.5	4.2	∖	∖	∖
$x = 5.5\%$	∖	∖	21.5	1.84	2.0	4.4	4.7	∖	∖	∖
$x = 5.7\%$	(OP)	∖	24.4	1.94	1.9	5.2	5.0	∖	∖	∖
$x = 6.0\%$	∖	∖	24.2	1.94	1.8	5.0	4.8	∖	∖	∖
$x = 6.5\%$	(OD)	∖	23.8	1.78	1.7	4.6	4.5	∖	∖	∖
$x = 7.5\%$	∖	∖	22.9	1.81	1.8	4.4	4.5	∖	∖	∖
$x = 7.6\%$	∖	∖	21.5	1.84	2.0	3.9	4.2	∖	∖	∖
$x = 9.0\%$	∖	∖	20.7	1.62	1.8	3.8	4.3	∖	∖	∖
$x = 11.0\%$	∖	∖	13.0	0.89	1.6	2.0	3.6	∖	∖	∖
$x = 11.3\%$	∖	∖	11.0	0.83	1.7	1.75	3.7	∖	∖	∖
$x = 11.6\%$	∖	∖	9.4	0.54	1.3	1.27	3.1	∖	∖	∖
$x = 12.0\%$	∖	∖	5.1	0.25	1.1	0.67	3.1	∖	∖	∖
$x = 6.0\%$	(UD)	∖	14	$4 \pm 2^*$	$7 \pm 3^*$	$8 \pm 2^*$	$13 \pm 3^*$	STS	Dynes-function fit	[201]
$x = 12.0\%$	(OD)	∖	20	$5 \pm 2^*$	$6 \pm 3^*$	$10 \pm 2^*$	$11 \pm 3^*$	∖	∖	∖
$x = 10\%$	∖	thin film	∖	1.85 ± 0.15	2.1 ± 0.2	≥ 3.5	≥ 4.0	optics	optical conductivity	[342]
$x = 6.5\%$	(OP)	FeAs-flux	24.5	3.3	3.1	5.0	4.7	∖	∖	[343]
$x = 4.9\%$	(UD)	∖	15.8	0.8	1.2	3.0	4.4	MFM	penetration depth	[344]
$x = 5.1\%$	∖	∖	18.6	1.1	1.4	3.7	4.6	∖	∖	∖
$x = 7.0\%$	(OP)	∖	22.4	2.5	2.6	6.4	6.6	∖	∖	∖
$x = 8.5\%$	(OD)	∖	19.6	1.0	1.2	3.2	3.8	∖	∖	∖
$x = 11\%$	∖	∖	13.5	0.7	1.2	2.0	3.4	∖	∖	∖
EuFe₂(As_{1-x}P_x)₂, isovalently substituted (EFAP)										
$x = 18\%$	(OP)	Bridgman	28	—	—	4.7	3.8	optics	optical conductivity	[345]
Sr(Fe_{1-x}Co_x)₂As₂, electron-doped (SFCA)										
$x = 7.5\%$	(OP)	Sn-flux	19.5	1.4	1.7	8.6	10.2	STS	peak-to-peak	[346]
$x = 12.5\%$	(OD)	FeAs-flux	13.3	1.3 ± 0.3	2.3 ± 0.5	3.7 ± 0.4	6.5 ± 0.7	μ SR	penetration depth	[347]
$x = 13\%$	∖	∖	15.5	$1.8 \pm 0.3^*$	$2.7 \pm 0.5^*$	—	—	PCAR	Pb & Au junctions	[195]
BaNi₂As₂, 100% electron-doped (BNA)										
N/A	Pb-flux	0.68	—	—	0.095	3.24	calorimetry	specific heat	[197]	

Continued on next page

Doping level	sample	T_c (K)	$\Delta_<$ (meV)	$2\Delta_</k_B T_c$	$\Delta_>$ (meV)	$2\Delta_>/k_B T_c$	Experiment	Method	Reference	
1111-family of ferropnictides										
LaFeAsO_{1-x}F_x, electron-doped (La-1111)										
$x = 8\%$ (UD)	polycryst.	23	3.0	3.0	7.5	7.5	⁷⁵ As-NQR	spin-lattice relax.	[348]	
$x = 10\%$ (OP)	\	26	3.9 ± 0.7	3.5 ± 0.6	—	—	PCAR	BTK-fit	[349]	
\	\	\	3.4 ± 0.5	3.0 ± 0.5	—	—	calorimetry	specific heat	[350]	
\	\	\	4.0 ± 0.6	3.6 ± 0.5	—	—	magnetization	lower critical field	[333]	
\	\	27	3.8 ± 0.4	3.3 ± 0.3	10.0 ± 0.6	8.5 ± 0.5	PCAR	generalized BTK-fit	[351]	
PrFeAsO_{1-x}F_x, electron-doped (Pr-1111)										
$x = 11\%$ (UD)	polycryst.	45	4.3	2.2	13.7	7.1	⁷⁵ As- & ¹⁹ F-NMR		[352]	
NdFeAsO_{1-x}F_x, electron-doped (Nd-1111)										
$x = 10\%$ (OP)	polycryst.	51	5.1 ± 0.2*	2.6 ± 0.1*	11.7 ± 1.2*	5.7 ± 0.5*	PCAR	Pt junctions	[211]	
\	\	sol.-state	53	—	15 ± 1.5	6.6 ± 0.7	ARPES	symmetrization	[353]	
SmFeAsO_{1-x}F_x, electron-doped (Sm-1111)										
$x = 20\%$ (OP)	monocryst.	51.2	6.45 ± 0.25	3.0 ± 0.2	16.6 ± 1.6	7.7 ± 0.9	PCAR	Au contact, BTK fit	[354]	
\	\	\	49.5	8.0	3.7	—	TRS	reflectivity	[355]	
$x = 10\%$	\	polycryst.	51.5	3.7 ± 0.4	1.7 ± 0.2	10.5 ± 0.5	4.7 ± 0.2	PCAR	Pt/Ir or Au junctions	[356]
$x = 20\%$	\	\	52	6.15 ± 0.45	2.7 ± 0.2	18 ± 3	8.0 ± 1.3	\	Ag-paste contact	[357]
$x = 9\%$ (UD)	\	42	4.9 ± 0.5	2.7 ± 0.3	15 ± 1	8.3 ± 0.6	\	\	\	
$x = 15\%$	\	\	6.7 ± 0.15	3.7 ± 0.1	—	—	\	Au junctions	[358]	
SmFeAsO_{1-x}, oxygen-deficient (Sm-1111)										
$x = 15\%$ (OP)	polycryst.	52	8.25 ± 0.25	3.7 ± 0.1	—	—	STS	<i>d</i> -wave model	[359]	
TbFeAsO_{1-x}F_x, electron-doped (Tb-1111)										
$x = 10\%$ (UD)	polycryst.	50	5.0 ± 0.8	2.3 ± 0.4	8.8 ± 0.5	4.1 ± 0.2	PCAR	Au junctions	[360]	
111-family of ferropnictides										
Li_{1+δ}FeAs, undoped (Li-111 or LFA)										
N/A	self-flux	18	1.0 ± 0.5	1.3 ± 0.6	3.2	4.1	ARPES	Dynes-function fit	[62]	
	\	17	—	—	3.0 ± 0.2	4.1 ± 0.3	SANS+ARPES	penetration depth	[361]	
	\	16.9	1.2	1.6	2.6	3.6	calorimetry	specific heat	[362]	
	\	17	1.4 ± 0.4	1.9 ± 0.6	2.96 ± 0.05	4.0 ± 0.1	MSI	penetration depth	[199]	
	Bridgman	17.5	1.4 ± 0.1	1.9 ± 0.13	2.9 ± 0.2	3.8 ± 0.3	magnetization	lower critical field	[363]	
	\	\	1.2 ± 0.1	1.6 ± 0.13	2.9 ± 0.2	3.8 ± 0.3	\	lower critical field	\	
	\	\	1.7	2.22	2.8	3.77	TDR	penetration depth	[200]	
	polycryst.	17	1.9	2.6	4.4	6.0	⁷⁵ As-NQR	spin-lattice relax.	[198]	
	\	15	0.7	1.2	2.3	3.5	calorimetry	specific heat	[364]	
	grains	\	0.6 ± 0.13	1.0 ± 0.4	3.3 ± 1.0	5.4 ± 1.6	magnetization	lower critical field	[365]	
NaFe_{1-x}Co_xAs, electron-doped (Na-111)										
$x = 5\%$ (OD)	self-flux	18	—	—	6.5 ± 0.5	8.3 ± 0.6	ARPES	symmetrization	[366]	

Continued on next page

Continued from previous page

Doping level	sample	T_c (K)	$\Delta_<$ (meV)	$2\Delta_</k_B T_c$	$\Delta_>$ (meV)	$2\Delta_>/k_B T_c$	Experiment	Method	Reference
arsenic-free Fe-based superconductors									
FeSe_{1-x}, chemically deficient									
$x = 15\%$	(OD) polycryst.	8.3	0.38 ± 0.01	1.1 ± 0.02	1.60 ± 0.02	4.45 ± 0.06	μ SR	penetration depth	[367]
FeTe_{1-x}Se_x, isovalently substituted									
$x = 50\%$	(OP) Bridgman	14.6	0.51 ± 0.03	0.8 ± 0.05	2.61 ± 0.09	4.15 ± 0.14	μ SR	penetration depth	[368]
\	\ polycryst.	14.4	0.87 ± 0.06	1.4 ± 0.1	2.6 ± 0.1	4.2 ± 0.2	\	\	[369]
\	\ self-flux	13.9	—	—	2.2	3.7	calorimetry	specific heat	[370]
$x = 45\%$	\ unidirect.	14	2.5	4.1	5.1	8.5	optics	optical conductivity	[371]
\	\ solidificat.	14.2	—	—	3.8	6.2	PCAR	<i>c</i> -axis Au junctions	[372]
$x = 43\%$	\ self-flux	14.7	2.5	3.92	3.7	5.84	calorimetry	specific heat	[373]
$x = 15\%$	\ \	14	—	—	2.3	3.8	STS	Dynes-function fit	[374]
Fe_{1-x}Mn_xTe_{0.5}Se_{0.5}									
$x = 2\%$	(OP) self-flux	14.4	—	—	2.7	4.4	calorimetry	specific heat	[370]
A_x(Fe_{1-δ}Se)₂ (A=K, Rb, Cs), heavily electron-doped (highest T_c among arsenic-free Fe-based superconductors)									
K, $x = 0.7$	(UD) Bridgman	28	1.5	1.3	—	—	optics	optical conductivity	[375]
Tl _{0.63} K _{0.37}	\ \	29	—	—	8.5 ± 1.0	6.8 ± 0.8	ARPES	symmetrization	[304]
Tl _{0.45} K _{0.34}	\ \	28	—	—	8.0	6.6	\	\	[305]
K, $x = 0.7$	(OP) \	32	—	—	9.0	6.5	\	\	\
Tl _{0.58} Rb _{0.42}	\ \	\	—	—	12.5 ± 2.5	9.1 ± 1.8	\	\	[306]
K, $x = 0.8$	\ self-flux	31.7	—	—	10.3 ± 2	7.5 ± 1.5	\	\	[376]
\ \	\ \	30	—	—	10.8 ± 2	7.6 ± 1.0	⁷⁷ Se NMR	spin-lattice relax	[377]
\ \	\ \	\	—	—	10.3 ± 2	7.9 ± 1.5	\	\	\

Table A.1: Summary of the energy gap measurements in Fe-based superconductors. The gap values are obtained from the published results of point-contact Andreev-reflection (PCAR) or tunneling spectroscopy, scanning tunneling spectroscopy (STS), ARPES and optical spectroscopy measurements that directly probe the electronic density of states, as well as indirectly from the calorimetric measurements of the electronic specific heat, magnetization measurements of the lower critical field (H_{c1}), muon-spin-rotation (μ SR), small-angle neutron scattering (SANS), microwave surface-impedance (MSI), tunnel-diode resonator (TDR), or MFM measurements of the London penetration depth, from the NMR or nuclear-quadrupolar-resonance (NQR) measurements of the spin-lattice relaxation rate, and from the time-resolved femtosecond spectroscopy (FTS) via the temperature-dependence of the photoinduced reflectivity. The error values marked by an asterisk represent the spread of the gap values measured in different points on the sample or using different junctions. They can be therefore larger than the uncertainty of the average.

Compound	sample	T_c (K)	ω_{res} (meV)		$\omega_{\text{res}}/k_B T_c$		$2\Delta_>$ (meV)	$\omega_{\text{res}}/2\Delta_>$		Reference
			$q_z = 0$	$q_z = \pi$	$q_z = 0$	$q_z = \pi$		$q_z = 0$	$q_z = \pi$	
Ba _{1-x} K _x Fe ₂ As ₂ , hole-doped (BKFA)										
$x = 40\%$	(OP) polycryst.	38	—	14.0 ± 1.0	—	4.3 ± 0.3	22.9 ± 1.0	—	0.61 ± 0.05	[213]
$x = 33\%$	\ \ self-flux	\ \	15.0 ± 1.0	16.0 ± 1.0	4.6 ± 0.3	4.9 ± 0.3	22.9 ± 1.0	0.66 ± 0.05	0.70 ± 0.05	[240]
Ba(Fe _{1-x} Co _x) ₂ As ₂ , electron-doped (BFCA)										
$x = 4\%$	(UD) self-flux	11	—	4.5 ± 0.5	—	4.7 ± 0.5	4.4 ± 0.9	—	1.0 ± 0.2	[233]
$x = 4.7\%$	\ \ \ \	17	9.0 ± 1.0	5.0 ± 0.5	6.1 ± 0.7	3.4 ± 0.4	4.7 ± 1.3	1.9 ± 0.6	1.1 ± 0.3	[229]
$x = 7.5\%$	(OP) \ \	25	9.7 ± 0.5	9.0 ± 0.5	4.5 ± 0.3	4.2 ± 0.3	12.3 ± 0.9	0.79 ± 0.07	0.73 ± 0.07	[160]
$x = 8\%$	(OD) \ \	22	8.6 ± 0.5	8.6 ± 0.5	4.5 ± 0.3	4.5 ± 0.3	10.8 ± 0.8	0.80 ± 0.07	0.70 ± 0.05	[223]
Ba(Fe _{1-x} Ni _x) ₂ As ₂ , electron-doped (BFNA)										
$x = 3.7\%$	(UD) self-flux	12.2	7.0 ± 0.8	5.0 ± 0.5	6.7 ± 0.8	4.8 ± 0.5	unknown (no direct measurements)		[235]	
$x = 4.5\%$	\ \ \ \	18	8.9 ± 0.8	6.5 ± 1.0	5.7 ± 0.5	4.2 ± 0.6	\ \		[50]	
$x = 5\%$	(OP) \ \	20	9.1 ± 0.4	7.2 ± 0.5	5.3 ± 0.3	4.2 ± 0.3	\ \		[224]	
\ \	\ \ \ \	\ \	8.7 ± 0.4	7.2 ± 0.7	5.1 ± 0.3	4.2 ± 0.4	\ \		[225]	
\ \	\ \ \ \	\ \	8.0 ± 0.5	—	4.6 ± 0.3	—	\ \		[232]	
$x = 7.5\%$	(OD) \ \	15.5	8.0 ± 2.0	6.0 ± 0.5	6.0 ± 1.5	4.5 ± 0.4	\ \		[235]	
BaFe ₂ (As _{1-x} P _x) ₂ , isovalently substituted (BFAP)										
$x = 35\%$	(OP) polycryst.	30	—	11.5 ± 1.5	—	4.5 ± 0.6	unknown (no direct measurements)		[237]	
LaFeAsO _{1-x} F _x , electron-doped (La-1111)										
$x = 8\%$	(OP) polycryst.	29	—	13.0 ± 1.0	—	5.2 ± 0.4	20.0 ± 1.2	—	0.65 ± 0.06	[231]
Li _{1+δ} FeAs, undoped (Li-111 or LFA)										
N/A	polycryst.	17	—	8.0 ± 2.0	—	5.5 ± 1.4	6.1 ± 0.5	—	1.3 ± 0.4	[238]
FeTe _{1-x} Se _x , isovalently substituted (11-family)										
$x = 0.4$	(OP) self-flux	14	—	6.5 ± 0.5	—	5.3 ± 0.4	6.9 ± 1.2	—	0.94 ± 0.18	[227]
\ \	\ \ \ \	\ \	6.0 ± 0.5	—	5.0 ± 0.4	—	\ \	0.87 ± 0.17	—	[228]
$x = 0.5$	\ \ unidirect. solidif.	\ \	6.2 ± 0.5	—	5.1 ± 0.4	—	\ \	0.90 ± 0.17	—	[230]
\ \	\ \ Bridgman	\ \	6.5 ± 0.5	—	5.3 ± 0.4	—	\ \	0.94 ± 0.18	—	[236]
Rb ₂ Fe ₄ Se ₅ , heavily electron-doped (245-family)										
—	(OP) Bridgman	32	—	14.0 ± 0.5	—	5.1 ± 0.4	20 ± 4	—	0.70 ± 0.10	[243]

Table A.2: Summary of the spin resonance energies (ω_{res}), corresponding onset energies of the particle-hole continuum ($2\Delta_>$), normalized resonance energies ($\omega_{\text{res}}/k_B T_c$), and the $\omega_{\text{res}}/2\Delta_>$ ratios in Fe-based superconductors.

Bibliography

- [1] J. Bardeen, L. N. Cooper, and J. R. Schrieffer, Phys. Rev. **108**, 1175 (1957).
- [2] J. Bardeen, L. N. Cooper, and J. R. Schrieffer, Phys. Rev. **106**, 162 (1957).
- [3] V. L. Ginzburg, Annual Review of Materials Science **2**, 663 (1972).
- [4] J. G. Bednorz and K. A. Müller, Z. Phys. B **64**, 189 (1986).
- [5] A. Schilling, M. Cantoni, J. D. Guo, and H. R. Ott, Nature **363**, 56 (1993).
- [6] N. Sato *et al.*, Nature **410**, 340 (2001).
- [7] M. R. Norman, D. Pines, and C. Kallin, Advances in Physics **54**, 715 (2005).
- [8] J. M. Tranquada *et al.*, Nature **375**, 561 (1995).
- [9] Y. Kamihara *et al.*, J. Am. Chem. Soc. **128**, 10012 (2006).
- [10] Y. Kamihara, T. Watanabe, M. Hirano, and H. Hosono, J. Am. Chem. Soc. **130**, 3296 (2008).
- [11] H. Takahashi *et al.*, Nature **453**, 376 (2008).
- [12] P. M. Grant, Nature **453**, 1000 (2008).
- [13] C. Xu and S. Sachdev, Nat. Phys. **4**, 898 (2008).
- [14] H.-H. Wen, Advanced Materials **20**, 3764 (2008).
- [15] C. W. Chu, Nat. Phys. **5**, 787 (2009).
- [16] K. Ishida, Y. Nakai, and H. Hosono, J. Phys. Soc. Jpn. **78**, 062001 (2009).
- [17] Z.-A. Ren and Z.-X. Zhao, Advanced Materials **21**, 4584 (2009).
- [18] P. M. Aswathy, J. B. Anooja, P. M. Sarun, and U. Syamaprasad, Supercond. Sci. and Technol. **23**, 073001 (2010).
- [19] J. A. Wilson, J. Phys.: Condens. Matter **22**, 203201 (2010).

- [20] J. Paglione and R. L. Greene, *Nat. Phys.* **6**, 645 (2010).
- [21] I. I. Mazin, *Nature* **464**, 183 (2010).
- [22] A. Cho, *Science* **327**, 1320 (2010).
- [23] P. C. Canfield and S. L. Bud'ko, *Annu. Rev. Condens. Matter Phys.* **1**, 27 (2010).
- [24] D. C. Johnston, *Advances in Physics* **59**, 803 (2010).
- [25] D. N. Basov and A. V. Chubukov, *Nat. Phys.* **7**, 272 (2011).
- [26] G. R. Stewart, *Rev. Mod. Phys.* **83**, 1589 (2011).
- [27] L. Boeri, O. V. Dolgov, and A. A. Golubov, *Phys. Rev. Lett.* **101**, 026403 (2008).
- [28] C. Wang *et al.*, *EPL* **83**, 67006 (2008).
- [29] W. K. Yeoh *et al.*, *Phys. Rev. Lett.* **106**, 247002 (2011).
- [30] E. Wiesenmayer *et al.*, *Phys. Rev. Lett.* **107**, 237001 (2011).
- [31] T. Moriya, *Spin Fluctuations in Itinerant Electron Magnetism* (Springer, Dordrecht, 1985).
- [32] J.-H. Chu, J. G. Analytis, C. Kucharczyk, and I. R. Fisher, *Phys. Rev. B* **79**, 014506 (2009).
- [33] H. Ogino *et al.*, *Supercond. Sci. and Technol.* **22**, 075008 (2009).
- [34] J. Guo *et al.*, *Phys. Rev. B* **82**, 180520 (2010).
- [35] A. F. Wang *et al.*, *Phys. Rev. B* **83**, 060512 (2011).
- [36] A. Krzton-Maziopa *et al.*, *J. Phys.: Condens. Matter* **23**, 052203 (2011).
- [37] M. Rotter, M. Pangerl, M. Tegel, and D. Johrendt, *Angewandte Chemie International Edition* **47**, 7949 (2008).
- [38] M. Rotter *et al.*, *Phys. Rev. B* **78**, 020503 (2008).
- [39] J. H. Tapp *et al.*, *Phys. Rev. B* **78**, 060505 (2008).
- [40] S. Li *et al.*, *Phys. Rev. B* **80**, 020504 (2009).
- [41] D. J. Singh, *Phys. Rev. B* **78**, 094511 (2008).
- [42] V. Brouet *et al.*, *Phys. Rev. B* **80**, 165115 (2009).

- [43] V. B. Zabolotnyy *et al.*, *Nature* **457**, 569 (2009).
- [44] C. Liu *et al.*, *Nat. Phys.* **6**, 419 (2010).
- [45] I. I. Mazin *et al.*, *Phys. Rev. B* **78**, 085104 (2008).
- [46] S. Raghu *et al.*, *Phys. Rev. B* **77**, 220503(R) (2008).
- [47] M. M. Korshunov and I. Eremin, *Phys. Rev. B* **78**, 140509 (2008).
- [48] A. V. Chubukov, D. V. Efremov, and I. Eremin, *Phys. Rev. B* **78**, 134512 (2008).
- [49] M. M. Korshunov *et al.*, *Phys. Rev. Lett.* **102**, 236403 (2009).
- [50] J. T. Park *et al.*, *Phys. Rev. B* **82**, 134503 (2010).
- [51] C. Kittel, *Introduction to Solid State Physics*, 6th ed. (John Wiley & Sons, Inc., New York, 1986).
- [52] N. Ashcroft and N. Mermin, *Solid State Physics* (Saunders College, Philadelphia, 1976).
- [53] D. J. Singh and M. H. Du, *Phys. Rev. Lett.* **100**, 237003 (2008).
- [54] I. I. Mazin, D. J. Singh, M. D. Johannes, and M. H. Du, *Phys. Rev. Lett.* **101**, 057003 (2008).
- [55] C.-H. Lin *et al.*, *Phys. Rev. Lett.* **107**, 257001 (2011).
- [56] I. I. Mazin and M. D. Johannes, *Nat. Phys.* **5**, 141 (2009).
- [57] C. de la Cruz *et al.*, *Nature* **453**, 899 (2008).
- [58] H. H. Klauss *et al.*, *Phys. Rev. Lett.* **101**, 077005 (2008).
- [59] W. Malaeb *et al.*, *J. Phys. Soc. Jpn.* **78**, 123706 (2009).
- [60] J. Fink *et al.*, *Phys. Rev. B* **79**, 155118 (2009).
- [61] C. Liu *et al.*, *Phys. Rev. Lett.* **102**, 167004 (2009).
- [62] S. V. Borisenko *et al.*, *Phys. Rev. Lett.* **105**, 067002 (2010).
- [63] H. Ding *et al.*, *EPL* **83**, 47001 (2008).
- [64] C. Liu *et al.*, *Phys. Rev. Lett.* **101**, 177005 (2008).
- [65] H. Liu *et al.*, *Phys. Rev. B* **78**, 184514 (2008).

- [66] D. V. Evtushinsky *et al.*, Phys. Rev. B **79**, 054517 (2009).
- [67] R. Yoshida *et al.*, J. Phys. Soc. Jpn. **78**, 034708 (2009).
- [68] S. E. Sebastian *et al.*, J. Phys.: Condens. Matter **20**, 422203 (2008).
- [69] J. G. Analytis *et al.*, Phys. Rev. Lett. **103**, 076401 (2009).
- [70] J. G. Analytis *et al.*, Phys. Rev. B **80**, 064507 (2009).
- [71] A. I. Coldea *et al.*, Phys. Rev. Lett. **103**, 026404 (2009).
- [72] N. Ni *et al.*, Phys. Rev. B **78**, 014507 (2008).
- [73] X. F. Wang *et al.*, Phys. Rev. Lett. **102**, 117005 (2009).
- [74] P. A. Lee, N. Nagaosa, and X.-G. Wen, Rev. Mod. Phys. **78**, 17 (2006).
- [75] A. I. Goldman *et al.*, Phys. Rev. B **78**, 100506(R) (2008).
- [76] J. Q. Yan *et al.*, Phys. Rev. B **78**, 024516 (2008).
- [77] Q. Huang *et al.*, Phys. Rev. Lett. **101**, 257003 (2008).
- [78] P. Popovich *et al.*, Phys. Rev. Lett. **105**, 027003 (2010).
- [79] D. L. Sun, Y. Liu, J. T. Park, and C. T. Lin, Supercond. Sci. and Technol. **22**, 105006 (2009).
- [80] L. J. Li *et al.*, New J. Phys. **11**, 025008 (2009).
- [81] N. Ni *et al.*, Phys. Rev. B **80**, 024511 (2009).
- [82] F. Rullier-Albenque *et al.*, Phys. Rev. B **81**, 224503 (2010).
- [83] S. Jiang *et al.*, J. Phys.: Condens. Matter **21**, 382203 (2009).
- [84] K. Ahilan *et al.*, Phys. Rev. B **79**, 214520 (2009).
- [85] L. Fang *et al.*, Phys. Rev. B **80**, 140508 (2009).
- [86] C. Hess *et al.*, EPL **87**, 17005 (2009).
- [87] J. S. Kim *et al.*, Phys. Rev. B **82**, 024510 (2010).
- [88] M. Rotter, M. Tegel, and D. Johrendt, Phys. Rev. Lett. **101**, 107006 (2008).
- [89] K. Sasmal *et al.*, Phys. Rev. Lett. **101**, 107007 (2008).
- [90] H. S. Jeevan *et al.*, Phys. Rev. B **78**, 092406 (2008).

- [91] H. Fukazawa *et al.*, J. Phys. Soc. Jpn. **78**, 083712 (2009).
- [92] K. Hashimoto *et al.*, Phys. Rev. B **82**, 014526 (2010).
- [93] H. Kawano-Furukawa *et al.*, Phys. Rev. B **84**, 024507 (2011).
- [94] J. T. Park *et al.*, Phys. Rev. Lett. **102**, 117006 (2009).
- [95] A. A. Aczel *et al.*, Phys. Rev. B **78**, 214503 (2008).
- [96] T. Goko *et al.*, Phys. Rev. B **80**, 024508 (2009).
- [97] M. H. Julien *et al.*, EPL **87**, 37001 (2009).
- [98] C. Liu *et al.*, Phys. Rev. B **84**, 020509 (2011).
- [99] T. Yoshida *et al.*, Phys. Rev. Lett. **106**, 117001 (2011).
- [100] S. Thirupathaiah *et al.*, Phys. Rev. B **84**, 014531 (2011).
- [101] Z. Wang *et al.*, J. Phys.: Condens. Matter **21**, 495701 (2009).
- [102] M. Rotter, C. Hieke, and D. Johrendt, Phys. Rev. B **82**, 014513 (2010).
- [103] A. S. Sefat, Reports on Progress in Physics **74**, 124502 (2011).
- [104] S. A. J. Kimber *et al.*, Nat. Mater. **8**, 471 (2009).
- [105] G. M. Zhang *et al.*, EPL **86**, 37006 (2009).
- [106] F. Rullier-Albenque, D. Colson, A. Forget, and H. Alloul, Phys. Rev. Lett. **103**, 057001 (2009).
- [107] B. Sales, M. McGuire, A. Sefat, and D. Mandrus, Physica C: Superconductivity **470**, 304 (2010).
- [108] J. Dong *et al.*, EPL **83**, 27006 (2008).
- [109] C. Cao, P. J. Hirschfeld, and H.-P. Cheng, Phys. Rev. B **77**, 220506(R) (2008).
- [110] Z. P. Yin *et al.*, Phys. Rev. Lett. **101**, 047001 (2008).
- [111] T. Yildirim, Phys. Rev. Lett. **101**, 057010 (2008).
- [112] M. Ishikado *et al.*, J. Phys. Soc. Jpn. **78**, 043705 (2009).
- [113] A. N. Yaresko, G.-Q. Liu, V. N. Antonov, and O. K. Andersen, Phys. Rev. B **79**, 144421 (2009).

- [114] Q. Si and E. Abrahams, Phys. Rev. Lett. **101**, 076401 (2008).
- [115] Q. Si, E. Abrahams, J. Dai, and J.-X. Zhu, New J. Phys. **11**, 045001 (2009).
- [116] J. Zhao *et al.*, Nat. Phys. **5**, 555 (2009).
- [117] A. L. Wysocki, K. D. Belashchenko, and V. P. Antropov, Nat. Phys. **7**, 485 (2011).
- [118] J. Zhao *et al.*, Phys. Rev. B **78**, 140504 (2008).
- [119] K. Kaneko *et al.*, Phys. Rev. B **78**, 212502 (2008).
- [120] Y. Su *et al.*, Phys. Rev. B **79**, 064504 (2009).
- [121] Y. Xiao *et al.*, Phys. Rev. B **79**, 060504 (2009).
- [122] K. Matan, R. Morinaga, K. Iida, and T. J. Sato, Phys. Rev. B **79**, 054526 (2009).
- [123] M. Kofu *et al.*, New J. Phys. **11**, 055001 (2009).
- [124] S. D. Wilson *et al.*, Phys. Rev. B **79**, 184519 (2009).
- [125] A. Jesche *et al.*, Phys. Rev. B **78**, 180504 (2008).
- [126] M. Tegel *et al.*, J. Phys.: Condens. Matter **20**, 452201 (2008).
- [127] Z. P. Yin, K. Haule, and G. Kotliar, Nat. Mater. **10**, 932–935 (2011).
- [128] H. Chen *et al.*, EPL **85**, 17006 (2009).
- [129] D. S. Inosov *et al.*, Phys. Rev. B **79**, 224503 (2009).
- [130] D. Johrendt and R. PAttgen, Physica C: Superconductivity **469**, 332 (2009).
- [131] M. Rotter *et al.*, New J. Phys. **11**, 025014 (2009).
- [132] D. K. Pratt *et al.*, Phys. Rev. Lett. **103**, 087001 (2009).
- [133] S. Nandi *et al.*, Phys. Rev. Lett. **104**, 057006 (2010).
- [134] C. Bernhard *et al.*, New J. Phys. **11**, 055050 (2009).
- [135] P. Marsik *et al.*, Phys. Rev. Lett. **105**, 057001 (2010).
- [136] Y. Laplace *et al.*, Phys. Rev. B **80**, 140501 (2009).
- [137] F. Ning *et al.*, J. Phys. Soc. Jpn. **78**, 013711 (2009).
- [138] F. Massee *et al.*, Phys. Rev. B **79**, 220517 (2009).

- [139] R. M. Fernandes and J. Schmalian, Phys. Rev. B **82**, 014521 (2010).
- [140] J. Zhao *et al.*, Phys. Rev. Lett. **101**, 167203 (2008).
- [141] R. J. McQueeney *et al.*, Phys. Rev. Lett. **101**, 227205 (2008).
- [142] L. W. Harriger *et al.*, Phys. Rev. Lett. **103**, 087005 (2009).
- [143] R. A. Ewings *et al.*, Phys. Rev. B **78**, 220501 (2008).
- [144] S. O. Diallo *et al.*, Phys. Rev. Lett. **102**, 187206 (2009).
- [145] C. Lester *et al.*, Phys. Rev. B **81**, 064505 (2010).
- [146] H.-F. Li *et al.*, Phys. Rev. B **82**, 140503 (2010).
- [147] L. W. Harriger *et al.*, Phys. Rev. B **84**, 054544 (2011).
- [148] K. Kitagawa *et al.*, J. Phys. Soc. Jpn. **77**, 114709 (2008).
- [149] S. H. Baek *et al.*, Phys. Rev. B **78**, 212509 (2008).
- [150] S. H. Baek *et al.*, Phys. Rev. B **79**, 052504 (2009).
- [151] K. Kitagawa, N. Katayama, K. Ohgushi, and M. Takigawa, J. Phys. Soc. Jpn. **78**, 063706 (2009).
- [152] R. A. Ewings *et al.*, Phys. Rev. B **83**, 214519 (2011).
- [153] M. Holt, O. P. Sushkov, D. Stanek, and G. S. Uhrig, Phys. Rev. B **83**, 144528 (2011).
- [154] P. Goswami, R. Yu, Q. Si, and E. Abrahams, Phys. Rev. B **84**, 155108 (2011).
- [155] D.-X. Yao and E. W. Carlson, Phys. Rev. B **78**, 052507 (2008).
- [156] J. J. Pulikkotil *et al.*, Supercond. Sci. and Technol. **23**, 054012 (2010).
- [157] D. Stanek, O. P. Sushkov, and G. S. Uhrig, Phys. Rev. B **84**, 064505 (2011).
- [158] E. Kaneshita and T. Tohyama, Phys. Rev. B **82**, 094441 (2010).
- [159] S. O. Diallo *et al.*, Phys. Rev. B **81**, 214407 (2010).
- [160] D. S. Inosov *et al.*, Nat. Phys. **6**, 178 (2010).
- [161] T. A. Maier, S. Graser, D. J. Scalapino, and P. Hirschfeld, Phys. Rev. B **79**, 134520 (2009).

- [162] I. Eremin and A. V. Chubukov, Phys. Rev. B **81**, 024511gr (2010).
- [163] I. Mazin and J. Schmalian, Physica C: Superconductivity **469**, 614 (2009).
- [164] M. Vojta, Advances in Physics **58**, 699 (2009).
- [165] G. Grüner, Rev. Mod. Phys. **60**, 1129 (1988).
- [166] G. Grüner, *Density Waves in Solids* (Addison-Wesley, Reading, MA, 1994).
- [167] E. Fawcett, Rev. Mod. Phys. **60**, 209 (1988).
- [168] G. Grüner, Rev. Mod. Phys. **66**, 1 (1994).
- [169] R. A. Borzi *et al.*, Science **315**, 214 (2007).
- [170] V. Hinkov *et al.*, Science **319**, 597 (2008).
- [171] D. Haug *et al.*, Phys. Rev. Lett. **103**, 017001 (2009).
- [172] C. Fang *et al.*, Phys. Rev. B **77**, 224509 (2008).
- [173] C. Xu, M. Mueller, and S. Sachdev, Phys. Rev. B **78**, 020501 (2008).
- [174] J. Knolle, I. Eremin, A. Akbari, and R. Moessner, Phys. Rev. Lett. **104**, 257001 (2010).
- [175] T. M. Chuang *et al.*, Science **327**, 181 (2010).
- [176] J.-H. Chu *et al.*, Science **329**, 824 (2010).
- [177] M. Tinkham, *Introduction to Superconductivity* (Dover Publications, Inc., Mineola, New York, 2004).
- [178] D. Scalapino, Physics Reports **250**, 329 (1995).
- [179] K. Seo, B. A. Bernevig, and J. Hu, Phys. Rev. Lett. **101**, 206404 (2008).
- [180] Y. Wan and Q.-H. Wang, EPL **85**, 57007 (2009).
- [181] G. A. Ummaryino, M. Tortello, D. Daghero, and R. S. Gonnelli, Phys. Rev. B **80**, 172503 (2009).
- [182] L. Craco and M. S. Laad, Phys. Rev. B **80**, 054520 (2009).
- [183] S. Onari and H. Kontani, Phys. Rev. Lett. **103**, 177001 (2009).
- [184] T. Saito, S. Onari, and H. Kontani, Phys. Rev. B **82**, 144510 (2010).

- [185] Y. Yanagi, Y. Yamakawa, N. Adachi, and Y. Ono, *J. Phys. Soc. Jpn.* **79**, 123707 (2010).
- [186] M. Yashima *et al.*, *J. Phys. Soc. Jpn.* **78**, 103702 (2009).
- [187] A. Damascelli, Z. Hussain, and Z.-X. Shen, *Rev. Mod. Phys.* **75**, 473 (2003).
- [188] K. Nakayama *et al.*, *EPL* **85**, 67002 (2009).
- [189] D. V. Evtushinsky *et al.*, *New J. Phys.* **11**, 055069 (2009).
- [190] K. Terashima *et al.*, *Proc. Natl. Acad. Sci. USA* **106**, 7330 (2009).
- [191] Y. Zhang *et al.*, *Phys. Rev. Lett.* **105**, 117003 (2010).
- [192] Y.-M. Xu *et al.*, *Nat Phys* **7**, 198 (2011).
- [193] T. Shimojima *et al.*, *Science* **332**, 564 (2011).
- [194] T. Hanaguri, S. Niitaka, K. Kuroki, and H. Takagi, *Science* **328**, 474 (2010).
- [195] X. Zhang *et al.*, *Phys. Rev. B* **82**, 020515 (2010).
- [196] F. Hardy *et al.*, *EPL* **91**, 47008 (2010).
- [197] N. Kurita *et al.*, *Phys. Rev. Lett.* **102**, 147004 (2009).
- [198] Z. Li *et al.*, *J. Phys. Soc. Jpn.* **79**, 083702 (2010).
- [199] Y. Imai *et al.*, *J. Phys. Soc. Jpn.* **80**, 013704 (2011).
- [200] H. Kim *et al.*, *Phys. Rev. B* **83**, 100502 (2011).
- [201] M. L. Teague *et al.*, *Phys. Rev. Lett.* **106**, 087004 (2011).
- [202] O. V. Dolgov, I. I. Mazin, D. Parker, and A. A. Golubov, *Phys. Rev. B* **79**, 060502 (2009).
- [203] L. Shan *et al.*, *Phys. Rev. B* **83**, 060510 (2011).
- [204] L. Shan *et al.*, *Nat Phys* **7**, 325 (2011).
- [205] L. Wray *et al.*, *Phys. Rev. B* **78**, 184508 (2008).
- [206] X. Lu *et al.*, *Supercond. Sci. and Technol.* **23**, 054009 (2010).
- [207] P. Szabo *et al.*, *Phys. Rev. B* **79**, 012503 (2009).
- [208] M. Hiraishi *et al.*, *J. Phys. Soc. Jpn.* **78**, 023710 (2009).

- [209] R. Khasanov *et al.*, Phys. Rev. Lett. **102**, 187005 (2009).
- [210] Z. Shermadini *et al.*, Phys. Rev. B **82**, 144527 (2010).
- [211] P. Samuely *et al.*, Physica C: Superconductivity **469**, 507 (2009).
- [212] Y. Yin *et al.*, Phys. Rev. Lett. **102**, 097002 (2009).
- [213] A. D. Christianson *et al.*, Nature **456**, 930 (2008).
- [214] J. Schrieffer, *Theory of Superconductivity* (Benjamin, Reading, MA, 1964).
- [215] N. Bulut and D. J. Scalapino, Phys. Rev. B **53**, 5149 (1996).
- [216] T. Das and A. V. Balatsky, Journal of Physics: Condensed Matter **24**, 182201 (2012).
- [217] M. Eschrig, Advances in Physics **55**, 47 (2006).
- [218] J. Rossat-Mignod *et al.*, Physica C: Superconductivity **185 - 189**, 86 (1991).
- [219] H. F. Fong *et al.*, Phys. Rev. Lett. **75**, 316 (1995).
- [220] H. F. Fong *et al.*, Nature **398**, 588 (1999).
- [221] H. He *et al.*, Phys. Rev. Lett. **86**, 1610 (2001).
- [222] H. He *et al.*, Science **295**, 1045 (2002).
- [223] M. D. Lumsden *et al.*, Phys. Rev. Lett. **102**, 107005 (2009).
- [224] S. Chi *et al.*, Phys. Rev. Lett. **102**, 107006 (2009).
- [225] S. Li *et al.*, Phys. Rev. B **79**, 174527 (2009).
- [226] D. Parshall *et al.*, Phys. Rev. B **80**, 012502 (2009).
- [227] Y. Qiu *et al.*, Phys. Rev. Lett. **103**, 067008 (2009).
- [228] D. N. Argyriou *et al.*, Phys. Rev. B **81**, 220503 (2010).
- [229] D. K. Pratt *et al.*, Phys. Rev. B **81**, 140510 (2010).
- [230] J. Wen *et al.*, Phys. Rev. B **81**, 100513 (2010).
- [231] S.-i. Shamoto *et al.*, Phys. Rev. B **82**, 172508 (2010).
- [232] J. Zhao *et al.*, Phys. Rev. B **81**, 180505 (2010).
- [233] A. D. Christianson *et al.*, Phys. Rev. Lett. **103**, 087002 (2009).

- [234] S.-H. Lee *et al.*, Phys. Rev. B **81**, 220502 (2010).
- [235] M. Wang *et al.*, Phys. Rev. B **81**, 174524 (2010).
- [236] H. A. Mook *et al.*, Phys. Rev. Lett. **104**, 187002 (2010).
- [237] M. Ishikado *et al.*, Phys. Rev. B **84**, 144517 (2011).
- [238] A. E. Taylor *et al.*, Phys. Rev. B **83**, 220514 (2011).
- [239] J.-P. Castellán *et al.*, Phys. Rev. Lett. **107**, 177003 (2011).
- [240] C. Zhang *et al.*, Sci. Rep. **1**, 1 (2011).
- [241] N. Qureshi *et al.*, Phys. Rev. Lett. **108**, 117001 (2012).
- [242] L. W. Harriger *et al.*, Phys. Rev. B **85**, 054511 (2012).
- [243] J. T. Park *et al.*, Phys. Rev. Lett. **107**, 177005 (2011).
- [244] G. Friemel *et al.*, Phys. Rev. B **85**, 140511 (2012).
- [245] V. Tsurkan *et al.*, Phys. Rev. B **84**, 144520 (2011).
- [246] R. Morinaga *et al.*, Jpn. J. Appl. Phys. **48**, 013004 (2009).
- [247] S. Blundell, *Magnetism in Condensed Matter* (Oxford University Press Inc., New York, 2001).
- [248] Z. Wang *et al.*, Phys. Rev. B **83**, 140505 (2011).
- [249] V. Ksenofontov *et al.*, Phys. Rev. B **84**, 180508 (2011).
- [250] Z. Shermadini *et al.*, Phys. Rev. B **85**, 100501 (2012).
- [251] P. Cai *et al.*, Phys. Rev. B **85**, 094512 (2012).
- [252] A. Charnukha *et al.*, Phys. Rev. B **85**, 100504 (2012).
- [253] S. W. Lovesey, *Theory of Neutron Scattering from Condensed Matter* (Oxford University Press Inc., New York, 1984).
- [254] G. L. Squires, *Introduction to the Theory of Thermal Neutron Scattering* (Cambridge University Press, Cambridge, UK, 1978).
- [255] G. Shirane, S. M. Shapiro, and J. M. Tranquada, *Neutron Scattering with a Triple-Axis Spectrometer* (Cambridge University Press, Cambridge, UK, 2004).
- [256] R. W. Cheary *et al.*, J. Res. Natl. Inst. Stand. Technol. **109**, 1 (2004).

- [257] J. Zhao *et al.*, Nat. Mater. **7**, 953 (2008).
- [258] A. Leineweber, J. Appl. Crystallogr. **39**, 509 (2006).
- [259] A. Leineweber, J. Appl. Crystallogr. **40**, 362 (2007).
- [260] R. Mittal *et al.*, Phys. Rev. B **78**, 224518 (2008).
- [261] M. Rahlenbeck *et al.*, Phys. Rev. B **80**, 064509 (2009).
- [262] J. H. Brewer, *Muon Spin Rotation/Relaxation/Resonance* (VCH Publishers, NY, USA., 1995), Vol. Encyclopedia of Applied Physics Vol. 11.
- [263] Y. J. Uemura *et al.*, Phys. Rev. Lett. **62**, 2317 (1989).
- [264] C. Niedermayer *et al.*, Phys. Rev. Lett. **80**, 3843 (1998).
- [265] C. R. Rotundu *et al.*, Phys. Rev. B **85**, 144506 (2012).
- [266] D. S. Inosov *et al.*, Phys. Rev. B **83**, 214520 (2011).
- [267] C. Lester *et al.*, Phys. Rev. B **79**, 144523 (2009).
- [268] P. C. Canfield *et al.*, Phys. Rev. B **80**, 060501 (2009).
- [269] H. F. Fong *et al.*, Phys. Rev. B **61**, 14773 (2000).
- [270] E. Demler and S.-C. Zhang, Nature **396**, 733 (1998).
- [271] D. K. Morr and D. Pines, Phys. Rev. Lett. **81**, 1086 (1998).
- [272] S. Pailhès *et al.*, Physical Review Letters **96**, 257001 (2006).
- [273] Y. Sidis *et al.*, Comptes Rendus Physique **8**, 745 (2007).
- [274] F. Hardy *et al.*, Phys. Rev. Lett. **102**, 187004 (2009).
- [275] G. Wang *et al.*, Phys. Rev. Lett. **104**, 047002 (2010).
- [276] P. Vilmercati *et al.*, Phys. Rev. B **79**, 220503(R) (2009).
- [277] I. Eremin, D. K. Morr, A. V. Chubukov, and K. Bennemann, Phys. Rev. B **75**, 184534 (2007).
- [278] T. Zhou, Z. D. Wang, and J.-X. Li, Phys. Rev. B **75**, 024516 (2007).
- [279] E. Berg, S. A. Kivelson, and D. J. Scalapino, New J. Phys. **11**, 085007 (2009).
- [280] M. D. Lumsden and A. D. Christianson, J. Phys.: Condens. Matter **22**, 203203 (2010).

- [281] R. M. Fernandes and J. Schmalian, arXiv:1204.3694v2 -, (2012).
- [282] Y. Lee *et al.*, Phys. Rev. B **81**, 060406 (2010).
- [283] P. J. Brown *et al.*, Phys. Rev. B **82**, 024421 (2010).
- [284] K. Matan *et al.*, Phys. Rev. B **82**, 054515 (2010).
- [285] J. Callaway and C. S. Wang, Journal of Physics F: Metal Physics **5**, 2119 (1975).
- [286] J. Callaway, C. S. Wang, and D. G. Laurent, Phys. Rev. B **24**, 6491 (1981).
- [287] M. Dressel and G. Gruener, *Electrodynamics of Solids: Optical Properties of Electrons in Matter* (Cambridge University Press, Cambridge, 2002).
- [288] S. Graser *et al.*, Phys. Rev. B **81**, 214503 (2010).
- [289] S. Graser, T. A. Maier, P. J. Hirschfeld, and D. J. Scalapino, New J. Phys. **11**, 025016 (2009).
- [290] M. M. Qazilbash *et al.*, Nat Phys **5**, 647 (2009).
- [291] P. Larson and S. Satpathy, Phys. Rev. B **79**, 054502 (2009).
- [292] M. D. Lumsden *et al.*, Nat. Phys. **6**, 182 (2010).
- [293] S. Li *et al.*, Phys. Rev. Lett. **105**, 157002 (2010).
- [294] C. H. Lee *et al.*, Phys. Rev. Lett. **106**, 067003 (2011).
- [295] M. Braden *et al.*, Phys. Rev. B **66**, 064522 (2002).
- [296] J. Zhang, R. Sknepnek, and J. Schmalian, Phys. Rev. B **82**, 134527 (2010).
- [297] I. Mazin, Physics **4**, 26 (2011).
- [298] Z. Shermadini *et al.*, Phys. Rev. Lett. **106**, 117602 (2011).
- [299] F. Chen *et al.*, Phys. Rev. X **1**, 021020 (2011).
- [300] X.-W. Yan, M. Gao, Z.-Y. Lu, and T. Xiang, Phys. Rev. Lett. **106**, 087005 (2011).
- [301] I. Shein and A. Ivanovskii, Physics Letters A **375**, 1028 (2011).
- [302] I. Nekrasov and M. Sadoyskii, JETP Letters **93**, 166 (2011).
- [303] T. Qian *et al.*, Phys. Rev. Lett. **106**, 187001 (2011).
- [304] X.-P. Wang *et al.*, EPL **93**, 57001 (2011).

- [305] L. Zhao *et al.*, Phys. Rev. B **83**, 140508 (2011).
- [306] D. Mou *et al.*, Phys. Rev. Lett. **106**, 107001 (2011).
- [307] T. A. Maier, S. Graser, P. J. Hirschfeld, and D. J. Scalapino, Phys. Rev. B **83**, 100515 (2011).
- [308] F. Wang *et al.*, EPL **93**, 57003 (2011).
- [309] T. Das and A. V. Balatsky, Phys. Rev. B **84**, 014521 (2011).
- [310] T. Saito, S. Onari, and H. Kontani, Phys. Rev. B **83**, 140512 (2011).
- [311] I. I. Mazin, Phys. Rev. B **84**, 024529 (2011).
- [312] P. Zavalij *et al.*, Phys. Rev. B **83**, 132509 (2011).
- [313] V. Y. Pomjakushin *et al.*, Phys. Rev. B **83**, 144410 (2011).
- [314] R. H. Liu *et al.*, EPL **94**, 27008 (2011).
- [315] Y. J. Yan *et al.*, Sci. Rep. **2**, 1 (2012).
- [316] X.-W. Yan, M. Gao, Z.-Y. Lu, and T. Xiang, Phys. Rev. B **84**, 054502 (2011).
- [317] C. Cao and J. Dai, Phys. Rev. Lett. **107**, 056401 (2011).
- [318] W.-G. Yin, C.-C. Lee, and W. Ku, Phys. Rev. Lett. **105**, 107004 (2010).
- [319] T. Das and A. V. Balatsky, Phys. Rev. B **84**, 115117 (2011).
- [320] A. Ricci *et al.*, Phys. Rev. B **84**, 060511 (2011).
- [321] L. Li *et al.*, Phys. Rev. B **84**, 174501 (2011).
- [322] Y. Texier *et al.*, arxiv:1203.1834 -, (2012).
- [323] M. Wang *et al.*, Phys. Rev. B **84**, 094504 (2011).
- [324] F. Ye *et al.*, Phys. Rev. Lett. **107**, 137003 (2011).
- [325] C.-H. Li *et al.*, Phys. Rev. B **83**, 184521 (2011).
- [326] L. Ma *et al.*, Phys. Rev. B **84**, 220505 (2011).
- [327] V. Hinkov *et al.*, Nat Phys **3**, 780 (2007).
- [328] G. Yu *et al.*, Phys. Rev. B **81**, 064518 (2010).
- [329] G. Yu, Y. Li, E. M. Motoyama, and M. Greven, Nat Phys **5**, 873 (2009).

- [330] K. Nakayama *et al.*, Phys. Rev. B **83**, 020501 (2011).
- [331] K. Matano *et al.*, EPL **87**, 27012 (2009).
- [332] G. Li *et al.*, Phys. Rev. Lett. **101**, 107004 (2008).
- [333] C. Ren *et al.*, Phys. Rev. Lett. **101**, 257006 (2008).
- [334] Z. Lin *et al.*, Chinese Physics Letters **25**, 4402 (2008).
- [335] Y. S. Kwon *et al.*, arXiv:1007.3617 -, (2010).
- [336] K. Hashimoto *et al.*, Phys. Rev. Lett. **102**, 017002 (2009).
- [337] T. Nishizaki, Y. Nakajima, T. Tamegai, and N. Kobayashi, J. Phys. Soc. Jpn. **80**, 014710 (2011).
- [338] J. J. Tu *et al.*, Phys. Rev. B **82**, 174509 (2010).
- [339] M. Tortello *et al.*, Phys. Rev. Lett. **105**, 237002 (2010).
- [340] T. J. Williams *et al.*, Phys. Rev. B **80**, 094501 (2009).
- [341] F. Hardy *et al.*, Phys. Rev. B **81**, 060501 (2010).
- [342] E. G. Maksimov *et al.*, Phys. Rev. B **83**, 140502 (2011).
- [343] K. W. Kim *et al.*, Phys. Rev. B **81**, 214508 (2010).
- [344] L. Luan *et al.*, Phys. Rev. Lett. **106**, 067001 (2011).
- [345] D. Wu *et al.*, arXiv:1011.1207 -, (2010).
- [346] J. Park *et al.*, New Journal of Physics **13**, 033005 (2011).
- [347] R. Khasanov *et al.*, Phys. Rev. Lett. **103**, 067010 (2009).
- [348] S. Kawasaki *et al.*, Phys. Rev. B **78**, 220506(R) (2008).
- [349] L. Shan *et al.*, EPL **83**, 57004 (2008).
- [350] M. Gang *et al.*, Chinese Physics Letters **25**, 2221 (2008).
- [351] R. S. Gonnelli *et al.*, Phys. Rev. B **79**, 184526 (2009).
- [352] K. Matano *et al.*, EPL **83**, 57001 (2008).
- [353] T. Kondo *et al.*, Phys. Rev. Lett. **101**, 147003 (2008).
- [354] J. Karpinski *et al.*, Physica C: Superconductivity **469**, 370–380 (2009).

- [355] T. Mertelj *et al.*, Phys. Rev. Lett. **102**, 117002 (2009).
- [356] Y.-L. Wang *et al.*, Supercond. Sci. and Technol. **22**, 015018 (2009).
- [357] D. Daghero *et al.*, Phys. Rev. B **80**, 060502(R) (2009).
- [358] T. Y. Chen *et al.*, Nature **453**, 1224 (2008).
- [359] O. Millo *et al.*, Phys. Rev. B **78**, 092505 (2008).
- [360] K. A. Yates *et al.*, New J. Phys. **11**, 025015 (2009).
- [361] D. S. Inosov *et al.*, Phys. Rev. Lett. **104**, 187001 (2010).
- [362] U. Stockert *et al.*, Phys. Rev. B **83**, 224512 (2011).
- [363] Y. J. Song *et al.*, EPL **94**, 57008 (2011).
- [364] F. Wei *et al.*, Phys. Rev. B **81**, 134527 (2010).
- [365] K. Sasmal *et al.*, Phys. Rev. B **81**, 144512 (2010).
- [366] Z.-H. Liu *et al.*, Phys. Rev. B **84**, 064519 (2011).
- [367] R. Khasanov *et al.*, Phys. Rev. B **78**, 220510 (2008).
- [368] M. Bendele *et al.*, Phys. Rev. B **81**, 224520 (2010).
- [369] P. K. Biswas *et al.*, Phys. Rev. B **81**, 092510 (2010).
- [370] A. Gunther *et al.*, Supercond. Sci. and Technol. **24**, 045009 (2011).
- [371] C. C. Homes *et al.*, Phys. Rev. B **81**, 180508 (2010).
- [372] W. K. Park *et al.*, arXiv:1005.0190 -, (2010).
- [373] J. Hu *et al.*, Phys. Rev. B **83**, 134521 (2011).
- [374] T. Kato *et al.*, Phys. Rev. B **80**, 180507(R) (2009).
- [375] R. H. Yuan *et al.*, Sci. Rep. **2**, 1 (2012).
- [376] Y. Zhang *et al.*, Nat Mater **10**, 273 (2011).
- [377] W. Yu *et al.*, Phys. Rev. Lett. **106**, 197001 (2011).

Acknowledgements

First of all, I would like to thank Prof. Bernhard Keimer having me here at the Max Planck Institute as a doctoral student. Without his scientific and personal support, it would be almost impossible to finish my PhD work decently. Especially, his wealth knowledge of high- T_c superconductors and inelastic neutron scattering brought me to be confident about my research on the iron-based superconductors. I am also grateful to Prof. Harald Giessen being a committee member of my thesis.

I am very thankful to my two (present and former) supervisors Dr. Dmytro Inosov and Dr. Vladimir Hinkov who helped me to earn deep insight into the experimental physics in general and encouraged me a lot during my PhD period. Your everyday support was one of main sources to work hard. I also learnt many miscellaneous things from them, such as organizing a network of collaborations, beautiful graphical design, European-style philosophy. All these would be helpful for the next step in my research career. I really enjoyed working with you for 24/7, and it was wonderful being a part of “dream team” (named by Vladimir)!

All the neutron scattering experiments which I conducted were done under strong support from local contact scientists at the neutron sources: Dr. Philippe Bourges and Dr. Yvan Sidis at the Laboratoire Léon Brillouin, Dr. Alexander Ivanov at the Institut Laue-Langevin, and Dr. Klaudia Hradil, Dr. Peter Links, Dr. Thomas Keller, Dr. Astrid Schneidewind, and Dr. Enrico Faulhaber at the Forschungsneutronenquelle Heinz Maier-Leibnitz. I also would like to appreciate to Dr. Yuan Li (now he is a professor at the Peking University) whom I learnt a lot of useful technique for an inelastic neutron scattering experiment.

I appreciate to members of crystal growth group led by Dr. Chengtian Lin at the MPI for timely providing sizable single crystals. Especially, I thank Dr. Dunlu Sun who spent most of his time at MPI for growing big size single crystals for our neutron experiments. I also profited from collaboration with Dr. Vladimir Tsurkan at the University of Augsburg and Prof. Yong Sung Kwon at the DGIST Korea.

Our experimental work on pnictide system became tremendously strengthen by theoretical support. I am grateful to Dr. Alexander Yaresko in the Abt. Andersen at MPI and Prof. Siegfried Graser at the University of Augsburg for their theoretical calculations. Thanks for being patient with my stupid questions during all discussions

we had.

It was a great pleasure working and traveling with members (former and present) in the neutron spectroscopy group: Gerd Friemel, Dr. Daniel Haug, Dr. Hoyoung Jang, Dr. Jungwha Kim, Toshi Lowe, Dr. Markus Raichle, and Dr. Anton Suchaneck. I thank for all your help during the beamtimes we had together. I personally appreciate to Gerd for translating the summary of thesis into German. Vielen Dank!

One very nice thing staying at the MPI was that there are always clever theoreticians around. I sometimes bothered them with idiotic questions, but they seemed to be happy to discuss with me (it's purely my opinion though!). Thanks to Dr. Jiri Chaloupka, Dr. Dmitri Efremov, Dr. Giniyat Khaliullin, and Dr. George Jackeli.

I deeply appreciate to Alex Charnukha, Dr. Darren Peets, and Dr. Andrew Walters for their careful proofreading on this thesis.

I pretty much enjoyed talking to my officemates, Aliaksei Charnukha, Dr. Vladimir Damljanovic, Alex Frano, Michaela Souliou, Friederike Wrobel. Thanks for exciting stories and useful discussions. Never sign anything when you are drunken! I also would like to thank all of our group members for their support and discussions.

I am grateful to Korean mafia at the MPI for their personal support and "sometimes" scientific advices. Thanks for being kind friends in Korean way.

There has been a constant support from my family in Korea, my parents, parents-in-law, and sister. Thanks a lot.

Special thanks to my beloved wife Sun-Hee Lee for her entire support and trust on me. It could be a difficult decision to come to foreign country leaving her prospective job career and family in Korea. I am sincerely appreciated it. Last but not least, I would like to mention that how much I love my two children, Youngwha Park and Youngjoon Park who were born during my PhD period.